AD-A066 195 AIR FORCE INST OF TECH WRIGHT-PATTERSON AFB OHIO SCH--ETC F/G 17/8
ESTIMATION OF AIRCRAFT TARGET MOTION USING PATTERN RECOGNITION --ETC(U)
DEC 78 J D KENDRICK

UNCLASSIFIED AFIT/DS/EE/78-6 NL

1 OF 3
AD
A066195

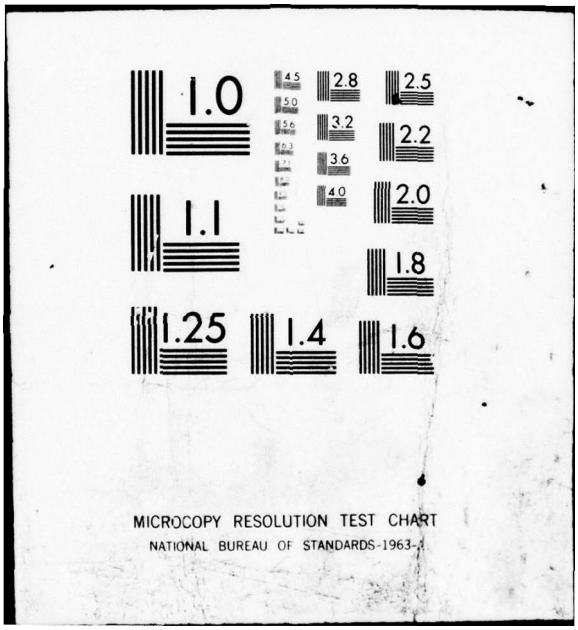
1.0
1.1
1.25
1.4
1.6
1.8
2.0
2.2
2.5
2.8
3.2
3.6
4.0
4.5
5.0
5.6
6.3
7.1
MICROCOPY RESOLUTION TEST CHART
NATIONAL BUREAU OF STANDARDS-1963-A

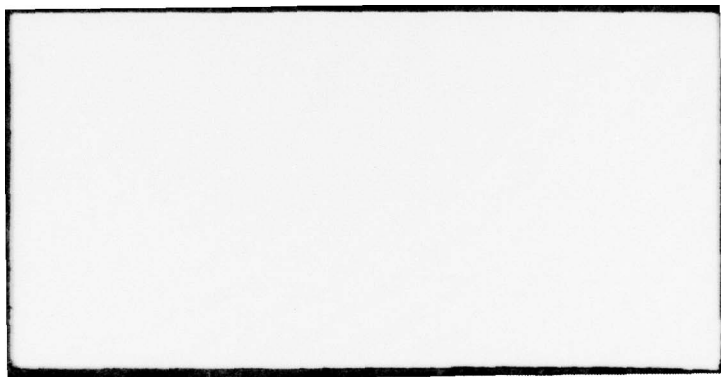

AFIT/DS/EE/78-6

(1)

AD A066195

DDC
RECEIVED
MAR 22 1979
C

DDC FILE COPY

(6) ESTIMATION OF AIRCRAFT TARGET MOTION USING PATTERN RECOGNITION ORIENTATION MEASUREMENTS.

DISSERTATION

(9) Doctoral thesis,

(14) AFIT/DS/EE/78-6

(10) Jerry D. Kendrick
Captain USAF

(11) Dec 78

(12) 207p

Approved for public release; distribution unlimited

012225

79 03 19 021

AFIT/DS/EE/78-6

# ESTIMATION OF AIRCRAFT TARGET MOTION USING PATTERN RECOGNITION ORIENTATION MEASUREMENTS

DISSERTATION

Presented to the Faculty of the School of Engineering
of the Air Force Institute of Technology
Air University
in Partial Fulfillment of the
Requirements for the Degree of
Doctor of Philosophy

by

Jerry D. Kendrick, BSEE, MEE
Captain USAF

Approved for public release; distribution unlimited

AFIT/DS/EE/78-6

# ESTIMATION OF AIRCARFT TARGET MOTION USING PATTERN RECOGNITION ORIENTATION MEASUREMENTS

by

Jerry D. Kendrick, BSEE, MEE

Captain USAF

Approved:

Dr. Peter S. Maybeck, Chairman _____

Capt J. Gary Reid, PhD _____

Dr. David R. Barr _____

Dr. Lynn E. Wolaver
Dean's Representative _____

Accepted:

J. S. Przemieniecki
Dean, School of Engineering _____

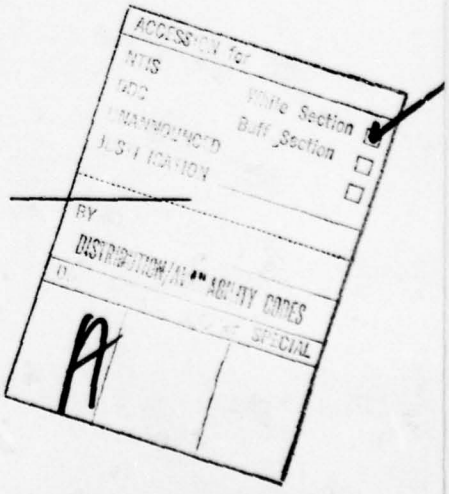

## Acknowledgements

This research was sponsored by the Fire Control Branch of the Reconnaissance and Weapon Delivery Division of the Air Force Avionics Laboratory (AFAL), Wright-Patterson AFB, Ohio. I am grateful for the support of the lab during my tour from September 1975 to April 1978. Continuing dialogs with AFAL fire control engineers Mr. Ralph Bryan, Capt William Ashton and Capt Robert Lutter were especially beneficial during the developmental and simulation portions of this research.

I wish to thank my advisor Dr. Peter S. Maybeck for his encouragement during the rough times and his constant enthusiasm for this research effort since its inception. A special acknowledgement is due Capt J. Gary Reid for his vision of an integrated electro-optical/radar system for improved state estimation of highly maneuvering aircraft targets. His position in AFAL and his experience in the area of pattern recognition provided the unique ingredients to set this research in motion. I also wish to thank AFIT professor Dr. David Barr for his valuable contributions in the statistical modeling of acceleration for the interactive filter developed herein.

I wish to express my appreciation for the understanding of management at my current assignment, the Air Force Technical Applications Center. Without their strong support from April, completion in 1978 would not have been possible. Finally, I thank Mrs. Mary Hilton for an excellent job of typing the final manuscript.

## Contents


| | | Page |
|---|---|---|
| Acknowledgements | | iii |
| List of Figures | | vi |
| List of Tables | | xii |
| Abstract | | xiii |
| I. | Introduction | 1 |
| 1.1 | The Pointing, Tracking and State Estimation Problem | 1 |
| 1.2 | A New Approach | 11 |
| 1.3 | Organization of Remaining Chapters | 14 |
| II. | Interactive Target State Estimator | 15 |
| 2.1 | System Description | 15 |
| 2.2 | Mathematical Formulation of Target Kinematic Model | 20 |
| 2.2.1 | Dynamic State Equations | 20 |
| 2.2.2 | Measurement Equations | 30 |
| 2.3 | Mathematical Formulation of Target Aspect Model | 31 |
| 2.3.1 | Dynamic State Equations | 40 |
| 2.3.2 | Measurement Equations | 41 |
| 2.3.2.1 | Target Velocity Used to Define Roll Axis | 42 |
| 2.3.2.2 | Target Aspect Using Angle of Attack | 43 |
| 2.4 | Interactive Filter Formulation | 45 |
| 2.4.1 | Computer Logic Structure | 46 |
| 2.4.2 | Timing Sequence For Interactive Filter | 57 |
| III. | Performance Analysis and Computer Simulation | 60 |
| 3.1 | Interactive Filter System Performance Analysis | 60 |
| 3.1.1 | Scenarios | 60 |
| 3.1.2 | Monte Carlo Simulation Technique | 67 |
| 3.1.3 | Figures of Merit | 67 |
| 3.1.4 | Comparative Radar Filter | 72 |
| 3.1.5 | Tuning | 73 |
| 3.1.6 | Performance Analysis Plan | 75 |
| 3.2 | Computer Simulation | 79 |

## Contents


| | | Page |
|---|---|---|
| IV. | Results and Discussion | 81 |
| | 4.1 Figures of Merit | 81 |
| | 4.2 Criticality of Filter Parameters | 83 |
| | 4.3 Recovery and Sensitivity Characteristics | 85 |
| | 4.3.1 Bad Initial Conditions | 85 |
| | 4.3.2 One-Time Bad Measurements | 85 |
| | 4.3.3 Unmodeled Radar Errors | 87 |
| | 4.4 Aspect Error Analysis | 89 |
| | 4.5 Aspect Noise Analysis | 90 |
| | 4.5.1 Measurement Noise Increased | 90 |
| | 4.5.2 Measurement Bias | 92 |
| | 4.5.3 Different Noise Model | 92 |
| | 4.6 E-O/PR System Not Available | 93 |
| V. | Considerations For Real-Time Implementation | 95 |
| | 5.1 Parallel Processing | 95 |
| | 5.2 Sparse Matrix Techniques | 96 |
| | 5.3 Fixed-Gain Filter | 98 |
| | 5.4 Scalar Processing of Measurements | 99 |
| | 5.5 Quasi-Static Filter Approximation | 100 |
| | 5.6 Filter Linearization | 102 |
| | 5.7 Angle Approximations | 105 |
| VI. | Conclusions and Recommendations For Future Research | 106 |
| Bibliography | | 110 |
| Appendix A: | Graphical Simulation Results | 114 |
| Appendix B: | Coordinate Transformations | 155 |
| Appendix C: | Statistical Characteristics of Modeled Normal Load Acceleration Magnitude | 164 |
| Appendix D: | Kinematically Derived Target Aspect | 174 |
| Appendix E: | Pre-Tuning and Tuned Filter Parameters | 183 |
| VITA | | 191 |

## List of Figures


| Figure | | Page |
|---|---|---|
| 1-1 | Singer Model For Target Acceleration Probability Density | 5 |
| 1-2 | Kolibaba Model For Target Acceleration Probability Density | 6 |
| 2-1 | Aircraft Body Axes | 16 |
| 2-2 | Interactive State Estimation System | 18 |
| 2-3 | Aircraft Load Acceleration in Level Turn | 22 |
| 2-4 | First Order Probability Density Function For Normal Load Acceleration During Evasive Maneuver | 27 |
| 2-5 | Measurement Geometry | 30 |
| 2-6 | Image Plane Orientation | 35 |
| 2-7 | Typical Target and Attacker Turning Plane Geometry For Pure Pursuit and Several Initial Angles-Off | 39 |
| 2-8 | Alternative Image Plane Orientation | 40 |
| 2-9 | Flow Chart, Interactive Filter, Simulation Version | 47 |
| 2-10 | Timing Sequence, Interactive Filter | 59 |
| 3-1 | Scenario 1, Distant Break | 62 |
| 3-2 | Scenario 2, Close-In Break With Attacker Overshoot | 63 |
| 3-3 | Scenario 3, Roll Followed By High-g Break | 64 |
| 3-4 | Scenario 4, Head-On Pass | 65 |
| 3-5 | Computer Simulation System | 80 |
| 4-1 | Acceleration pdf For Several Choices of Parameters $\alpha, \beta, \gamma$ | 84 |
| 5-1 | Parallel Processing Filter Cycle | 97 |
| 5-2 | Gaussian Approximations To pdf In Non-Linear Model | 104 |

## List of Figures


| Figure | | Page |
|---|---|---|
| A-1 | Scenario 1, Average Error in Predicted Target Position, Interactive Filter . . . . . | 115 |
| A-2 | Scenario 1, Average Error in Predicted Target Position, Comparative Filter . . . . . | 115 |
| A-3 | Scenario 1, Average Error in Predicted Cross-Range Target Position, Interactive Filter . . . . . | 116 |
| A-4 | Scenario 1, Average Error in Predicted Cross-Range Target Position, Comparative Filter . . . . . | 116 |
| A-5 | Scenario 1, Average CEP, Interactive Filter . . . . . | 117 |
| A-6 | Scenario 1, Average CEP, Comparative Filter . . . . . | 117 |
| A-7 | Scenario 1, Average Error in Predicted Target Position, Interactive Filter, $\alpha = 8$, $\beta = -2$, $\gamma = 0.5$ . . . . . | 118 |
| A-8 | Scenario 1, Average Error in Predicted Target Position, Interactive Filter, $\alpha = 8$, $\beta = -1$, $\gamma = 0.5$ . . . . . | 119 |
| A-9 | Scenario 1, Average Error in Predicted Target Position, Interactive Filter, Bad Initial Conditions . . . . . | 120 |
| A-10 | Scenario 1, Average Error in Predicted Target Position, Comparative Filter, Bad Initial Conditions . . . . . | 120 |
| A-11 | Scenario 1, Average Error in Predicted Target Position, Interactive Filter, One-time Bad Measurement 5 Seconds Into Scenario . . . . . | 121 |
| A-12 | Scenario 1, Average Error in Predicted Target Position, Comparative Filter, One-time Bad Measurement 5 Seconds Into Scenario . . . . . | 121 |
| A-13 | Scenario 1, Average Error in Predicted Cross-Range Target Position, Interactive Filter, One-time Bad Measurement 5 Seconds Into Scenario . . . . . | 122 |
| A-14 | Scenario 1, Average Error in Predicted Cross-Range Target Position, Comparative Filter, One-time Bad Measurement 5 Seconds Into Scenario . . . . . | 122 |

## List of Figures


| Figure | | Page |
|---|---|---|
| A-15 | Scenario 1, Average Error in Predicted Target Position, Interactive Filter, Large Unmodeled Radar Errors | 123 |
| A-16 | Scenario 1, Average Error in Predicted Target Position, Comparative Filter, Large Unmodeled Radar Errors | 123 |
| A-17 | Scenario 1, Average Error in Predicted Cross-Range Target Position, Interactive Filter, Large Unmodeled Radar Errors | 124 |
| A-18 | Scenario 1, Average Error in Predicted Cross-Range Target Position, Comparative Filter, Large Unmodeled Radar Errors | 124 |
| A-19 | Scenario 1, Average CEP, Interactive Filter, Large Unmodeled Radar Errors | 125 |
| A-20 | Scenario 1, Average CEP, Comparative Filter, Large Unmodeled Radar Errors | 125 |
| A-21 | Scenario 1, Average Error in Kalman Filter Estimated Target Aspect | 126 |
| A-22 | Scenario 1, Average Error in Kinematically Derived Target Aspect | 127 |
| A-23 | Scenario 1, Average Error in Predicted Target Position, Interactive Filter, E-O/PR Aspect Measurement Noise 25 Degrees (1$\sigma$), Filter Unaware | 128 |
| A-24 | Scenario 1, Average Error in Predicted Cross-Range Target Position, Interactive Filter, E-O/PR Aspect Measurement Noise 25 Degrees (1$\sigma$), Filter Unaware | 129 |
| A-25 | Scenario 1, Average CEP, Interactive Filter, E-O/PR Aspect Measurement Noise 25 Degrees (1$\sigma$), Filter Unaware | 130 |
| A-26 | Scenario 1, Average Error in Predicted Target Position, Interactive Filter, E-O/PR Aspect Measurement Noise 25 Degrees (1$\sigma$), Filter Aware | 131 |
| A-27 | Scenario 1, Average Error in Predicted Cross-Range Target Position, Interactive Filter, E-O/PR Aspect Measurement Noise 25 Degrees (1$\sigma$), Filter Aware | 132 |

## List of Figures


| Figure | | Page |
|---|---|---|
| A-28 | Scenario 1, Average CEP, Interactive Filter, E-O/PR Aspect Measurement Noise 25 Degrees (1σ), Filter Aware | 133 |
| A-29 | Scenario 1, Average Error in Kalman Filter Estimated Target Aspect, E-O/PR Aspect Measurement Noise 25 Degrees (1σ), Filter Aware | 134 |
| A-30 | Scenario 1, Average Error in Kinematically Derived Target Aspect, E-O/PR Aspect Measurement Noise 25 Degrees (1σ), Filter Aware | 135 |
| A-31 | Scenario 1, Average Error in Predicted Target Position, Interactive Filter, 5 Degrees Fixed Bias Added to All Yaw, Pitch and Roll E-O/PR Measurements | 136 |
| A-32 | Scenario 1, Average Error in Predicted Cross-Range Target Position, Interactive Filter, Five Degrees Fixed Bias Added to All Yaw, Pitch and Roll E-O/PR Measurements | 137 |
| A-33 | Scenario 1, Average CEP, Interactive Filter, Five Degrees Fixed Bias Added to All Yaw, Pitch and Roll E-O/PR Measurements | 138 |
| A-34 | Scenario 1, Average Error in Kalman Filter Estimated Target Aspect, Five Degrees Fixed Bias Added to All Yaw, Pitch and Roll E-O/PR Measurements | 139 |
| A-35 | Scenario 1, Average Error in Kinematically Derived Target Aspect, Five Degrees Fixed Bias Added to All Yaw, Pitch and Roll E-O/PR Measurements | 140 |
| A-36 | Scenario 1, Average Error in Predicted Target Position, Interactive Filter, No E-O/PR Aspect Measurements Provided | 141 |
| A-37 | Scenario 1, Average Error in Predicted Cross-Range Target Position, Interactive Filter, No E-O/PR Aspect Measurements Provided | 142 |
| A-38 | Scenario 1, Average CEP, Interactive Filter, No E-O/PR Aspect Measurements Provided | 143 |
| A-39 | Scenario 1, Average Error in Kalman Filter Estimated Target Aspect, No E-O/PR Aspect Measurements Provided | 144 |

## List of Figures


| Figure | | Page |
|---|---|---|
| A-40 | Scenario 1, Average Error in Kinematically Derived Target Aspect, No E-O/PR Aspect Measurements Provided . . . . | 145 |
| A-41 | Scenario 2, Average Error in Predicted Target Position, Interactive Filter . . . . . | 146 |
| A-42 | Scenario 2, Average Error in Predicted Target Position, Comparative Filter . . . . . | 146 |
| A-43 | Scenario 2, Average Error in Predicted Cross-Range Target Position, Interactive Filter . . . . . | 147 |
| A-44 | Scenario 2, Average Error in Predicted Cross-Range Target Position, Comparative Filter . . . . . | 147 |
| A-45 | Scenario 2, Average CEP, Interactive Filter . . . . . | 148 |
| A-46 | Scenario 2, Average CEP, Comparative Filter . . . . . | 148 |
| A-47 | Scenario 3, Average Error in Predicted Target Position, Interactive Filter . . . . . | 149 |
| A-48 | Scenario 3, Average Error in Predicted Target Position, Comparative Filter . . . . . | 149 |
| A-49 | Scenario 3, Average Error in Predicted Cross-Range Target Position, Interactive Filter . . . . . | 150 |
| A-50 | Scenario 3, Average Error in Predicted Cross-Range Target Position, Comparative Filter . . . . . | 150 |
| A-51 | Scenario 3, Average CEP, Interactive Filter . . . . . | 151 |
| A-52 | Scenario 3, Average CEP, Comparative Filter . . . . . | 151 |
| A-53 | Scenario 4, Average Error in Predicted Target Position, Interactive Filter . . . . . | 152 |
| A-54 | Scenario 4, Average Error in Predicted Target Position, Comparative Filter . . . . . | 152 |
| A-55 | Scenario 4, Average Error in Predicted Cross-Range Target Position, Interactive Filter . . . . . | 153 |
| A-56 | Scenario 4, Average Error in Predicted Cross-Range Target Position, Comparative Filter . . . . . | 153 |

## List of Figures


| Figure | | Page |
|---|---|---|
| A-57 | Scenario 4, Average CEP, Interactive Filter . . . . . | 154 |
| A-58 | Scenario 4, Average CEP, Comparative Filter . . . . . | 154 |
| B-1 | Tracker Line-of-Sight Geometry . . . . . | 158 |
| B-2 | Image Plane Geometry . . . . . | 160 |
| C-1 | Autocorrelation Function For Normal Load Acceleration Magnitude and State Variable, $\underline{\varepsilon}$ . . . . . | 173 |
| D-1 | Angle-of-Attack Geometry . . . . . | 177 |

## List of Tables


| Tables | | Page |
|---|---|---|
| I | Comparison of Air-To-Air To Generic Problem | 13 |
| II | Parameters Read From Trajectory Tape | 54 |
| III | Initial Parameters For Scenarios | 66 |
| IV | Performance Analysis Plan | 76 |
| V | Interactive Filter Vs. Radar-Only Filter, Approximate Steady-State Performance Values | 82 |
| VI | Approximate Steady-State Performance Values, Various Filter Parameters, Scenario 1 | 86 |
| VII | Radar Measurement Noise Levels, Large Unmodeled Errors | 88 |
| VIII | Average Steady-State Performance Values, With Large Unmodeled Radar Errors | 89 |
| B-I | Angles and Corresponding Trigonometric Functions | 163 |
| D-I | Aspect Angle Determination, Example | 182 |
| E-I | Kinematic Initial State Covariance, $P_o$ | 183 |
| E-II | Kinematic Modeling Covariance, Q | 184 |
| E-III | Kinematic Measurement Covariance, R | 185 |
| E-IV | Aspect Initial State Covariance, $P_{a_o}$ | 186 |
| E-V | Aspect Modeling Covariance, $Q_a$ | 186 |
| E-VI | Aspect Measurement Covariance, $R_a$ | 187 |
| E-VII | Remaining Filter Parameters, Interactive Filter | 188 |
| E-VIII | Radar Initial State Covariance, $P_o$ | 189 |
| E-IX | Radar Modeling Covariance, Q | 190 |
| E-X | Remaining Filter Parameters, Radar Filter | 190 |

## Abstract

A new approach to estimating motion of a highly maneuvering aircraft target in an air-to-air tracking scenario is presented. An interactive filter system is developed which provides an improved estimate of target motion states by conditioning kinematic filter estimates upon target aspect angle data. Pattern recognition techniques used with an electro-optical tracker are presumed to provide this target aspect information. A target orientation filter processes the aspect angle measurements by statistically weighting measured aspect angles with the current best estimate of target kinematics. The aerodynamic lift equation is used to relate approximate angle of attack to target velocity and acceleration. A novel statistical model for aircraft target normal acceleration is also developed to better represent unknown target accelerations. Simulation results of realistic three-dimensional scenarios are presented to evaluate the performance of the interactive filter system.

# I. Introduction

## 1.1 The Pointing, Tracking and State Estimation Problem

The subject of treatment in this dissertation is the general class of estimation and control problems known as "pointing and tracking," and in particular pointing and tracking against a highly maneuvering aircraft target. The ability to align some observer-based coordinate frame relative to the line-of-sight (LOS) to a target (pointing) and to maintain that alignment as the target moves (tracking) depends, among other things, on the observer's certainty of the target's motion behavior. The degree of certainty in an observer's knowledge of target behavior is a function of three variables: (1) believability of the observer's sensor systems, (2) the degree of coupling between the parameters measured and those about which knowledge is desired, and (3) the uncertainty in the target's behavior between observations. The extreme case of continuous observations of all the desired parameters with perfect sensors clearly yields no uncertainty in current target behavior. The more practical case is that of periodic measurements of some related parameters with imperfect sensors.

It was this latter case which motivated the use of the mathematical science of estimation theory. In this theory, statistical models are proposed to account for uncertainties in each of the three areas. The product of this theory, the estimator, accepts observations of pertinent parameters, relates these to the desired states of interest, accounts

for the likely movement of states between these observations, and even attempts to model the uncertainty in its own ability to estimate the states of interest.

Given a particular sensor system with its known or assumed characteristics and location, the questions raised in (1) and (2) above can readily be resolved. One of the principal problems in pointing and tracking, and addressed by many investigators, is that of (3) above, improving accuracy and responsiveness of the estimator in a setting of uncertain dynamics of the target.

A distinction can be made between targets with "known" dynamics (except perhaps for unknown parameters), and targets with "unknown" dynamics. The usual choice of one of these two classes for the target depends on the uncertainty in the equations describing the target's state. An object moves in a medium in response to forces acting upon it. In most practical problems, those forces are either reasonably well understood and directly observable, or reasonably well understood but not directly observable. These two cases are illustrated by the following examples. A non-thrusting, earth-orbiting satellite has well-modeled dynamics, even though there are many small unmodeled disturbing forces acting on it, because the dominant forces are known. Once the satellite orbit has been determined, prediction of future position is limited primarily by the effects of these small perturbing forces. The satellite is said to have "known" dynamics. As another example, an aircraft maneuvers through the air controlled by movable surfaces on its airfoils. The dynamic behavior of the aircraft is well-modeled if these airfoil surface positions are known, as on an instrumented aircraft. There are still unmodeled uncertainties, but the dominant forces are known. This cooperative aircraft has "known" dynamics. If, however,

the control surface positions are not observable, such as on an uncooperative target, the mathematical equations which had modeled the dynamic behavior would no longer be appropriate. The uncooperative aircraft target would then be classified as having "unknown" dynamics even though some parameters of its motion through the air are still observable. Unknown dynamics can mean a large uncertainty in the nature of the dominant forces causing the dynamic behavior, but it usually means that the dominant forces are not observable.

One of the most common techniques for modeling target behavior, when dynamics are "unknown," is based upon the principle that kinematic parameters, such as velocity and acceleration, are time-correlated. The dynamic models discussed below treat the target as a point mass, thus restricting the description of target motion to kinematics of the center of mass. Fitts [15] assumes that the relative motion of the target undergoes a random acceleration in each inertial axis, i.e.,

$$\ddot{\underline{x}}_i(t) = \underline{\xi}_i(t) \qquad i = 1, 2, 3 \tag{1-1}$$

and that $\underline{\xi}_i(t)$ is time-correlated, i.e.,

$$\dot{\underline{\xi}}_i(t) = -\omega_o \underline{\xi}_i(t) + \underline{\xi}_i'(t) \tag{1-2}$$

where $\underline{\xi}_i'(t)$ is white noise, and

$$E\left[\underline{\xi}_i(t)\underline{\xi}_i(t+\tau)\right] = \sigma_{\xi_i}^2 e^{-\omega_o|\tau|} \tag{1-3}$$

Singer [46] reduces the set of differential equations (1-1) and (1-2) to difference equations,

$$\underline{x}_i(t_{k+1}) = A(\Delta T, \omega_o)\, \underline{x}_i(t_k) + \underline{W}_i(t_{k+1}) \tag{1-4}$$

$$t_{k+1} = t_k + \Delta T, \qquad i = 1, 2, 3 \tag{1-5}$$

$$A(\Delta T,\omega_o) = \begin{bmatrix} 1 & \Delta T & \frac{1}{\omega_o^2}(-1+\omega_o\Delta T+e^{-\omega_o\Delta T}) \\ 0 & 1 & \frac{1}{\omega_o}(1-e^{-\omega_o\Delta T}) \\ 0 & 0 & e^{-\omega_o\Delta T} \end{bmatrix} \tag{1-6}$$

and

$$\underline{W}_i(t_{k+1}) = \int_{t_k}^{t_{k+1}} A(t_{k+1}-\tau,\omega_o) \begin{bmatrix} 0 \\ 0 \\ \underline{\xi}_i(\tau) \end{bmatrix} d\tau \tag{1-7}$$

This set of equations reduces, for small sampling intervals $\Delta T$, to

$$\underline{x}_i(t_{k+1}) = A(\Delta T)\underline{x}_i(t_k) + \begin{bmatrix} 0 \\ 0 \\ \underline{W}_i(t_{k+1}) \end{bmatrix} \tag{1-8}$$

where

$$A(\Delta T) = \begin{bmatrix} 1 & \Delta T & \frac{\Delta T^2}{2} \\ 0 & 1 & \Delta T \\ 0 & 0 & 1 \end{bmatrix} \tag{1-9}$$

and $E\,[\underline{W}_i(t_k)\underline{W}_i^T(t_k)]$ reduces to

$$Q_i(t_k) = \begin{bmatrix} 0 & 0 & 0 \\ 0 & 0 & 0 \\ 0 & 0 & 2\omega_o\Delta T\sigma_{\xi_i}^2 \end{bmatrix} \tag{1-10}$$

Singer asserts that a suitable probability density for each component of total acceleration of a maneuvering target is as sketched below.

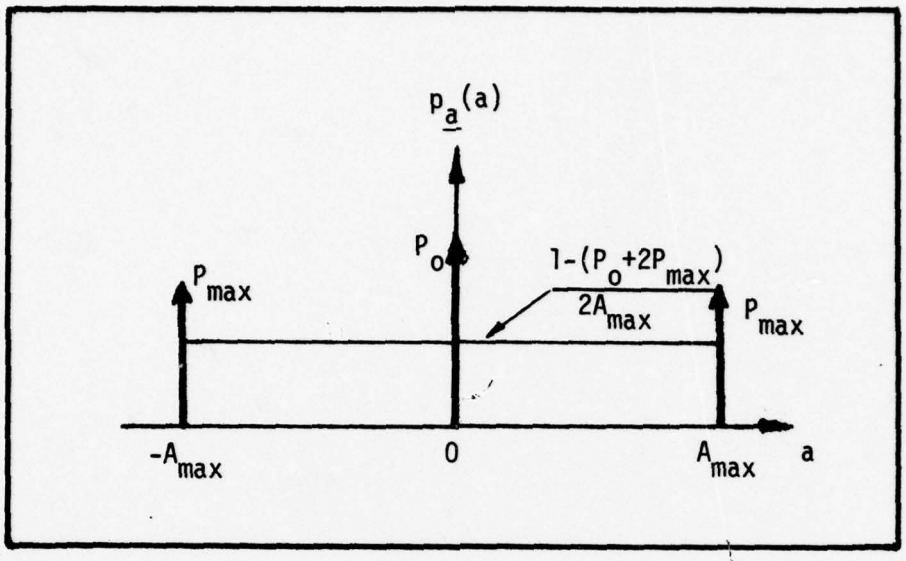


Fig. 1-1. Singer Model For Target Acceleration Probability Density

The target is assumed to undergo no acceleration with probability $P_o$, undergo maximum acceleration with probability $P_{max}$ in either direction, and exhibit accelerations between limits $-A_{max}$ and $A_{max}$ according to the appropriate uniform distribution.

Perhaps a more realistic probability density function (pdf) for maneuvering target acceleration is proposed by Kolibaba and Asher [29] as sketched in Fig. 1-2. Unfortunately, neither this pdf shape nor the one proposed by Singer is exploited in their filter implementations. Instead, only the variance is extracted and acceleration noise is modeled as a zero-mean, time-correlated, Gaussian process.

Other investigators have modeled target acceleration as time-correlated random processes. Landau [31] models total target acceleration as a first-order Markov process, while Pearson [41], in considering a range/range rate estimator, allows that the component of total target

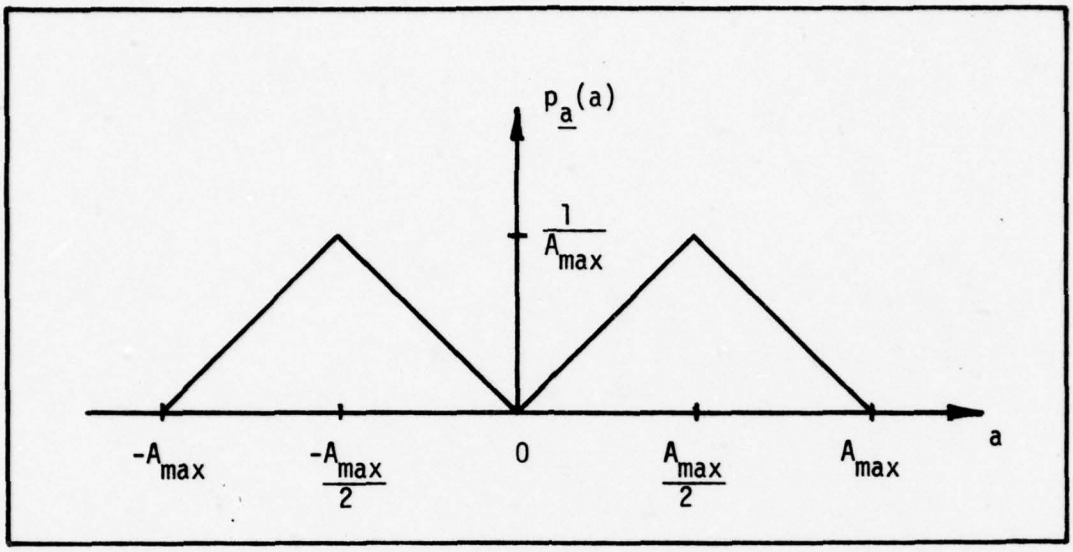


Fig. 1-2. Kolibaba Model For Target Acceleration Probability Density

acceleration along the line-of-sight is adequately modeled as first-order Gauss-Markov.

Consideration of relative target kinematics, with respect to a line-of-sight coordinate frame, often leads to a direct estimation of range and range rate with these states as observations [15] [41] [46]. The following is one such formulation.

$$\dot{\underline{R}} = \underline{V}_r \tag{1-11}$$

$$\dot{\underline{V}}_r = \omega^2 \underline{R} + \underline{a}_{T_r} - a_{I_r} \tag{1-12}$$

$$\dot{\underline{a}}_{T_r} = -\frac{1}{\tau_a} \underline{a}_{T_r} + \underline{W}_r \tag{1-13}$$

where

$$\omega^2 = \omega^2_{LS_e} + \omega^2_{LS_d} \tag{1-14}$$

$\omega_{LS_e}$, $\omega_{LS_d}$ = attacker-to-target line-of-sight rates about the e and d (cross-range, east and down) LOS coordinates

$\underline{a}_{T_r}$ = total target acceleration along the LOS

$a_{I_r}$ = ownship acceleration along the LOS

$\tau_a$ = correlation time of the random acceleration process

$\underline{W}_r$ = white noise driving the acceleration random process

Note that LOS angle rate appears as a parameter in the kinematic equation for the radial component of relative target velocity. This line-of-sight angle rate can be provided from a separate angle filter whose observations are azimuth and elevation pointing errors. This leads to a beneficial, interactive exchange of information, as the angle filter needs estimates of range and range rate in its formulation. Note also in the foregoing formulation that the LOS component of total target acceleration is modeled as a first-order Markov process.

The usual formulations which model total target acceleration assume the availability of ownship acceleration. An alternative approach was proposed by Farrell, et al [14], in which incremental ownship INS velocity change since time $t_k$, q, is modeled in the state dynamics by

$$\underline{x}(t) = [\Phi(t,t_k)]\,\underline{x}_k - \begin{bmatrix} q(t-t_k) \\ q \\ 0 \end{bmatrix} \tag{1-15}$$

where

$$\underline{x} = \begin{bmatrix} \underline{R}, \text{ relative position} \\ \underline{V}, \text{ relative velocity} \\ \underline{a}_T, \text{ total target acceleration} \end{bmatrix} \tag{1-16}$$

$$\Phi(t,t_k) \triangleq \begin{bmatrix} I_{3x3} & (t-t_k)\, I_{3x3} & \tfrac{1}{2}(t-t_k)^2\, I_{3x3} \\ & I_{3x3} & (t-t_k)\, I_{3x3} \\ 0_{6x3} & & \\ & 0_{3x3} & \delta I_{3x3} \end{bmatrix} \tag{1-17}$$

and

$$\delta = \text{Exp}\left\{-(t-t_k)/\tau_a\right\} \doteq 1 - \frac{t-t_k}{\tau_a} \tag{1-18}$$

This is a reasonable approach since pulse torque loop accelerometers provide a pulse rate which is proportional to acceleration. Thus, q may be determined by counting pulses. Observations for this filter are assumed to be range, azimuth and elevation angles.

The expectation that the target is maneuvering does not imply that the mathematical description of the problem must necessarily model target acceleration in order to achieve satisfactory results in motion estimation. However, neglect of any attempt to model acceleration will imply a preference for constant velocity trajectories. For the formulation in which position and velocity are estimated from range measurements only [19], the dynamics (one dimension only) are given by

$$\begin{bmatrix} \underline{x}(t_{k+1}) \\ \dot{\underline{x}}(t_{k+1}) \end{bmatrix} = \begin{bmatrix} 1 & T \\ 0 & 1 \end{bmatrix} \begin{bmatrix} \underline{x}(t_k) \\ \dot{\underline{x}}(t_k) \end{bmatrix} + \begin{bmatrix} T^2/2 \\ T \end{bmatrix} \underline{w}(t_k) \tag{1-19}$$

$$\underline{z}(t_k) = [1 \quad 0] \begin{bmatrix} \underline{x}(t_k) \\ \dot{\underline{x}}(t_k) \end{bmatrix} + \underline{v}(t_k) \tag{1-20}$$

where T is the sampling interval. $\underline{w}(\cdot)$ accounts for error created by this truncated expansion which neglects acceleration and higher order terms. Note that if the model uncertainty term, $\underline{w}$, were zero, then

$\dot{x}(t_{k+1}) = \dot{x}(t_k)$ for all k, which implies a constant velocity trajectory.

Clearly, uncertainty in target motion varies with the trajectory. A target in straight and level flight is more predictable than one which is rapidly changing its motion. An estimation algorithm is typically tuned to provide acceptable performance over an ensemble of trajectories, thus compromising between overdependence on the dynamic model which propagates the states between observations and overdependence on the raw measurement data. A maneuvering target is generally attempting to change its direction of travel, a premise which motivates the notion of adapting the filter in response to detected maneuvers. The adaptive estimation problem becomes first, one of detecting and declaring the maneuver, and second, one of adapting the filter parameters properly.

Adaptivity can be built into the tracker in several different ways. McAulay and Denlinger [38] used statistical decision theory to derive an optimal test for detecting the aircraft maneuver; a more practical suboptimal test is then deduced from the optimal test. When no maneuver has been declared, a simpler filter, based on a constant-velocity model, is used to track the aircraft. When a maneuver is detected, the tracker is reinitialized using stored data, up-dated to the present time, and then normal tracking is resumed as new data arrives. This is a form of limited memory filtering.

Hampton and Cooke [19] construct an adaptive filter which alters a scalar parameter in the filter algorithm, with the adjustment having the effect of creating a fading memory in the algorithm itself.

Heller [20] uses a tracker with a random input acceleration covariance matrix, Q, whose elements increase when a maneuver is declared. When the target is traveling in a straight line, the elements of Q are

reduced. The detection of a maneuver is based on simultaneous satisfaction of criteria requiring measurement error residuals to be sufficiently large and a given number of errors to be of the same sign. This technique results in a time delay in declaring a maneuver, a disadvantage it shares with many other maneuver detection schemes.

Demetry and Titus [10] achieve satisfactory adaptation by observing build-up in the prediction difference term (measurement residual). When two or more consecutive differences are of the same sign and outside the limits of a $3\sigma$ gate, the target is declared to be maneuvering. To recover from the bias introduced by such a maneuver, the raw observation data must be weighted more heavily than would be the case if subsequent filter gains were taken from the routine gain schedule, i.e., there is a backsliding in the gain schedule. Reprocessing of the n most recent measurements is then accomplished, where n is the number of differences upon which the bias detector bases its maneuver decisions. The n most recent measurements have been stored for this eventuality. The data is reprocessed by basically going into the gain schedule at a point where the relatively high gains of the early part of the schedule are brought to bear on the most recent measurements, those thought to be taken during a target maneuver. The reprocessing continues until the n most recent measurements are reprocessed, whereupon normal filtering and maneuver detection processes are resumed. The filter gain, however, is not restored to its premaneuver point in the schedule, but proceeds sequentially from the backstep point.

## 1.2 A New Approach

The target behavior models discussed in the previous section were based on kinematic considerations. Dynamics of flight were not a part of these models because no observations were assumed to be available which relate to target orientation. The physics of flight, however, dictate a significant degree of coupling between an aircraft's orientation in the atmospheric medium and its consequent motion through it. The coupling is so pronounced, in fact, that several general comments summarize this relationship over most realistic flight regimes:

(1) The velocity of the aircraft is nearly along its longitudinal axis, the offset being angle of attack and sideslip.

(2) Dominant accelerations (lift) are normal to the velocity vector and nearly normal to the wings.

(3) Positive lift is more likely than negative lift due to both pilot physiological factors and to structural loading design.

(4) Accelerations in the velocity direction (drag/thrust) are generally smaller in magnitude and of shorter duration than the lift (normal) accelerations.

(5) Angle of attack is nearly proportional to the magnitude of normal acceleration, and inversely proportional to the square of the speed.

With such a significant coupling between acceleration and orientation, a new approach to estimating aircraft target states which exploits this coupling appears reasonable. This new approach uses postulated target orientation measurements together with standard measurements of relative range and angles. An integrated filter is then designed to estimate both target orientation and the target kinematic states of vector position, velocity and acceleration simultaneously. Finally, a more

realistic statistical model of the target's normal acceleration is developed and incorporated into the estimator.

Simulation studies conducted with this new estimator design show that the response time for estimating the changing target accelerations is greatly reduced from cases in which the orientation information is not included. This not only provides a much more accurate state estimate and predictive capability in highly dynamic engagements, but it also provides much lower estimation residuals. This, in turn, would help prevent breaking lock in dynamic tracking situations.

Although hardware mechanizations are not specifically considered in the research study, it is noted that the ability to obtain such target orientation measurements as presumed by the estimator is within the projected state of the art. The advent of precision electro-optical (E-O) trackers combined with the appropriate pattern recognition (PR) methodologies (e.g., [12], [44], [48]) make the concept technically feasible.

The air-to-air pointing, tracking, and state estimation problem is one of a class of problems in which the object being observed has a significant degree of coupling between its motion and its orientation. Other objects with this characteristic include missiles and ships. Table I compares the pertinent characteristics of the interactive air-to-air estimator with those of a generic problem in this class. A comparison of this kind underscores the basic nature of the problem, i.e., the requirement to estimate the kinematics of a moving object such that its motion through the medium and its orientation in the medium are physically coupled. The problem assumes also that the kinematic description can be given a reasonable mathematical model and that ongoing measurements of

both motion and orientation of the object are available.

Table I. Comparison of Air-To-Air To Generic Problem

| GENERIC | AIR-TO-AIR |
|---|---|
| 1. A moving object whose motion relates in some way to its orientation in the medium of travel. | 1. A target aircraft whose velocity is "nearly" along its longitudinal axis and whose acceleration is "nearly" along its normal axis. |
| 2. Some description of the dynamics of motion. | 2. Differential equation which models the kinematics and dynamics of airplane flight. |
| 3. Ongoing measurements of motion parameters. | 3. Periodic measurements of radar range, range rate, line-of-sight angle and rate. |
| 4. Ongoing measurements of object orientation. | 4. Periodic two-dimensional target images from E-O sensor. |
| 5. Reference coordinate system of known position and orientation. | 5. Stabilized platform onboard pursuit aircraft. |

## 1.3 Organization of Remaining Chapters

This introduction has motivated the potential for interaction between kinematic and aspect state estimation. With this motivation established, the remainder of the dissertation develops a particular formulation for an interactive filter system and evaluates its performance over a variety of test conditions.

Chapter II develops the mathematical basis for both the kinematic and aspect Kalman filters. It also presents a computational algorithm to implement the interactive filter on a computer. A performance analysis plan is outlined in Chapter III which structures the areas and methods for investigating intrinsic performance of the interactive filter, and performance as it compares to that of a typical comparative filter system which uses radar measurements only. The results of this performance analysis are presented and discussed in Chapter IV. Chapter V considers several techniques for reducing the computational burden in implementing the interactive filter system on an operational computer. Included are the topics of parallel processing, linearization, scalar processing of measurements and quasi-static filter approximation. Conclusions are drawn in Chapter VI on the success and shortcomings of this interactive filter system in modeling the behavior of the chosen class of maneuvering targets. Finally, recommendations for future research are also described in Chapter VI. Detailed graphical results are placed in Appendix A for centralization and to make the text more readable. The remaining four appendices are included to elaborate upon pertinent, specific areas which, for the sake of brevity and continuity, were not included in the text.

# II. Interactive Target State Estimator

## 2.1 System Description

The target state estimator developed and evaluated in this dissertation is based upon a model which couples the separate concepts of target motion and target orientation in a unique manner. Only targets with some degree of motion/orientation interaction can be so modeled. Clearly, a uniform non-rotating sphere in motion through a medium lacks this interaction entirely since its motion is independent of its orientation and vice versa. Other classes of potential targets such as aircraft, missiles and ships exhibit this interaction to a significant degree.

One of the important issues in formulating a pointing and tracking problem is the choice of a mathematical model for target behavior. In one particular class of targets, that of high-speed fighter aircraft, the target is generally highly dynamic and has considerable latitude in its orientation and subsequent motion. Also, target kinematics and orientation are only indirectly available through observations from the tracking aircraft, sometimes designated as "attacker" or "ownship". The description of kinematic uncertainties becomes an important element in the process of modeling target behavior.

The high-speed fighter aircraft will represent the class of targets considered for the approach subsequently developed. A brief analysis of its dynamic characteristics follows. Fig. 2-1 shows the instantaneous

roll (x), pitch (y) and yaw (z) axes of an aircraft. Roll, pitch and yaw are the angular rotations about the respective axes, positive in the right-hand sense. The direction of motion is along the velocity vector which is offset from the roll, or longitudinal, axis by the aircraft angle of attack, $\alpha_a$ (subscript "a" for attacker, "t" for target).

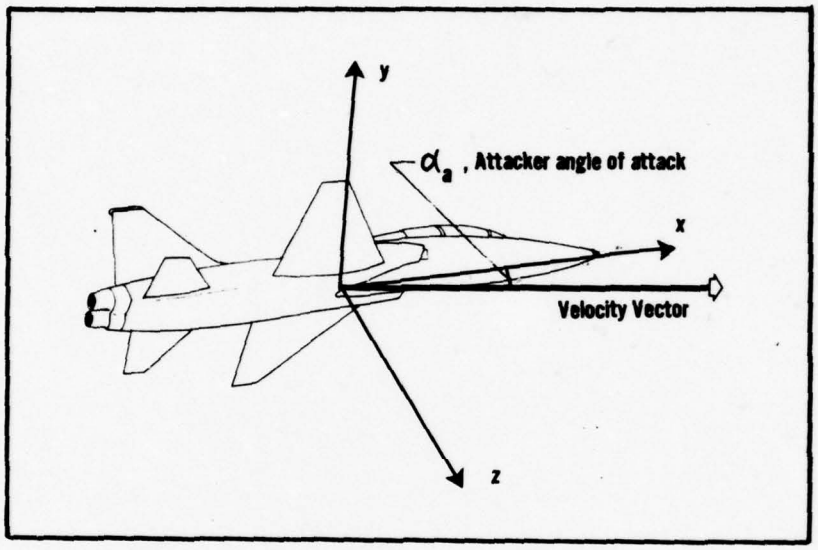


Fig. 2-1. Aircraft Body Axes

Except for airspeed changes and uncoordinated turns [in which the lateral, or y, component of velocity is non-zero; may be intentional, as with direct side force application for control configured vehicles (CCVs)], the direction of load acceleration generally lies normal to the velocity vector in the plane of the velocity vector and the instantaneous yaw axis. (Load acceleration, a vector quantity useful in describing motion of bodies traveling in a gravity force field, is acceleration minus the gravity vector, and is sometimes designated as specific force.) The mechanical structure of the aircraft, as well as the human pilot, is capable of undergoing

considerably greater acceleration along the negative yaw axis than along the positive. The modern F-15 jet fighter, for example, has acceleration limits of 9g in the negative yaw direction (up) but only 3g in the positive yaw direction (down)[50]. Any acceleration model which attempts to structure a realistic probability envelope about the target should reflect this asymmetric behavior of normal load acceleration.

The proposed interactive target state estimator is shown in Fig. 2-2. The sensor subsystem provides measured motion data to the kinematic state estimator. This data is representative of modern airborne radar systems--range, range rate, azimuth and elevation angles and angle rates. Angle rate measurements are not essential but can be used if available. If not available directly, as from rate gyros, angular rate data is sometimes achieved by pre-filtering angle measurements. The sensor subsystem also provides two-dimensional imagery data to the pattern recognition algorithm. The imagery data is of the target as observed from the attacker and hence is in a plane perpendicular to the target line-of-sight, designated as the image plane. The function of the pattern recognition algorithm is to deduce from the two-dimensional imagery, the orientation of the three-dimensional target relative to a coordinate system with an axis perpendicular to the image plane. The target orientation is specified as Euler aspect angles relative to the image plane coordinate system. By knowing the orientation of the image plane frame relative to the inertial frame, these angles can be transformed to Euler angles relative to the inertial frame. They are then filtered to reduce sensor and process noise. Thus the target orientation becomes known relative to the inertial frame.

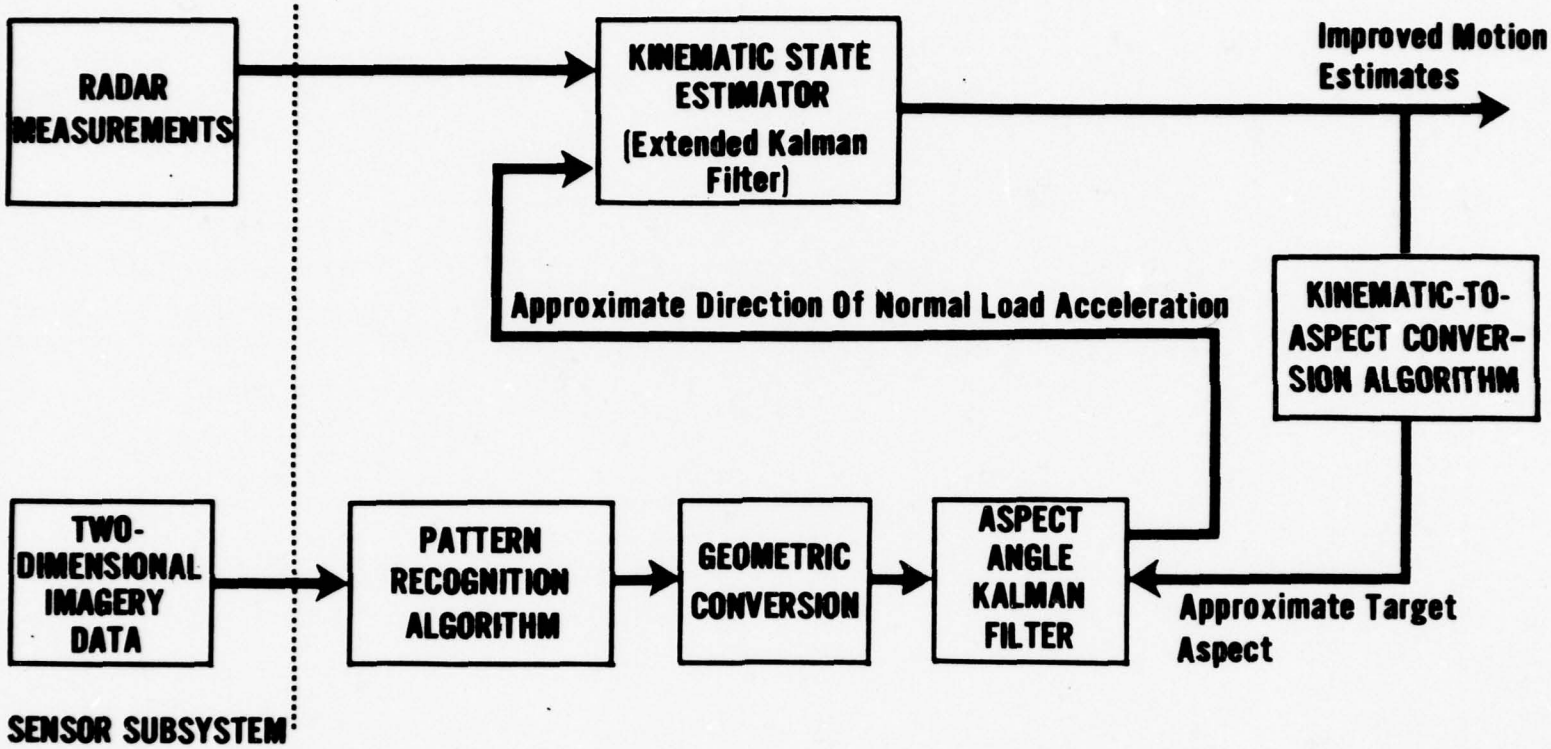


Fig. 2-2. Interactive State Estimation System

Direction of normal load acceleration is extracted from this best estimate of target orientation and is provided to the kinematic filter. The kinematic filter uses this normal load acceleration direction to enhance its estimate of target position, velocity and acceleration relative to the attacker. Ownship velocity and acceleration are added to these relative estimates to obtain estimates of total target kinematics. Approximate target angle of attack is computed from total target velocity and acceleration (to be discussed later). This approximate angle of attack is combined with target velocity and acceleration information to form a measure of target orientation as derived from kinematics. This aspect data is then provided as a measurement to the aspect angle filter as indicated by the feedback path in Fig. 2-2. This interactive exchange of information, as will be demonstrated in this dissertation, provides an estimate of target kinematics that exceeds the performance capabilities of filters which do not exploit orientation information.

The target state estimator computes in the inertially stabilized coordinate frame in the attacker aircraft. This frame is assumed to be aligned with an earth-fixed frame which, for the short duration of the encounter, is considered to be inertial.

The target tracker is assumed to be inertially stabilized. Angle and angle rate measurements of the target position are referenced directly to the inertially stabilized frame, thereby eliminating additional intermediate transformations involving the attacker body reference frames. This simplifying assumption lessens the computational burden for the simulation, but does not degrade the demonstration of feasibility for the filter system. The derivation of pertinent

coordinate transformations is in Appendix B. The detailed mathematical model is formulated in the following section.

## 2.2 Mathematical Formulation of Target Kinematic Model

2.2.1 Dynamic State Equations. This section derives the equations which model the target kinematics. The underbar (_) indicates a random variable or random process while the overbar (¯) indicates a vector quantity. The subscripts t, a and I refer respectively to target, attacker and inertial systems. Thus, "t/a" denotes a relative parameter of the target with respect to the attacker. Superscripts refer to the coordinate system in which the vector is expressed. The inertial $x^I$, $y^I$, $z^I$ axes are north (n), east (e), and down (d), respectively.

The velocity of the target relative to the attacker is modeled by setting the time rate of change of target position relative to the attacker equal to relative velocity. Expressed in inertial coordinates, this is

$$\dot{\underline{\bar{p}}}^I_{t/a} = \underline{\bar{V}}^I_{t/a} \tag{2-1}$$

The following equation for relative acceleration uses knowledge of ownship acceleration. It also allows the dominant normal acceleration term to be modeled separately from the remaining lateral and tangential accelerations. The advantage this feature holds over the usual first-order Markov model will be pointed out during the remaining discussion. Target relative acceleration is modeled as

$$\dot{\underline{\bar{V}}}^I_{t/a} = \underline{\bar{a}}^I_N + \bar{g}^I + \underline{\delta\bar{a}}^I - \dot{\bar{V}}^I_{a/I} + \underline{\bar{W}}^I_{acc} \tag{2-2}$$

where

$\underline{\bar{a}}_N$ = component of total load acceleration which is along the normal direction, i.e., normal to the velocity vector in the plane of the velocity vector and the instantaneous yaw axis. Modeling of the magnitude of $\underline{\bar{a}}_N$ ($|\underline{\bar{a}}_N|$ or $\underline{a}_N$) will be discussed later in this section.

$\bar{g}$ = gravity vector assumed to be in the $+z^I$ direction (sometimes called "gravitation", i.e., force due only to mass attraction).

$\underline{\overline{\delta a}}$ = correlated noise process which models the remaining (lateral and tangential) acceleration of the target. The lateral and tangential acceleration (i.e., having no component along the normal load acceleration direction) will be termed "non-normal" acceleration.

$\underline{\dot{\bar{V}}}_{a/I}$ = attacker total acceleration which is available from an inertial navigation system (INS). INS errors are assumed negligible after compensation is done elsewhere. The inclusion of the white noise term $\underline{\bar{W}}_{acc}$ could, of course, account for a simple model of INS errors. More elaborate INS error models could be added to this model if deemed necessary.

$\underline{\bar{W}}_{acc}$ = zero-mean Gaussian white noise process to account for uncorrelated errors in $\underline{\overline{\delta a}}$. It also accounts for modeling errors in both direction and magnitude of $\underline{\bar{a}}_N$, and any other inadequacies of the model for relative acceleration.

The gravity vector $\bar{g}$ is necessary in this formulation to offset the apparent acceleration component introduced from the gravity force

field. A pilot would sense the same apparent acceleration cues in straight and level flight (no acceleration) in a one-g gravity force field as an actual one-g normal acceleration in a no-gravity environment (e.g., in space travel). This concept is also illustrated by considering an aircraft in a constant altitude, banked turn. In this type maneuver, there are horizontal velocity changes but there is no acceleration in the vertical direction. Figure 2-3 illustrates that with constant airspeed in a coordinated turn, the pilot senses a normal load acceleration related to the bank angle by the equation

$$|\bar{a}_N| = \frac{|\bar{g}|}{\cos\phi} \tag{2-3}$$

and that

$$\frac{d\bar{V}}{dt} = \bar{a}_N + \bar{g} \tag{2-4}$$

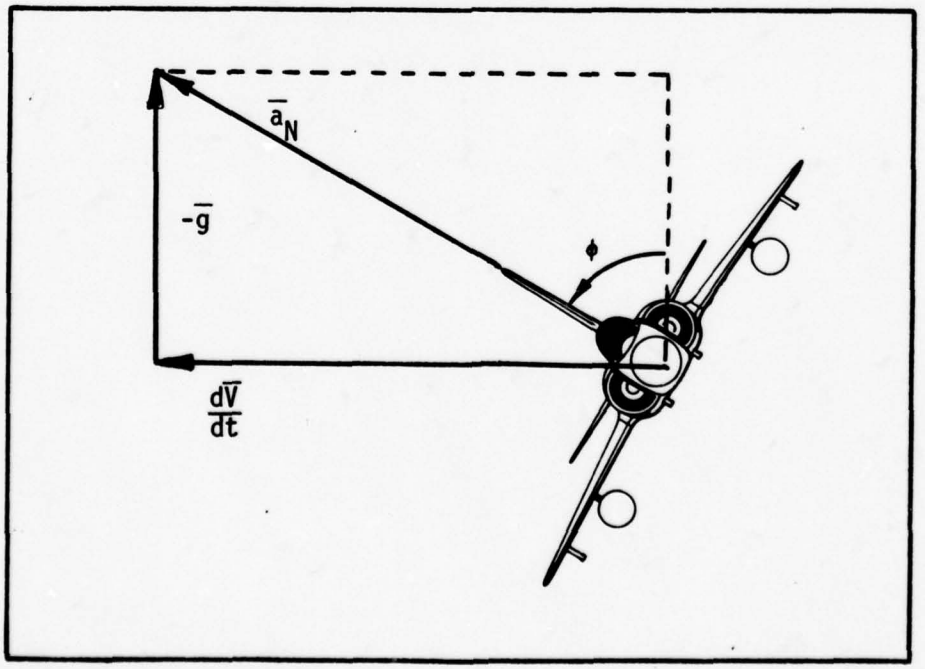


Fig. 2-3. Aircraft Load Acceleration in Level Turn

The predominant target acceleration is the normal term, so non-normal acceleration will be generally small. Modeled as a random process, non-normal acceleration will likely be symmetrically distributed since it models a small perturbation from the predominant normal acceleration term. It will also likely exhibit the time-correlation property characteristic of kinematic parameters of moving bodies. Hence, a suitable model for non-normal acceleration is the first-order Gauss-Markov process,

$$\dot{\underline{\delta a}}^{I} = -\frac{1}{\tau_{\delta a}} \underline{\delta a}^{I} + \underline{\bar{W}}_{\delta a}^{I} \qquad (2\text{-}5)$$

where

$\tau_{\delta a}$ is the process time constant, assumed the same in all three inertial directions, and

$\underline{\bar{W}}_{\delta a}$ is a zero-mean Gaussian white noise process of strength qI, i.e., no apriori knowledge is assumed of correlation among inertial components of non-normal acceleration.

The choice of values for $\tau_{\delta a}$ and strength for the noise process $\underline{\bar{W}}_{\delta a}$ will be decided during the tuning process. Initial estimates of these parameters should consider the dynamics of aircraft flight. High-speed maneuvering aircraft generally hold a particular maneuvering configuration for no more than several seconds but can alter their attitude significantly in less than a second. A time constant of one second is not an unreasonable estimate at which to begin the tuning process. Non-normal acceleration includes air-speed changes and lateral acceleration due to wind gusts and uncoordinated turns. It is reasonable to expect these acceleration contributions to be small since the predominant acceleration is normal to the velocity vector. Changes in

non-normal acceleration of one-half g or more during one second are not likely to occur so tuning will begin at a noise strength corresponding to this value.

Continuing with the discussion of Eq (2-2), the normal load acceleration is modeled as a vector whose direction is provided by the aspect angle filter and whose magnitude is modeled as an asymmetrically distributed, time-correlated random process. Asymmetry of the probability density function (pdf) for normal load acceleration magnitude can be synthesized by forming $\underline{a}_N$ as a deterministic, non-linear function of an intermediate time-correlated zero-mean Gaussian random process. In this manner, the intermediate Gaussian random process can be propagated directly as a first-order Gauss-Markov process. This technique allows $\underline{a}_N$ to be propagated indirectly and thus maintain a specified asymmetrical pdf throughout the estimation process. Besides the utility of allowing propagation of the asymmetric pdf, the particular non-linear function chosen allows synthesizing a hard limit in acceleration magnitude, a feature not possible with the simpler Gauss-Markov model. This non-linear model is discussed below.

The magnitude of load acceleration in the normal direction can be modeled by

$$\underline{a}_N = \alpha + \beta e^{\gamma \underline{\varepsilon}} \tag{2-6}$$

where

$\alpha, \beta, \gamma$ are constant for a particular class or type of target aircraft,

$\underline{\varepsilon}$ is a zero-mean Gaussian colored noise process with unit variance.

$\underline{a}_N$ denotes the magnitude of the bidirectional normal load acceleration vector including the sign, i.e., a negative

realization for $\alpha+\beta e^{\gamma \underline{\varepsilon}}$ indicates a load acceleration along the negative normal direction. The first order pdf for $\underline{a}_N$ is derived in Appendix C and is given by

$$p_{\underline{a}_N}(a_N) = \begin{cases} [\sqrt{2\pi}\ \gamma\ |a_N-\alpha|]^{-1} \exp\left\{-\frac{1}{2}\left[\frac{1}{\gamma}\ln\left(\frac{a_N-\alpha}{\beta}\right)\right]^2\right\}, & \frac{a_N-\alpha}{\beta} > 0 \\ 0, & \frac{a_N-\alpha}{\beta} \leq 0 \end{cases} \tag{2-7}$$

Parameter $\alpha$ tends to represent a maximum acceleration limit while both $\beta$ and $\gamma$ affect peakedness. The pdf is sketched in Fig. 2-4 for particular values of $\alpha$, $\beta$ and $\gamma$. This particular choice of target parameters produces a first-order pdf of normal load acceleration magnitude which is typical of modern piloted aircraft in evasive maneuvers. In this typical case, a hard limit occurs between 7 and 8 g's, typical maneuvers are at 3-6 g's, and there is an occasional negative-g maneuver of small magnitude. In an operational setting, target parameters $\alpha$, $\beta$ and $\gamma$ could be selected at the initiation of the engagement to match the known characteristics of the particular target. If the target type were not known, a set of parameters for a generic fighter would have been selected before beginning the engagement. Some pdf plots using other values of these target parameters are shown later in Chapter III, Performance Analysis and Computer Simulation.

Finally, the intermediate random process, $\underline{\varepsilon}$, from Eq (2-6), is modeled as first-order Gauss-Markov (State 10),

$$\dot{\underline{\varepsilon}} = -\frac{1}{\tau_\varepsilon}\underline{\varepsilon} + \underline{W}_\varepsilon \tag{2-8}$$

Then not only can $\underline{a}_N$ be propagated indirectly through $\underline{\varepsilon}$ and maintain

its asymmetrical pdf, but because of the exponential correlation for $\underline{\varepsilon}$, $\underline{a}_N$ will also have exponential correlation (biased). In this model, $\underline{W}_\varepsilon$ is a zero-mean Gaussian white noise process. Also, since $\underline{\varepsilon}$ is to have unit variance, the variance of $\underline{W}_\varepsilon$ is set to the value $2/\tau_\varepsilon$. (See Appendix C.)

With the dummy variable $\underline{\varepsilon}$ so modeled, the autocorrelation of $\underline{a}_N$ has the form

$$R_{\underline{a}_N}(\tau) = C_1 + C_2 \exp\left[C_3 \exp\left(-|\tau|/\tau_\varepsilon\right)\right] \tag{2-9}$$

where

$$\begin{aligned} C_1 &= \alpha^2 + 2\alpha\beta e^{\gamma^2/2} \\ C_2 &= \beta^2 e^{\gamma^2} \\ C_3 &= \gamma^2 \end{aligned} \tag{2-10}$$

If $C_3$ is small (e.g., $\gamma \leq 0.5$), this may be approximated by

$$R_{\underline{a}_N}(\tau) \approx C_4 + C_5 \exp\left(-|\tau|/\tau_\varepsilon\right) \tag{2-11}$$

where

$$\begin{aligned} C_4 &= C_1 + C_2 \\ C_5 &= C_2 C_3 \end{aligned} \tag{2-12}$$

The normal load acceleration component, like the lateral and tangential acceleration components, exhibits a near-exponential correlation as would be the case if it had been modeled as simply a Gauss-Markov process. Current acceleration models display this characteristic but symmetry of the pdf is generally their shortcoming. Also note from Eq (2-11) that $\tau_\varepsilon$ is the time constant governing the correlation of $\underline{a}_N$. Finally, note that the bias term $C_4$ results from the asymmetry of the pdf for $\underline{a}_N$, and corresponds to the square of the mean of $\underline{a}_N$ which is

given by

$$M_{\underline{a}_N} = \alpha + \beta e^{\gamma^2/2} \tag{2-13}$$

Additional details of the autocorrelation for $\underline{a}_N$ are contained in Appendix C.

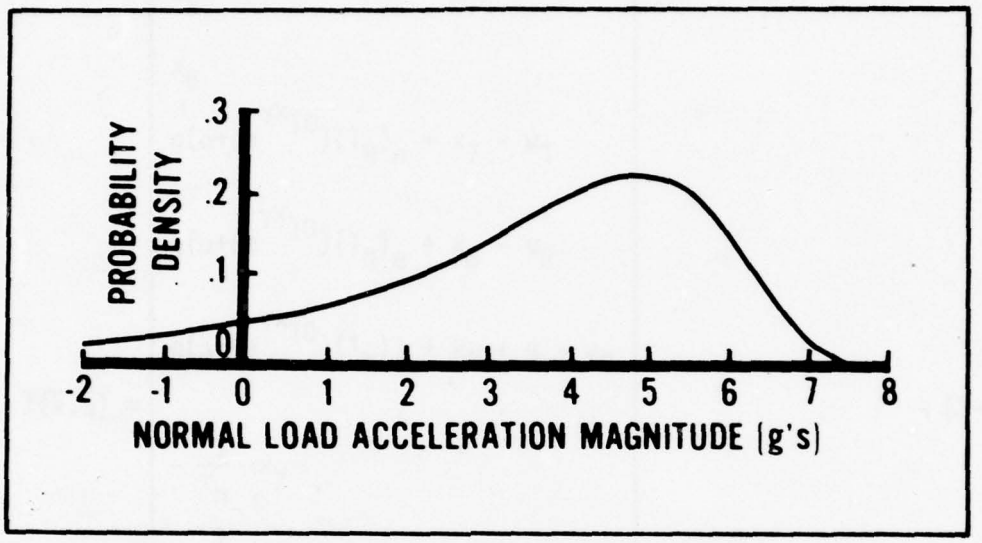


Fig. 2-4. First Order Probability Density Function For Normal Load Acceleration During Evasive Maneuver; $\alpha = 8$, $\beta = -4$, $\gamma = 0.5$

An alternative approach would be to model $\underline{a}_N$ as a nonzero-mean first-order Gauss-Markov process. Some details of this alternative approach are discussed in Chapter V, although no comparison of performance has been made with the above technique.

Eqs (2-1), (2-2), (2-5) and (2-8) form the ten-state non-linear propagation model. An extended Kalman filter algorithm is chosen over a higher order non-linear filter for ease in implementation. The equations are summarized below for future reference.

$$\dot{\overline{x}} = \overline{f}(\overline{x},\overline{u}) + G\overline{W} \tag{2-14}$$

where

$$\bar{x} = [\underline{p}_{t/a_n} \; \underline{p}_{t/a_e} \; \underline{p}_{t/a_d} \; \underline{V}_{t/a_n} \; \underline{V}_{t/a_e} \; \underline{V}_{t/a_d} \; \underline{\delta a}_n \; \underline{\delta a}_e \; \underline{\delta a}_d \; \underline{\varepsilon}]^T \qquad (2\text{-}15)$$

$$\bar{f}(\bar{x},\bar{u}) = \begin{bmatrix} x_4 \\ x_5 \\ x_6 \\ g(\alpha+\beta e^{\gamma x_{10}})(1_N)_n + x_7 - u_1 \\ g(\alpha+\beta e^{\gamma x_{10}})(1_N)_e + x_8 - u_2 \\ g(\alpha+\beta e^{\gamma x_{10}})(1_N)_d + x_9 + g - u_3 \\ -\frac{1}{\tau_n} x_7 \\ -\frac{1}{\tau_e} x_8 \\ -\frac{1}{\tau_d} x_9 \\ -\frac{1}{\tau_\varepsilon} x_{10} \end{bmatrix} \qquad (2\text{-}16)$$

and

$$\bar{u} = \left[\dot{V}_{a/I_n} \; \dot{V}_{a/I_e} \; \dot{V}_{a/I_d}\right]^T \qquad (2\text{-}17)$$

g = magnitude of acceleration due to gravity which is assumed constant at 32.17 ft/sec. $\bar{u}$ consists of the north, east and down components of total attacker acceleration, assumed available with negligible uncertainty.

The target aspect is changing as the kinematics are changing, i.e.,

the target aircraft is changing its orientation in order to direct the predominant normal acceleration vector and thus effect a trajectory which will evade the attacker. However, the time constant for aspect changes is generally significantly larger than the sampling interval. For this reason, the normal load acceleration unit vector components $(1_N)_n$, $(1_N)_e$, and $(1_N)_d$ are considered deterministic functions of time, and approximated as constant over a sampling interval. A possible extension to this research would be to investigate performance using a piece-wise affine, rather than piece-wise constant, unit vector determination. This might be particularly beneficial if the pattern recognition algorithm is capable of determining angular rates, an assumption not made for the generic algorithm supposed in this research.

The Gaussian, zero-mean white noise components are combined into vector form as

$$\underline{\overline{W}} = \left[\underline{W}_{V_n}\ \underline{W}_{V_e}\ \underline{W}_{V_d}\ \underline{W}_{\delta a_n}\ \underline{W}_{\delta a_e}\ \underline{W}_{\delta a_d}\ \underline{W}_{\epsilon}\right]^T \tag{2-18}$$

G is given by

$$G = \begin{bmatrix} 0\ (3x7) \\ \hline I\ (7x7) \end{bmatrix} \tag{2-19}$$

and

$$E\left[\underline{\overline{W}}(t)\ \underline{\overline{W}}^T(t+\tau)\right] = Q\delta(\tau) \tag{2-20}$$

Stationarity of model noise is assumed here for simplicity. Q is assumed diagonal. Also, no pseudonoise is added to position derivative equations. This could be added if additional fine-tuning of the filter were desired. Q component values are tabulated in Appendix E.

2.2.2 Measurement Equations. The attacking aircraft is assumed to be equipped with a modern radar system providing the following measurements (Refer to Figure 2-5): range, $r$ (distance to target); range rate, $\dot{r}$ (time rate of change of range); azimuth angle, $\eta$ (measured from north in the horizontal plane); elevation angle, $\xi$ (measured up from the horizontal plane); azimuth angle rate, $\dot{\eta}$ ; and elevation angle rate, $\dot{\xi}$ .

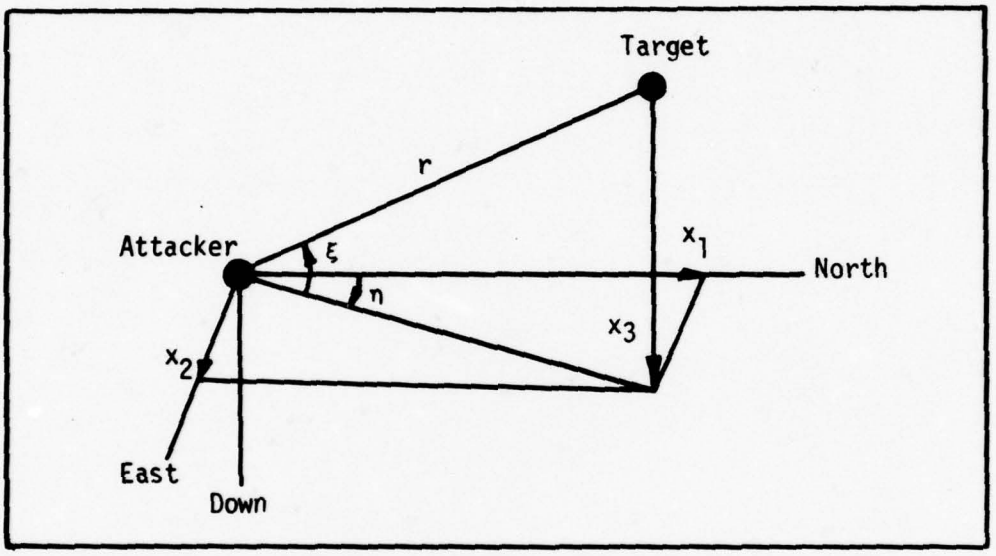


Fig. 2-5. Measurement Geometry

Each measurement is assumed noisy and is modeled as being corrupted with zero-mean Gaussian white noise, $\underline{\bar{v}}$. This choice for a radar noise model is often made and is reasonably valid for many applications. However, a possible extension of this research would be to define a more realistic (i.e., more complex) radar noise model and compare filter performance using the two different models. The measurements can be related to the states defined in Eq (2-15) as follows

$$\underline{\bar{z}} = \underline{\bar{h}}(\underline{\bar{x}}) + \underline{\bar{v}} \qquad (2\text{-}21)$$

$$\bar{h}(\bar{x}) = \begin{bmatrix} r \\ \eta \\ \xi \\ \dot{r} \\ \dot{\eta} \\ \dot{\xi} \end{bmatrix} = \begin{bmatrix} (x_1^2+x_2^2+x_3^2)^{\frac{1}{2}} \\ \tan^{-1}(\frac{x_2}{x_1}) \\ \tan^{-1}\left(\frac{-x_3}{(x_1^2+x_2^2)^{\frac{1}{2}}}\right) \\ \frac{x_1x_4+x_2x_5+x_3x_6}{(x_1^2+x_2^2+x_3^2)^{\frac{1}{2}}} \\ \frac{x_1x_5-x_2x_4}{x_1^2+x_2^2} \\ \frac{x_3(x_1x_4+x_2x_5)-x_6(x_1^2+x_2^2)}{(x_1^2+x_2^2+x_3^2)(x_1^2+x_2^2)^{\frac{1}{2}}} \end{bmatrix} \qquad (2\text{-}22)$$

$$E\left[\bar{v}(t_i)\bar{v}^T(t_j)\right] = R\delta_{ij}$$

Stationarity of measurement noise is assumed for simplicity. R is also assumed diagonal. More realistic models may be added if dictated by a particular implementation. R component values are tabulated in Appendix E.

## 2.3 Mathematical Formulation of Target Aspect Model

The attacker is provided with an electro-optical (E-O) imaging system which tracks the target during its maneuvers. System performance parameters (e.g., tracker stability, pointing accuracy, resolution, spectral response) must be of sufficient quality to allow the imagery data to

be processed into orientation information. This processing is accomplished in a unit designated as the pattern recognition (PR) algorithm. The PR algorithm "recognizes" that the image pattern represents a particular target orientation by performing prescribed algorithmic computations on the image data.

Several pattern recognition techniques are applicable to this type of problem. A theme underlying many of the applicable schemes is that much of the significant information required for recognition is contained in the edges, i.e., in the boundary curve of an isolated shape. A review of feature extraction techniques which are based on edges and contours is included in a survey by Levine [ 33] . As pointed out by Richard and Hermami [44], the advantage of using boundary curve descriptions is that features may be chosen which are independent of translation, rotation and the size of similar shapes. These authors apply a particular boundary curve classification technique to aircraft aspect determination. In this technique, a one-dimensional Fourier expansion of the complex valued boundary curve Z(t) is made. This Z(t) is the set of complex numbers with parametric representation

$$Z(t) = (x(t),y(t)), \quad t \in [0, 1], \qquad Z(0) = Z(1) \tag{2-23}$$

where x and y are continuous real valued functions representing the abscissa and ordinate values on the boundary of the two-dimensional image (referenced to some arbitrary fixed frame, e.g., centered at the image center of mass). The parameter t is proportional to arc length around the boundary and speed $|dZ/dt|$ is constant. The complex valued function Z for $t \in (-\infty,\infty)$ is considered the periodic extension of Z for $t \in [0,1]$. The periodic function Z(t) is represented by its Fourier series

$$Z(t) = \sum_{k=-\infty}^{\infty} c_k \exp(j2\pi kt) \tag{2-24}$$

where

$$c_k = \int_0^1 Z(t) \exp(-j2\pi kt)dt \qquad (2\text{-}25)$$

The Fourier series of a given contour is then filtered by an ideal low pass filter and is normalized. A finite set of Fourier descriptors $\{c_{ki}^*, k = 0, \pm1, \pm2, \ldots, \pm m\}$, representing the truncated series, is stored for each prototype $Z_i^*$, $i = 1, 2, \ldots, P$. An unknown contour Z with coefficients $\{c_k\}$ is then classified in that prototype class i for which a particular distance metric is minimized. The authors successfully applied this technique to recognition not only of aircraft type (among four, including F-4 Phantom, Mirage IIIC, MIG 21 and F-105) but also of aircraft yaw, pitch and roll relative to the image plane. To simulate the effect of detector noise in the authors' computer simulation, zero-mean white Gaussian noise was added to each coordinate of each of the 512 points making up the boundary. Time-correlated noise models were suggested for further research.

Another technique, which has been applied to aircraft recognition, is also based upon using outlines or silhouettes for principal identity clues. Sklansky and Davison [48] compute the density of slopes of the edge of the silhouette. Slope density of a silhouette is $1/\Delta\theta$ times the fraction of the silhouette's perimeter whose slopes lie in the half-open interval $[\theta,\theta+\Delta\theta)$, where $\theta$ varies from 0 to $2\pi$. Conceptually, a polygon is constructed which consists of a sequence of vectors, each no longer than $\delta$, connected head to tail, the tail and head of each vector lying on the boundary of the silhouette. $\theta_i$ denotes the angle of the $i^{th}$ vector relative to the horizontal axis, and n denotes the number of elements of the set $\{\theta_i \mid \theta \leq \theta_i \leq \theta+\Delta\theta\}$. Slope density, $f(\theta)$, is defined as

$$f(\theta) = \lim_{\substack{\Delta\theta \to 0 \\ \delta \to 0}} \frac{n\delta}{\Delta\theta} \tag{2-26}$$

where $\delta$ and $\Delta\theta$ go to zero in such a manner that $n\delta$ is of the order of $\Delta\theta$. $f(\theta)$ is periodic, with period of $2\pi$. $f(\theta)$ is independent of silhouette translation, and is also independent of dilations and contractions if normalized so that

$$\int_0^{2\pi} f(\theta)d\theta = 1 \tag{2-27}$$

Rotation of the silhouette results in translation of $f(\theta)$. Feature space for this technique consists of the amplitudes of lower-order Fourier harmonics of the silhouette's slope density, and a nearest-neighbor decision rule is used for classifying a given silhouette into a particular prototype class. The authors' experiments do not include the addition of corrupting noise to simulate detector uncertainties. Also, only roll angle aspects were analyzed in this study, and no follow-on research has been accomplished to extend this technique to a study of all aspects [8].

Another method, using the theory of two-dimensional image moments, was applied to automatic aircraft identification and aspect determination by Dudani [ 11 ] [ 12 ] . In this technique, two-dimensional $(p+q)^{th}$ order moments, defined as

$$m_{pq} = \frac{1}{N} \sum_{i=1}^{N} x_i^{\,p} \, y_i^{\,q} \quad , \quad p + q = 0, 1, 2, \ldots \tag{2-28}$$

are applied to coordinates $(x_i, y_i)$ of the N points equally distributed along the boundary of a given pattern. Central moments are then defined in terms of these ordinary moments. Six non-linear expressions are then

formed from these central moments--two involving second-order moments and four involving third-order moments. One of these six (which happens to be the square of radius of gyration) is used to normalize the other five, resulting in five scalar functions which characterize a given image. These five functions are raised to different powers. The resulting five elements then form the characterizing vector in five-dimensional feature space. Again, a nearest-neighbor decision rule is used to select the prototype class into which to place a given sample image.

Regardless of the recognition technique implemented, the output required from the pattern recognition algorithm is target orientation. Target orientation is referenced to the image plane which is perpendicular to the line of sight from the attacker to the target. By assumption, the image plane $x^i$ axis is to the right in the horizontal plane, the $y^i$ axis is up and the $z^i$ axis is out of the image plane toward the attacker, as illustrated in Fig. 2-6.

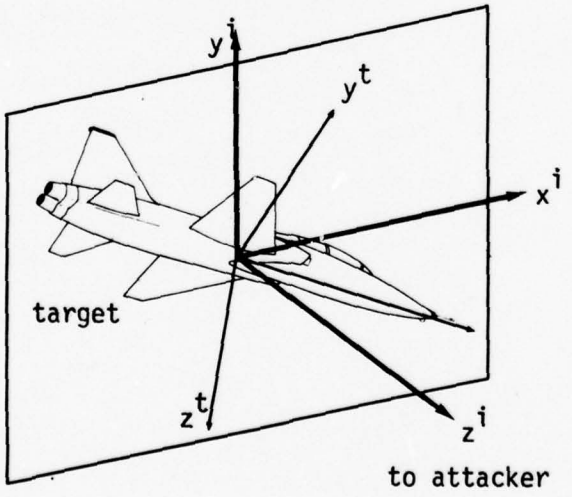


Fig. 2-6. Image Plane Orientation

An alternative image plane frame definition is discussed later in this section which is better for avoiding angular indeterminacy in the typical tail chase maneuver. The imaging tracker is assumed to be inertially stabilized so that image right and up correspond to positive azimuth and elevation, respectively. The typical manner for specifying image aspect is through Euler angles which give orientation of the target with respect to the image plane. A zero value of image yaw, pitch and roll occurs when the target aircraft frame is aligned with the image frame, i.e., the target nose is to the right, the right wing is up and the aircraft underside is the image view. The usual order for Euler rotations is assumed--yaw, then pitch and then roll. Image yaw is rotation about the z axis from the reference image frame. Image pitch is rotation about the newly formed lateral- or intermediate y axis. Image roll is rotation about the newly formed longitudinal- or x axis.

Indeterminate points can occur at image pitch angles of ±90 degrees. The following example illustrates the problem. Zero yaw, 90° pitch and 90° roll is the same orientation as -90° yaw, 90° pitch and zero roll. The solution to this non-uniqueness problem is motivated by considering the dynamics of flight. Rolling motion about the longitudinal axis is considerably easier to effect than are heading changes. The target pilot may attempt several rolling maneuvers without appreciably changing relative heading. It is better to track roll, in this case, than to assume zero roll and track a contrived heading (yaw). Hence, for the case of ±90° pitch, yaw is taken to be zero so that roll then uniquely defines the orientation.

The assumption of zero yaw at ±90° of pitch has the apparent disadvantage of causing yaw to drop to zero (from some value between - 180° and +180° ) when image pitch of ±90° occurs. Yaw would then switch

instantaneously from zero to a (possibly different) value after the ±90° pitch situation had past. This situation, however, is not likely to occur. Consider the ±90° cases separately.

The -90° image pitch corresponds to a head-on pass or to the target chasing the attacker. The second of these possibilities is not considered here since, if tracker lock-on should be lost, sufficient time for reacquisition would occur in converting from a defensive to an offensive position. The head-on pass does occur in air-to-air combat although much less frequently than the tail-chase. In the head-on pass, each aircraft directs its velocity vector generally toward the other. Since little normal acceleration is required to accomplish this, the angle of attack will be small. Hence, the longitudinal axes of the aircraft can be nearly aligned. The engagement will likely be terminated abruptly prior to crossing as one (or both) of the two aircraft breaks off to seek a tail-chase (offensive) position. The advantage of roll attitude tracking prior to break-off is more important in that it provides a direction of probable acceleration after the break. The disadvantage of (possibly) not rapidly reacquiring image yaw after the -90° pitch situation has occurred, therefore, is minimized since little or no weapon firing opportunities will occur during this scenario after the break-off.

The air combat maneuver which is more likely to occur is the tail-chase in which the +90° image pitch situation would apparently occur. Actually, an image pitch of +90° seldom occurs in the tail-chase because of two important engagement parameters, angle-off and angle-of-attack. Angle-off is the (generally acute) angle from the negative target velocity vector to the attacker line-of-sight. The typical engagement is described as follows. The target is aware of its defensive role and is pulling

several g's in order to evade the attacker. The angle of attack, which is proportional to load acceleration magnitude, will be relatively large (typically 15-25 degrees). The attacker is behind the target a half mile to a mile. The attacker orients its wings and hence its predominant normal acceleration vector so as to stay in the target's turning plane. The attacker attempts to direct its velocity vector toward the target (pure pursuit) or slightly ahead of the target (lead pursuit) in order to sustain the engagement. Fig. 2-7 illustrates the typical tail-chase maneuver as seen in the turning plane for several angles-off. The turning plane need not be horizontal. Note that the effects of angle-off and angle-of-attack combine to move the target longitudinal axis a significant angular displacement from the line-of-sight.

It was reasoned above that indeterminate points at ±90° image pitch occur seldomly, and with short duration in typical air combat engagements. However, if implementation experience determines this to be a problem area, the following alternative image orientation provides even less opportunity for the indeterminate point to occur. Redefine zero image yaw, pitch and roll to be target nose along line-of-sight, right wing to the right and aircraft underside down, respectively. The image frame is shown in Fig. 2-8. This definition of aspect has the advantage of placing the longitudinal axis of the target at right angles to the line-of-sight at the troublesome ±90° image pitch. This particular configuration will not occur in a pursuit mode because of the required angle-off. It would occur only for paralleling trajectories or for a short duration during side-shot engagements (target crossing attacker's path within firing range).

The foregoing discussion relates to deducing target aspect angles

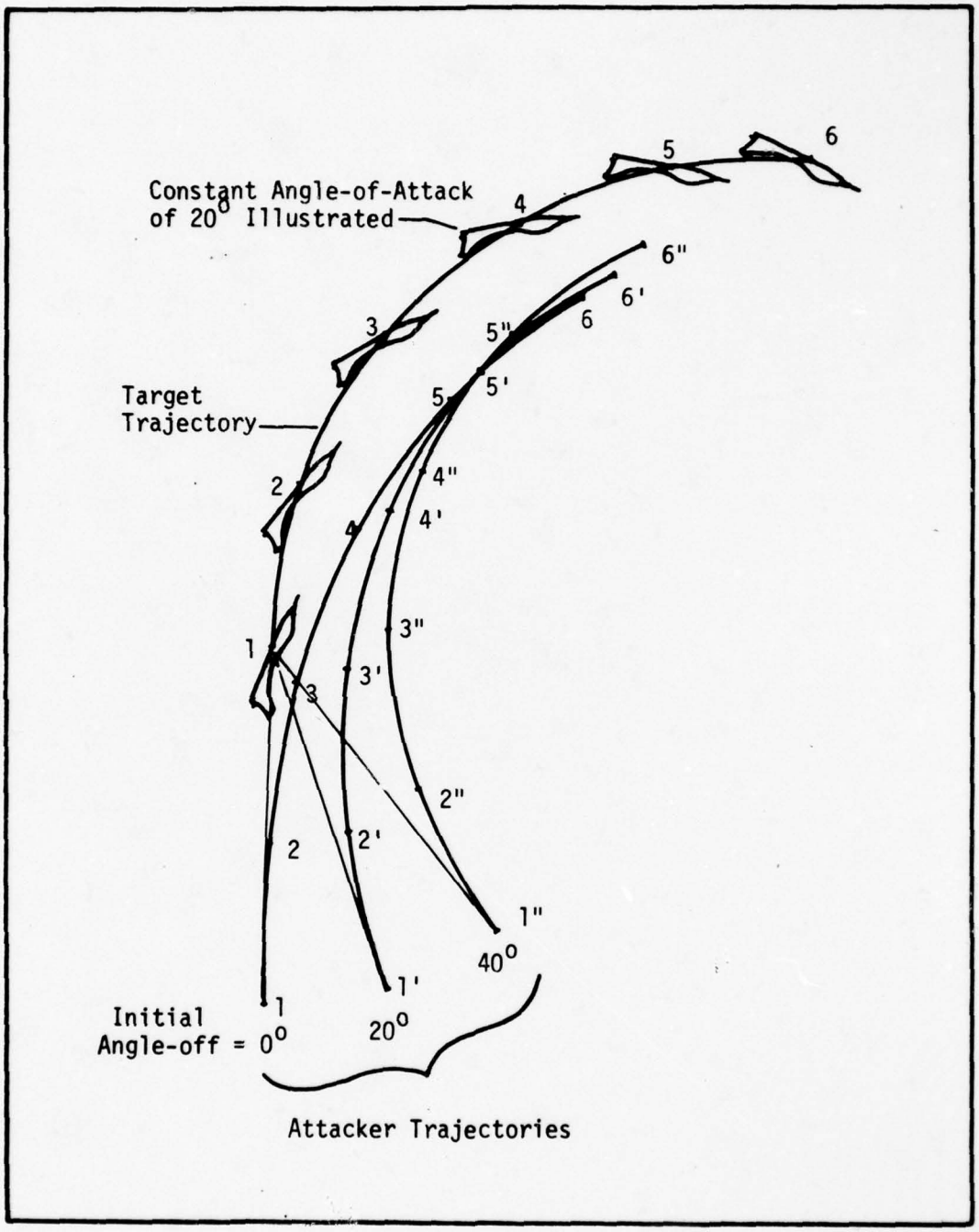


Fig. 2-7. Typical Target and Attacker Turning Plane Geometry For Pure Pursuit and Several Initial Angles-Off

relative to the image plane. Target aspect is then converted to orientation relative to the inertial frame through a transformation which involves tracker azimuth and elevation angles.

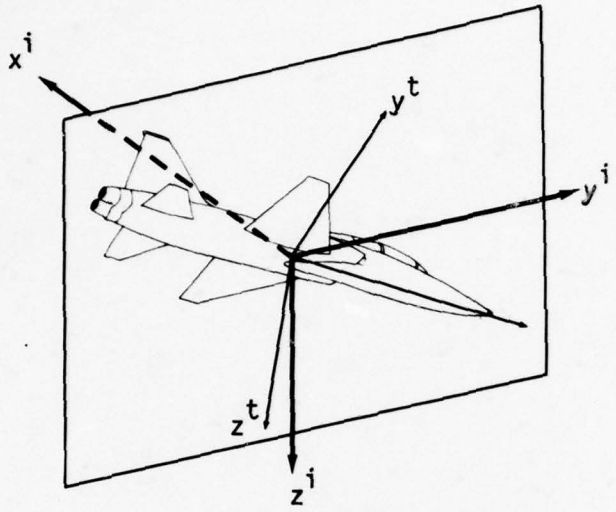


Fig. 2-8. Alternative Image Plane Orientation

The details of the transformation are included in Appendix B. The recognition process and subsequent transformation described earlier in this section result in a conversion of target imagery data into a measure of target aircraft orientation relative to inertial space. The Euler angles deduced in this manner are tracked with the filter algorithm described in the next two sections. Direction cosines or quaternions may be used as alternative expressions of target orientation.

2.3.1 Dynamic State Equations. The following first-order equation models the behavior of the inertially referenced target aspect between measurements updates.

$$\dot{\underline{\bar{X}}} = F\underline{\bar{X}} + G\underline{\bar{\omega}} \qquad (2\text{-}29)$$

where

$$\bar{X} = [\psi\ \theta\ \phi\ \dot{\psi}\ \dot{\theta}\ \dot{\phi}]^T \tag{2-30}$$

$$F = \left[\begin{array}{c|c} 0 & I_{3x3} \\ \hline 0 & 0 \end{array}\right] \tag{2-31}$$

$$G = \left[\begin{array}{c} 0 \\ \hline I_{3x3} \end{array}\right] \tag{2-32}$$

$$\bar{\omega} = [\omega_\psi\ \omega_\theta\ \omega_\phi]^T \tag{2-33}$$

$$E\,[\bar{\omega}(t)\bar{\omega}^T(t+\tau)] = Q_a\,\delta(\tau)$$

$\psi$, $\theta$, $\phi$ represent yaw, pitch and roll of the target aircraft relative to the inertial frame, and

$\bar{\omega}$ is a zero-mean Gaussian white noise process.

This dynamic equation models target Euler angle rates as Brownian motion. This model was chosen because it is simple. Plant noise is assumed stationary, although, depending on the characteristics of the pattern recognition algorithm and the electro-optical sensor, adaptively setting $Q_a$ might be feasible.

2.3.2 Measurement Equations. There are two sources of target aspect measurement data for the aspect filter. The primary source is the pattern recognition algorithm which converts the two-dimensional imagery data to target aspect Euler angles. In addition, target aspect can be deduced from target kinematic estimates which are available from the kinematic filter. This additional measure of target aspect can be accomplished in two different ways as outlined below. If a pattern recognition system is not available, kinematically derived target aspect

angles only can be provided to the aspect filter as measurements. This case is considered in the chapter on performance analyses.

2.3.2.1 Target Velocity Used to Define Roll Axis. A method which can be used to deduce target aspect from kinematics, ignores direction of acceleration and aircraft angle of attack by assuming that the velocity vector is along the longitudinal, or roll, axis of the target aircraft. By making this assumption, yaw and pitch angles are uniquely established. This is true because of the order of rotation of the Euler angles--first yaw, then pitch and finally roll. A measure of approximate yaw is available as the angle from the inertial $x^I$ (north) axis to the projection onto the $x^I$-$y^I$ (north-east) plane of the velocity vector. For brevity in the following discussion, let $\overline{V}^I_{t/I} \equiv \overline{V} = [V_x V_y V_z]^T$ Thus

$$\psi_k = \arctan\left(\frac{V_y}{V_x}\right) \tag{2-34}$$

or to avoid computational problems near $V_x = 0$,

$$\psi_k = \arccos\left(\frac{V_x}{\sqrt{V_x^2+V_y^2}}\right) \text{sign } (V_y) \tag{2-35}$$

where arccos denotes the principal value of the inverse cosine function. If $V_x$ and $V_y$ are both zero, $\psi_k$ is defined to be zero. A measure of approximate pitch is the angle from the $x^I$-$y^I$ plane up to the velocity vector. Thus

$$\theta_k = \arcsin\left(\frac{-V_z}{V}\right) \tag{2-36}$$

where

$$V = \sqrt{V_x^2+V_y^2+V_z^2} \tag{2-37}$$

For modeling simplicity, the measurements available to the aspect estimator can be modeled as corrupted with zero-mean Gaussian white noise and related to the states by the equation

$$\underline{z} = H\underline{x} + \underline{\nu} \tag{2-38}$$

where

$$H = \begin{bmatrix} 1 & 0 & 0 & 0 & 0 & 0 \\ 0 & 1 & 0 & 0 & 0 & 0 \\ 0 & 0 & 1 & 0 & 0 & 0 \\ 1 & 0 & 0 & 0 & 0 & 0 \\ 0 & 1 & 0 & 0 & 0 & 0 \end{bmatrix} \tag{2-39}$$

since a measure of yaw, pitch and roll are available from the pattern recognition algorithm and an additional measure of yaw and pitch is available using Eqs (2-35) and (2-36).

Also,

$$E[\underline{\nu}(t_i)\underline{\nu}^T(t_j)] = R_a\delta_{ij} \tag{2-40}$$

Measurement noise is assumed stationary and $R_a$ is assumed diagonal.

2.3.2.2 Target Aspect Using Angle of Attack. The method outlined in the previous section ignored angle of attack by assuming the velocity vector was along the longitudinal aircraft axis. The method developed below provides target attitude from

a) total target velocity in inertial coordinates,

b) total target acceleration in inertial coordinates, and

c) the relationship between angle of attack, normal load acceleration magnitude and airspeed:

$$nW = \tfrac{1}{2}\rho V^2 C_{L_\alpha} (\alpha_t - \alpha_{t_o}) S \qquad (2\text{-}41)$$

where

$n$ = load factor, i.e., magnitude of normal load acceleration expressed in g's

$W$ = weight (lbs; assume sea level gravity)

$\rho$ = air density (slugs/ft$^3$)

$V$ = airspeed (ft/sec)

$C_{L_\alpha}$ = coefficient of lift for $\alpha$ (dimensionless)

$\alpha_t$ = target angle of attack (radians)

$\alpha_{t_o}$ = target angle of attack for zero lift (radians)

$S$ = effective airfoil surface area (ft$^2$)

The method is outlined in the following procedure.

a) Find load acceleration normal to the velocity vector.

b) Form target velocity (v) frame:

$x^v$ - along velocity vector

$z^v$ - along negative normal acceleration direction

$y^v$ - forms a right-hand orthogonal set with $x^v$ and $z^v$.

c) Rotate target velocity frame about $y^v$ axis by angle of attack, to form body frame.

d) Extract Euler angles--yaw, pitch and roll--from inertial-to-body transformation.

The details of this procedure can be found in Appendix D. The result is

shown below.

$$\psi_k = \arctan\left[\left(\frac{V_y C\alpha_t}{V} + \frac{a_{N_y} S\alpha_t}{a_N}\right)/\left(\frac{V_x C\alpha_t}{V} + \frac{a_{N_x} S\alpha_t}{a_N}\right)\right] \tag{2-42}$$

$$\theta_k = \arcsin\left(\frac{V_z C\alpha_t}{V} + \frac{a_{N_z} S\alpha_t}{a_N}\right) \tag{2-43}$$

$$\phi_k = \arctan\left[\left(\frac{V_x a_{N_y} - V_y a_{N_x}}{V a_N}\right)/\left(\frac{V_z S\alpha_t}{V} - \frac{a_{N_z} C\alpha_t}{a_N}\right)\right] \tag{2-44}$$

where $\bar{a}^I_{N_{t/I}} \equiv \bar{a}_N = [a_{N_x}\ a_{N_y}\ a_{N_z}]^T$ is the target normal load acceleration, and $\alpha_t$ is the target angle of attack, related to load factor and airspeed through the aerodynamic lift equation. $S\alpha_t$ and $C\alpha_t$ are sin $(\alpha_t)$ and cos $(\alpha_t)$, respectively. The measurement equation is again Eq (2-38) with

$$H = \left[\begin{array}{c:c} I_{3x3} & \\ \hdashline I_{3x3} & 0_{6x3} \end{array}\right] \tag{2-45}$$

One potential source of uncertainty in this formulation is the angle of attack versus lift for certain enemy aircraft (i.e., coefficient of lift and effective wing surface area). Although certain performance data are not published for some aircraft (such as maximum available thrust), most countries do not attempt to control the dissemination of unclassified data, of which this information is certainly a part [50].

## 2.4 Interactive Filter Formulation

The interactive estimator shown in Fig. 2-2 will be discussed in detail in this section. The primary purpose of the interaction between the motion filter and the target aspect filter is to improve the motion state estimates and allow a better prediction of target position into the future. Another motivation for such interaction might be to improve

the estimation of target aspect. This could be useful for applications such as laser fire control, in which a precise estimate of orientation is crucial to maintaining the light beam on a small portion of the aircraft target. The dynamic model, used for motion state propagation between measurement updates, provides a good description of the acceleration uncertainties of an aircraft in motion (performing maneuvers typical of a fighter in an evasive situation.) This model depends, though, on some knowledge of the direction of target acceleration. This approximate acceleration direction is provided from the aspect filter as explained in a previous section. Measurement updates of both motion data and target attitude data are being periodically provided to the interactive filter by the sensor subsystem. With this overview, a more detailed examination of the computational logic will be made.

2.4.1 Computer Logic Structure. A top level flow chart of the interactive filter is shown in Fig. 2-9. The simulation, or test, version of the system is presented here, i.e., perfect trajectory values are corrupted with noise to simulate the presence of noise on actual radar and attitude data. The operational, or on-line version of the filter would

a) delete blocks 6, 9, 10 and 16,

b) cycle back to (B) after the (W) flag following block 15, and

c) replace "actual" with "measured" in block 8.

The significant contents of each block will be discussed below.

Block 1. Initialization

Initialization is composed of the following tasks:

a) All arrays are dimensioned,

b) The following filter parameters are read in:

(1) Filter constants,

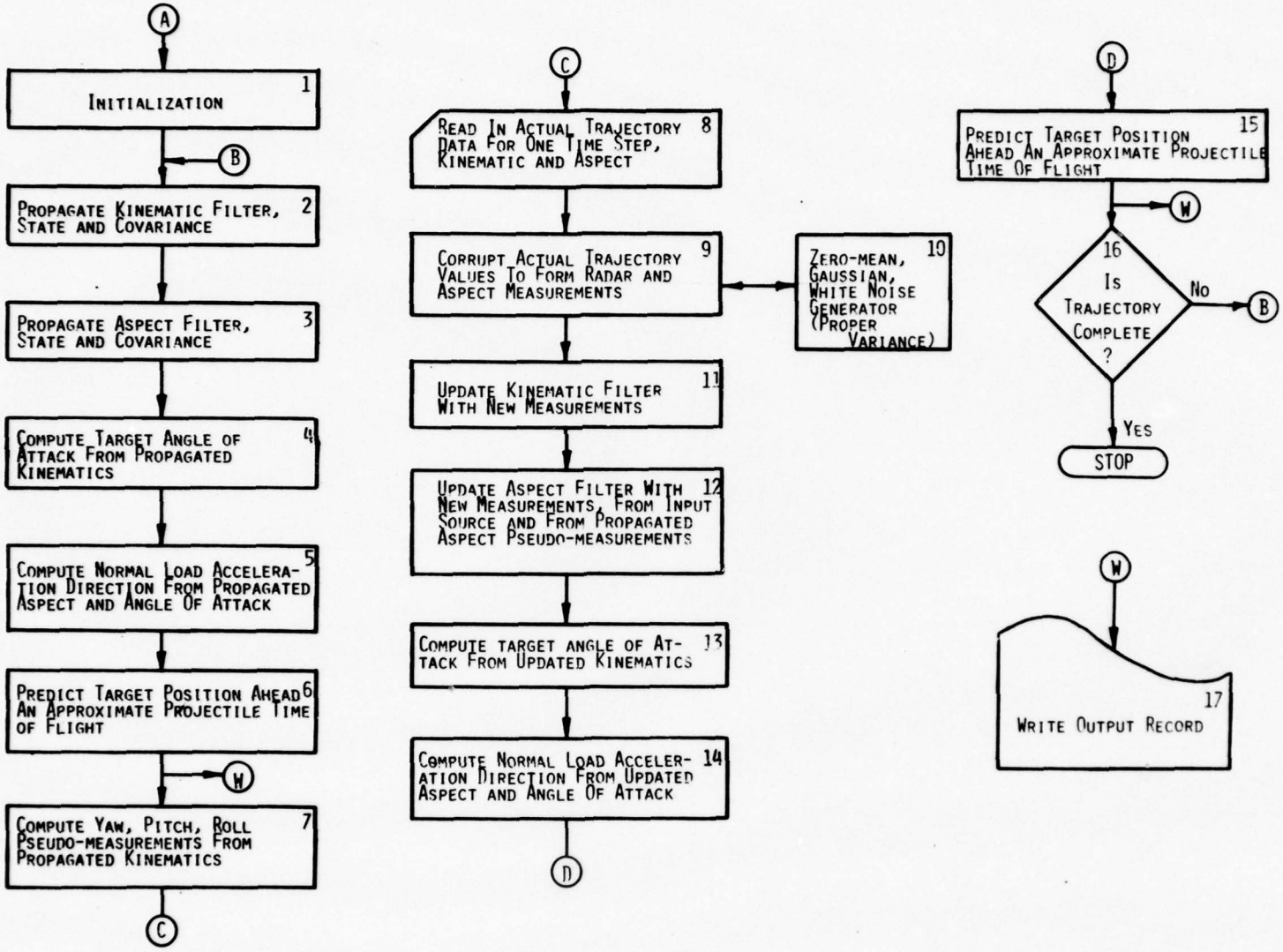


Fig. 2-9. Flow Chart, Interactive Filter, Simulation Version

(2) Update interval times for kinematic and aspect filters (same value read in for each, for this application -- $\Delta t$),

(3) Dimensions and upper diagonal element values of the symmetric covariance matrices $P_o$ (initial kinematic state), Q (kinematic plant noise), R (kinematic measurement noise), $P_{a_o}$ (initial aspect state), $Q_a$ (aspect plant noise) and $R_a$ (aspect measurement noise),

(4) $\sigma^2$ values for uncertainties imposed on radar and aspect measurements used to update interactive filter [six such $\sigma^2$ values for kinematic filter and six values for aspect filter]. (omitted for on-line version)

c) Good initial conditions are established for kinematic states, aspect states, angle of attack and normal acceleration direction by using the first set of actual trajectory data from the trajectory tape. (For on-line version, use first set of measured trajectory data.)

Block 2. Propagate Kinematic Filter, State and Covariance

The expected values of the kinematic state and corresponding state covariance are propagated forward over the interval between updates by integration from their previous updated values. A fourth-order Runge-Kutta integration algorithm is used for this purpose. This is an accurate, general purpose integration algorithm which will provide good results for a wide range of dynamics. It may be possible to use a simpler integration algorithm for an on-line version with these particular dynamics. Integration is from $t = t_k$ to $t = t_{k+1}$ where $t_{k+1} - t_k = \Delta t$. The state equation

$$\dot{\hat{\bar{x}}}(t|t_k) = \bar{f}[\hat{\bar{x}}(t|t_k), \bar{u}(t)] \qquad (2\text{-}46)$$

$$\hat{\bar{x}}(t_k|t_k) = \hat{\bar{x}}_k^+ \tag{2-47}$$

is integrated to yield $\hat{\bar{x}}_{k+1}^-$

and

$$\dot{P}(t|t_k) = F[t;\hat{\bar{x}}(t|t_k)]\, P(t|t_k) + P(t|t_k)F^T[t;\hat{\bar{x}}(t|t_k)] + GQG^T \tag{2-48}$$

$$P(t_k|t_k) = P_k^+ \tag{2-49}$$

is integrated to yield $P_{k+1}^-$

In Eq (2-48), F is given by

$$F[t;\hat{\bar{x}}(t|t_k)] = \left.\frac{\partial \bar{f}[\bar{x},\bar{u}(t)]}{\partial \bar{x}}\right|_{\bar{x} = \hat{\bar{x}}(t|t_k)} \tag{2-50}$$

i.e., an nxn matrix whose i-j component is given by

$$F_{ij}[t;\hat{\bar{x}}(t|t_k)] = \left.\frac{\partial f_i[\bar{x},\bar{u}(t)]}{\partial x_j}\right|_{\bar{x} = \hat{\bar{x}}(t|t_k)} \tag{2-51}$$

Differentiating Eq (2-16),

$$
F[t;\hat{\bar{x}}] = \left[\begin{array}{c:c:c}
 & & 0 \\
 & & 0 \\
 & & 0 \\
0_{6x3} & I_{6x6} & g\beta\gamma e^{\gamma\hat{x}}10(1_N)_n \\
 & & g\beta\gamma e^{\gamma\hat{x}}10(1_N)_e \\
 & & g\beta\gamma e^{\gamma\hat{x}}10(1_N)_d \\
\hdashline
 & -\frac{1}{\tau_n} \quad 0 \quad 0 & 0 \\
 & 0 \quad -\frac{1}{\tau_e} \quad 0 & 0 \\
0_{4x6} & 0 \quad 0 \quad -\frac{1}{\tau_d} & 0 \\
 & 0 \quad 0 \quad 0 & -\frac{1}{\tau_\varepsilon}
\end{array}\right] \qquad (2\text{-}52)
$$

Note from Eq (2-52) that F is time-varying since both $\hat{x}_{10}$ (which is $\hat{\varepsilon}$, related to the magnitude of normal load acceleration) and the normal load acceleration direction vary throughout the propagation cycle. The change in both of these parameters is small enough during the filter iteration interval, however, to assume them to be constant. No new direction information is being made available during the propagation cycle for varying the directional unit vector, and the time constant on $x_{10}$, $\tau_\varepsilon$,

is at least an order of magnitude larger than the cycle time. Thus, $F[t;\hat{\bar{x}}(t|t_k)]$ is approximated as $F[t_k;\hat{\bar{x}}(t_k|t_k)]$ for all $t\epsilon[t_k,t_{k+1})$.

The kinematic state covariance matrix is ten by ten or 100 elements in size. Because it is symmetric, however, only $\frac{10 \times 11}{2}$ or 55 elements are unique. The P matrix is converted to a 55-element vector so that it may be integrated using the Runge-Kutta subroutine. The integrated P vector is converted back to matrix form for subsequent update computations.

Block 3. Propagate Aspect Filter, State and Covariance

The state differential equation and measurement equations for the aspect filter {Eqs (2-29), (2-38)} are linear with constant coefficients. Hence a standard Kalman filter formulation is employed for estimating aspect states. State estimates are propagated using the state transition matrix. Before implementing the filter, covariance propagation equations were integrated analytically, so that $P^-_{a_{k+1}}$ is computed directly from $P^+_{a_k}$, $Q_a$ and $\Delta t$, without need for numerical integration.

Block 4. Compute Target Angle of Attack From Propagated Kinematics

Approximate target angle of attack is computed from the current best estimate of target velocity and acceleration using the technique described in detail in Appendix D. Current angle of attack is required in order to compute normal load acceleration direction as discussed in block 5 below.

Block 5. Compute Normal Load Acceleration Direction From Propagated Aspect and Angle of Attack

Normal load acceleration direction is computed from propagated target aspect states--yaw, pitch and roll--computed in block 3 and target angle of attack computed in block 4. A better estimate of normal load

acceleration direction is required to improve the prediction of target position. The unit vector in the direction of normal load acceleration is computed from the equation,

$$T_N^I = T_I^b \, T_b^v \begin{bmatrix} 0 \\ 0 \\ -1 \end{bmatrix} \tag{2-53}$$

where

$T_I^b = (T_b^I)^T$ is the transformation from b to I coordinates derived in Appendix B, in terms of yaw, pitch and roll,

$T_b^v$ is in terms of angle of attack, and

$[0 \;\; 0 \;\; -1]^T$ is a unit vector, expressed in the velocity frame, in the direction of expected normal load acceleration.

Block 6. Predict Target Position Ahead An Approximate Projectile Time-of-Flight

Predicted target position an approximate projectile time-of-flight ($t_f$) in the future will be computed from the approximate equation,

$$\hat{\bar{p}}_t(t_k+t_f|t_{k-1}) = \hat{\bar{p}}_t(t_k|t_{k-1}) + \hat{\bar{V}}_t(t_k|t_{k-1})(t_f) + \hat{\bar{a}}_t(t_k|t_{k-1})(\frac{t_f^2}{2}) \tag{2-54}$$

$$\hat{\bar{p}}_t(t_k|t_{k-1}) = \hat{\bar{p}}_{t/a}(t_k|t_{k-1}) + \bar{p}_a(t_k) \tag{2-55}$$

$$\hat{\bar{V}}_t(t_k|t_{k-1}) = \hat{\bar{V}}_{t/a}(t_k|t_{k-1}) + \bar{V}_a(t_k) \tag{2-56}$$

The subscripts "t" and "a" represent t/I and a/I, respectively.

Attacker position $\bar{p}_a(t_k)$ and velocity $\bar{V}_a(t_k)$ are assumed available from the attacker INS, while $\hat{\bar{p}}_{t/a}$ and $\hat{\bar{V}}_{t/a}$ are available from the kinematic filter directly. Total target acceleration is modeled directly in the

kinematic filter and is available without the requirement to add relative acceleration to attacker acceleration, i.e.,

$$\hat{\bar{a}}_t(t_k|t_{k-1}) = \hat{\bar{a}}_N(t_k|t_{k-1}) + \bar{g} + \hat{\overline{\delta a}}(t_k|t_{k-1}) \qquad (2\text{-}57)$$

Predicted target position (based on propagation equations) is then written onto an output record for later use. (For on-line version, predicted target position would not be required after propagation cycle, since the more accurate update value would be computed shortly thereafter. Block 6 would be deleted.)

Block 7. Compute Yaw, Pitch, Roll Pseudo-measurements From Propagated Kinematic

Approximate values of target yaw, pitch and roll angles are computed from current best estimates of total target velocity and acceleration. The computational procedure is outlined in section 2.3.2.2 and explained in detail in Appendix D. These approximate angles, based on propagated kinematic estimates, form pseudo-measurements for updating the aspect filter in block 12.

Block 8. Read In Actual Trajectory Data (Kinematic and Aspect) For One Time Step

Actual trajectory values for a single time step are read from the trajectory tape for both attacker and target. Table II identifies the actual trajectory parameters read in at each update time. (The on-line version would read in actual kinematic and aspect measurements.)

Block 9. Corrupt Actual Trajectory Values To Form Radar and Aspect Measurements

Actual trajectory values representing radar measurements, range, azimuth, elevation, range rate, azimuth rate, elevation rate and target

aspect angle measurements, yaw, pitch, and roll, are corrupted with white Gaussian noise to simulate system errors in an operational setting. (Block 9 is deleted for on-line version.)

Table II. Parameters Read From Trajectory Tape

| |
|---|
| Time (seconds) |
| Range (feet) |
| Azimuth, Elevation (radians) |
| Range Rate (ft/sec) |
| Azimuth rate, Elevation rate (rad/sec) |
| Target Yaw, Pitch, Roll (degrees) |
| North, east, down components of following kinematic parameters: (All are total, i.e., relative to inertial space, and expressed in inertial coordinates.) |
| Target: |
| Position (feet) |
| Velocity (ft/sec) |
| Acceleration ($ft/sec^2$) |
| Attacker: |
| Position (feet) |
| Velocity (ft/sec) |
| Acceleration ($ft/sec^2$) |

Block 10. Zero-mean, Gaussian White Noise Generator

Appropriate variances are provided to the noise generator. Realizations of a white, zero-mean, near-Gaussian random variable, $\underline{W}$, of unit variance is generated according to the relation

$$\underline{W} = \sum_{i=1}^{12} (\underline{y}_i - 0.5) \qquad (2\text{-}58)$$

where $\underline{y}_i$ is a realization of the random variable $\underline{y}$ uniformly distributed on the interval (0,1). If the output noise, $\underline{n}$, is to have variance $\sigma^2$, then $\underline{n}$ is set to

$$\underline{n} = \sigma \underline{W} \qquad (2\text{-}59)$$

(Block 10 is deleted for on-line version.)

Block 11. Update Kinematic Filter With New Measurements

Standard extended Kalman filter equations are used to update state estimates. Before implementing the filter, the non-linear measurement vector $\overline{h}(\overline{x})$ {Eq (2-22)} was differentiated analytically and the resulting (6x10) $H(\overline{x})$ matrix is recomputed at update time $t_k$ with $\overline{x} = \hat{\overline{x}}_k^-$ .

Block 12. Update Aspect Filter With New Measurements, From Input Source and From Propagated Aspect Pseudo-measurements

Standard Kalman update equations are used. Aspect pseudo-measurements from block 7 as well as simulated sensor measurements from block 9 are employed to update the estimate of aspect states.

Blocks 13 and 14. Compute Target Angle of Attack From Updated Kinematics, and Compute Normal Acceleration From Updated Aspect and Angle of Attack

Same as blocks 4 and 5, but using updated aspect and kinematics for angle of attack and normal direction computations.

Block 15. Predict Target Position Ahead An Approximate Projectile Time-of-Flight

Predicted target position after update is computed as

$$\tilde{\bar{p}}_t(t_k+t_f|t_k) = \hat{\bar{p}}_t(t_k|t_k) + \hat{\bar{V}}_t(t_k|t_k)(t_f) + \hat{\bar{a}}_t(t_k|t_k)(\frac{t_f^2}{2}) \quad (2\text{-}60)$$

where

$$\hat{\bar{p}}_t(t_k|t_k) = \hat{\bar{p}}_{t/a}(t_k|t_k) + \bar{p}_a(t_k) \quad (2\text{-}61)$$

$$\hat{\bar{V}}_t(t_k|t_k) = \hat{\bar{V}}_{t/a}(t_k|t_k) + \bar{V}_a(t_k) \quad (2\text{-}62)$$

This model does not account for rotation of the target aspect, and hence the acceleration direction, during the prediction time, i.e., a constant inertial direction for acceleration is assumed over the prediction interval. An improved position prediction is possible using a technique developed recently by Terry [51]. This prediction technique assumes that the angle between velocity and acceleration vectors, and not the inertial acceleration, will be nearly constant during the prediction interval. Hence, the velocity and acceleration are propagated together using a target body-fixed coordinate frame while maintaining a fixed angular relation.

Block 16. Trajectory Completion Decision

Trajectory completion is indicated by an end-of-file flag on the trajectory tape. After completion, the algorithm is exited at STOP. (Block 16 is deleted for on-line version.)

Block 17. Write Output Record

An output record of predicted target position (both propagated and

updated) is made for later processing. (The on-line version would provide predicted target position to the appropriate follow-on fire control algorithm. Predicted target position could be used, for example, to make subsequent flight control decisions, orient guns or make fire/no-fire decisions.)

2.4.2 Timing Sequence For Interactive Filter. Ordering of the computations outlined in the computer flow chart, Fig. 2-9, was governed by considering the timing aspects of real-time implementation. A schematic timing sequence chart is shown in Fig. 2-10. Update computations of both the kinematic and aspect filters are made following the measurements shown at $t_k$. Propagation computations are made in the remaining time before the next measurement is taken. In the simulation program, the results of both the propagation computation before $t_k$ and the update computation after $t_k$ are output as if they had occurred simultaneously at $t_k$.

Note that computation of yaw, pitch and roll pseudo-measurements from kinematic estimates is accomplished prior to its being needed to update the aspect filter but after the propagation cycle. The other alternative was to accomplish this task just after the kinematic filter update. This would provide more recent kinematic data for deducing aspect information. However, a bad kinematic measurement would affect the deduced aspect, which could have a destabilizing effect on the overall update. The insertion of this task between the kinematic and aspect filter updates would also, of course, increase the total update computation time (time from receipt of sensor measurements to computation of updated states), which one strives to minimize. Another alternative would be to update each filter separately, i.e., without using the

kinematic filter's $\hat{\bar{x}}(t_k|t_k)$ or $\hat{\bar{x}}(t_k|t_{k-1})$ to update the aspect filter. However, this alternative negates the interactiveness inherent in the approach assumed for this problem. A parallel processing approach is also discussed in a later chapter on real-time implementation considerations.

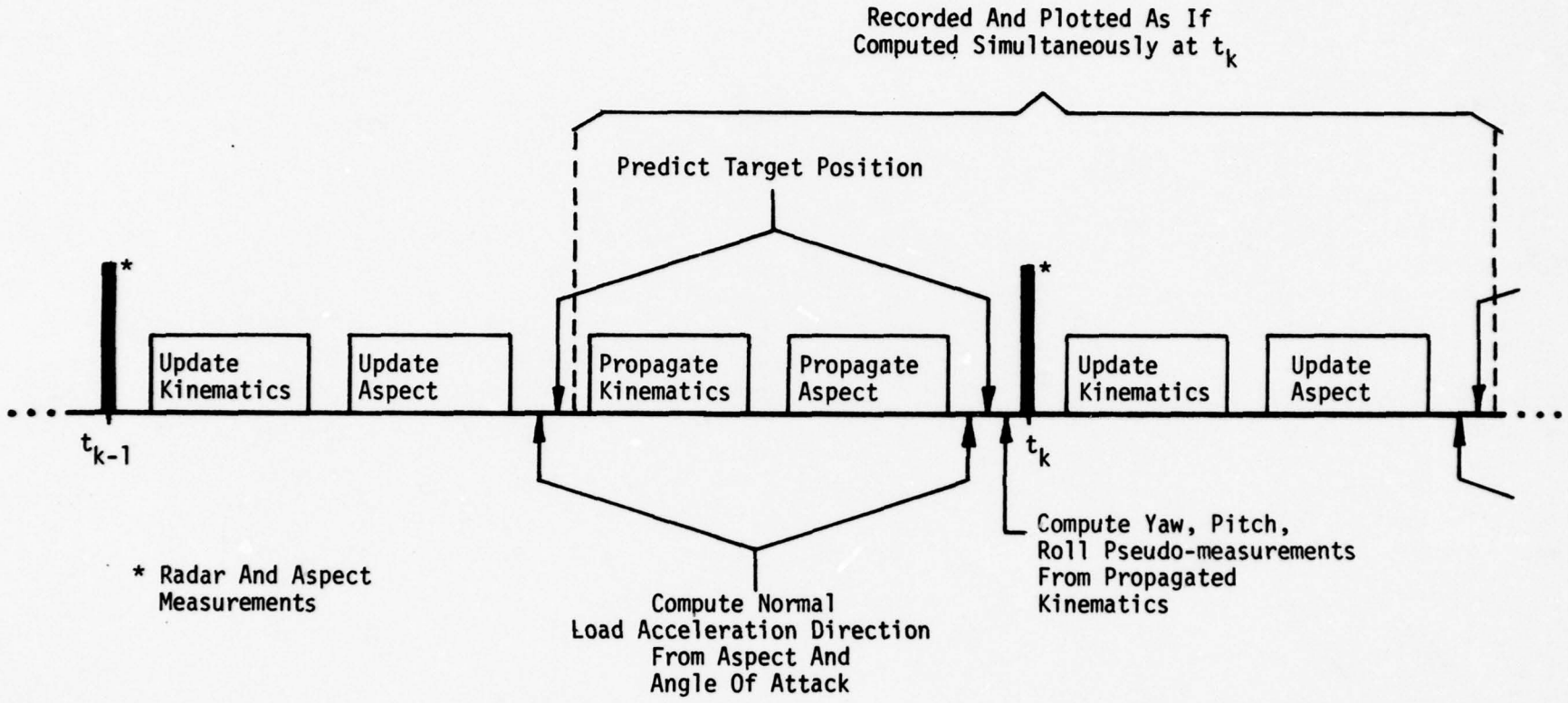


Fig. 2-10. Timing Sequence, Interactive Filter

# III. Performance Analysis and Computer Simulation

In Chapter II, mathematical formulations of the kinematic and target aspect filters were developed. Chapter II also presented a top level logic flow chart for a computer implementation of the interactive filter. The filter developed was the simulation version, so some details relating to simulation techniques were necessarily included. This chapter will outline the performance analysis plan used to validate the improved filter configuration and will discuss the computer simulation in more detail.

## 3.1 Interactive Filter System Performance Analysis

The system performance analysis is designed to demonstrate the improved target tracking characteristics of the interactive filter over a conventional tracking filter for a representative ensemble of scenarios. The analysis provides for an investigation of intrinsic filter behavior such as recovery characteristics, sensitivity to unmodeled errors and criticality of acceleration parameters $\alpha$, $\beta$, $\gamma$. The analysis also includes a comparison of interactive filter performance to an extended Kalman filter algorithm which uses radar measurements only.

3.1.1 Scenarios. Four realistic three-dimensional target engagement scenarios are chosen which encompass the following types of maneuvers:

| Type | Maneuvers |
|---|---|
| a) | Typical combat maneuvers |
| b) | Maneuvers which are typically difficult for other trackers |
| c) | Maneuvers for which the combined filter should show particularly |

improved performance

The four scenarios are listed below and are illustrated in Figs. 3-1 through 3-4.

1. Distant break (Type a)
2. Close-in break with attacker overshoot (Types a,b)
3. Roll followed by high-g break (Types a,b,c)
4. Head-on pass (Types b,c)

Table III provides some associated initial conditions. Each scenario is ten seconds in length and aircraft attitude is indicated in the figures every two seconds. In each scenarios, the attacker and target are initially at an altitude of 20,000 feet.

The computer simulation program employed to generate the combat engagements is FASTAC, [54] a two-aircraft, air-to-air combat evaluation program developed by Battelle Columbus Laboratories under contract with the Air Force Avionics Laboratory. It is basically an interactive version of TACTICS II developed by RAND Corporation [23].

The engagement simulations are realistic with the following qualifications. 1) An aircraft will not break off an engagement even if it has a speed advantage. It will continue maneuvering in an attempt to achieve a position advantage. 2) All turns are coordinated (i.e., no lateral component of velocity). 3) The attacker control strategy during a tail-chase segment is pure pursuit (i.e., the attacker attempts to direct its velocity vector along the instantaneous line-of-sight.) These qualifications do not significantly impact the performance analysis accomplished in this research for several reasons.

Qualification (1) has an impact on strategy but is not a limitation for the relatively short scenario length of ten seconds. Also the

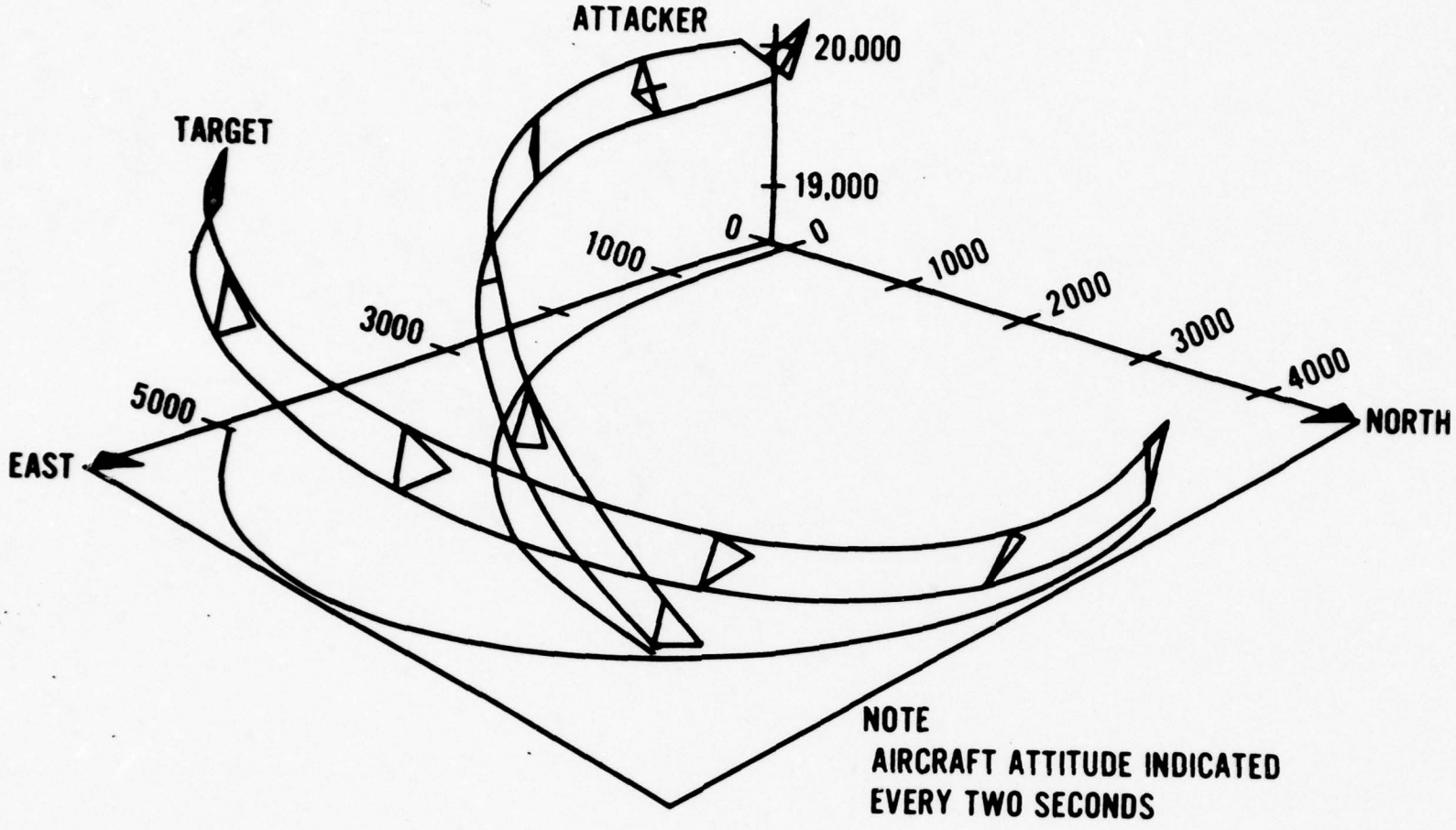


Fig. 3-1. Scenario 1, Distant Break

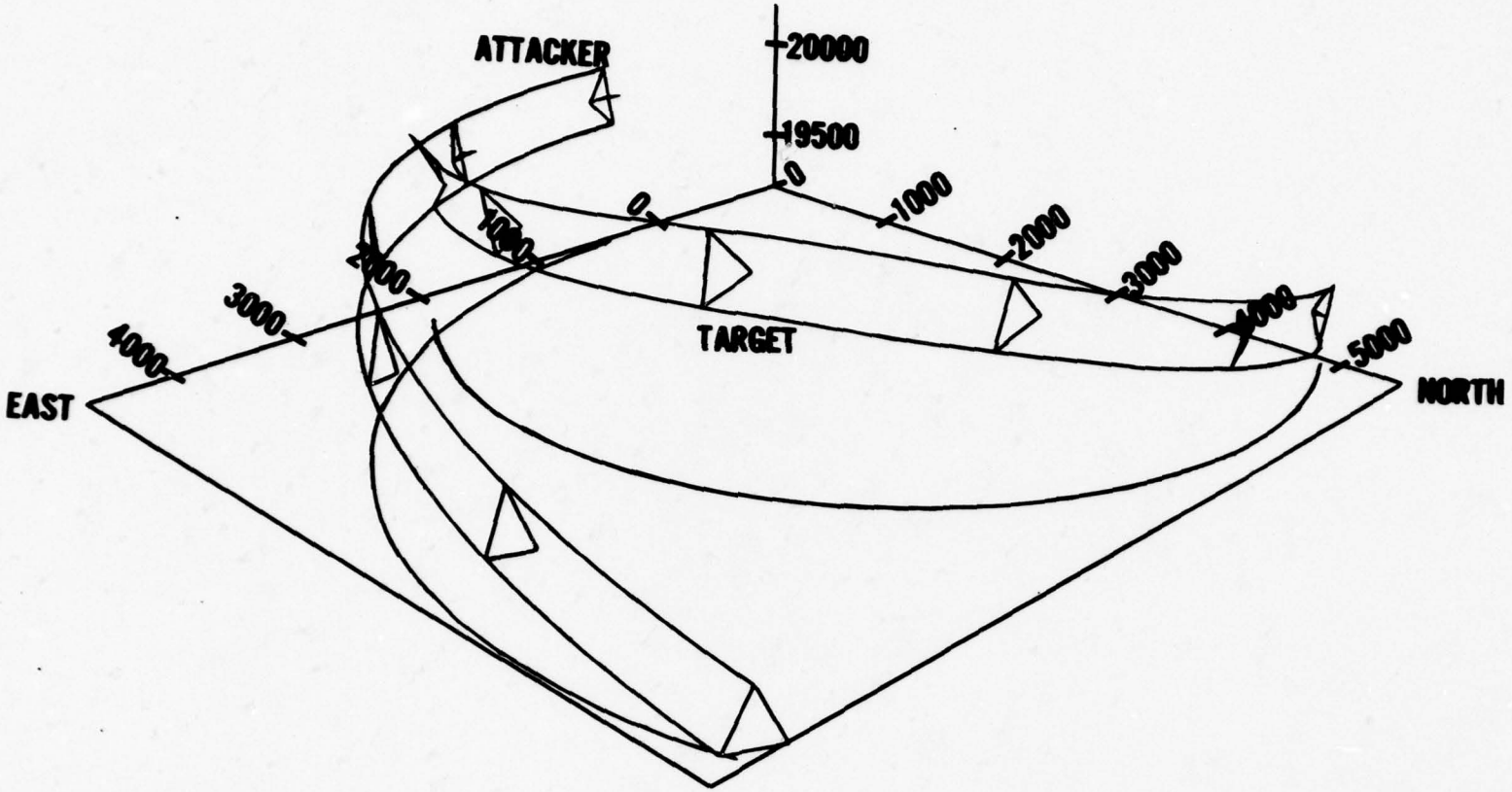


Fig. 3-2. Scenario 2, Close-in Break With Attacker Overshoot

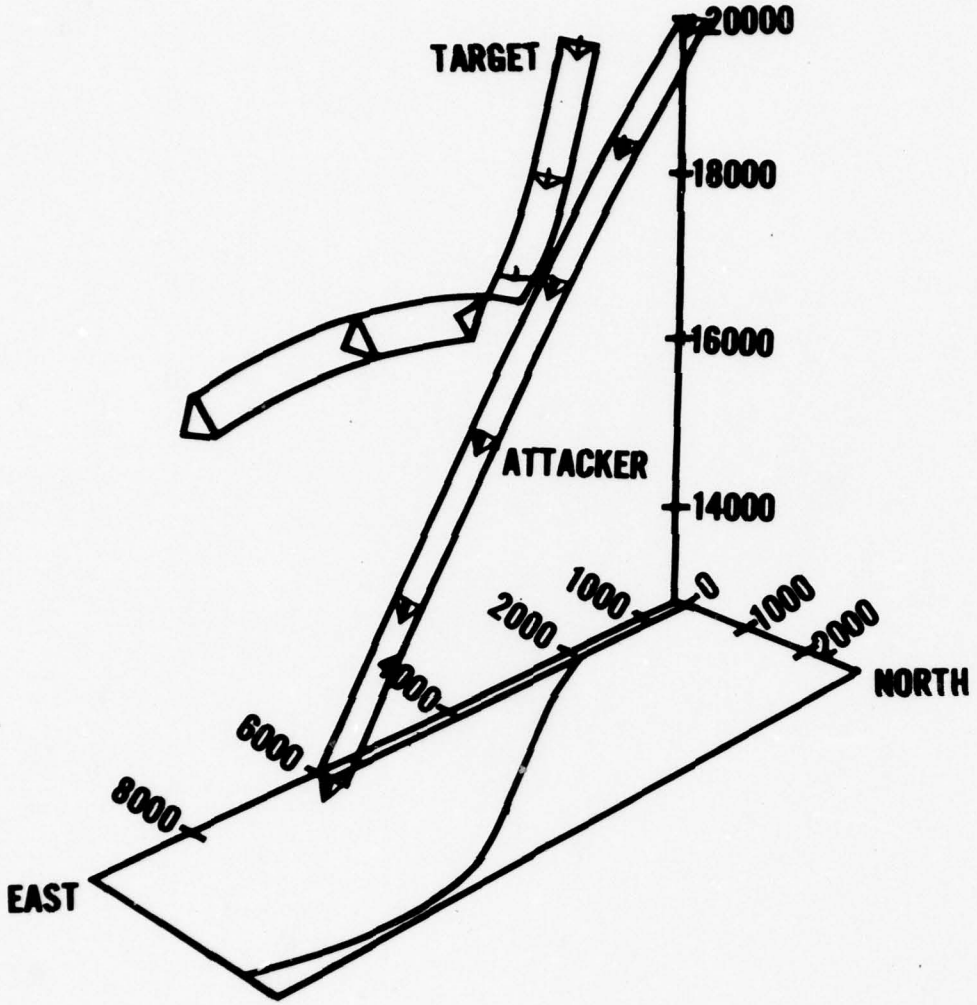


Fig. 3-3. Scenario 3, Roll Followed By High-g Break

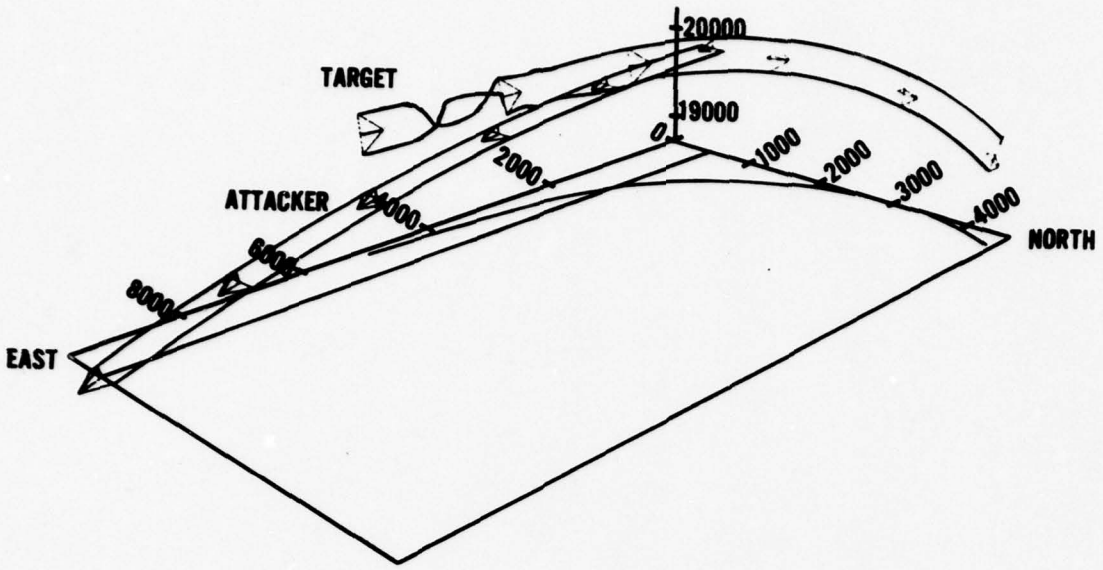


Fig. 3-4a. Scenario 4, Head-On Pass

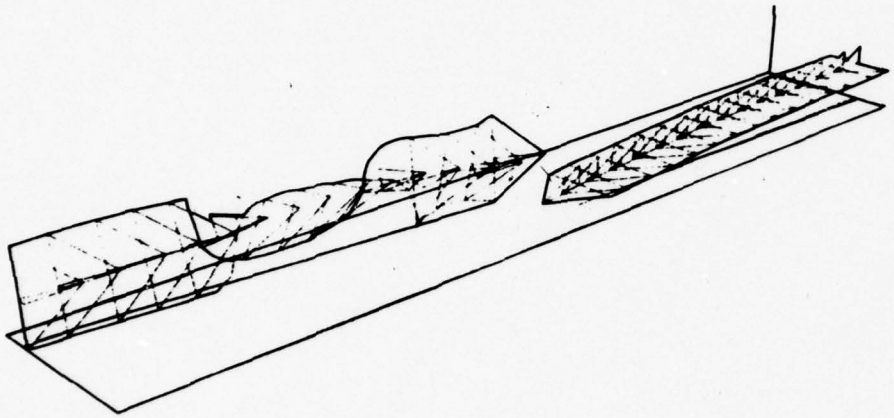

Fig. 3-4b. Scenario 4, First 2.8 Seconds

Table III. Initial Parameters For Scenarios

| Scenario | Initial Parameters | | | |
|---|---|---|---|---|
| | Range (ft) | Angle-Off (attacker relative to target) | Vert. Flight Path Angle | |
| | | | Target | Attacker |
| 1. Distant Break | 5000 | 45° | 0° | 0° |
| 2. Close-in Break With Attacker Overshoot | 1900 | 50° | 0° | 0° |
| 3. Roll Followed By High-G Break | 2000 | 20° | -60° | -45° |
| 4. Head-on Pass | 5025 | 180° | 0° | 0° |

scenarios are chosen to represent realistic defensive maneuvering situations which would occur even if overall strategy were slightly different. Qualification (2) is not an atypical assumption since the pilot attempts to achieve this condition in all air-to-air maneuvers (with recent advances in Control Configured Vehicles for exotic flight control/weapon delivery, being the exception). The pure pursuit mode indicated in qualification (3) is typical of many air-to-air pursuit engagements. Lead pursuit, in which the attacker velocity vector is made to lead the line-of-sight by a few degrees in the turning plane, is also used for some maneuvers. The difference between the two modes represents little effect on vehicle trajectories and aspects for the maneuvers considered.

3.1.2 Monte Carlo Analysis. A Monte Carlo simulation technique is used as a means of demonstrating performance. Measurement noise sequences are varied for each scenario during tuning and for performance analyses after the filter has been tuned. Pertinent performance figures of merit are averaged over all individual Monte Carlo runs to arrive at a composite performance time history of sample statistics which represents expected filter performance. Initial tuning was achieved using one run, intermediate tuning used 5 runs, while final performance results used 20 runs. More details of this simulation technique are presented in the simulation section later in this chapter.

3.1.3 Figures of Merit. The primary motivation for developing improved state estimators for this class of targets is to predict target position far enough into the future to aid in the implementation of weapon delivery algorithms. Hence, the best weighting for combining the estimated values of target position, velocity and acceleration, as

dictated by this application, is governed by the approximate prediction Eqs (2-54) and (2-60).

An approximate upper limit for projectile time of flight, $t_f$, is assumed in order to compute predicted target position. Target range typically varies from approximately 2000 feet to 5000 feet in air-to-air combat engagements. At a typical projectile speed of 4000 - 5000 feet/second, an assumption of 1.0 second for a nominal maximum projectile time-of-flight is reasonable.

The assumption of a constant, nominal maximum for projectile time-of-flight has advantages for the performance analysis. The assumption of a constant projectile flight time avoids the problem of including in the simulation an algorithm to compute projectile flight times from the engagement geometry, aircraft kinematics, and projectile dynamics. Also, because of having selected a nominally large value of $t_f$, actual target prediction accuracies will tend to be better than indicated here, so the performance analysis tends to represent a worst case.

Error in predicted target position is computed by comparing actual target position (approximately one projectile time-of-flight into the future) with predicted target position based upon the current estimate of target position, velocity and acceleration.

$$\bar{e}^I(t_k+t_f \mid t_k) = \frac{1}{m}\sum_{i=1}^{m} \bar{e}_i^I(t_k+t_f|t_k)$$

$$= \frac{1}{m}\sum_{i=1}^{m}[\hat{\bar{p}}^I_{t/I_i}(t_k+t_f|t_k) - \bar{p}^I_{t/I}(t_k+t_f)] \qquad (3\text{-}1)$$

$$= [\frac{1}{m}\sum_{i=1}^{m} \hat{\bar{p}}^I_{t/I_i}(t_k+t_f|\ t_k)] - \bar{p}^I_{t/I}(t_k+t_f)$$

where

k = update time index

m = number of Monte Carlo runs (varying measurement noise sequences)

i = Monte Carlo run index

$t_f$ = approximate projectile time-of-flight

$\bar{p}^I_{t/I}(t_k+t_f)$ = actual total target position at time $t_k+t_f$ expressed in inertial coordinates

$\hat{\bar{p}}^I_{t/I_i}(t_k+t_f|t_k)$ = prediction of total target position at time $t_k+t_f$ based upon measurements through $t_k$, for Monte Carlo run i.

Of interest is the uncertainty in the target position prediction. For a given scenario, the unbiased estimate of variance of the target prediction error at any sample time $t_k$ can be computed from the expression

$$\bar{\Sigma}^I_e(t_k+t_f) = \frac{1}{m-1}\sum_{i=1}^{m}\{[\bar{e}^I_i(t_k+t_f|t_k)][\bar{e}^I_i(t_k+t_f|t_k)]^T\} - \frac{m}{m-1}[\bar{e}^I(t_k+t_f|t_k)][\bar{e}^I(t_k+t_f|t_k)]^T \quad (3\text{-}2)$$

where

$\bar{e}^I(t_k+t_f|t_k)$ was defined in Eq (3-1),

$\bar{\Sigma}^I_e(t_k+t_f)$ = covariance of prediction error at time $t_k+t_f$, with respect to inertial coordinates.

The time-varying diagonal elements of the $\bar{\Sigma}^I_e$ matrix provide variance of the position prediction error components.

Two additional figures of merit are useful in characterizing filter

performance, viz., magnitude of the cross-range component of total target position error, and approximate circular error probable (CEP) expressed in terms of error variances normal to the impact line-of-sight. Position prediction error and error covariance in inertial coordinates is transformed to line-of-sight coordinates. This transformation allows characterization of error and error variance perpendicular to the line-of-sight from attacker to target at nominal time of projectile impact. Position prediction error in tracker line-of-sight (tl) coordinates is given by

$$\bar{e}^{tl}(t_k+t_f|t_k) = T^I_{tl}(t_k+t_f)\bar{e}^I(t_k+t_f|t_k) \tag{3-3}$$

and the corresponding error covariance is given by

$$\sum_{\bar{e}}^{tl}(t_k+t_f) = T^I_{tl}(t_k+t_f)\sum_{\bar{e}}^{I}(t_k+t_f)T^{tl}_I(t_k+t_f) \tag{3-4}$$

where

$T^I_{tl}(t_k+t_f)$ = direction cosine matrix from inertial to tracker line-of-sight coordinate frames, developed in Appendix B, evaluated at time of supposed projectile impact,

and

$$T^{tl}_I = (T^I_{tl})^T \tag{3-5}$$

The assumption is made that the projectile speed is significantly larger than the target speed. Hence, position prediction error in the direction of projectile velocity is not nearly as significant as the error in prediction of cross range position. Assume, additionally, that the projectile direction is nearly along the line-of-sight at time of impact.

Error variances perpendicular to the line-of-sight can be characterized in terms of approximate central circular error probable (CEP). Central CEP is the radius of a circle about the mean error in which half of the error values are statistically likely to occur. Omitting the covariance elements involving prediction error along the line-of-sight, $\underline{\Sigma}_{\underline{e}}^{tl}(t_k+t_f)$ can be expressed as

$$\underline{\Sigma}_{\underline{e}}^{tl}(t_k+t_f) = \begin{bmatrix} - & - & - \\ - & \sigma_y^2 & \sigma_{yz} \\ - & \sigma_{yz} & \sigma_z^2 \end{bmatrix} \tag{3-6}$$

(Cross-correlation term, $\sigma_{yz} = \rho_{yz}\sigma_y\sigma_z$, has the same units as $\sigma_y^2$ and $\sigma_z^2$, but is indicated without the (2) exponent since it can be negative.) Approximate CEP can be calculated by

$$CEP = \begin{cases} 0.675\,\sigma_p + \dfrac{\sigma_q^2}{1.2\sigma_p}, & 0 \leq \dfrac{\sigma_q}{\sigma_p} \leq 0.369 \\ 0.562\,\sigma_p + 0.615\,\sigma_q, & 0.369 < \dfrac{\sigma_q}{\sigma_p} \leq 1 \end{cases} \tag{3-7}$$

where

$$\sigma_p^2 = \sigma_z^2\sin^2\lambda + 2\sigma_{yz}\sin\lambda\cos\lambda + \sigma_y^2\cos^2\lambda \tag{3-8}$$

$$\sigma_q^2 = \sigma_z^2\cos^2\lambda - 2\sigma_{yz}\sin\lambda\cos\lambda + \sigma_y^2\sin^2\lambda \tag{3-9}$$

and

$$\tan\lambda = \frac{2\sigma_{yz}}{(\sigma_y^2-\sigma_z^2) + \sqrt{(\sigma_y^2-\sigma_z^2)^2 + 4\sigma_{yz}^2}} \tag{3-10}$$

where $\lambda$ is the angle of coordinate rotation required to accomplish decorrelation [53].

Note that these performance criteria indicate the merit of an estimator only as it reflects in predicted target position. This choice for figures of merit is based on the intended application of the estimator in a predictive fire control/weapon delivery system. In other words, the appropriate weighting on estimated target position, velocity and acceleration to indicate performance is that dictated by the truncated Taylor series prediction Eqs (2-59) and (2-60).

Some other application might suggest a different weighting on the kinematic (or even aspect) states. For example, a telescope pointing system might reward precise current estimates of position and aspect. While a good acceleration model would be required in order to achieve the highly precise position and aspect estimates, quality of the acceleration estimate need not be rewarded directly in the performance figures of merit. For this feasibility study, the three figures of merit, or performance criteria, discussed above were selected as a means of evaluating performance.

3.1.4 Comparative Radar Filter The performance evaluation of the interactive filter algorithm can be separated into two analysis areas, intrinsic and comparative. The latter evaluates the filter's performance as it compares to a filter which models target relative kinematics but does not model target aspect. The same radar measurements and measurement equations are assumed for this filter as for the interactive filter discussed in Chapter II. A non-adaptive nine-state extended Kalman filter with linear dynamics and first-order Gauss-Markov relative acceleration is used for the comparative filter. The model upon which this filter is

based is

$$\dot{\underline{x}} = \frac{d}{dt}\begin{bmatrix} \underline{p}_{t/a_n} \\ \underline{p}_{t/a_e} \\ \underline{p}_{t/a_d} \\ \underline{V}_{t/a_n} \\ \underline{V}_{t/a_e} \\ \underline{V}_{t/a_d} \\ \underline{a}_{t/a_n} \\ \underline{a}_{t/a_e} \\ \underline{a}_{t/a_d} \end{bmatrix} = \begin{bmatrix} 0 & 0 & 0 & 1 & 0 & 0 & 0 & 0 & 0 \\ 0 & 0 & 0 & 0 & 1 & 0 & 0 & 0 & 0 \\ 0 & 0 & 0 & 0 & 0 & 1 & 0 & 0 & 0 \\ 0 & 0 & 0 & 0 & 0 & 0 & 1 & 0 & 0 \\ 0 & 0 & 0 & 0 & 0 & 0 & 0 & 1 & 0 \\ 0 & 0 & 0 & 0 & 0 & 0 & 0 & 0 & 1 \\ 0 & 0 & 0 & 0 & 0 & 0 & \frac{-1}{\tau_n} & 0 & 0 \\ 0 & 0 & 0 & 0 & 0 & 0 & 0 & \frac{-1}{\tau_e} & 0 \\ 0 & 0 & 0 & 0 & 0 & 0 & 0 & 0 & \frac{-1}{\tau_d} \end{bmatrix} \underline{x} + G\underline{W} \qquad (3\text{-}11)$$

where

$$G = \begin{bmatrix} 0_{6x3} \\ \hline I_{3x3} \end{bmatrix} \qquad (3\text{-}12)$$

$$\underline{W} = [\ \underline{W}_{a_n}\ \underline{W}_{a_e}\ \underline{W}_{a_d}\ ]^T \qquad (3\text{-}13)$$

and

$$E\ [\underline{W}(t)\underline{W}^T(t+\tau)] = Q\delta(\tau) \qquad (3\text{-}14)$$

Values for Q are given in Appendix E.

3.1.5 Tuning Both the interactive filter and comparative filter must be tuned for proper operation. The comparative radar filter is tuned by adjusting modeling noise covariance, Q, and time constants $\tau_n$, $\tau_e$, $\tau_d$, in an attempt to get the "best" performance over all scenarios. The same value of a time constant or covariance element is used for all

three inertial components. This simplifies the tuning process and helps to preclude over-tuning to a particular scenario. It also, of course, reflects the expectation that, over an ensemble of maneuvers, target kinematics are independent of their representation in an inertial coordinate frame.

Tuning of the interactive filter is considerably more complex. Variations are made in time constants, Q, $Q_a$ and those elements of the aspect measurement matrix, $R_a$, which model uncertainty in the kinematically derived aspect angle pseudo-measurements. Possible variations in other filter parameters (such as $\alpha$, $\beta$, $\gamma$ and measurement noise covariance, R) are considered later as analysis techniques and not part of the tuning process. R was not varied during tuning, as the same radar noise variances were used in the filter model as were used in the radar noise generation.

A pre-tuning baseline configuration for filter parameters was assumed. The filter parameters are optimized (in the sense of yielding best performance according to the chosen figures of merit) during the tuning process. Six matrices ($P_o$, Q, R, $P_{a_o}$, $Q_a$, $R_a$) and several other parameters ($\alpha$, $\beta$, $\gamma$, $\tau_n$, $\tau_e$, $\tau_d$, $\tau_\varepsilon$ ) are needed to specify the interactive filter model. The radar model can be specified with three matrices ($P_o$, Q, R) and three parameters ($\tau_n$, $\tau_e$, $\tau_d$ ). However, one of these three matrices, the radar measurement noise covariance, R, is the same as that for the interactive filter and need not be repeated. Pre-tuning filter parameters and, where applicable, tuned parameters are tabulated in Appendix E. Only diagonal elements of matrices are specified. Off-diagonal elements are assumed zero.

Care was taken to avoid over-tuning the filters to a particular

scenario. Approximate values of tuning parameters were achieved during initial tuning, accomplished using only scenario 1 and a single noise sequence (a "Monte Carlo" of one). Subsequently, trial tuning parameters were repeatedly selected and figures of merit were checked for all scenarios (at the "intermediate" tuning level of five Monte Carlo runs) to select the "best" performance over the ensemble of trajectories. The process was somewhat subjective, as no composite figure of merit was defined for application across an ensemble of scenarios. Further research, particularly in the area of adaptivity, would likely improve performance if trajectory-dependent filter tuning were pursued.

3.1.6 Performance Analysis Plan The previous sections in this chapter have discussed the primary concerns in establishing a performance analysis. This section outlines specific questions or areas of investigation which are addressed in the demonstration of performance. Results are given in Chapter IV. The specific areas of investigation are listed in Table IV. The table indicates the methods used to examine performance in the various areas of investigation, and indicates whether an area is considered comparative or non-comparative.

Table IV. Performance Analysis Plan

| Area of Investigation | C or N* | Method |
|---|---|---|
| 1. Figures of Merit<br><br>Compare filters using figures of merit over all scenarios. | C | Once tuned, average total error magnitude, average cross-range error magnitude and CEP perpendicular to line-of-sight are compared for the two filters for each separate |
| 2. Criticality of Filter Parameters<br><br>Determine sensitivity of filter performance to choice of parameters $\alpha$, $\beta$ and $\gamma$. | N | Vary $\alpha$, $\beta$, $\gamma$; examine figures of merit. |
| 3. Recovery and Sensitivity Characteristics | C | |
| a. Bad initial conditions | | Set in bad initial conditions in states with errors of 100 feet in relative position, 100 ft/sec in relative velocity and 3 g's in total acceleration (relative acceleration for comparative filter). |
| b. One-time bad measurement after filter has reached steady-state operation | | Insert bad radar measurement after filter has reached steady-state ($3\sigma$ in worst-case combination) |
| c. Radar measurement errors consistently larger than modeled in filter | | Standard deviations made 3 times worse than modeled in filter. Compare figures of merit. |

*Comparative or Non-Comparative

(cont'd)

| Area of Investigation | C or N* | Method |
|---|---|---|
| 4. Aspect Error Analysis | N | |
| a. What is the average error (and variances) between true aspect and estimated aspect from the aspect filter? | | Estimates of aspect from the aspect filter output are compared to true aspect and resulting error averaged (Monte Carlo) and plotted for each aspect channel. |
| b. How does this compare with the average error (and variances) between true aspect and estimated aspect based on velocity and acceleration estimates? | | Compare with similar plots made from kinematically derived target aspect. |
| 5. Aspect Noise Analysis | N | |
| a. How does the interactive filter performance deteriorate as aspect measurement noise is increased? | | |
| 1) Filter unaware | | $R_a$ held constant, noise sigmas increased. Cases: a) times two, b) times five. |
| 2) Filter aware | | $R_a$ is increased as noise sigmas are increased. Same cases as 5a(1) above. |
| b. How would a bias on input aspect measurements affect filter performance (filter unaware)? | | Add 2-5 degree bias to all three aspect channels. |
| c. If some appropriate non-Gaussian noise model were used for aspect measurement corruption, what effect would this have on filter performance? | | Corrupt E-O aspect measurements with appropriate non-Gaussian noise (defined in text) but with filter unaware, i.e., still designed on the basis of white Gaussian corruption. |

(cont'd)

| Area of Investigation | C or N* | Method |
|---|---|---|
| 6. E-O/PR System Not Available<br><br>If there were no pattern recognition device available, could the aspect estimate based on velocity and acceleration be used for deriving normal load acceleration direction? | N | Restructure filter to eliminate E-O measurements but leave in aspect "pseudo-measurements". Observe performance for signs of instability and other degradations. |

## 3.2 Computer Simulation

This section outlines the computer implementation of the performance analysis plan developed in the previous section. The simulation is performed on a Control Data Corporation model 7700 computer with a SCOPE operating system and FORTRAN IV Extended program language. Fig. 3-5 shows the five phases of the simulation. These phases evolve naturally from the tasks to be performed. The representative trajectories are generated by the FASTAC program in phase I. The data must be reformatted in phase II to conform with conventions adopted for the filter formulation. The filter program in phase III is either the interactive filter shown in Fig. 2-2 or the radar comparative filter discussed in section 3.1.4. The output data generated by the filter in phase III contains m repetitions of the trajectory where m is the Monte Carlo runs. Phase IV computes the error statistics required in the performance analysis by comparing the filter outputs with the original noise-free trajectory. Finally, pertinent plots are generated in phase V.

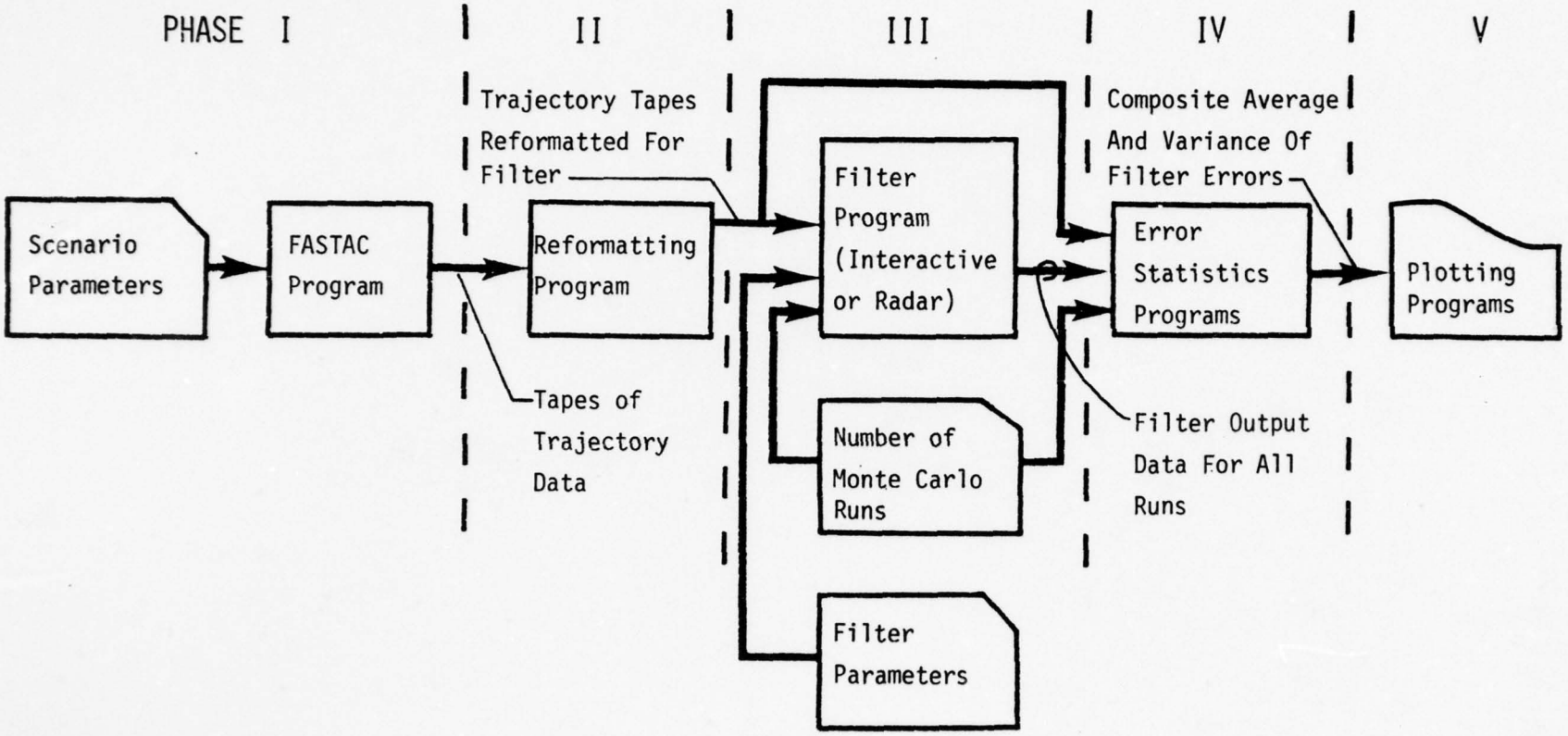


Fig. 3-5. Computer Simulation System

# IV. Results and Discussion

## 4.1 Figures of Merit

The results discussed in this and the following sections were established according the performance analysis plan presented in Table IV. Performance of the tuned interactive filter is compared to that of the tuned radar-only filter in Table V. Average and peak values of each of the figures of merit are compared for each of the scenarios. The average value is taken from the plots for steady-state operation (after initial transients have subsided, approximately one second into trajectory). The peak is taken at the worst error (but after initial transients have subsided). The plots for each of these figures of merit, for scenarios 1 through 4 are included in Appendix A as Figures A-1 to A- 6, A-41 to A-46, A-47 to A-52 and A-53 to A-58, respectively.

In each of the four scenarios, the average error and peak error in all three figures of merit are less for the interactive filter than for the radar-only filter. The comparison is particularly dramatic for scenario 4. The radar-only filter appears to break lock at approximately the time the target and attacker are abreast. The maximum average error is greater than 14,000 feet for the radar-only filter but is only 160 feet for the interactive filter. The radar-only filter had not fully recovered from this tracking loss at the end of the scenario six seconds later. The interactive filter, on the other hand, recovered to steady-state operation in less than two seconds after the dramatic maneuver, as shown in Fig. A-53.

AD-A066 195 AIR FORCE INST OF TECH WRIGHT-PATTERSON AFB OHIO SCH--ETC F/G 17/8
ESTIMATION OF AIRCRAFT TARGET MOTION USING PATTERN RECOGNITION --ETC(U)
DEC 78 J D KENDRICK

UNCLASSIFIED AFIT/DS/EE/78-6 NL

2 OF 3
AD
A066 195

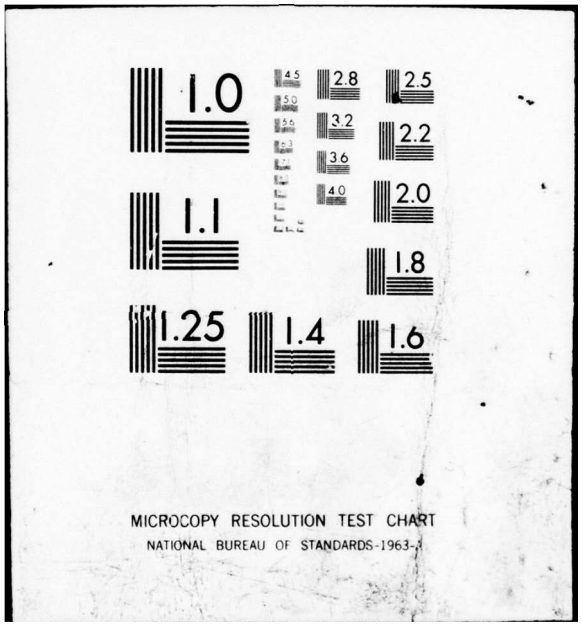
1.0
1.1
1.25
1.4
1.6
1.8
2.0
2.2
2.5
2.8
3.2
3.6
4.0
4.5
5.0
5.6
MICROCOPY RESOLUTION TEST CHART
NATIONAL BUREAU OF STANDARDS-1963-A

Table V. Interactive Filter Vs. Radar-Only Filter

Approximate Steady-State Performance Values

[Average/Peak, Values in Feet]

| Scenario | Total Predicted Position Error | | Cross-Range Predicted Position Error | | Cross-Range CEP | |
|---|---|---|---|---|---|---|
| | Interactive | Radar-Only | Interactive | Radar-Only | Interactive | Radar-Only |
| 1 | 20/30 | 50/70 | 5/15 | 12/22 | 12/15 | 16/22 |
| 2 | 22/35 | 50/70 | 15/28 | 15/34 | 12/20 | 16/25 |
| 3 | 15/46 | 20/130 | 15/32 | 17/86 | 12/18 | 15/22 |
| 4 | 15/155 | 40/14000 (broke track) | 8/160 | */8500 | 15/100 | 25/7000 |

* Too erratic to obtain a reasonable average

A comparison of average CEP in the plane perpendicular to the line-of-sight is not nearly so contrasting as for the other two figures of merit. There is little difference between the interactive and the radar-only filters for this performance criterion except for scenario 4. The average CEP appears to be nearly steady at about 12-16 feet for both filters for scenarios 1, 2 and 3. In scenario 4, however, the maximum CEP is over 6,000 feet for the radar-only filter and only 100 feet for the interactive filter (Figures A-57 and A-58).

## 4.2 Criticality of Filter Parameters

The parameters $\alpha$, $\beta$ and $\gamma$, which determine the shape of the pdf for acceleration magnitude, were varied to determine the sensitivity of filter performance to pdf shape. Fig. 4-1 shows the acceleration magnitude pdf for several combinations of these parameters. The parameter $\alpha$ represents a maximum acceleration limit. Hence, this parameter is set to 8 g's and is not varied for this study. The values for $\beta$ and $\gamma$ were selected empirically to model the density of probability at high acceleration values. Reducing the magnitude of the negative parameter $\beta$ shifts the mode of the pdf closer to the maximum limit $\alpha$, and for a given value $\gamma$ also makes the shape of the pdf more peaked. Reducing the value of the parameter $\gamma$ for a given $\beta$ also has a peaking effect.

Fig. 4-1a illustrates the choice of pdf parameters for the baseline filter for which filter performance has already been determined. Two additional parameter choices were selected for simulation in the interactive filter--Figures 4-1c and f. The trend in these two figures is toward greater peaking of the pdf at higher acceleration values which are typical of those occurring in these scenarios. The results of these choices are shown in Fig. A-7 and Fig. A-8. Approximate steady-state performance values are also shown in Table VI for the three cases

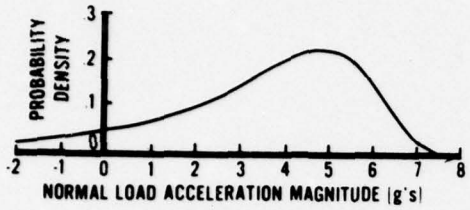


a. $\alpha=8$, $\beta=-4$, $\gamma=0.5$

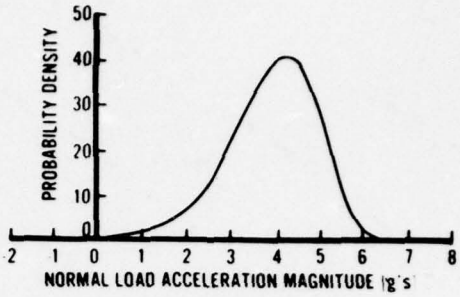


b. $\alpha=8$, $\beta=-4$, $\gamma=0.25$

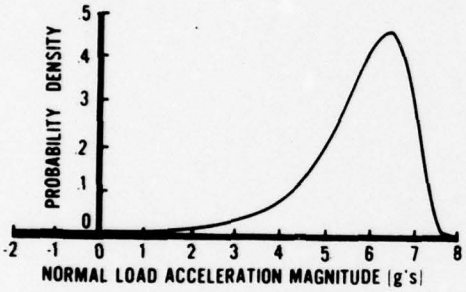


c. $\alpha=8$, $\beta=-2$, $\gamma=0.5$

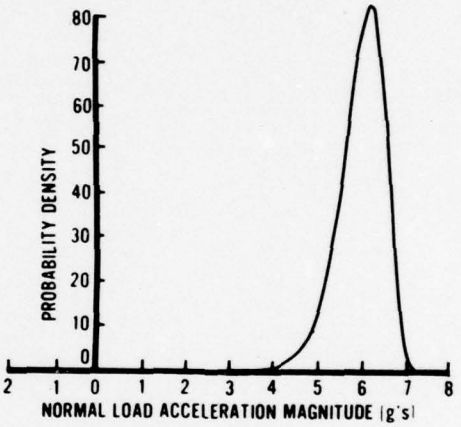


d. $\alpha=8$, $\beta=-2$, $\gamma=0.25$

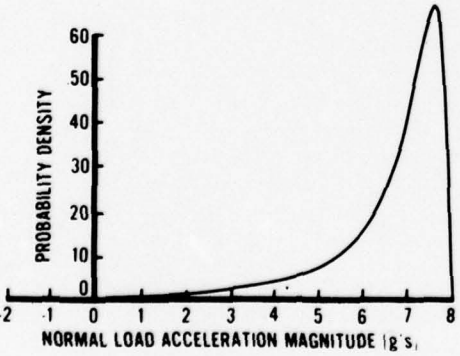


e. $\alpha=8$, $\beta=-1$, $\gamma=1$

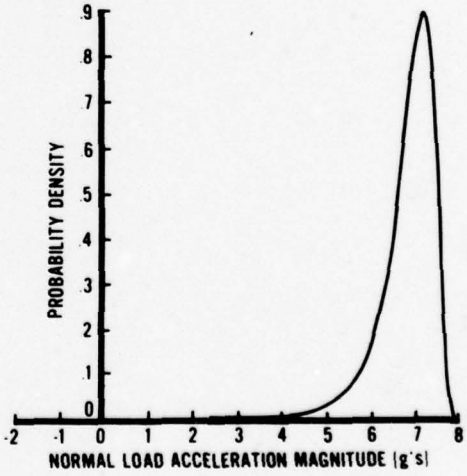


f. $\alpha=8$, $\beta=-1$, $\gamma=0.5$

Fig. 4-1. Acceleration pdf For Several Choices of Parameters $\alpha$, $\beta$, $\gamma$

represented by Fig. 4-1a, c and f. The steady-state value of average error magnitude for scenario 1 dropped from about 20 feet for Fig. 4-1a, to approximately 15 feet for Fig. 4-1c, to approximately 12 feet for Fig. 4-1f. Average cross-range predicted position error and cross-range CEP, however, show little change as a result of this parameter variation. Hence, these plots are not included.

## 4.3 Recovery and Sensitivity Characteristics

4.3.1 Bad Initial Conditions. Bad initial conditions were set in for kinematic filter states with errors of 100 feet in relative position, 100 ft/sec in relative velocity and 3 g's in total acceleration (relative acceleration for comparative filter). Figures A-9 and A-10 compare the total predicted position error for the interactive and radar-only filters for scenario 1. As can be seen, the time to reach steady-state operation is approximately the same (one second) for each filter, as is the magnitude of the initial transient.

4.3.2 One-Time Bad Measurement. A one-time bad radar measurement was inserted into otherwise normal measurement data at five seconds into scenario 1, in order to examine the sensitivity and recovery characteristics of the interactive filter as compared to the radar-only filter. This bad measurement was formed by corrupting all the true kinematic values (range, range rate, angles and rates) with $+3\sigma$ additive noise values, where $\sigma$ is the appropriate standard deviation for each particular measurement.

Plots of total and cross-range predicted position error for both the interactive and radar-only filters are shown in Figures A-11 through A-14 . Cross-range CEP showed virtually no effect from the bad measurement and hence is not included in the plots. The response to the bad measurement appears at six seconds, instead of five, because the plot shows position

Table VI. Approximate Steady-State Performance Values, Various Filter Paramters, Scenario 1 [Average/Peak, Values in Feet]

| | Total Predicted Position Error | Cross-Range Predicted Position Error | Cross-Range CEP |
|---|---|---|---|
| $\beta = -4$ | 20/30 | 5/15 | 12/15 |
| $\beta = -2$ | 15/22 | 6/13 | 12/15 |
| $\beta = -1$ | 12/18 | 7/16 | 12/15 |

Note: $\alpha = 8$, $\gamma = 0.5$; only $\beta$ varied as explained in text.

The three cases correspond to Fig. 4-1a, c and f, respectively.

error at the supposed time of projectile impact, with an assumed projectile time-of-flight of one second.

As shown in these figures, the interactive filter recovers quickly from the bad measurements (about 5 to 10 measurement cycles) as does the radar-only filter. The interactive filter shows a greater sensitivity to this bad measurement as evidenced by the larger predicted position error. The cross-range predicted position error plot for the radar-only filter actually shows an improvement, rather than a degradation, at the bad measurement. This is likely due to a filter update which, because of the particular combination of bad radar measurements, tends to lead or anticipate the maneuver, at least as projected into the cross-range plane. The interactive filter, with its different states to update, is more sensitive to this bad measurement. An extension to this research would treat the bad-measurement recovery and sensitivity problem by varying the magnitude and sign of the corruption composing the bad measurement, rather than assuming the same magnitude and sign of the corruption for each Monte Carlo sample as was done in this research.

4.3.3 Unmodeled Radar Errors. Using scenario 1, responses to radar measurement errors consistently larger than modeled in the filters are determined for both interactive and radar-only filters. This is done by increasing the standard deviations of the white, Gaussian, radar measurement noises by a factor of three. The radar noise levels are summarized in Table VII. The filter model is not changed and the measurement covariance matrix is as specified in Appendix E, Table E-III. Also, aspect noises levels are not changed.

The results of this comparison are plotted in Figures A-15 through A- 20 . Average steady-state values of total and cross-range predicted

position error, and average CEP are, respectively, 20 feet, 10 feet and 35 feet for the interactive filter. These compare, respectively, to 50 feet, 20 feet and 50 feet for the radar-only filter. Again, a factor of at least two is evident in the first two figures of merit and some improvement in the third. These results are summarized in Table VIII. They demonstrate that, as with the radar-only filter, the interactive filter is not overly sensitive to deviations in radar noise levels from those modeled in the filter.

Table VII. Radar Measurement Noise Levels, Large Unmodeled Errors

| Radar Measurement | Actual Noise Level, $1\sigma$ | Filter Assumed Noise Level, $1\sigma$ |
|---|---|---|
| Range | 150 feet | 50 feet |
| Azimuth Angle | 6 mrad | 2 mrad |
| Elevation Angle | 6 mrad | 2 mrad |
| Range Rate | 150 ft/sec | 50 ft/sec |
| Azimuth Rate | 12 mrad/sec | 4 mrad/sec |
| Elevation Rate | 12 mrad/sec | 4 mrad/sec |

Table VIII. Average Steady-State Performance Values, With Large Unmodeled Radar Errors (Values in Feet)

| | Total Predicted Position Error | | Cross-Range Predicted Position Errors | | Cross-Range CEP | |
|---|---|---|---|---|---|---|
| | Inter-Active | Radar-Only | Inter-Active | Radar-Only | Inter-Active | Radar-Only |
| Large Unmodeled Radar Errors | 20 | 50 | 10 | 20 | 35 | 50 |
| Correctly Modeled Radar Errors | 20 | 50 | 5 | 12 | 12 | 16 |

## 4.4 Aspect Error Analysis

Two forms of target aspect measurements are provided as inputs to the aspect Kalman filter--kinematically derived aspect and aspect based upon pattern recognition derivates from electro-optical imagery data. The latter of these two aspect measurement sources is simulated by corrupting true aspect with white, Gaussian noise in all three channels-- yaw (or heading), pitch and roll. Kinematically derived target aspect, as discussed in Chapter II and developed in detail in Appendix D, is a function of estimated target velocity, acceleration and computed angle of attack. Kinematically derived aspect is modeled in the filter as having a 10 degree one-sigma uncertainty, as compared to five degrees modeled for the E-O/PR aspect.

The estimated target aspect output from the Kalman filter (both propagated and updated values) can be compared to true aspect to form an error in all three channels. This average error, along with actual one-sigma deviations, is plotted for scenario 1 in Fig. A-21. This can be compared to error in kinematically derived target aspect, shown in Fig. A- 22 . (Note the difference in ordinate scales.)

Standard deviation appears to be approximately 2 degrees for estimated target aspect and approximately 2 degrees or less for the kinematically derived aspect. The guess of 10 degrees one-sigma for filter modeling of kinematically derived aspect is higher than the 2 degrees evidenced here. However, the filter anticipates (or, at least, models) a zero-mean error which this clearly is not.

A bias of approximately 3-5 degrees is evident in the yaw channel of Fig. A-22. This bias is likely due to a slight error in computing angle of attack from load acceleration magnitude. Recall that the computation of the kinematically derived aspect pseudo-measurements is based upon a velocity frame definition which depends directly on the value of angle of attack. (See Appendix D.) An error in angle of attack translates directly into errors in inertially-referenced heading and pitch, the exact amount into each depending upon the value of roll. For example, at zero degrees of roll, angle of attack error translates directly into only pitch error. Whereas, at 90° roll, an angle of attack error becomes a heading, or yaw, error. Note that for the nearly 90 degrees of roll occurring in scenarios 1 and 2, an error in the computation of angle of attack would result in a nearly equal error in the computation of yaw.

## 4.5 Aspect Noise Analysis

4.5.1 Measurement Noise Increased. An E-O/PR aspect measurement noise of five degrees ($1\sigma$) in each aspect channel was assumed for the baseline configuration discussed in the previous sections. Two additional cases were run--10°($1\sigma$) and 25° ($1\sigma$)--with the filter both aware and unaware, i.e., with the aspect measurement covariance both modeling and not modeling the increased input noise strengths. The results for the 25°

case are shown for scenario 1 in Figures A-23 through A-30.

An increase from 5° to 10° in one-sigma measurement error has an insignificant effect on performance, whether the proper noise strength is modeled in the filter or not. However, an increase from 5° to 25° one-sigma error degrades average predicted position error by about 35% and average CEP by more than 75%, for the case of the filter unaware. For the other case in which the increased aspect measurement noise in included in the filter model, the filter appears to develop an instability which worsens throughout the scenario. Average predicted position error is approximately twice that of the 5° one-sigma case. Cross-range predicted position error, in particular, shows a growing (and seemingly periodic) instability. Average CEP for this case, however, is only about 25% higher. Inclusion of plots of error in kinematically derived target aspect and Kalman filter estimated aspect helps to determine the nature of the instability. When the aspect filter is unaware of the degraded E-O/PR aspect measurements, the standard deviation of the error is greater than that of the aware filter. However, its mean is near zero since the measurement data, although noisier than known by the filter, is corrupted with zero-mean noise. The other filter, aware of greater uncertainty in the E-O/PR data, weights the kinematically derived aspect relatively more. Hence, the aspect filter output tends to track the input kinematic data, as shown in Figures A-29 and A-30 . Each filter in this case is tending to couple into the other increasingly bad information about target aspect. Without the stabilizing effect of measured aspect, the interactive filter system seems to exhibit instability. This tendency is examined further by eliminating the E-O/PR system altogether, the results of which are discussed later in this chapter.

4.5.2 Measurement Bias. A zero-mean, Gaussian white noise was added to each of the three aspect measurement channels for the baseline configuration discussed in earlier sections. This measurement noise attempts to simulate uncertainties introduced by the sensor and the generic pattern recognition algorithm. Subsequently, a fixed bias of five degrees was added to each of the zero-mean, Gaussian white noise corruptions (with the filter unaware) to determine the sensitivity of the interactive filter to aspect bias errors. Such errors might be due to imperfect pattern recognition techniques or to geometric conversions from image frame to inertial frame. Figures A-31 through A-33 illustrate the performance of the interactive filter with aspect measurement bias. All three figures of merit indicate only a slight degradation in performance from the baseline configuration. Figures A-34 and A-35 respectively illustrate the aspect errors from the filter and the errors in kinematically derived target aspect. The apparent transfer of the bias error directly into the filter output in Figure A-34, is due to the high weighting of the biased aspect measurement inputs, compared to the lower weighting of kinematically derived aspect, i.e., the filter was not made aware of the measurement bias error.

4.5.3 Different Noise Model. The preceding analyses have been performed using a relatively simple noise model for target aspect measurements. True, inertially referenced, target yaw, pitch and roll angles were corrupted with white, Gaussian noise and input to the Kalman filter. A more complex, and probably more realistic, noise model was devised to generate aspect measurements as follows. True, inertially-referenced, target aspect is transformed to image plane aspect via tracker azimuth and elevation angles. This image plane aspect is corrupted with white, Gaussian noise and the resulting angles rounded to the nearest five

degrees. This simulates a closest-neighbor/table-look-up pattern recognition technique, like that discussed in Chapter II. The corrupted, rounded, image plane aspect angles are then transformed back into the inertial reference frame and provided to the filter. This modeling technique is used with filter unaware, i.e., the white, Gaussian noise model is still assumed in the filter for aspect measurements. This model was run using scenario 1. The results of using this noise model are insignificantly different from results using the simpler model and, hence, the plots showing performance are not included. This result verifies the robustness of the filter model to variations in input aspect noise characteristics.

## 4.6 E-O/PR System Not Available

The section on Aspect Noise Analysis showed that performance of the interactive filter diminished as E-O/PR measurement noise was increased. The interactive filter can be restructured to eliminate E-O/PR measurements altogether. In this configuration, only the kinematically derived aspect pseudo-measurements are provided to the aspect Kalman filter, i.e., the only external measurements to the interactive filter are from the radar system. The chief concern in this "bootstrap" configuration is stability. The results for scenario 1, illustrated in Figures A-36 through A-40, show that the steady-state performance of this system is somewhat better than the radar-only comparative filter, until instability begins to set in at about 4 seconds into the trajectory. Standard deviation of the kinematically derived aspect error progressively increases between 4 seconds and 7 seconds and the error appears to become more oscillatory toward the end of the 10-second trajectory, as evidenced in Fig. A-40.

The interactive filter system appears to require an external source of target aspect measurements in order to avoid instability. A possible extension of this research would be to tune this interactive (no E-O/PR) system for maximum performance, which was not accomplished in this research.

# V. Considerations For Real-Time Implementation

This chapter discusses several real-time implementation techniques and their application to the computational system developed in the previous chapters. The benefit of a given technique can be measured quantitatively only if it is applied to a specific programming language and a particular machine. Language- and machine-dependent implementation considerations have been avoided in this feasibility demonstration in order to assess the merits of the proposed interactive system irrespective of detailed software and hardware structure. Hence, only a qualitative judgment will be made on the benefit drawn from a particular real-time implementation technique. The techniques considered are:

1. Parallel Processing
2. Sparse Matrix Techniques
3. Fixed-Gain Filter
4. Scalar Processing of Measurements
5. Quasi-Static Filter Approximation
6. Filter Linearization
7. Angle Approximations

## 5.1 Parallel Processing

The computational tasks diagrammed in the flow chart of Fig. 2-2 and in the timing sequence chart of Fig. 2-10, need not be accomplished in series. Updating of the kinematic filter and the aspect filters are independent operations and could be done in parallel. Likewise,

propagation for the two filters are unrelated and could be accomplished by separate processors. Interaction between filters need occur only after each propagation and update task has been accomplished. Fig. 5-1 illustrates how parallel processing may be utilized for the interactive filter system.

The attempt has been made here to indicate how several independent series of computations may be combined in a parallel structure. A detailed implementation of parallel processing must account for minimum and maximum times to complete a given computational task, and attempt, within this constraint, to minimize dead-time in each processor chain. That level of detail is not possible without choosing a particular (representative or generic) hardware/software structure.

## 5.2 Sparse Matrix Techniques

Real-time implementation of the interactive filter should consider techniques for reducing computations associated with state and covariance propagation. The need to compute state covariance in a real-time estimator exists only if gain computations are required at update times. The next section considers implementing a fixed gain filter which eliminates the need either to propagate or to update the state covariance matrix. If such a simplification is not permissible, this section considers a technique for at least reducing the burden of integrating $\dot{P}$, provided that the F matrix is relatively sparse.

The matrix $\dot{P}$ is formed in terms of the elements of P according to Eq (2-48). However, since P is symmetric, only (n) (n+1)/2 terms (in this case, 55, since P is 10x10) need be integrated. Althougn F is not symmetric, $FP + PF^T$ is symmetric and

$$FP + PF^T = FP + (FP)^T \qquad (5\text{-}1)$$

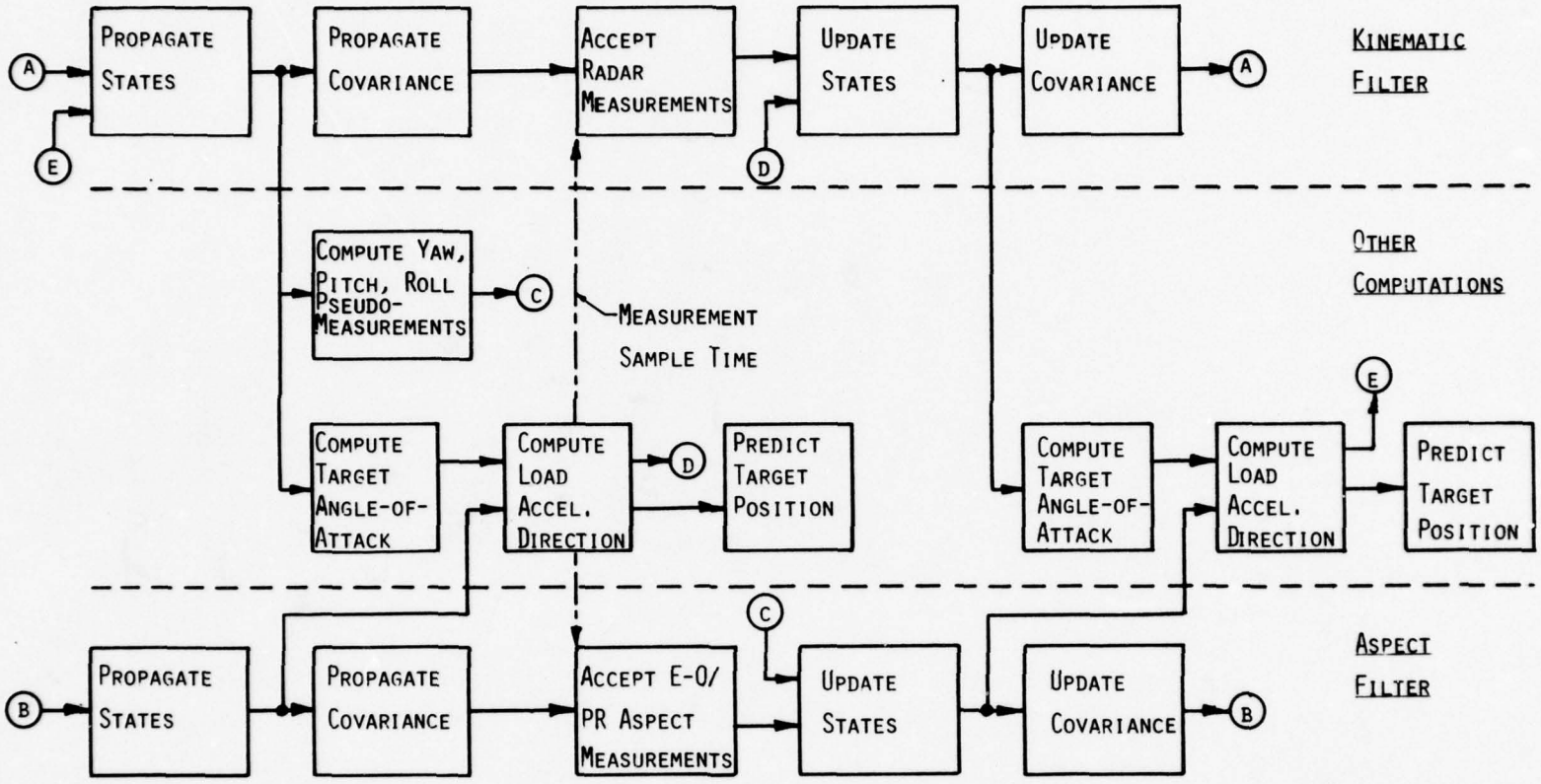


Fig. 5-1. Parallel Processing Filter Cycle

It is convenient to form the expression above as follows: Form FP as a matrix and add its transpose, $(FP)^T$ (which can be accomplished with $\frac{n(n+1)}{2}$ sums). Now form an (n) (n+1)/2 length vector of the unique elements of this matrix sum. Add the corresponding unique elements of the symmetric $GQG^T$ matrix. The resulting $\dot{P}$ vector can now be integrated using a suitable integration algorithm. The result of this integration is a P vector whose elements are the unique elements in the symmetric P matrix. Because F is sparse, however, all terms of F need not be retrieved from storage to perform this computation. All "zero" elements in F are flagged and no multiplication using these elements is performed. Also, all "one" elements are flagged and the corresponding elements of P are added appropriately, without the unnecessary multiplication by one. Values of only the non-zero, non-unity elements of F are required. Of the 100 elements in F, only 13 are non-zero and of these only 7 are non-unity. The computation of FP, for example, is reduced from 1000 multiplies and 900 adds to 70 multiplies and 30 adds. Another alternative, since F is so sparse, is to simply write out scalar equations.

## 5.3 Fixed Gain Filter

The update equation for the interactive extended Kalman filter developed in this research computes measurement update gain by the equation,

$$K_k = \bar{P}_k H^T (H \bar{P}_k H^T + R)^{-1} \qquad (5\text{-}2)$$

where $\bar{P}_k$, H and R are defined in Chapter II. The computation of gain is time-consuming primarily because of the m x m matrix inversion where m, here, is the length of the measurement vector. The following section discusses eliminating the matrix inversion in exchange for m scalar inversions. Another approach, which is frequently used for simplifying

linear Kalman filter implementations, approximates the variable gain, $K_k$, with a fixed gain, K. This approximation is a reasonably good one for the linear filter, since $P^-$ tends to steady-state as governed by the propagation model time constants, and H is constant. However, when both the dynamic model and the measurement geometry are non-linear, as in our case, $P_k^-$ and H are neither constant nor reach steady-state values.

One approach to forming this constant-gain model would be to examine values of gain K for an ensemble of scenarios, ranges of states and engagement conditions. Such a sensitivity study on K would also examine variations in $P^-$ and H over the ensemble. The goal of such an examination would be to determine the feasibility of modeling K as a piece-wise constant function (or other simple empirical function) of a small number of ranges for state values. After the feasibility were established, a trade-off study would need to be made considering the reduced accuracy and the need for table look-up procedures inherent in this approach. Drastic gain variations from scenario to scenario might suggest an adaptive technique for function evaluation. This is a potential area for future research.

## 5.4 Scalar Processing of Measurements

The measurement update equation for the extended Kalman filter developed in Chapter II uses a gain matrix which is computed by batch processing all six scalar measurements, i.e., updating both state and covariance only once with the combined effect of all six measurements, thus requiring inversion of $(HP^-H^T + R)$. An alternative approach, which eliminates the 6x6 matrix inversion, uses the scalar formulation

of the update equation. Each of the six scalar measurements is processed individually, so that the matrix inversion is replaced with simple scalar inversions. In this technique, both state and covariance are updated after each scalar measurement, necessitating as many separate updates as there are measurements, in this case, six. However, this additional computational burden is offset by the elimination of the matrix inversion, a time-consuming task.

## 5.5 Quasi-Static Filter Approximation

The state dynamic equation [Eq (2-2 )] is non-linear in that normal load acceleration magnitude is modeled by the equation

$$\underline{a}_N = \alpha + \beta e^{\gamma \underline{\varepsilon}} \tag{2-6}$$

where $\underline{\varepsilon}$ is a state and is modeled as a zero-mean, first-order Gauss-Markov random process, and $\underline{a}_N$ is in units of g's. [The factor g in Eq (2-16) converts $a_N$ to ft/sec$^2$.] The direction of normal load acceleration is given by the unit vector $\bar{T}_N$ provided from the aspect angle filter. As discussed in Section 2.4.1, the change in $\varepsilon$ and $\bar{T}_N$ is small enough during the propagation interval to assume them to be constant. Hence, F [in Eq (2-52)] may be considered piece-wise constant. With this approximation, the state covariance matrix may be propagated using the piece-wise constant state transition matrix instead of by integrating $\dot{P}$ equation [Eq (2-48)] directly, i.e.,

$$P(t_{k+1}|t_k) = \Phi(t_{k+1},t_k)\, P(t_k,t_k)\, \Phi^T(t_{k+1},t_k) + \int_{t_k}^{t_{k+1}} \Phi(t_{k+1},\tau)\, GQG^T\, \Phi^T(t_{k+1},\tau)\, d\tau \tag{5-3}$$

where

$$\Phi(t_{k+1},t_k) = \Phi(t_{k+1}-t_k) = \exp\left[F_{t_k^+}(t_{k+1}-t_k)\right] \tag{5-4}$$

and

$$F_{t_k^+} = F[t_k;\ \hat{\underline{x}}(t_k|t_k)]$$

$$= \left[\begin{array}{c|c|c} & & 0 \\ & & 0 \\ 0_{6x3} & I_{6x6} & 0 \\ & & g\beta\gamma e^{\gamma\hat{x}_{10}(t_k|t_k)}(1_N)_n \\ & & g\beta\gamma e^{\gamma\hat{x}_{10}(t_k|t_k)}(1_N)_e \\ & & g\beta\gamma e^{\gamma\hat{x}_{10}(t_k|t_k)}(1_N)_d \\ \hline & -\frac{1}{\tau_n}\ 0\ \ 0 & 0 \\ & 0\ -\frac{1}{\tau_e}\ 0 & 0 \\ 0_{4x6} & 0\ \ 0\ -\frac{1}{\tau_d} & 0 \\ & 0\ \ 0\ \ 0 & -\frac{1}{\tau_\varepsilon} \end{array}\right] \tag{5-5}$$

The advantage of this approach is that the multiplications and the integrations in Eq (5-3) may be carried out explicitly prior to implementation, thus eliminating the need for real-time integration of the

state covariance matrix. The same is true, of course, for propagating the state equation, i.e., integration of Eq (2-46) is replaced by the explicit state propagation equation,

$$\hat{\bar{x}}(t_{k+1}|t_k) = \Phi(t_{k+1}-t_k)\,\hat{\bar{x}}(t_k|t_k) \tag{5-6}$$

This technique has an advantage over numerical integration only if the functions represented by $\Phi$ and $\int \Phi G Q G^T \Phi^T d\tau$ can readily be stored and utilized.

## 5.6 Filter Linarization

A linearization technique may be utilized to approximate the probability density function for $\underline{a}_N$ [Eq (2-7), Fig. 2-4] by a Gaussian pdf with appropriate mean and variance. The state equations [Eq (2-1), (2-2), (2-5) and (2-8)] are replaced with the following linear state model:

$$\dot{\bar{p}}_{t/a} = \bar{V}_{t/a} \tag{5-7}$$

$$\dot{\bar{V}}_{t/a} = g(a_{N_m} + \underline{a}_{N_\sigma})(\bar{T}_N) + \overline{\underline{\delta a}} + \bar{g} - \dot{\bar{V}}_{a/I} + \bar{W}_{acc} \tag{5-8}$$

$$\dot{\overline{\underline{\delta a}}} = -\frac{1}{\tau_{\delta a}}\,\overline{\underline{\delta a}} + \bar{W}_{\delta a} \tag{5-9}$$

$$\dot{\underline{a}}_{N_\sigma} = -\frac{1}{\tau_{a_N}}\,\underline{a}_{N_\sigma} + W_{a_N} \tag{5-10}$$

In this model, $\underline{a}_{N_\sigma}$ is zero-mean, colored and Gaussian and $a_{N_m}$ is a positive scalar parameter of such a value that the random process $(a_{N_m} + \underline{a}_{N_\sigma})$ approximates, in some sense, the non-linear random process,

$$\underline{a}_N = \alpha + \beta e^{\gamma \underline{\varepsilon}} \quad , \quad \underline{\varepsilon} \sim N(0,1) \tag{5-11}$$

Fig. 5-2 illustrates the approximating Gaussian pdf for the following cases:

1) the parameter $a_{N_m}$ and the variance of $\underline{a}_{N_\sigma}$ equal, respectively, the mean and variance of $\underline{a}_N$, i.e., referring to Appendix C ,

$$a_{N_m} = \alpha + \beta e^{\frac{\gamma^2}{2}} \approx 3.47 \tag{5-12}$$

$$\sigma^2_{a_{N_\sigma}} = \beta(e^{2\gamma^2} - e^{\gamma^2}) \approx 5.835 \tag{5-13}$$

or

$$\sigma_{a_{N_\sigma}} \approx 2.416 \tag{5-14}$$

2) $a_{N_m}$ is set equal to the mode of $\underline{a}_N$,

$$a_{N_m} = \sigma + \beta e^{-\gamma^2} \approx 4.885 \tag{5-15}$$

and the variance of $\underline{a}_{N_\sigma}$ is set to such a value that the density functions for $\underline{a}_N$ and $\underline{a}_{N_\sigma}$ are set to the same value at their modes, i.e.,

$$\frac{1}{\sqrt{2\pi}\sigma} = \frac{e^{\frac{\gamma^2}{2}}}{\sqrt{2\pi}\,\gamma|\beta|} \approx 0.226 \tag{5-16}$$

or

$$\sigma \approx 1.765 \tag{5-17}$$

3) Another approach could be used to determine a normal pdf to approximate the non-Gaussian pdf so as to maximize the area overlap of

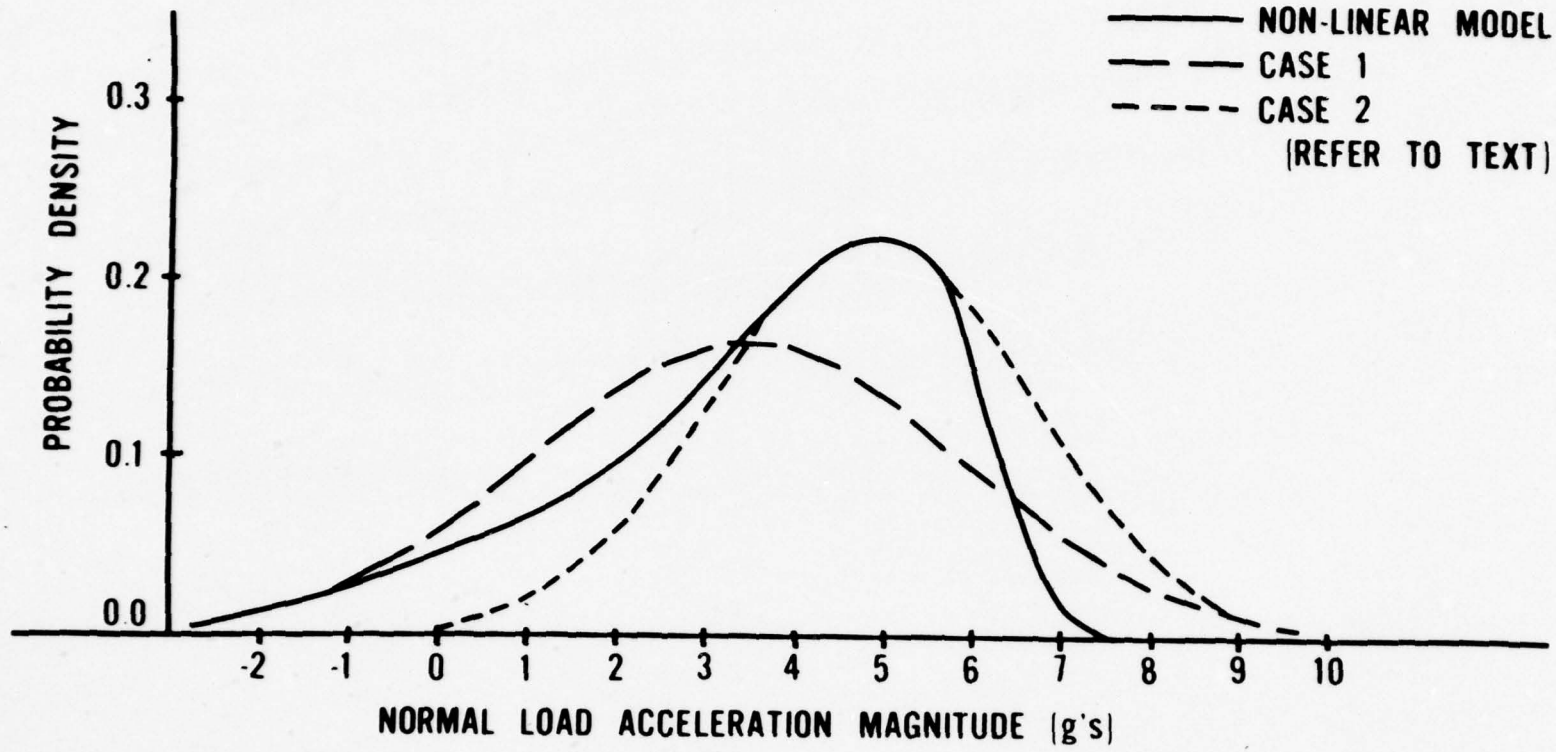


Fig. 5-2. Gaussian Approximations to pdf In Non-Linear Model

the two pdf's: Convolve the non-Gaussian pdf with a normal pdf whose mean and variance are treated as parameters. Differentiate the convolved function with respect to both mean and variance, set to zero, and solve the two resulting simultaneous equations for mean and variance values. Case (3) has not been developed further. No sensitivity results from Monte Carlo simulations have been obtained for any of these approximations.

## 5.7 Angle Approximations

Several angles are required in the formulation of the interactive filter system-- $\eta$, $\xi$, $\psi$, $\theta$, $\phi$ and $\alpha_t$. Trigonometric functions of these angles may be approximated, in order to simplify computations for real-time implementation. One such simplifying technique approximates the trigonometric functions of these angles by polynomial expansions. The number of terms in these approximating expansions is determined by the requirement for accuracy in a given relationship employing the angle, and by the range of values anticipated for the particular angle. While $\psi$, $\phi$ and $\eta$ have $2\pi$ ranges, $\xi$ and $\theta$ have ranges of only $\pi$ radians and $\alpha_t$ has a limited range of slightly over one-half radian ($-5^\circ$ to $+25^\circ$). Polynomial expansions may have an advantage over table look-up interpolation methods when memory storage is a premium. The expansion is formulated as a succession of alternating multiply and add operations, with storage required only for polynomial coefficients.

## VI. Conclusions and Recommendations For Future Research

For the class of targets considered in this research, target orientation provides information about current and future target motion beyond that provided by point-mass observation systems such as radar. This is true because of the interdependency of orientation and motion for the vehicles considered. The methodology developed in coupling the electro-optical and radar sensor subsystems through separate but interactive Kalman filter estimation algorithms in order to enhance target prediction capabilities is a unique contribution to the field of target motion state estimation.

The particular mechanization of this concept is one in which 1) normal load acceleration magnitude is modeled realistically by a non-linear function of a time-correlated Gaussian random process, 2) direction of normal load acceleration is provided by offsetting the Kalman-estimated target attitude by kinematically derived angle of attack (using the aerodynamic lift equation), and 3) the target aspect filter is provided with measures of target aspect, not only from (simulated) pattern recognition derivates of electro-optical imagery data, but also from kinematically derived target aspect, which is based upon estimates of target velocity, acceleration and angle of attack. This unique system for dynamic interchange of motion and orientation information serves not only as a basis for future research in this fruitful area, but also provides a particular formulation which has the potential for real-time implementation in a high-performance aircraft.

The four air-to-air scenarios investigated in this research are realistic and typical of engagements encountered in military combat missions. The high-g, break after roll, and nigh line-of-sight angle rate maneuvers are generally considered difficult for point-mass tracking systems such as radar and non-imaging electro-optical systems. These scenarios provide a good data base for performance comparisons using the interactive filter.

The performance analysis demonstrated that the interactive filter provided better performance than a comparative radar-only filter in all chosen figures of merit and over all four scenarios. Although it varied slightly with scenario, a factor of two improvement is realized for target position prediction error (predicting one second forward in time) using the interactive filter over the radar-only filter. For the scenario in which successive target roll maneuvers and high line-of-sight angle rates were involved (scenario 4), the interactive filter did significantly better than the radar-only filter, recovering from the dramatic maneuvers in approximately two seconds, compared to more than six seconds for the comparative filter.

The interactive filter is not highly sensitive to choices for "target-type" filter parameters $\alpha$, $\beta$ and $\gamma$. Comparisons of performance show some improvement, however, when these parameters are selected to match the trajectory acceleration profile. The particular parameter choices implemented here kept $\alpha$ and $\gamma$ fixed and varied $\beta$. The pdf shapes which resulted suggests that varying $\beta$ alone is sufficient to provide the shapes needed in the filter model. This, in turn, suggests a fruitful area for future research. This research area would attempt to adapt the value of $\beta$ on-line according to the value of normal load

acceleration magnitude.

The interactive filter recovers quickly from one-time bad measurements and is reasonably insensitive to large unmodeled radar measurement errors. Performance in the area of recovery and sensitivity to unmodeled errors is comparable to that of the comparative radar-only filter.

Interactive filter performance deteriorates as electro-optical/pattern recognition aspect measurement noise is increased. An increase in measurement noise standard deviation from five degrees to ten degrees has little effect on performance. An increase to 25 degrees, however, has a significantly degrading effect. And, if the increased noise variance is also modeled in the filter measurement noise covariance matrix, the filter shows signs of instability. If the electro-optical/pattern recognition aspect measurements are eliminated altogether, the filter output becomes unstable. A potential area of research would investigate techniques for stabilizing the filter in the absense of external aspect measurements.

A five-degree bias added to all three aspect input channels at each measurement update (but with filter unaware) results in only slight degradation in filter performance. This is a significant result, as most pattern recognition methods should be able to maintain bias uncertainties below this level.

The more complex aspect noise model, in which inertial aspect is converted to the image plane, corrupted with white Gaussian noise, rounded to five-degree increments, and converted back to inertial reference, shows little difference in filter performance compared to the simpler noise model used in the baseline analysis. This result indicates some insensitivity to aspect noise type. It also gives credence to the table

look-up technique inherent in several pattern recognition schemes.

Additional areas for future study can be recommended as a result of this research. Probably the largest and most fruitful, is the area of applying specific pattern recognition techniques to electro-optical imagery data in order to extract or derive target aspect. An important concern in this area is the development of good models for aspect noise corruptions for particular pattern recognition techniques. Other potential areas include: on-line applicability in which computational efficiency and storage requirements will be important concerns for real-time implementations; better radar noise models; other implementations for integrating electro-optical and radar sensor systems; a comparison of the linearized offset-Gaussian dynamic model with the non-linear model investigated here; the investigation of an interactive system in which both motion and orientation data are provided by an imaging electro-optical sensor, such as the one currently being developed by the AF Avionics Laboratory; application of this technique to other types of problems including (1) ground-site tracking of a cooperative (instrumented test) aircraft in which attitude is being telemetered to the ground tracking site, (2) ground-site tracking of an uncooperative target, and (3) electro-optical tracking of missiles.

## Bibliography


1. Andrews, H. C., Introduction to Mathematical Techniques in Pattern Recognition, Wiley-Interscience, New York, NY, 1972.

2. Berg, R. L., et al, "Advanced Gun Fire Control System Design Study (Phase II)," Technical Report AFAL-TR-74-198, prepared for Air Force Avionics Laboratory, Wright-Patterson AFB, OH, Sep 1974.

3. Bierman, G. J., Factorization Methods for Discrete Sequential Estimation, Academic Press, New York, NY, 1977.

4. Brown, C. M. and C. F. Price, "A Comparison of Adaptive Tracking Filters for Targets of Variable Maneuverability," Technical Report TR-480-6, prepared for Air Force Weapons Laboratory, Kirtland AFB, NM, Apr 1976.

5. Brown, C. M. and C. F. Price, "Adaptive Tracking Filter Design and Evaluation for Gun Fire Control Systems," Technical Report TR-387-1, prepared for Naval Ordnance Systems Command, Arlington, VA, Jan 1974.

6. Carl, J. W. and C. F. Hall, "The Application of Filtered Transforms to the General Classification Problem, IEEE Trans Comp, Jul 1972, p 785.

7. Conversations with Captains R. N. Lutter and W. Ashton, former Air Force Instructor Pilots, on tactics in air combat, Air Force Avionics Laboratory, 1976-77.

8. Conversation with Dr. J. Sklansky, University of California, Irvine, Apr 1978.

9. Day, W. R., et al, "Air Combat Simulator Analysis," Technical Report AFATL-TR-76-162, prepared for Air Force Armament Laboratory, Eglin AFB, FL, Dec 1976.

10. Demetry, J. S. and H. A. Titus, "Adaptive Tracking of Maneuvering Targets," Technical Report NPS-52DE8041A, Naval Postgraduate School, Monterey, CA, 15 Apr 1968.

11. Dudani, S. A., "An Experimental Study of Moment Methods for Automatic Identification of Three-Dimensional Objects from Television Images," PhD Dissertation, Ohio State University, Aug 1973.

12. Dudani, S. A., "Moment Methods for the Identification of Three-Dimensional Objects from Optical Images," MS Thesis, Ohio State University, Aug 1971.

13. Duff, I. S., "A Survey of Sparse Matrix Research," Proc of the IEEE, Vol 65, No 4, Apr 1977.

14. Farrell, J. L., et al, "Dynamic Scaling For Air-to-Air Tracking," NAECON, Dayton, OH, Jun 1975.

15. Fitts, J. M., "Aided Tracking as Applied to High Accuracy Pointing Systems," IEEE Trans on Aero and Elect Sys, Vol AES-9, No 3, May 1973.

16. Friedland, B., "Optimum Steady-State Position and Velocity Estimation Using Noisy Sampled Position Data," IEEE Trans on Aero and Elect Sys, Vol AES-9, No 6, Nov 1973.

17. Guild, R. E., "The Effect of Target Maneuvering on Kill Probability in Air-to-Air Gunnery," MS Thesis, Air Force Institute of Technology, Jun 1972.

18. Hampton, R. L. T., "Adaptive Tracking Filters," Technical Note 404-129, Naval Weapons Center, China Lake, CA, Dec 1971.

19. Hampton, R. L. T. and J. R. Cooke, "Unsupervised Tracking of Maneuvering Vehicles," IEEE Trans on Aero and Elect Sys, Vol AES-9, No 2, Mar 1973.

20. Heller, B. J., "Adapting an Alpha Beta Tracker in a Maneuvering Target Environment," Technical Note 304-154, Naval Weapons Center, China Lake, CA, Jul 1967.

21. Heller, B. J., "Progress Report on an Adaptive Filter Design," Technical Note 304-128, Naval Weapons Center, China Lake, CA, Sep 1966.

22. Hohwiesner, W., "Principles of Airborne Fire Control," Lecture Notes, US Air Force Academy, Dec 1975.

23. Hutcheson, J. H. and R. L. Segerblom, "TACTICS: A Three-Body Three-Dimensional Intercept Simulation Program," Memorandum RM-5759-PR, prepared for Air Force Project RAND, RAND Corp, Santa Monica, CA, Oct 1969.

24. Jazwinski, A. H., Stochastic Processes and Filtering Theory, Academic Press, New York, NY, 1970.

25. Johnson, C. D., "A Mathematical Analysis of the Problem of Pointing," IEEE Trans on Aero and Elect Sys, Vol AES-8, No 5, Sep 1972.

26. Johnson, F. V. and P. Briggs, "Formulation of an Advanced Anti-Aircraft Gun Director Through Kalman Estimation Techniques," Technical Report prepared for United States Army Frankford Arsenal, Philadelphia, PA, Dec 1973.

27. Kirk, D. E., "Evaluation of State Estimators and Predictors for Fire Control Systems," Technical Report NPS-52KI74101, Naval Postgraduate School, prepared for Naval Ship Weapons Systems Engineering Station, Port Hueneme, CA, Oct 1974.

28. Kolibaba, R. L., "Precision Radar Pointing and Tracking Using an Adaptive Extended Kalman Filter," MS Thesis, Air Force Institute of Technology, Jun 1973.

29. Kolibaba, R. L. and R. B. Asher, "Adaptive Filtering for Precision Pointing and Tracking Problems in Weapon Delivery," Technical Report AFAL-TR-73-320, Wright-Patterson AFB, OH, Jan 1974.

30. LaJeunesse, T., "AIM-9L Six-Degree-of-Freedom Simulation," Technical Memorandum TM-2813, Naval Weapons Center, China Lake, CA, Oct 1976, p 46.

31. Landau, M. I., "Radar Tracking of Airborne Targets, NAECON, Dayton, OH, May 1976.

32. Laughlin, H. J., "Investigation of Real-Time Satellite-to-Satellite Tracking Using Extended Kalman Filtering," MS Thesis, Air Force Institute of Technology, Mar 1978.

33. Levine, M. D., "Feature Extraction: A Survey, " Proc of the IEEE, Vol 57, No 8, Aug 1969.

34. Lindberg, E. K., "A Radar Error Model and Kalman Filter for Predicting Target States in an Air-to-Air Environment," MS Thesis, Air Force Institute of Technology, Dec 1974.

35. Lindgren, B. W., Statistical Theory, Macmillan Company, New York, NY, 1968, p 269.

36. Lutter, R. N., "Application of an Extended Kalman Filter to an Advanced Fire Control System," MS Thesis, Air Force Institute of Technology, Dec 1976.

37. Maybeck, P. S., "Stochastic Estimation and Control Systems," Lecture Notes, Air Force Institute of Technology, 1975.

38. McAulay, R. J. and E. Denlinger, "A Decision-Directed Adaptive Tracker," IEEE Trans on Aero and Elect Sys, Vol AES-9, No 2, Mar 1973.

39. McGhee, R. B., "A Lower Bound on Prediction Errors for Randomly Accelerating Targets," IEEE Trans on Aero and Elect Sys, Vol AES-5, No 6, Nov 1969.

40. Nagy, G., "State of the Art in Pattern Recognition," Proc of the IEEE, Vol 56, No 5, May 1968.

41. Pearson, J. B., III, "Basic Studies in Airborne Radar Tracking Systems," PhD Dissertation, UCLA, 1970.

42. Pearson, J. B., III and E. B. Stear, "Kalman Filter Applications in Airborne Radar Tracking," IEEE Trans on Aero and Elect Sys, Vol AES-10, No 3, May 1974.

43. Radoy, C. H., "Pattern Recognition by Fourier Series Transformations," MS Thesis, Air Force Institute of Technology, 1967.

44. Richard, C. W. and H. Hermami, "Identification of Three-Dimensional Objects Using Fourier Descriptors of the Boundary Curve," IEEE Trans on Systems, Man and Cybernetics, Vol SMC-4, No 4, Jul 1974.

45. Roberson, R. S., "Application of an Image Classification Model to the Reconnaissance Problem," MS Thesis, Air Force Institute of Technology, 1971.

46. Singer, R. A., "Estimating Optimal Tracking Filter Performance for Manned Maneuvering Targets," IEEE Trans on Aero and Elect Sys, Vol AES-6, No 4, Jul 1970.

47. Singer, R. A., "Real-Time Tracking Filter Evaluation and Selection for Tactical Applications," IEEE Trans on Aero and Elect Sys, Vol AES-7, No 1, Jan 1971.

48. Sklansky, J. and G. A. Davison, Jr., "Recognizing Three-Dimensional Objects by Their Silhouettes," AGARD Conf Proc, No 94 on Artificial Intelligence, May 1971, p 15.1-15.11.

49. Spingarn, K. and H. L. Weidemann, "Linear Regression Filtering and Prediction for Tracking Maneuvering Aircraft Targets," IEEE Trans on Aero and Elect Sys, Vol AES-8, No 6, Nov 1972.

50. Taylor, J. W. R. (Editor), Jane's All The World's Aircraft 1977-78, Jane's Yearbooks, London, England, 1978.

51. Terry, J. G., "Improving Aided Track Performance During Periods of Tracker Sensor Failure by Utilizing a Target Body Fixed Coordinate System," MS Thesis, Air Force Institute of Technology, Dec 1977.

52. Thorp, J. S., "Optimal Tracking of Maneuvering Targets," IEEE Trans on Aero and Elect Sys, Vol AES-9, No 4, Jul 1973.

53. Valstar, J. E., "The Fifty-Percent Coverage Problem of the General Bivariate Gaussian Distribution," Proc of NAECON, 1970, p 200-207.

54. Welp, D. W., "Development of an Avionics Evaluation Program for Air-to-Air Mission Analysis," Technical Report AFAL-TR-75-159, prepared for Air Force Avionics Laboratory, Wright-Patterson AFB, OH, Nov 1975.

55. Wrigley, W. and J. Hovorka, Fire Control Principles, McGraw-Hill Book Co, Inc, New York, NY, 1959.

56. Zahn, C. T. and R. Z. Roskies, "Fourier Descriptors for Plane Closed Curves," IEEE Trans Comp, Vol C-21, No 3, Mar 1972.

# APPENDIX A

## Graphical Simulation Results

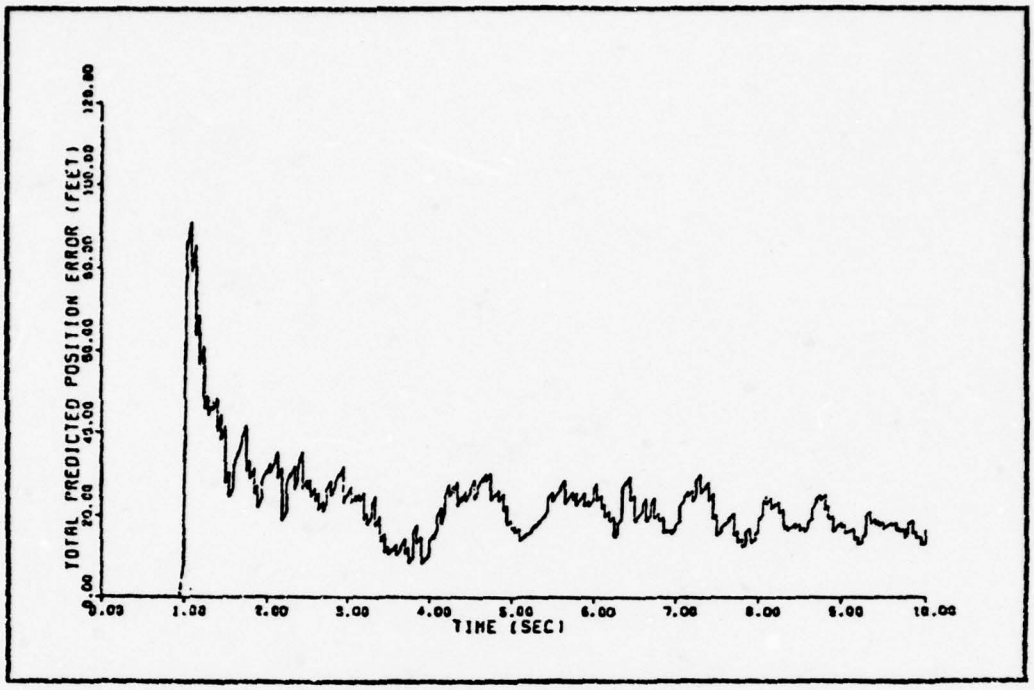


Fig. A- 1. Scenario 1, Average Error in Predicted Target Position, Interactive Filter

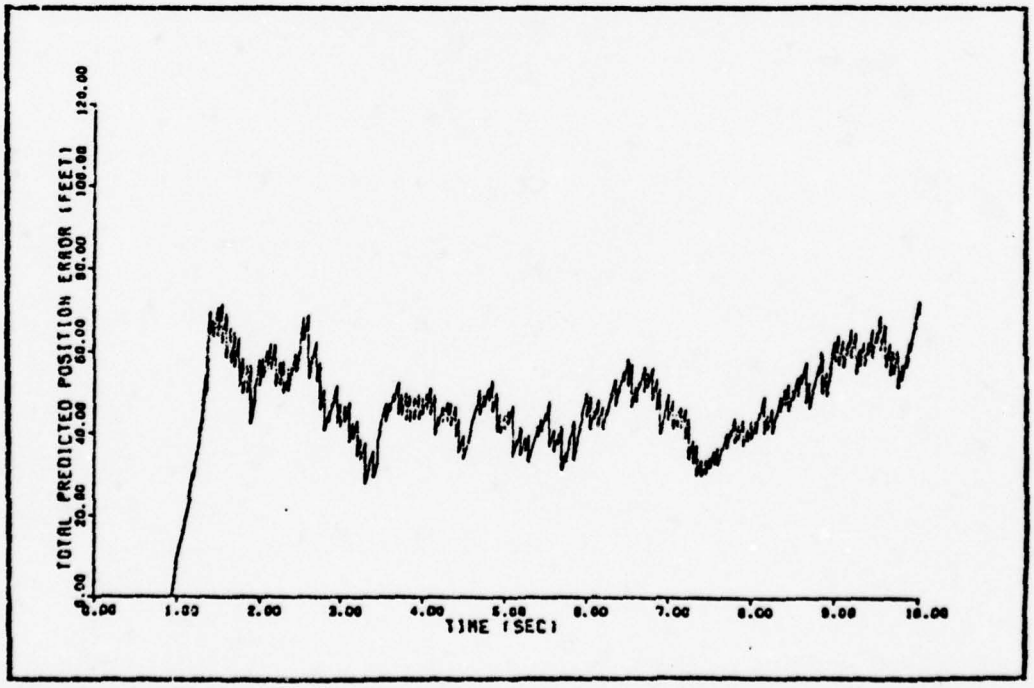


Fig. A- 2. Scenario 1, Average Error in Predicted Target Position, Comparative Filter

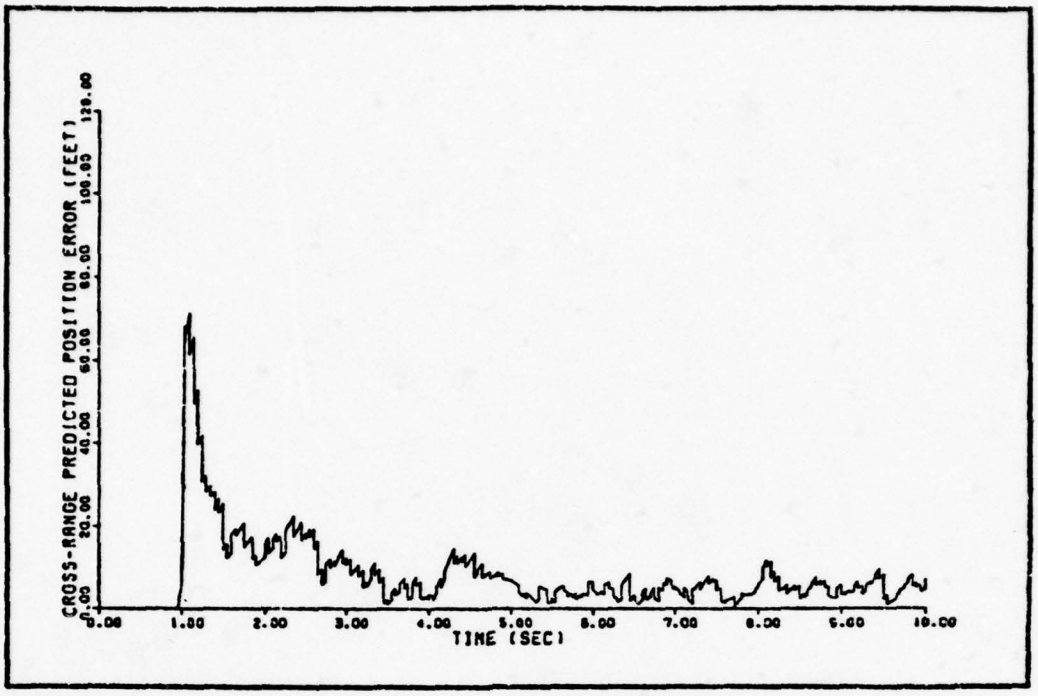


Fig. A- 3. Scenario 1, Average Error in Predicted Cross-Range Target Position, Interactive Filter

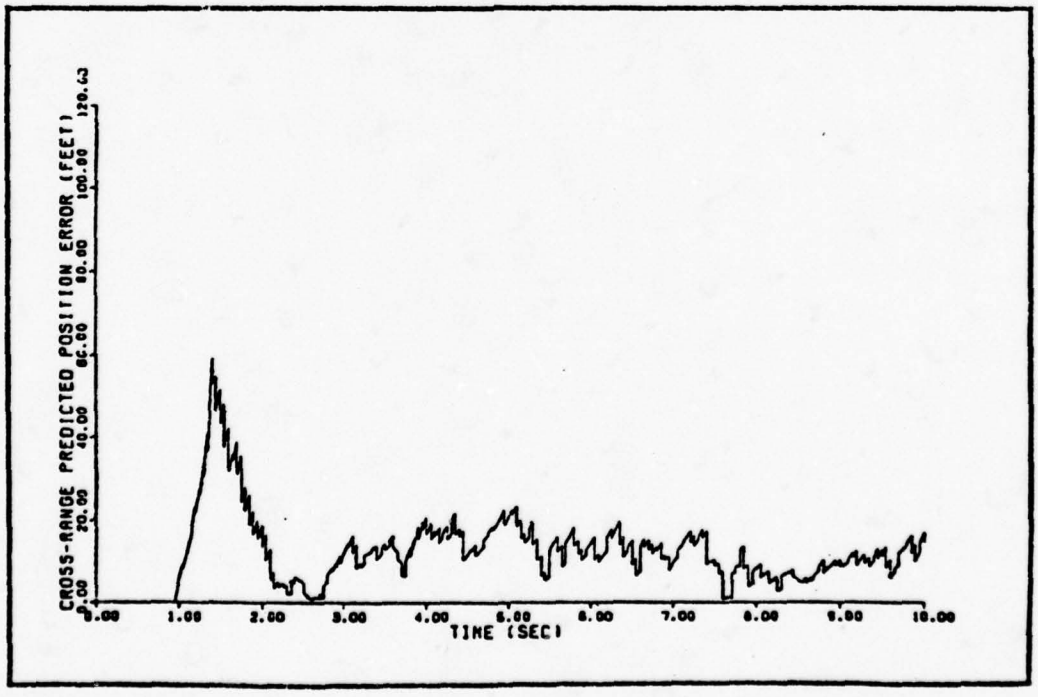


Fig. A- 4. Scenario 1, Average Error in Predicted Cross-Range Target Position, Comparative Filter

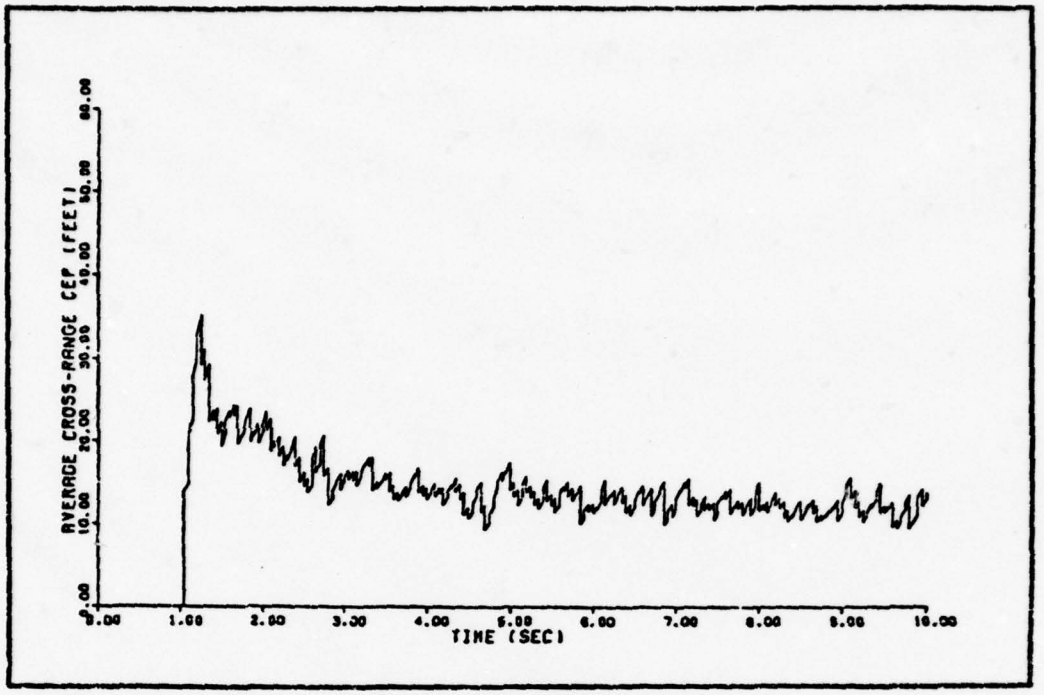


Fig. A- 5. Scenario 1, Average CEP, Interactive Filter

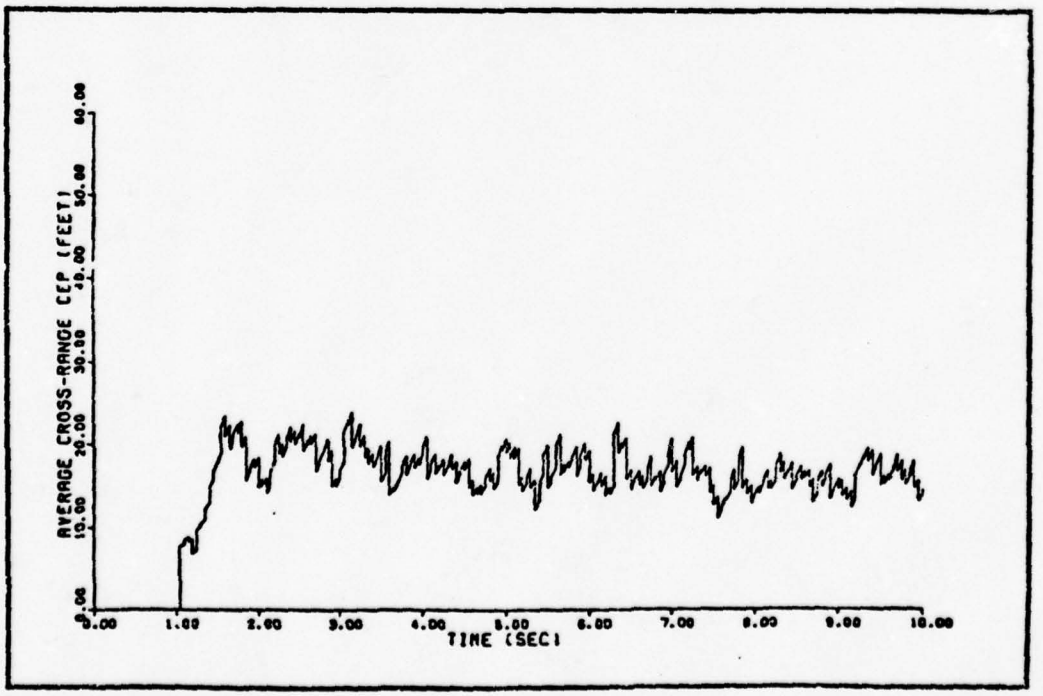


Fig. A- 6. Scenario 1, Average CEP, Comparative Filter

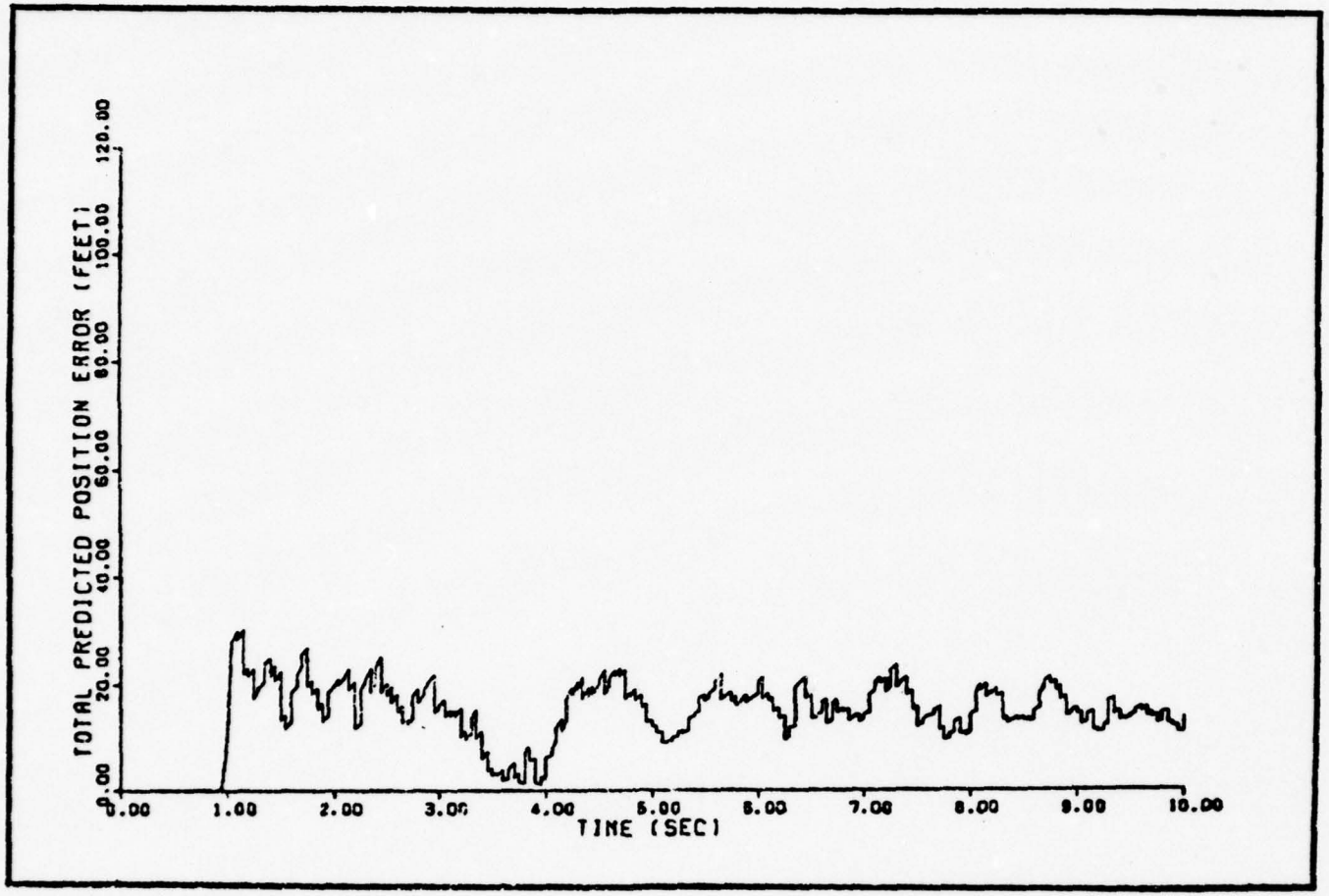


Fig. A- 7. Scenario 1, Average Error in Predicted Target Position, Interactive Filter, $\alpha = 8$, $\beta = -2$, $\gamma = 0.5$

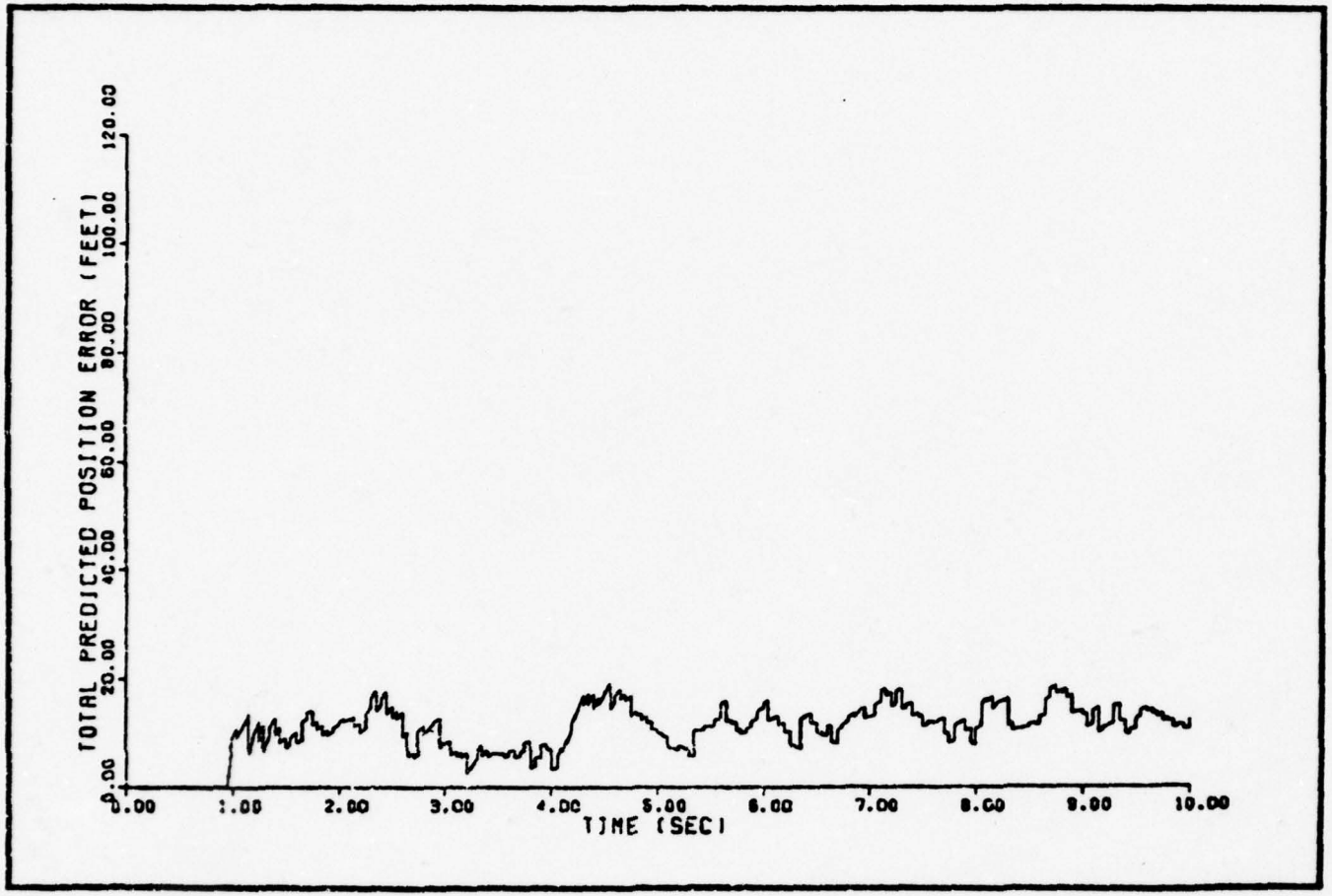


Fig. A- 8. Scenario 1, Average Error in Predicted Target Position, Interactive Filter, $\alpha = 8$, $\beta = -1$, $\gamma = 0.5$

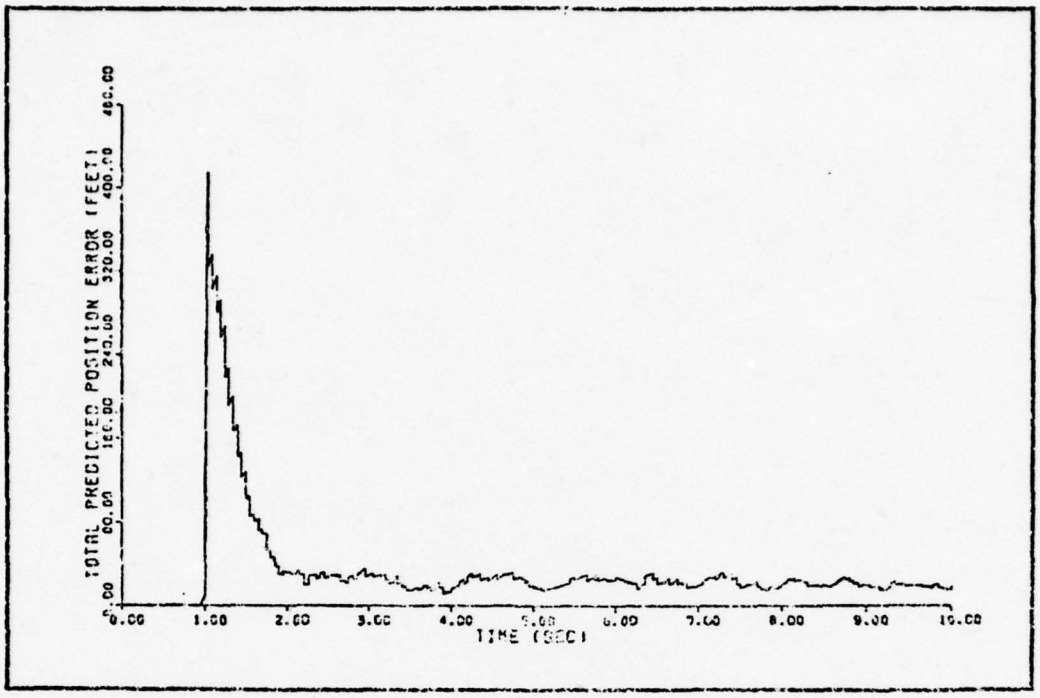


Fig. A-9. Scenario 1, Average Error in Predicted Target Position, Interactive Filter, Bad Initial Conditions

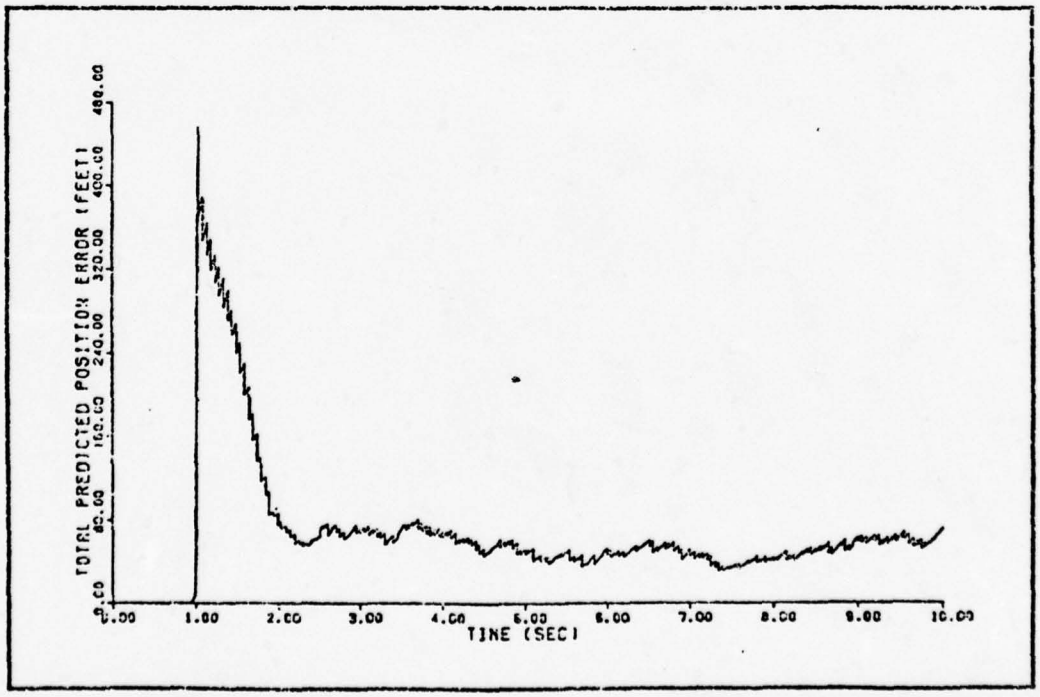


Fig. A-10. Scenario 1, Average Error in Predicted Target Position, Comparative Filter, Bad Initial Conditions

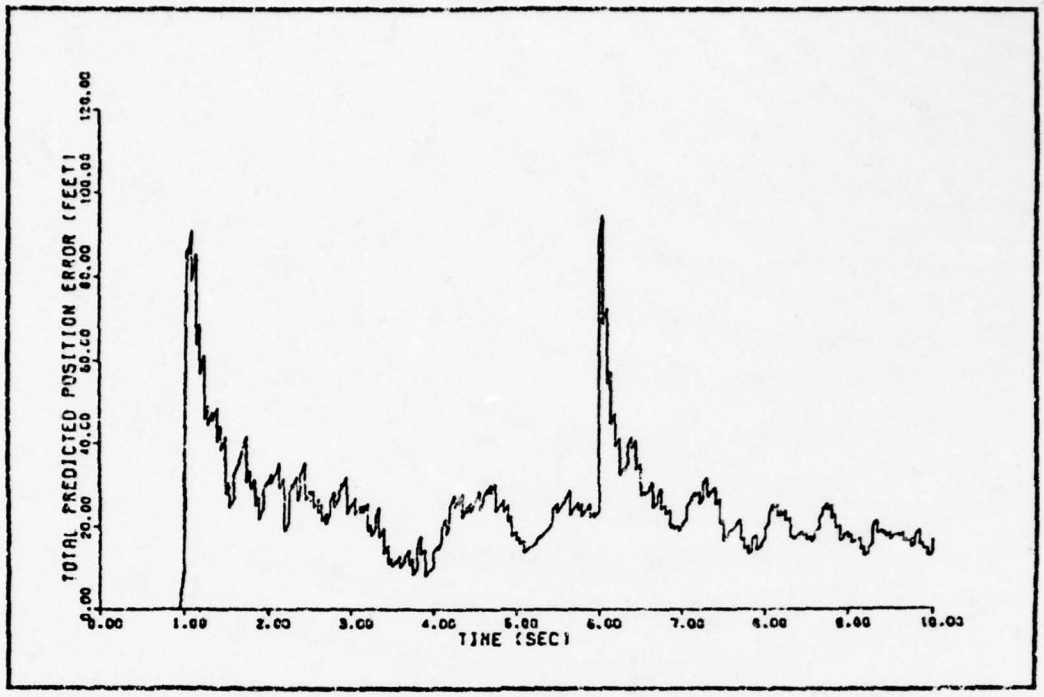


Fig. A-11. Scenario 1, Average Error in Predicted Target Position, Interactive Filter, One-time Bad Measurement 5 Seconds Into Scenario

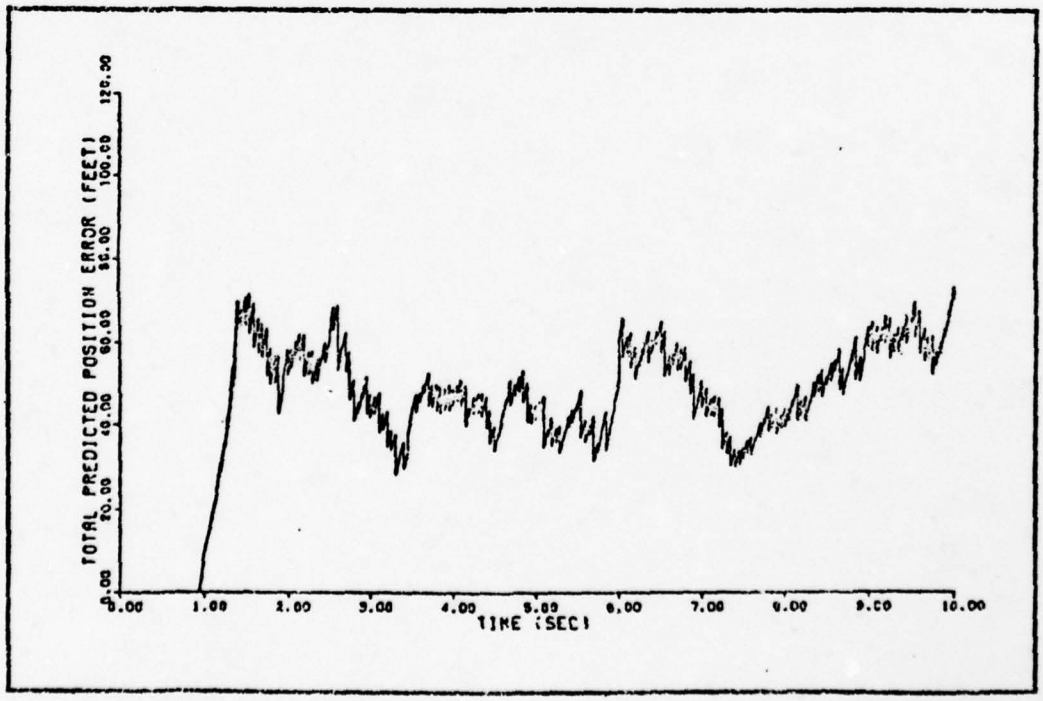


Fig. A-12. Scenario 1, Average Error in Predicted Target Position, Comparative Filter, One-time Bad Measurement 5 Seconds Into Scenario

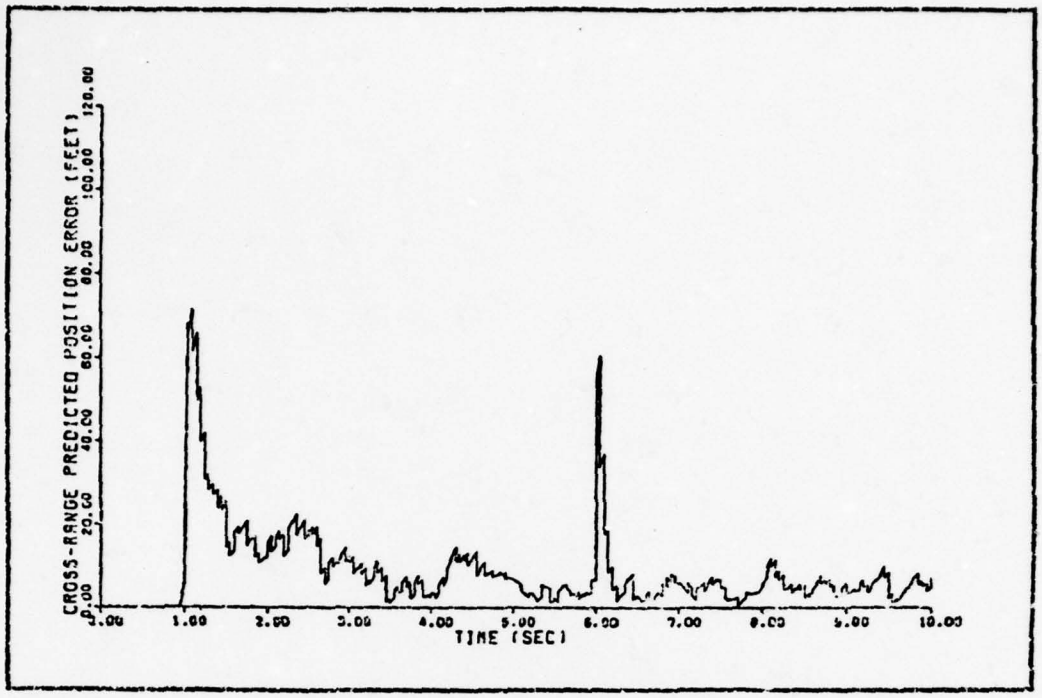


Fig. A- 13. Scenario 1, Average Error in Predicted Cross-Range Target Position, Interactive Filter, One-time Bad Measurement 5 Seconds Into Scenario

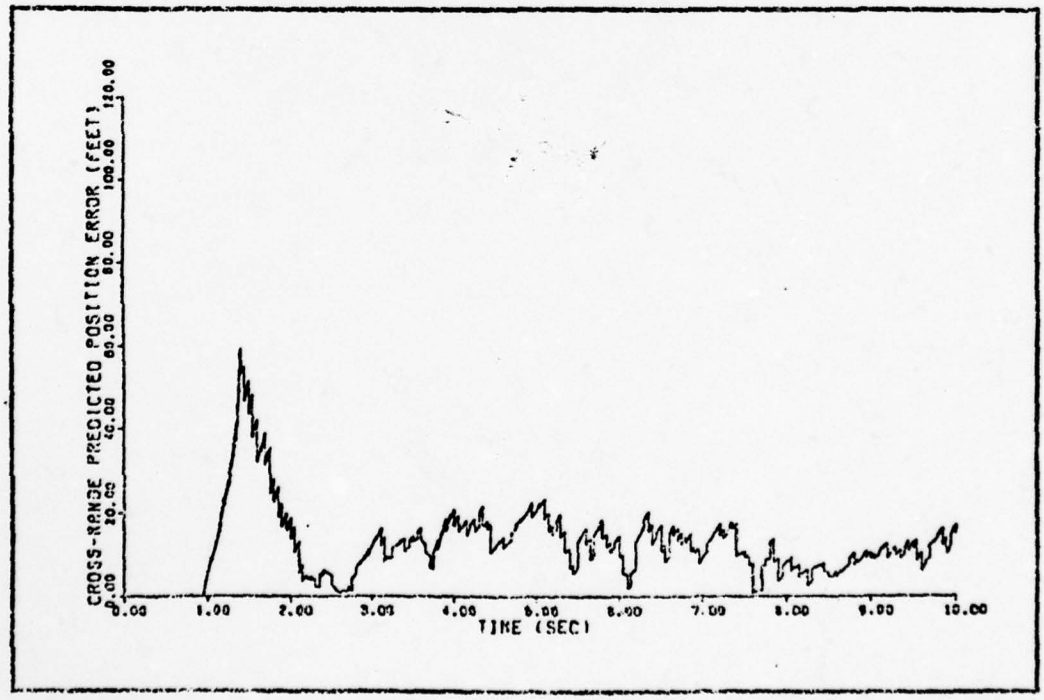


Fig. A- 14. Scenario 1, Average Error in Predicted Cross-Range Target Position, Comparative Filter, One-time Bad Measurement 5 Seconds Into Scenario

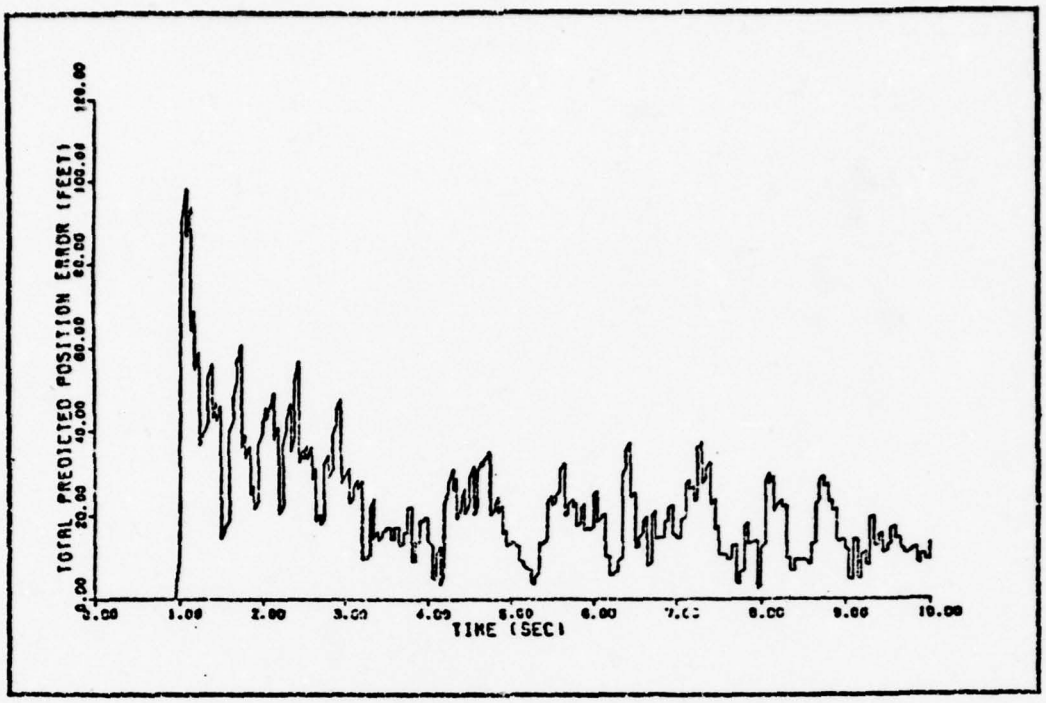


Fig. A-15. Scenario 1, Average Error in Predicted Target Position, Interactive Filter, Large Unmodelled Radar Errors

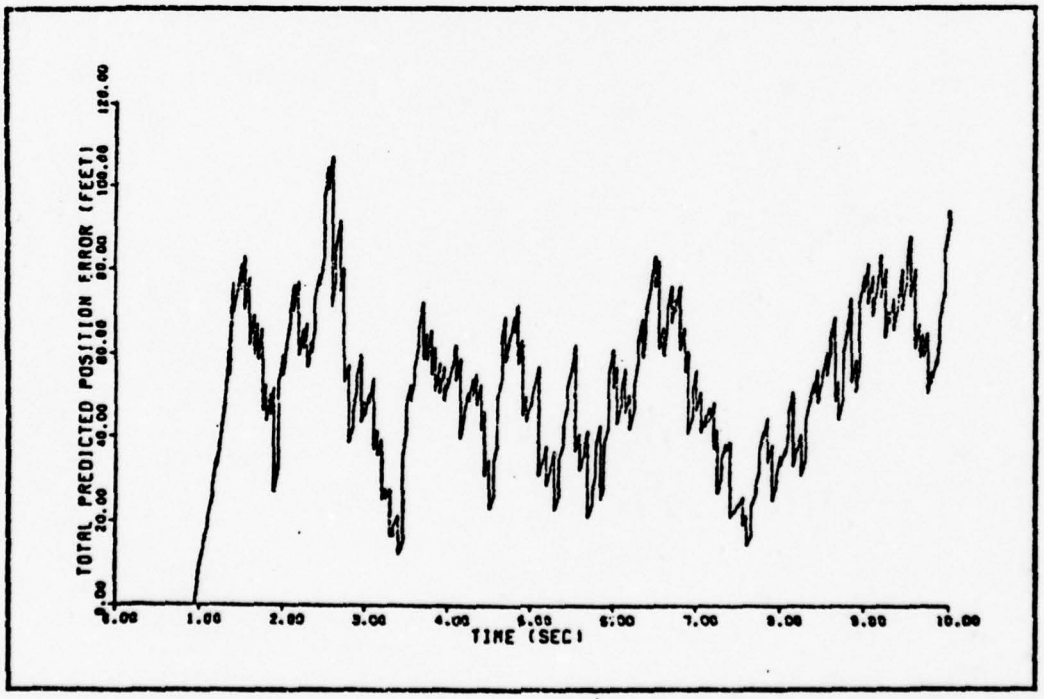


Fig. A-16. Scenario 1, Average Error in Predicted Target Position, Comparative Filter, Large Unmodelled Radar Errors

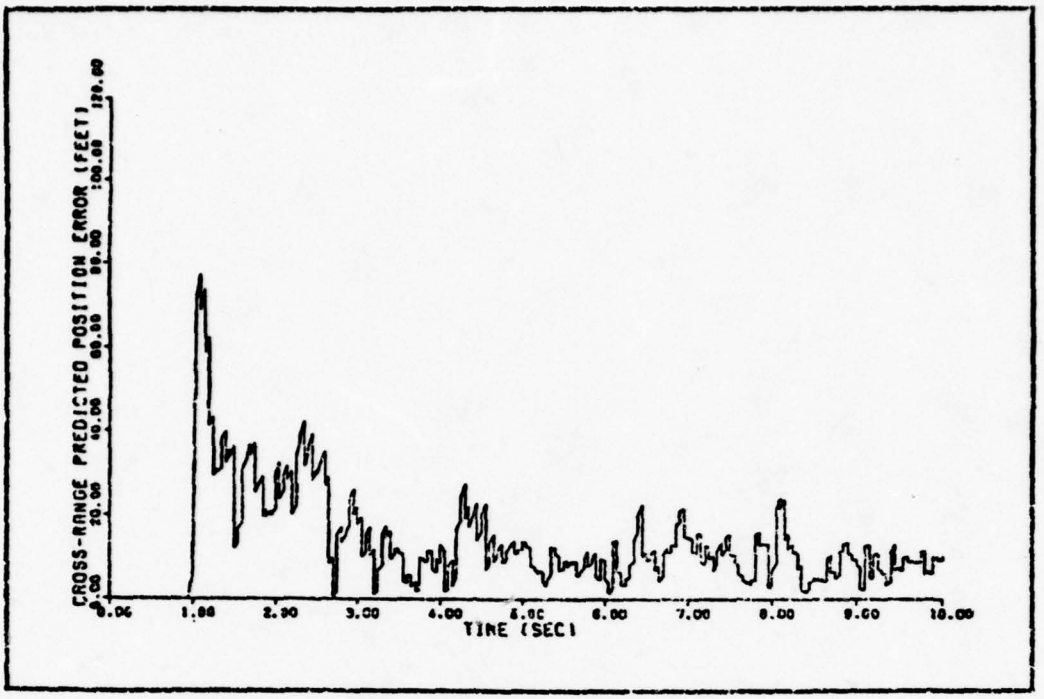


Fig. A-17. Scenario 1, Average Error in Predicted Cross-Range Target Position, Interactive Filter, Large Unmodelled Radar Errors

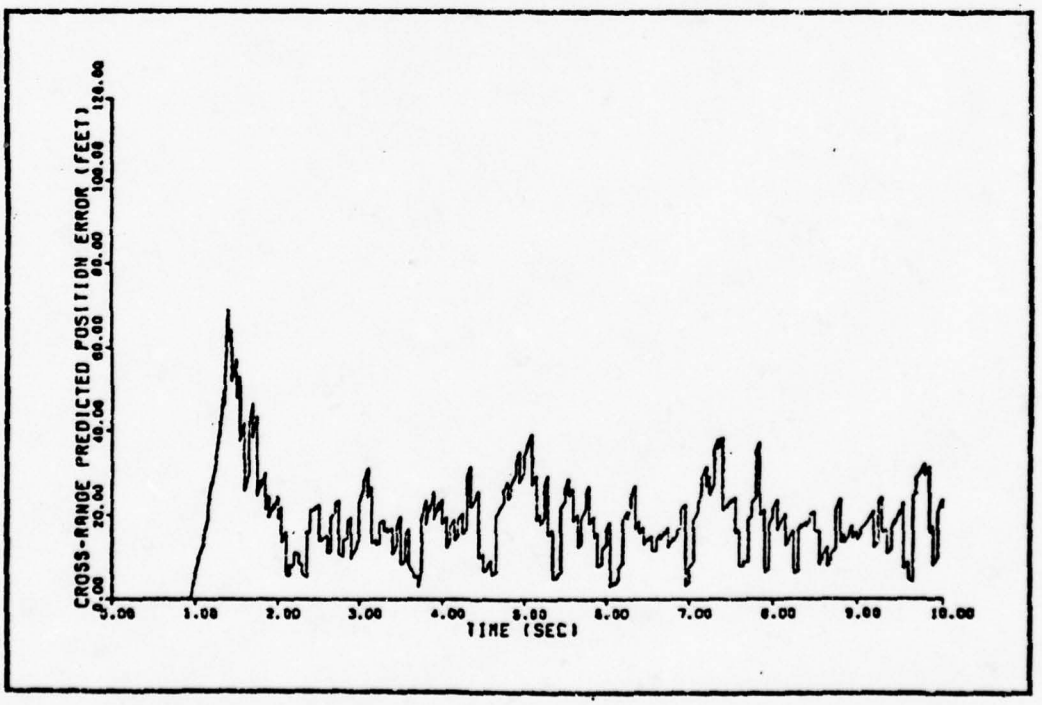


Fig. A-18. Scenario 1, Average Error in Predicted Cross-Range Target Position, Comparative Filter, Large Unmodelled Radar Errors

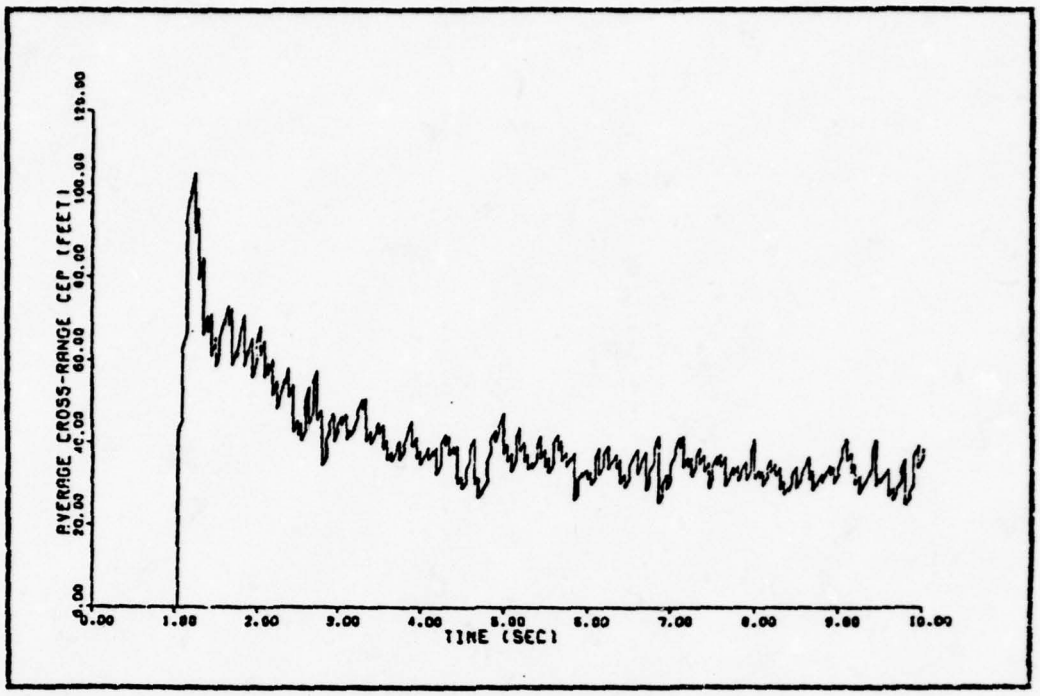


Fig. A-19. Scenario 1, Average CEP, Interactive Filter, Large Unmodelled Radar Errors

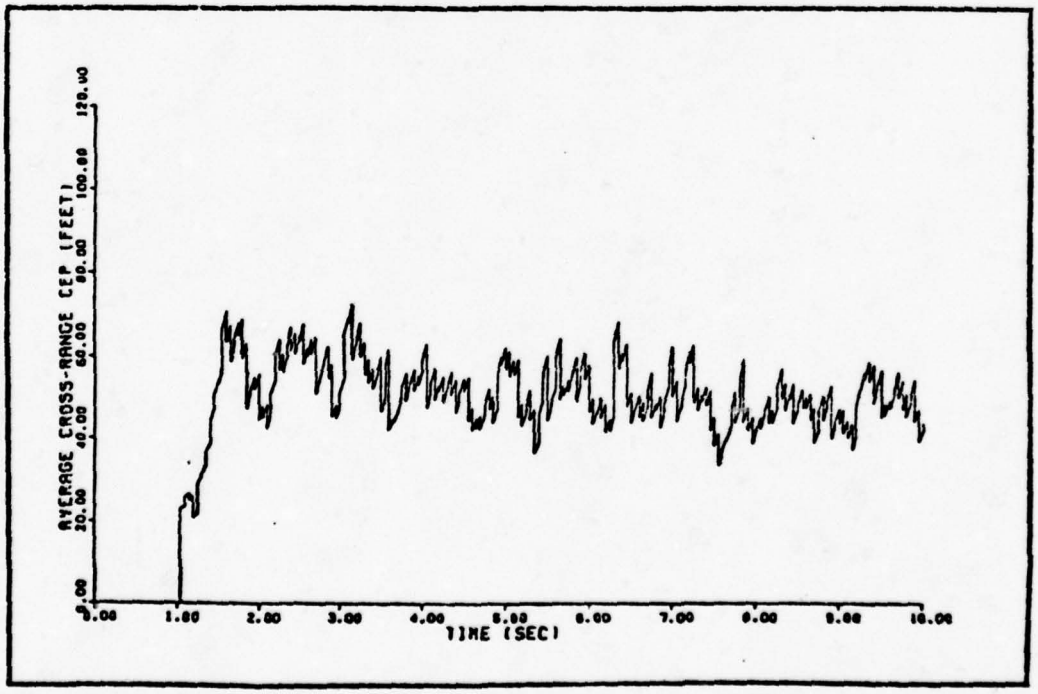


Fig. A-20. Scenario 1, Average CEP, Comparative Filter, Large Unmodelled Radar Errors

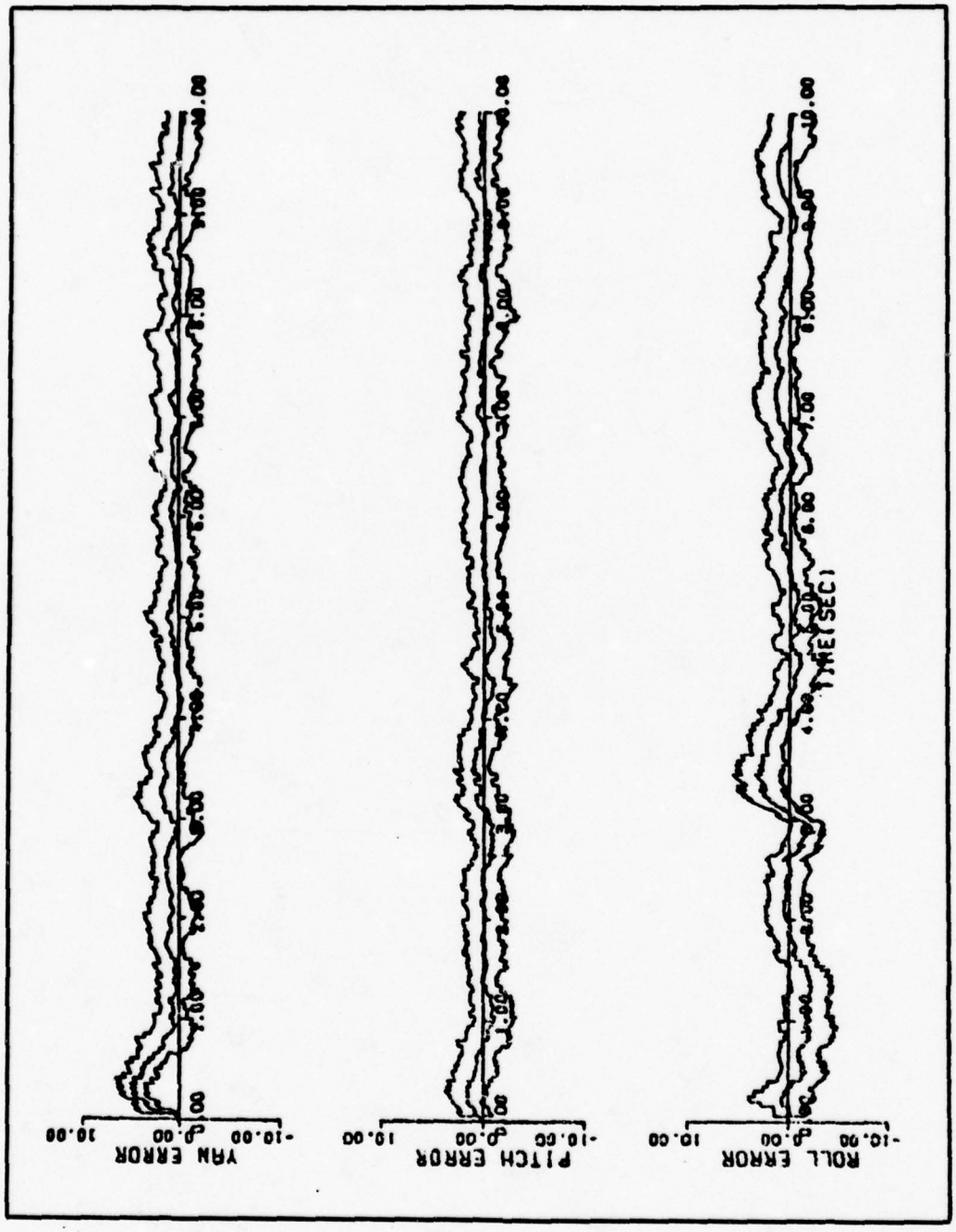


Fig. A-21. Scenario 1, Average Error in Kalman Filter Estimated Target Aspect

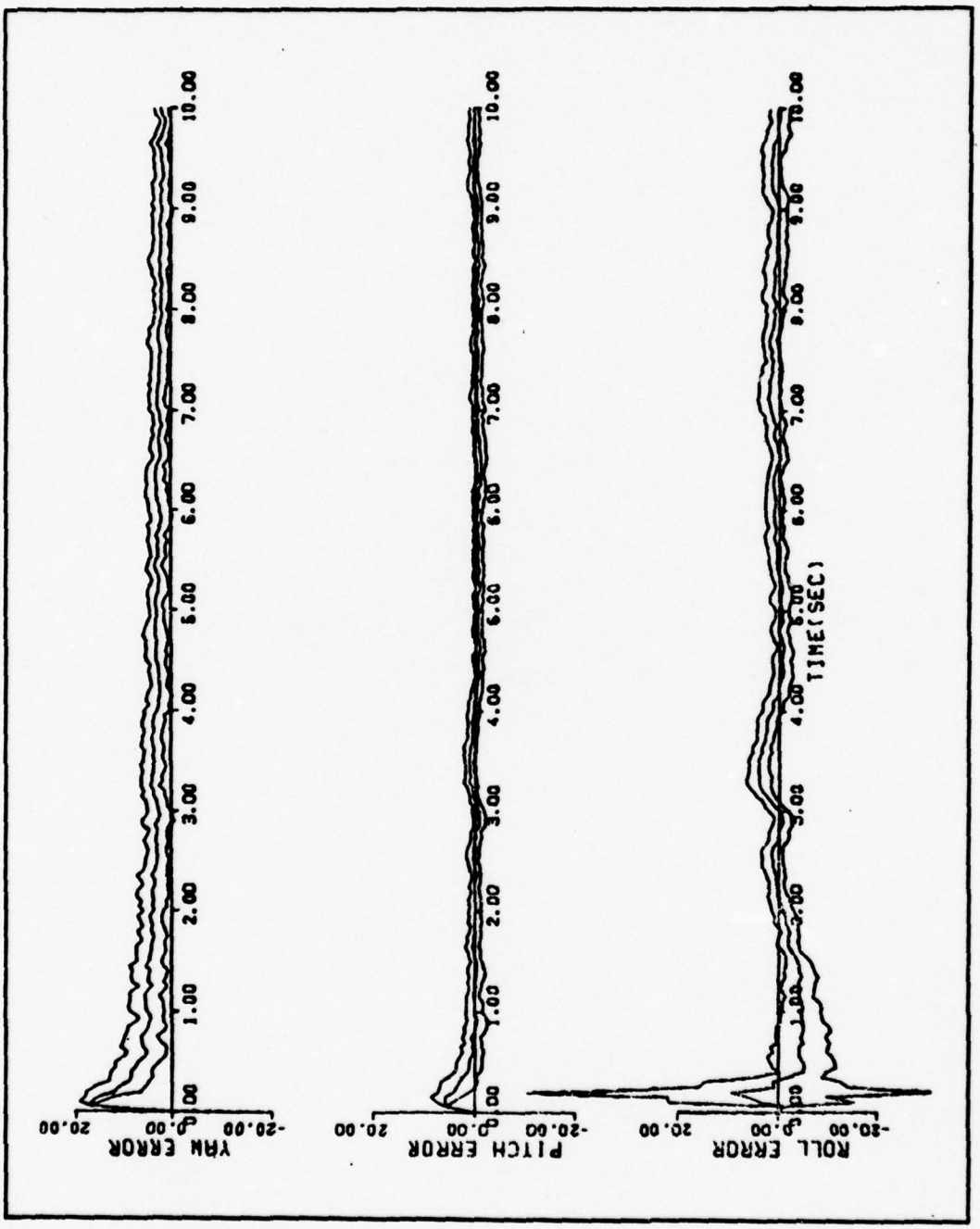


Fig. A-22. Scenario 1, Average Error in Kinematically Derived Target Aspect

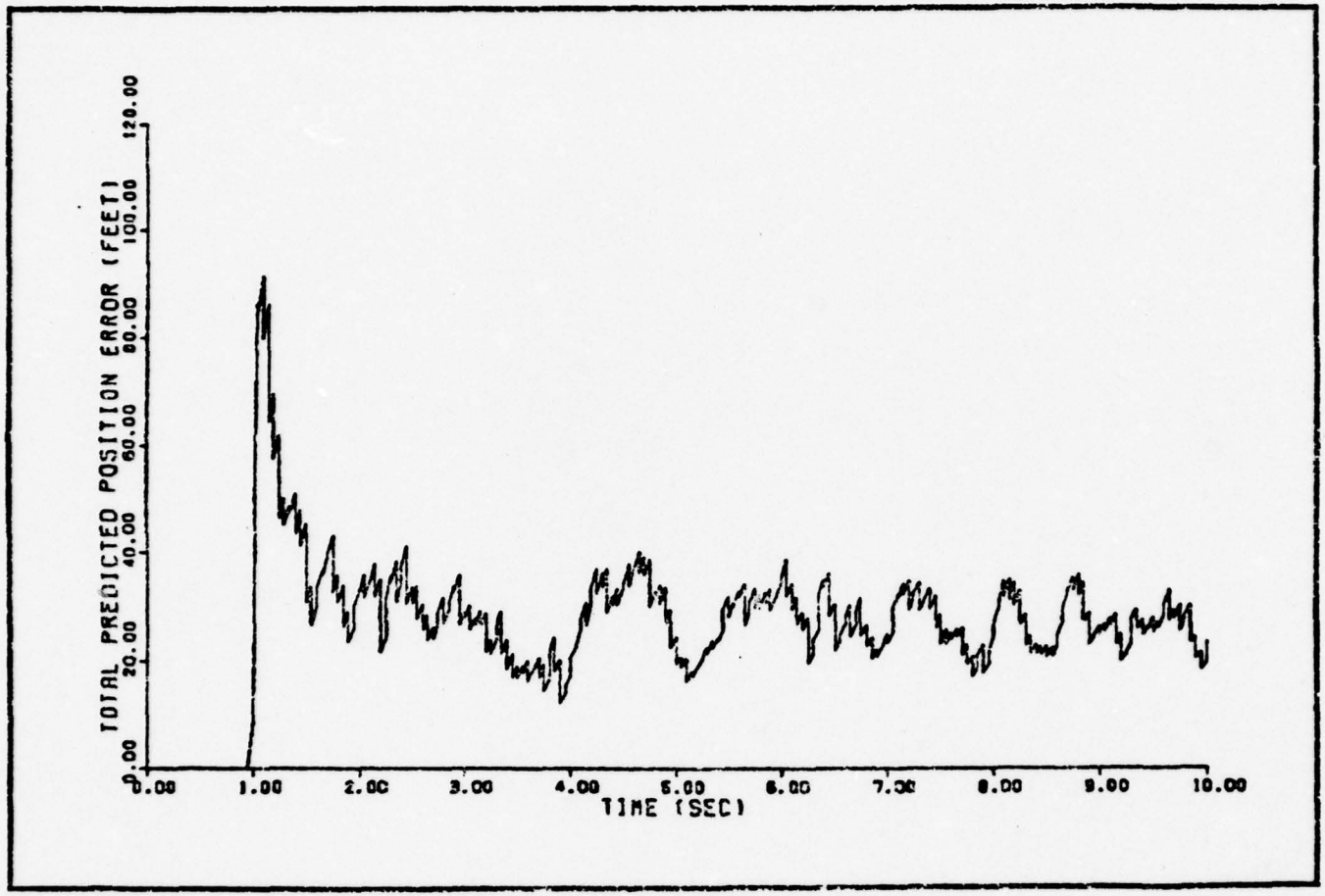


Fig. A-23. Scenario 1, Average Error in Predicted Target Position, Interactive Filter, E-O/PR Aspect Measurement Noise 25 degrees (1$\sigma$), Filter Unaware

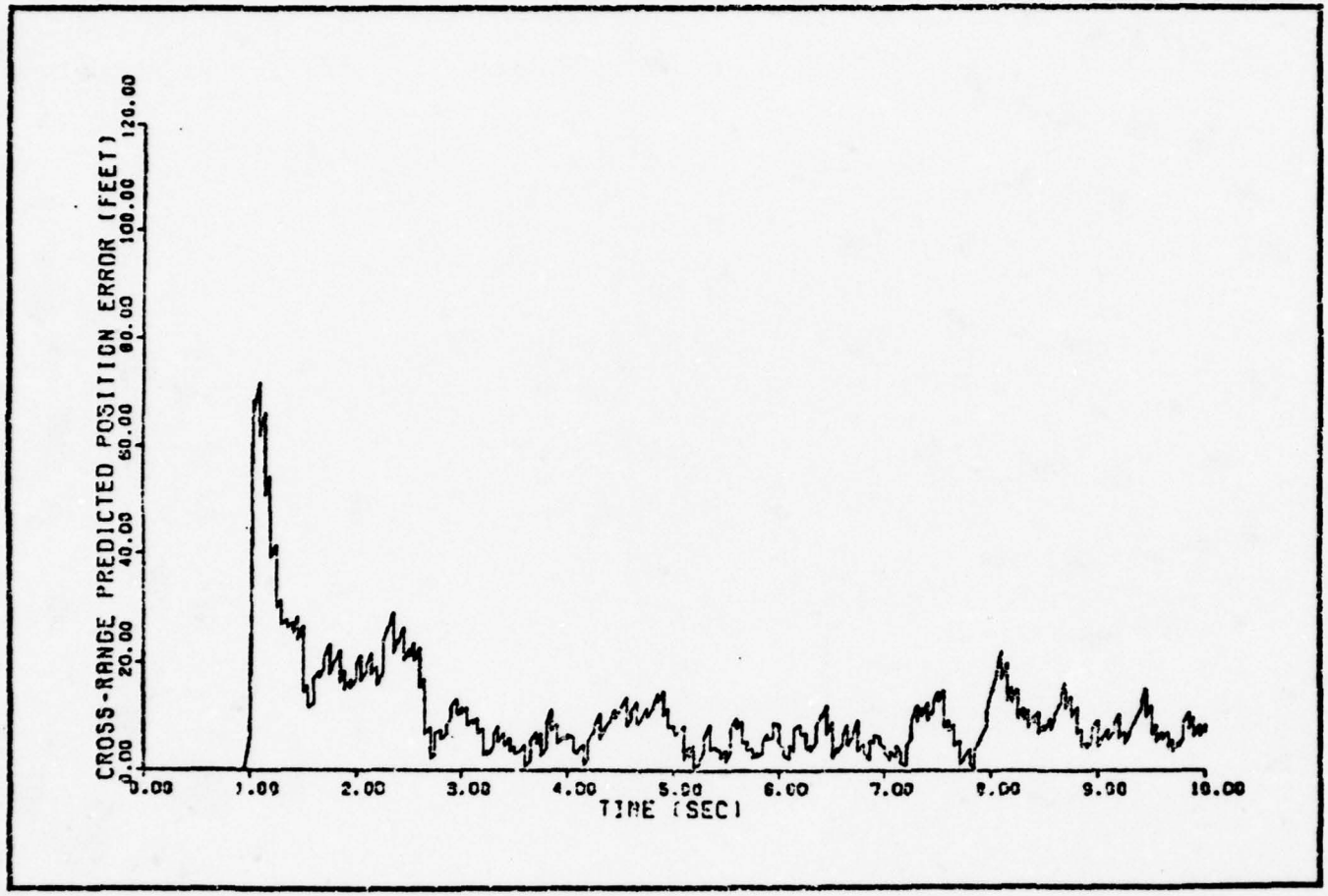


Fig. A-24. Scenario 1, Average Error in Predicted Cross-Range Target Position, Interactive Filter, E-O/PR Aspect Measurement Noise 25 degrees (1σ), Filter Unaware

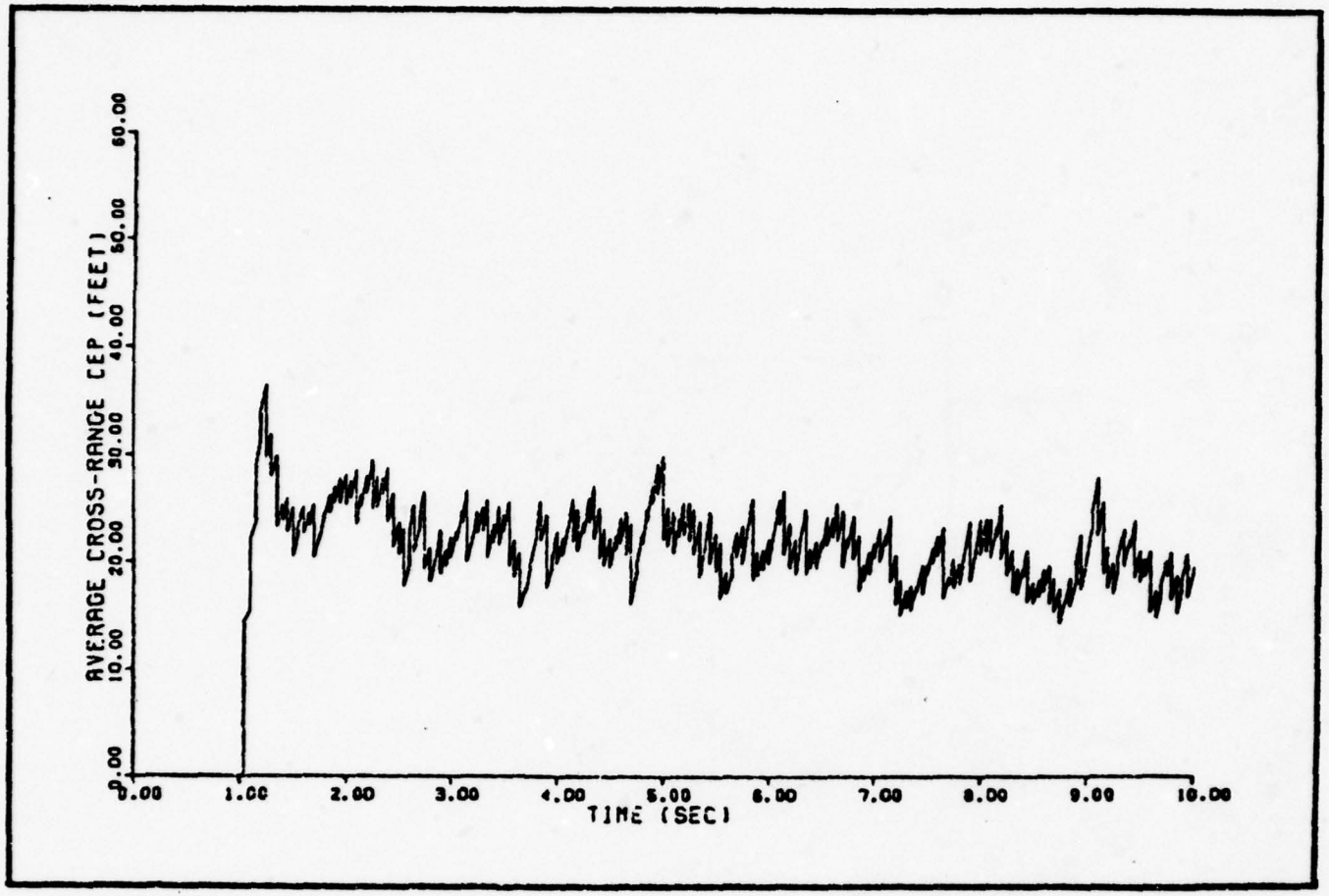


Fig. A-25. Scenario 1, Average CEP, Interactive Filter, E-O/PR Aspect Measurement Noise 25 degrees (1σ), Filter Unaware

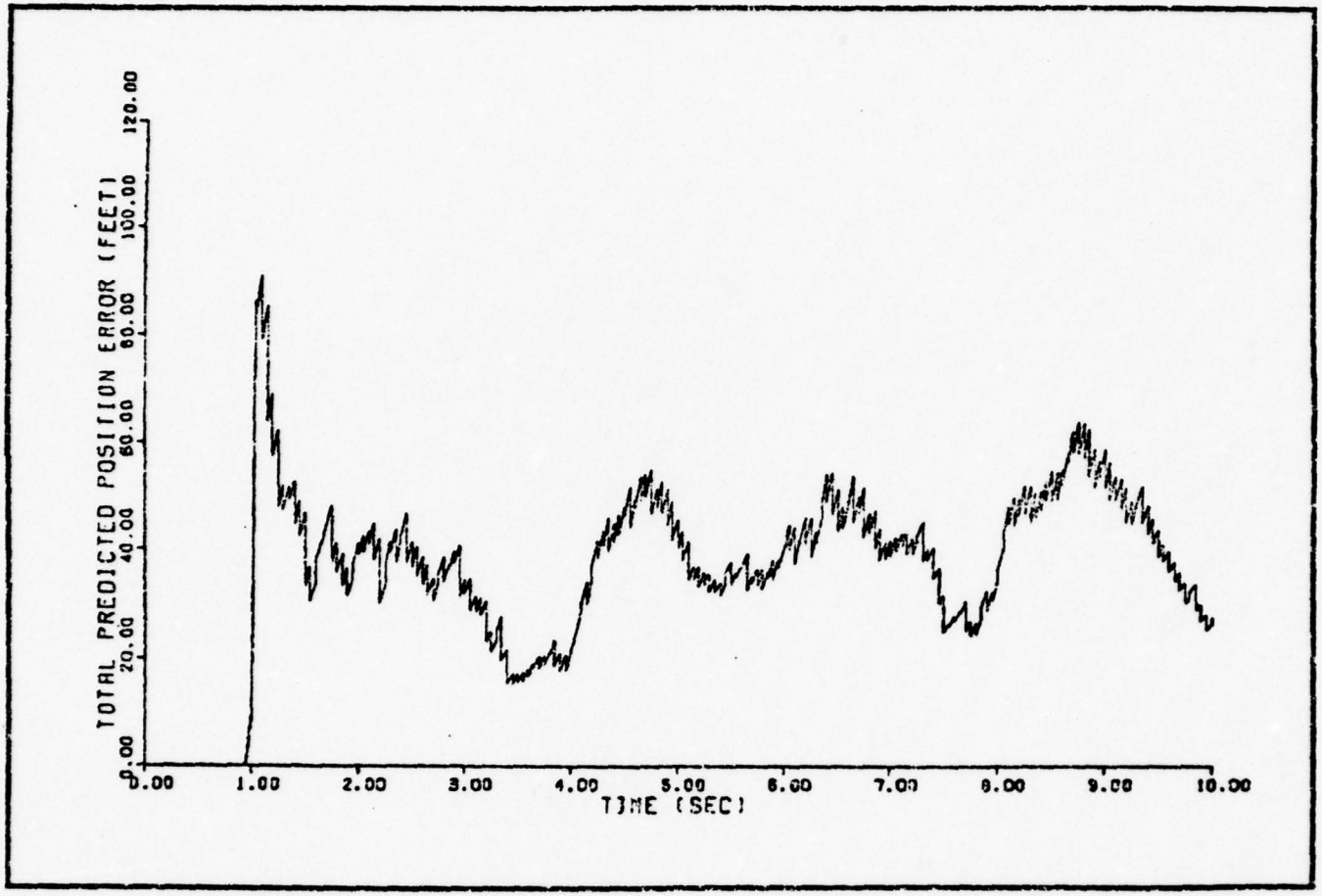


Fig. A-26. Scenario 1, Average Error in Predicted Target Position, Interactive Filter, E-O/PR Aspect Measurement Noise 25 degrees (1σ), Filter Aware

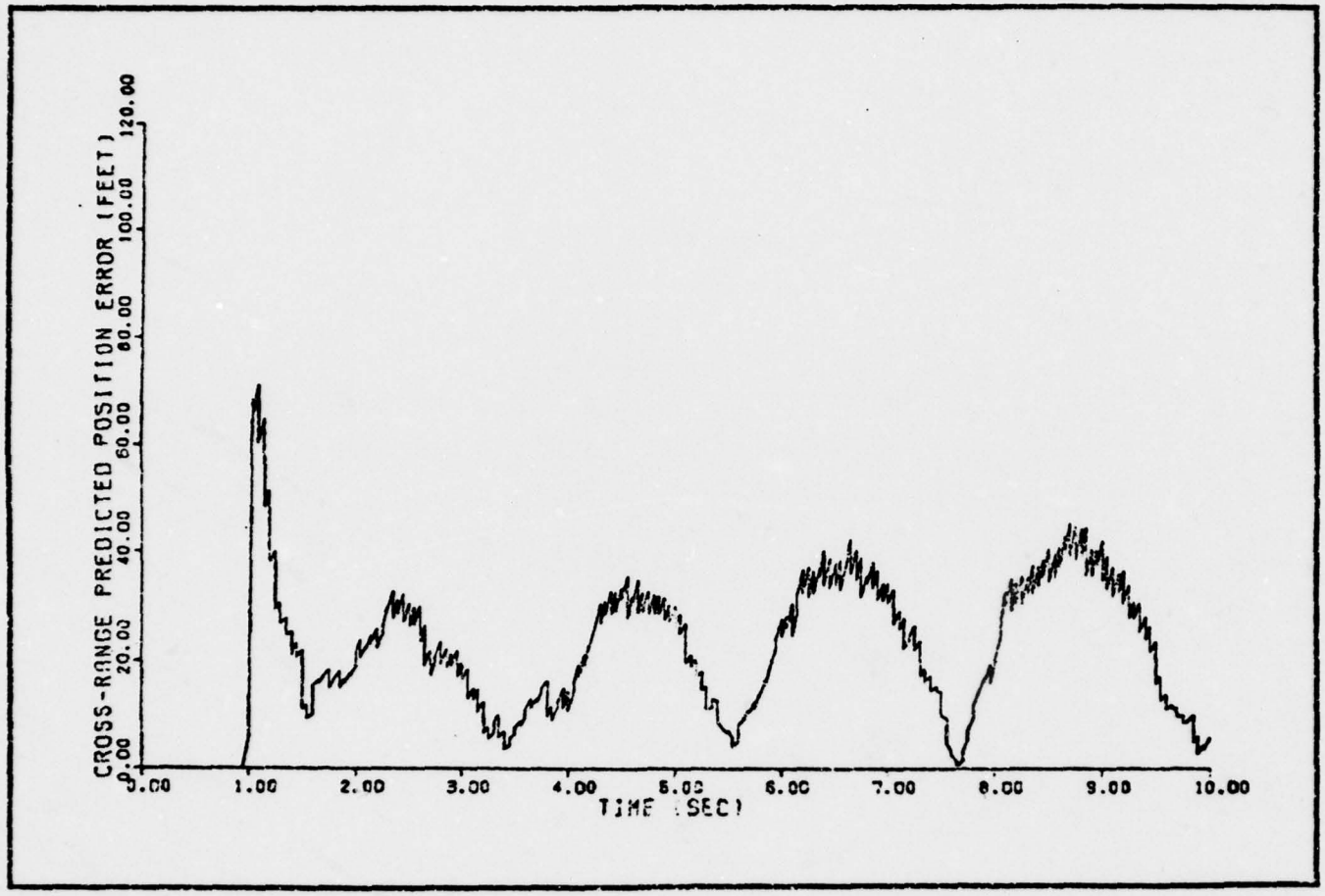


Fig. A-27. Scenario 1, Average Error in Predicted Cross-Range Target Position, Interactive Filter, E-O/PR Aspect Measurement Noise 25 degrees (1σ), Filter Aware

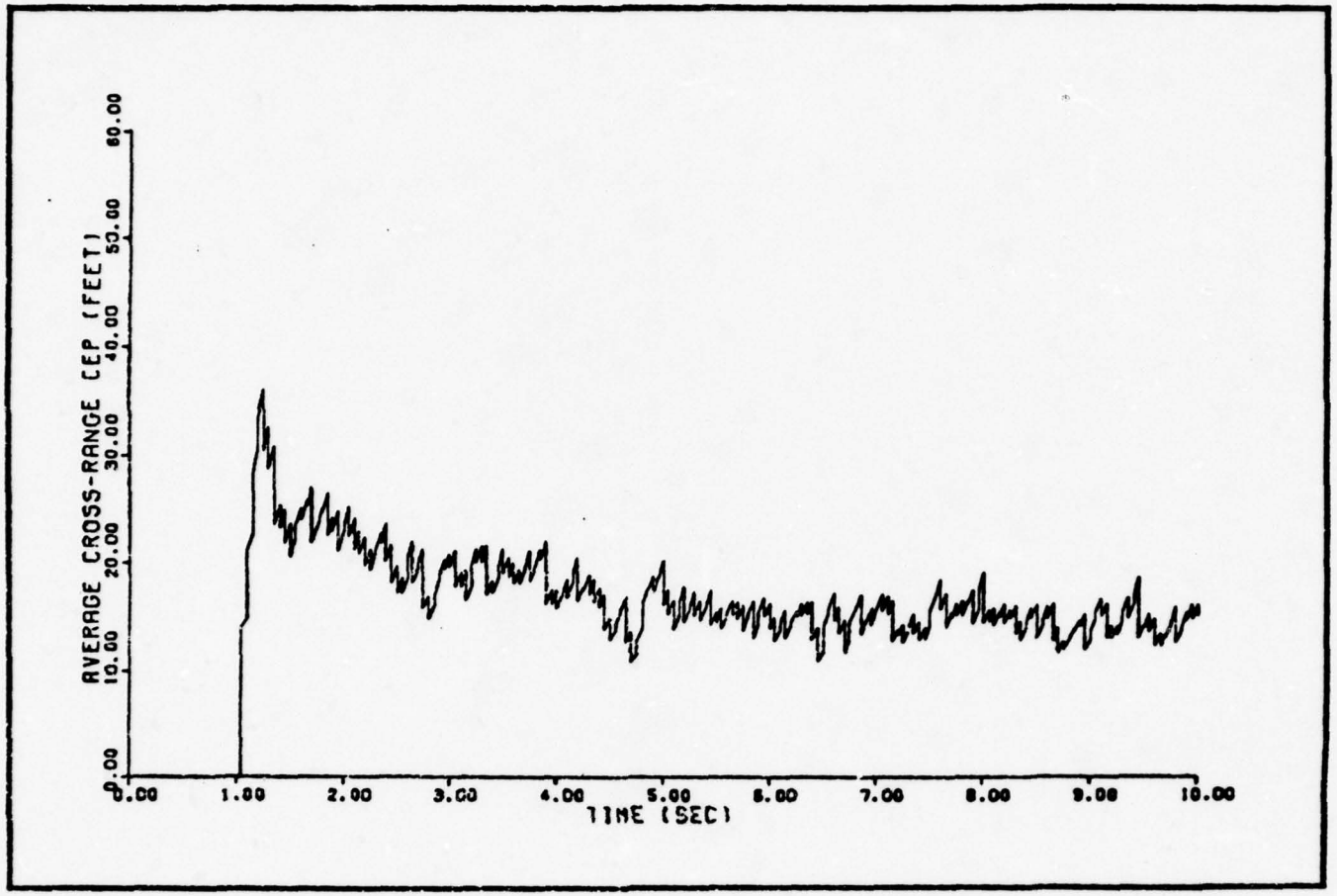


Fig. A-28. Scenario 1, Average CEP, Interactive Filter, E-O/PR Aspect Measurement Noise 25 degrees (1σ), Filter Aware

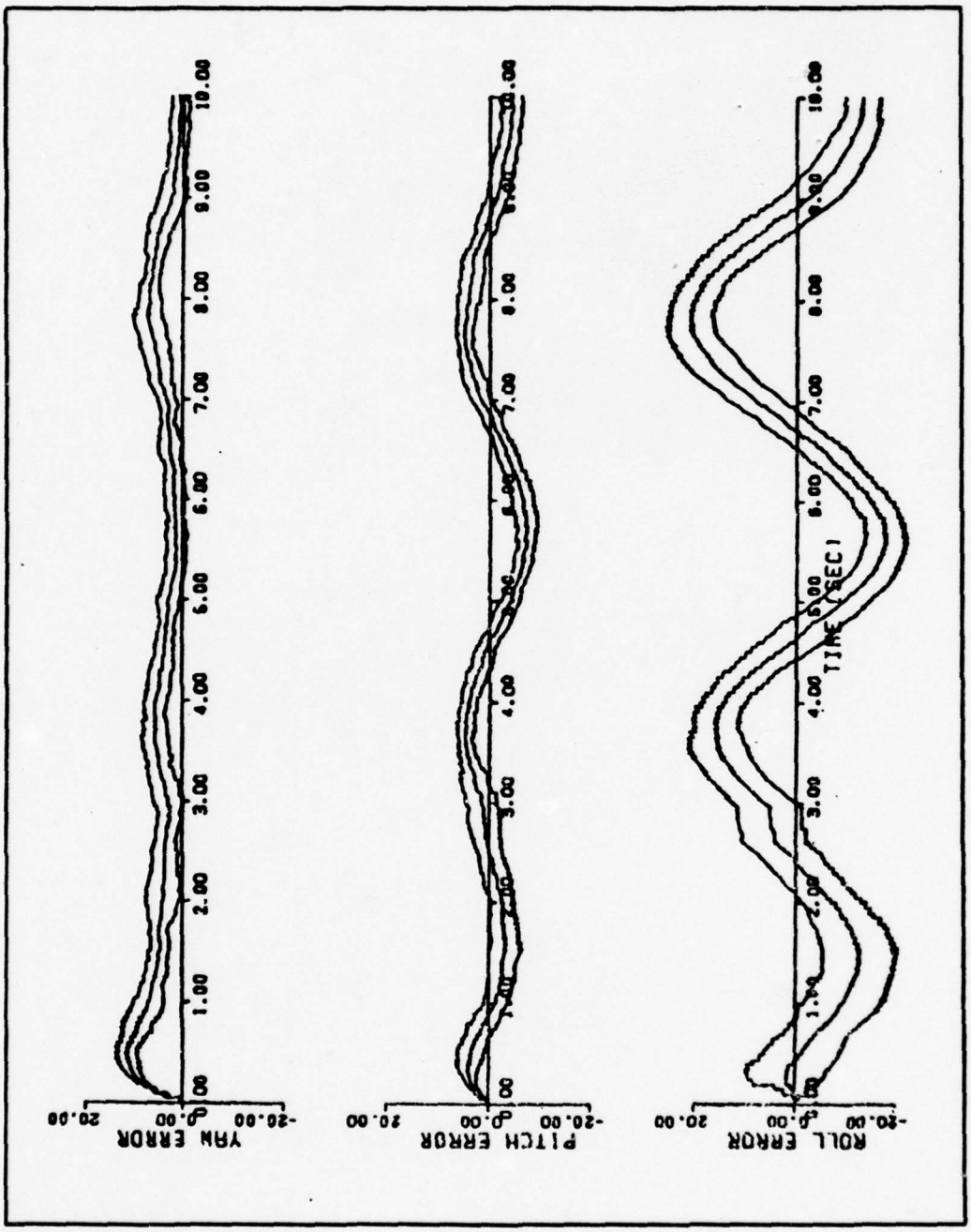


Fig. A-29. Scenario 1, Average Error in Kalman Filter Estimated Target Aspect, E-O/PR Aspect Measurement Noise $25^{0}$ ($1\sigma$), Filter Aware

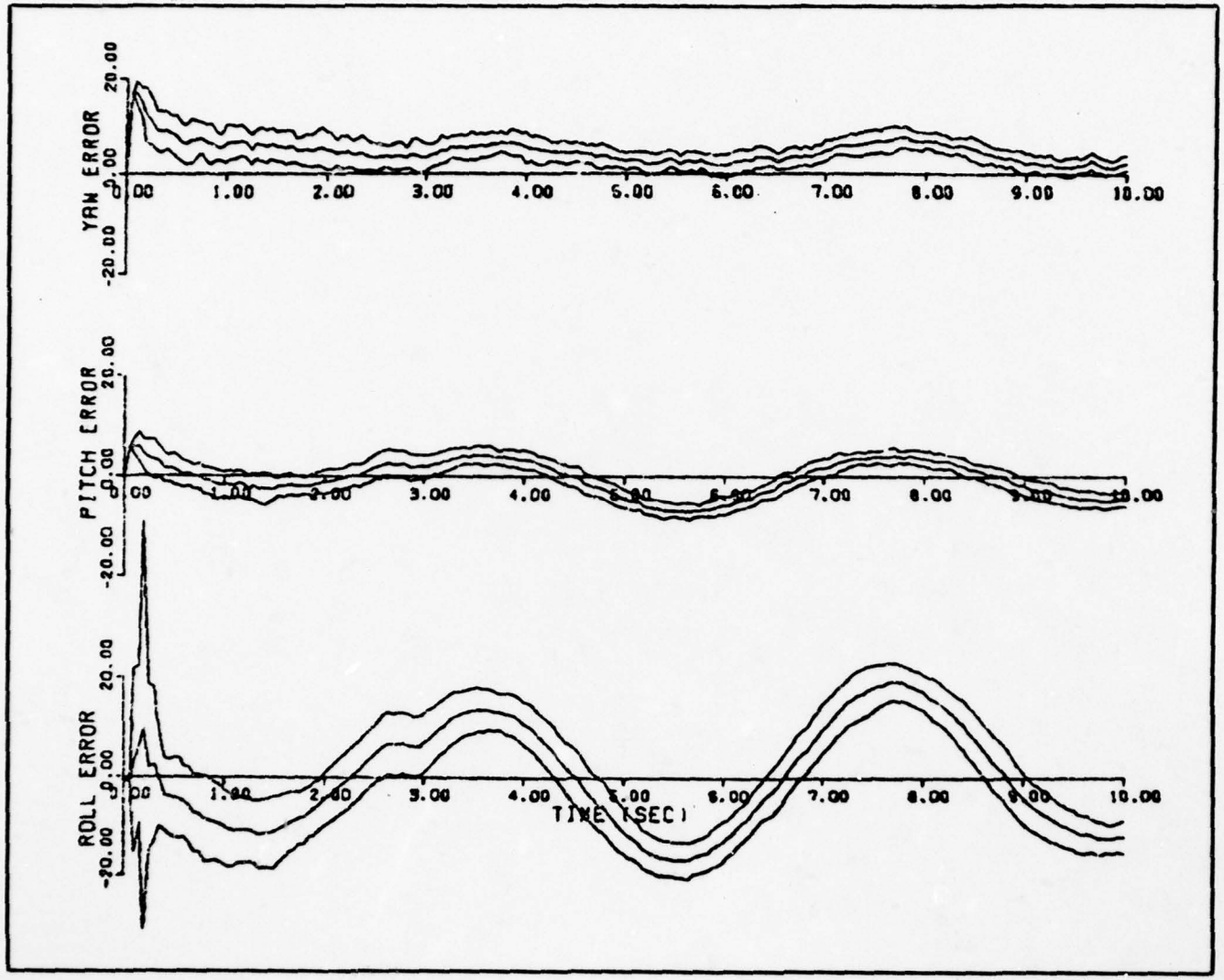


Fig. A-30. Scenario 1, Average Error in Kinematically Derived Target Aspect, E-O/PR Aspect Measurement Noise $25^{o}$ ($1\sigma$), Filter Aware

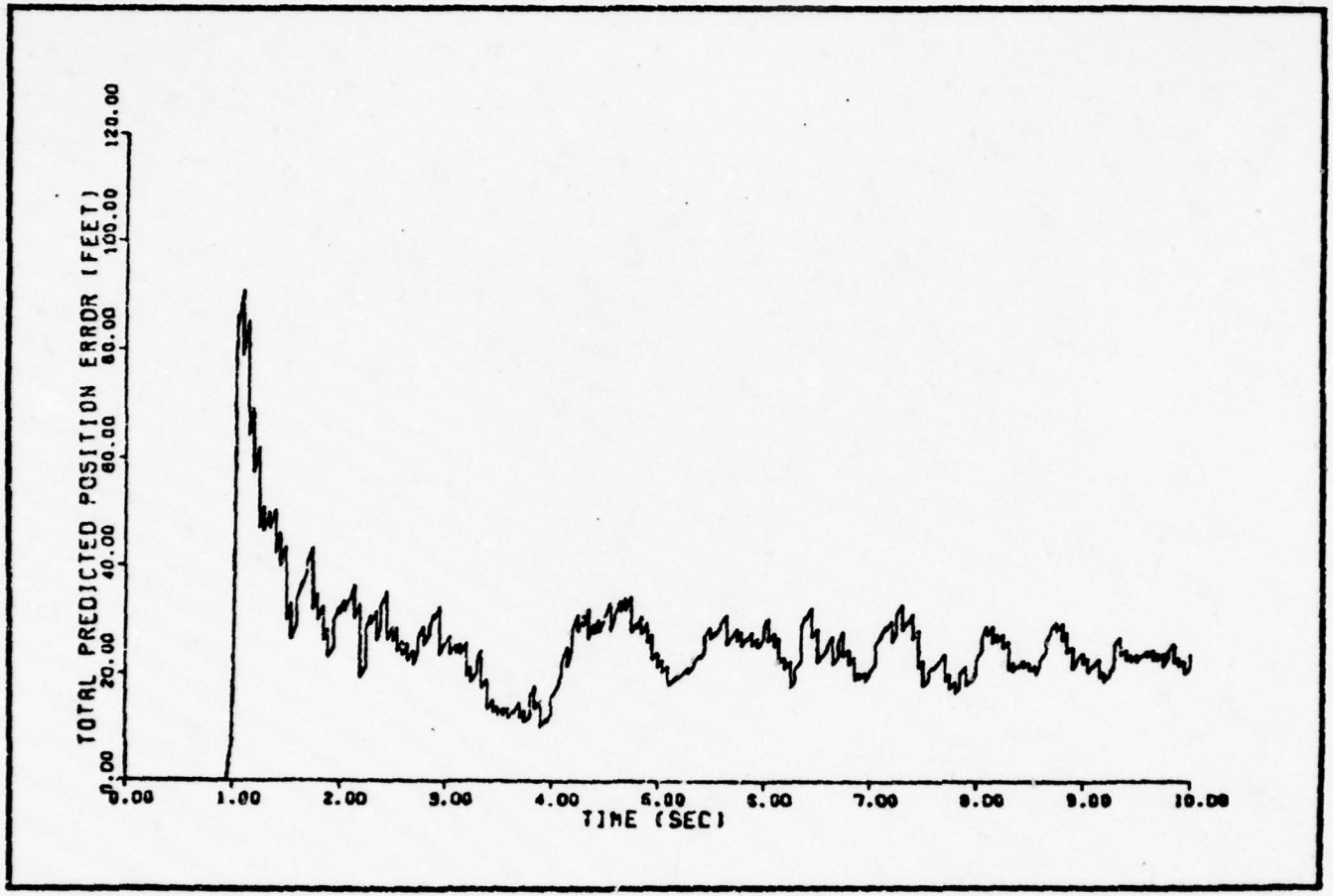


Fig. A-31. Scenario 1, Average Error in Predicted Target Position, Interactive Filter, $5^{o}$ Fixed Bias Added to All Yaw, Pitch and Roll E-O/PR Measurements

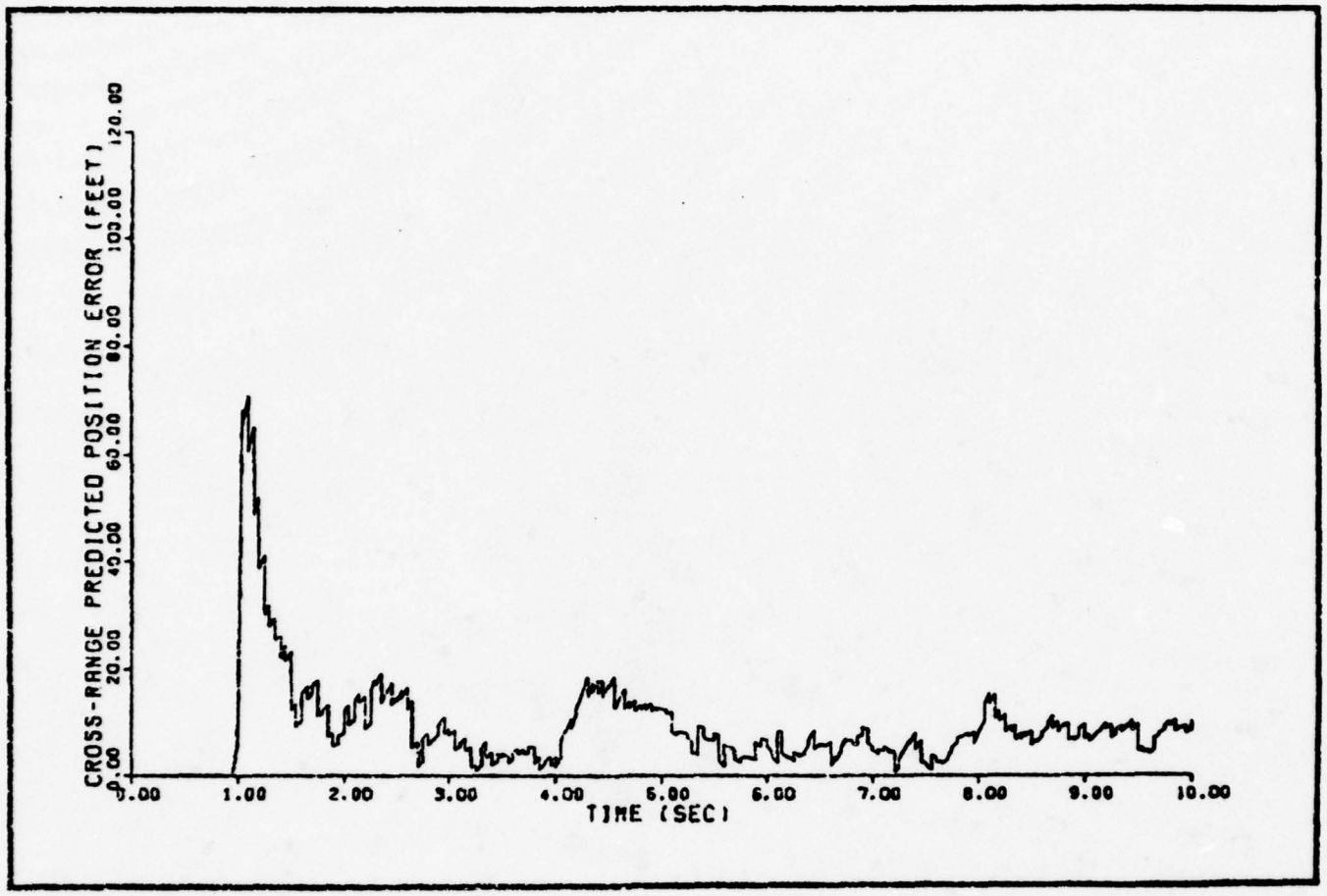


Fig. A-32. Scenario 1, Average Error in Predicted Cross-Range Target Position, Interactive Filter, $5^{0}$ Fixed Bias Added to All Yaw, Pitch and Roll E-O/PR Measurements

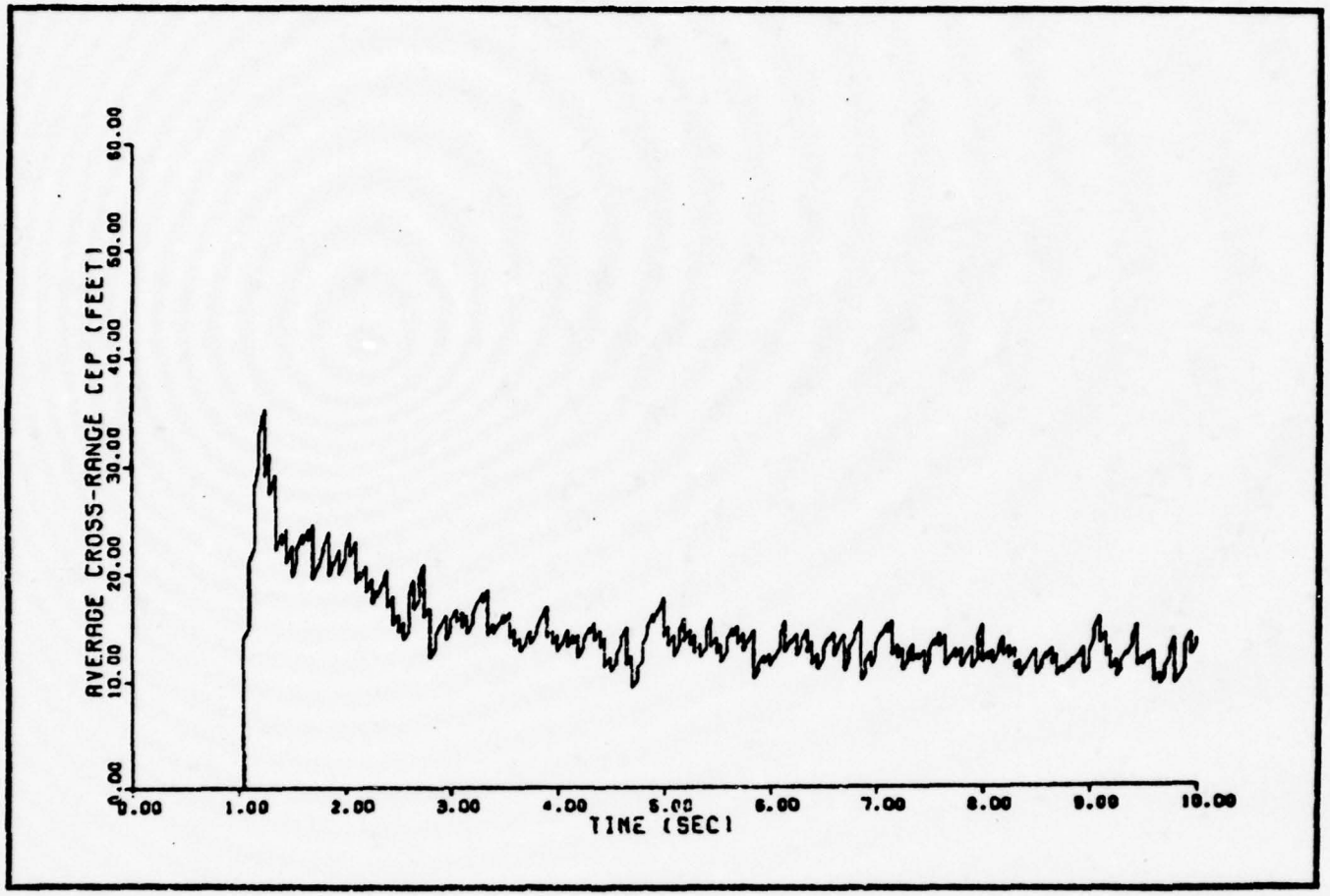


Fig. A-33. Scenario 1, Average CEP, Interactive Filter, $5^{o}$ Fixed Bias Added to All Yaw, Pitch and Roll E-O/PR Measurements

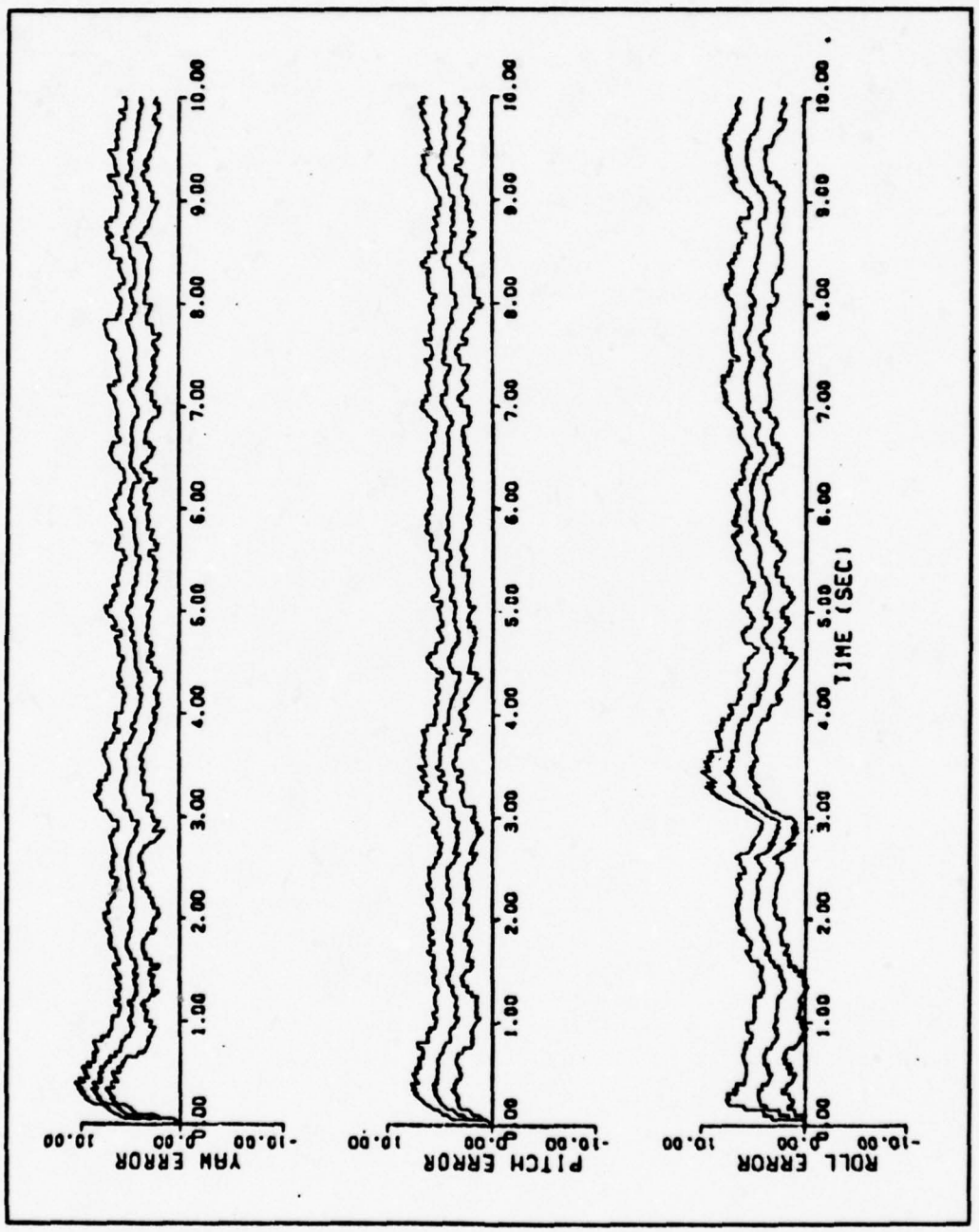


Fig. A-34. Scenario 1, Average Error in Kalman Filter Estimated Target Aspect, Five Degrees Fixed Bias Added to All Yaw, Pitch and Roll E-O/PR Measurements

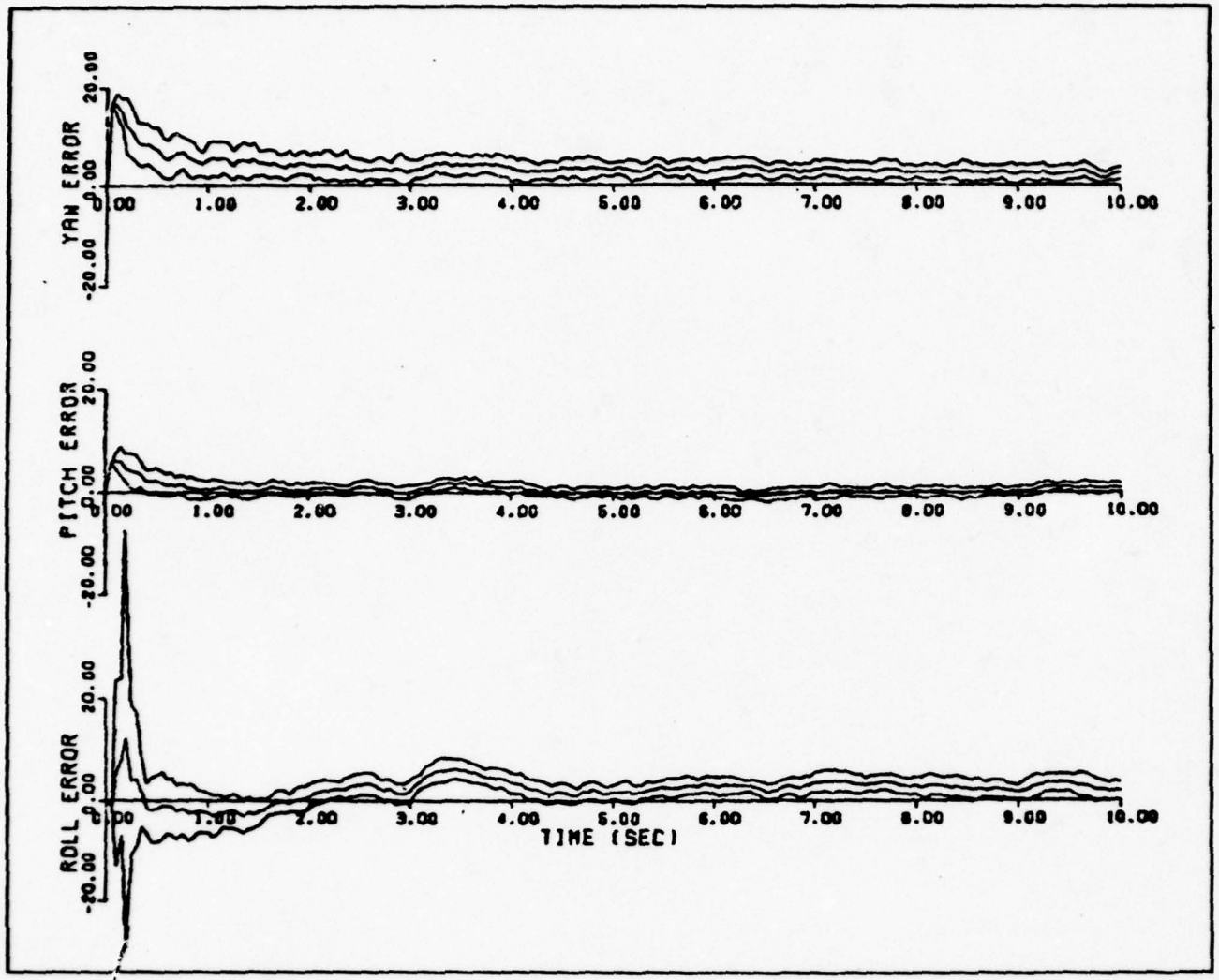


Fig. A-35. Scenario 1, Average Error in Kinematically Derived Target Aspect, Five Degrees Fixed Bias Added to All Yaw, Pitch and Roll E-O/PR Measurements

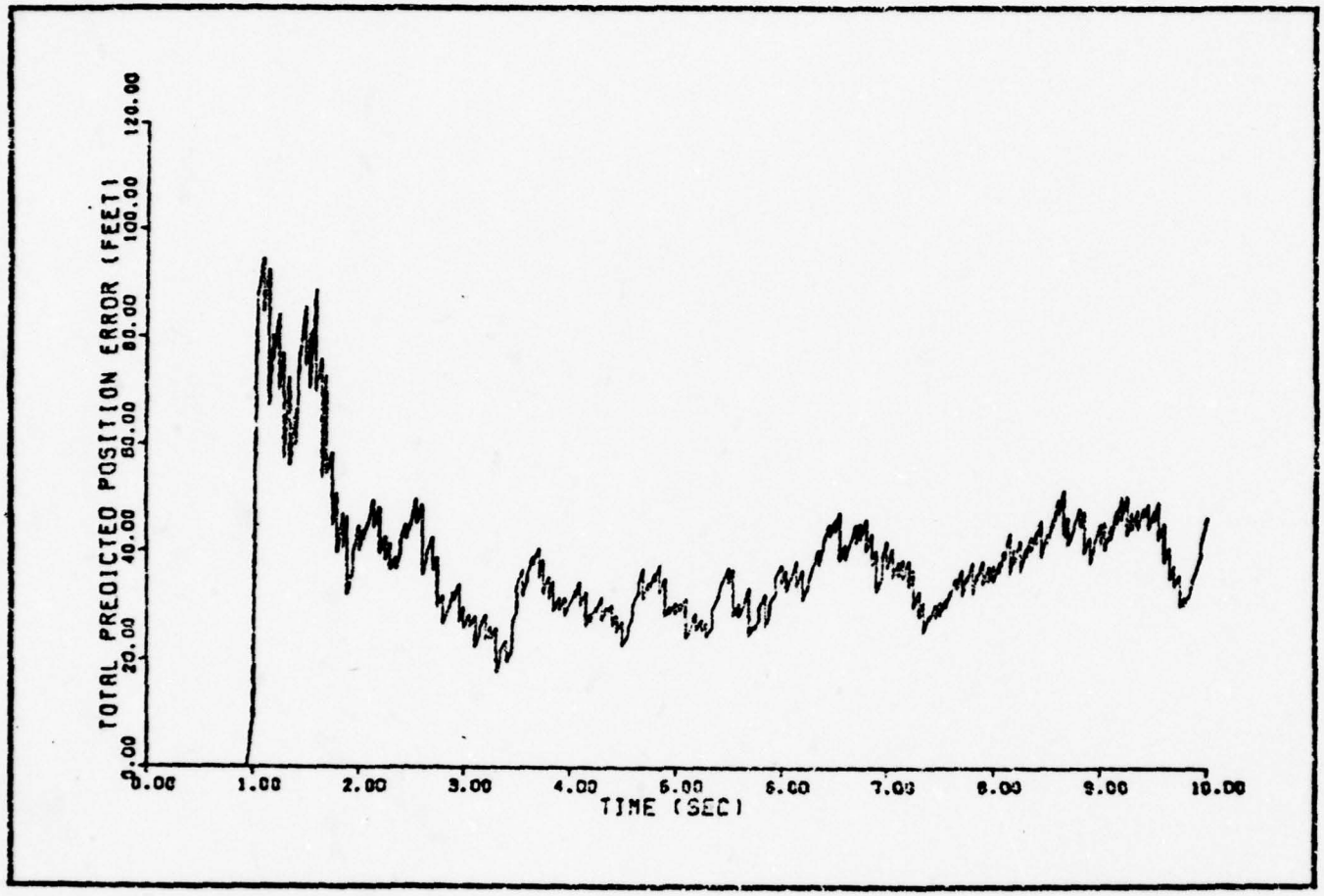


Fig. A-36. Scenario 1, Average Error in Predicted Target Position, Interactive Filter, No E-O/PR Aspect Measurements Provided

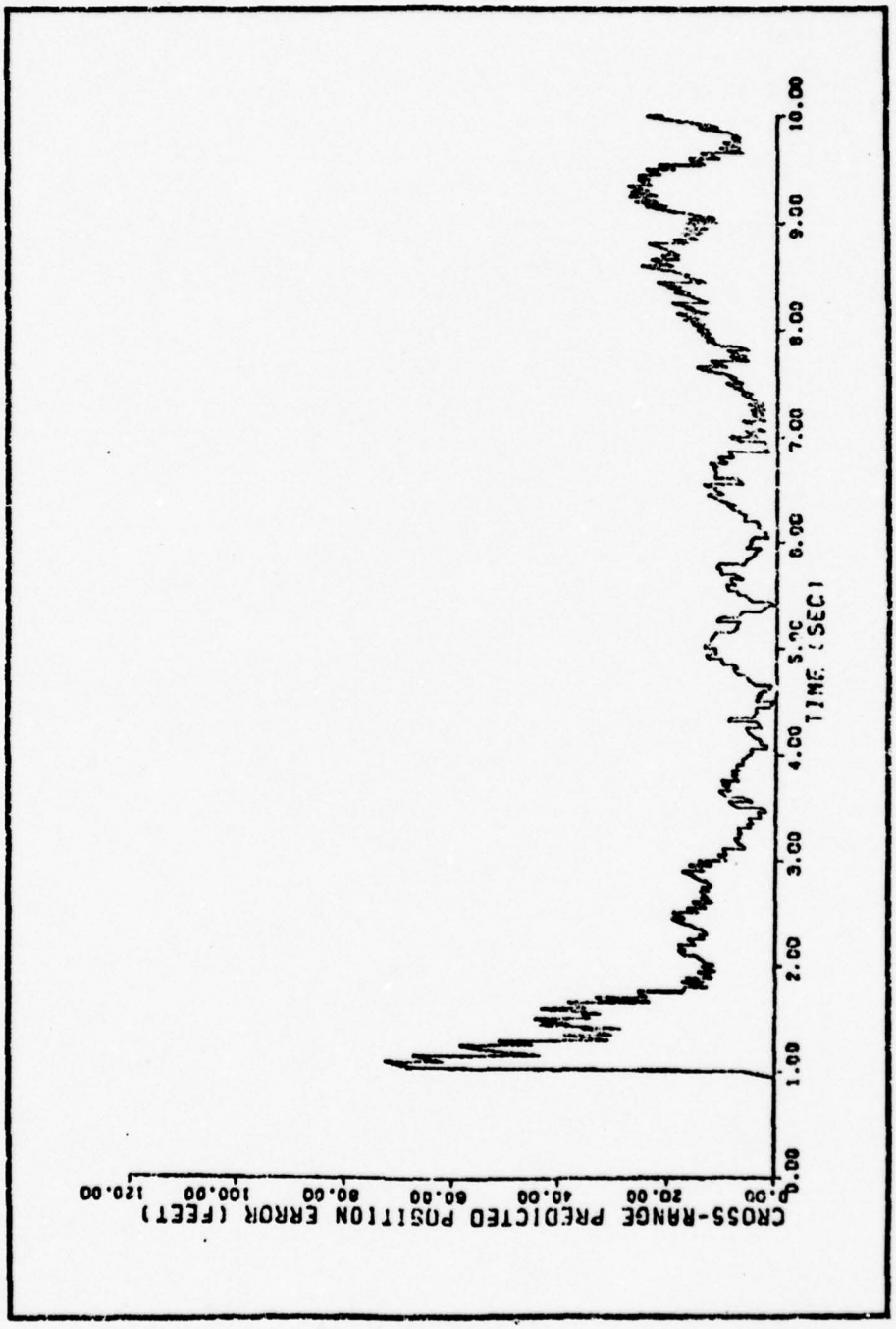


Fig. A-37. Scenario 1, Average Error in Predicted Cross-Range Target Position, Interactive Filter, No E-O/PR Aspect Measurements Provided

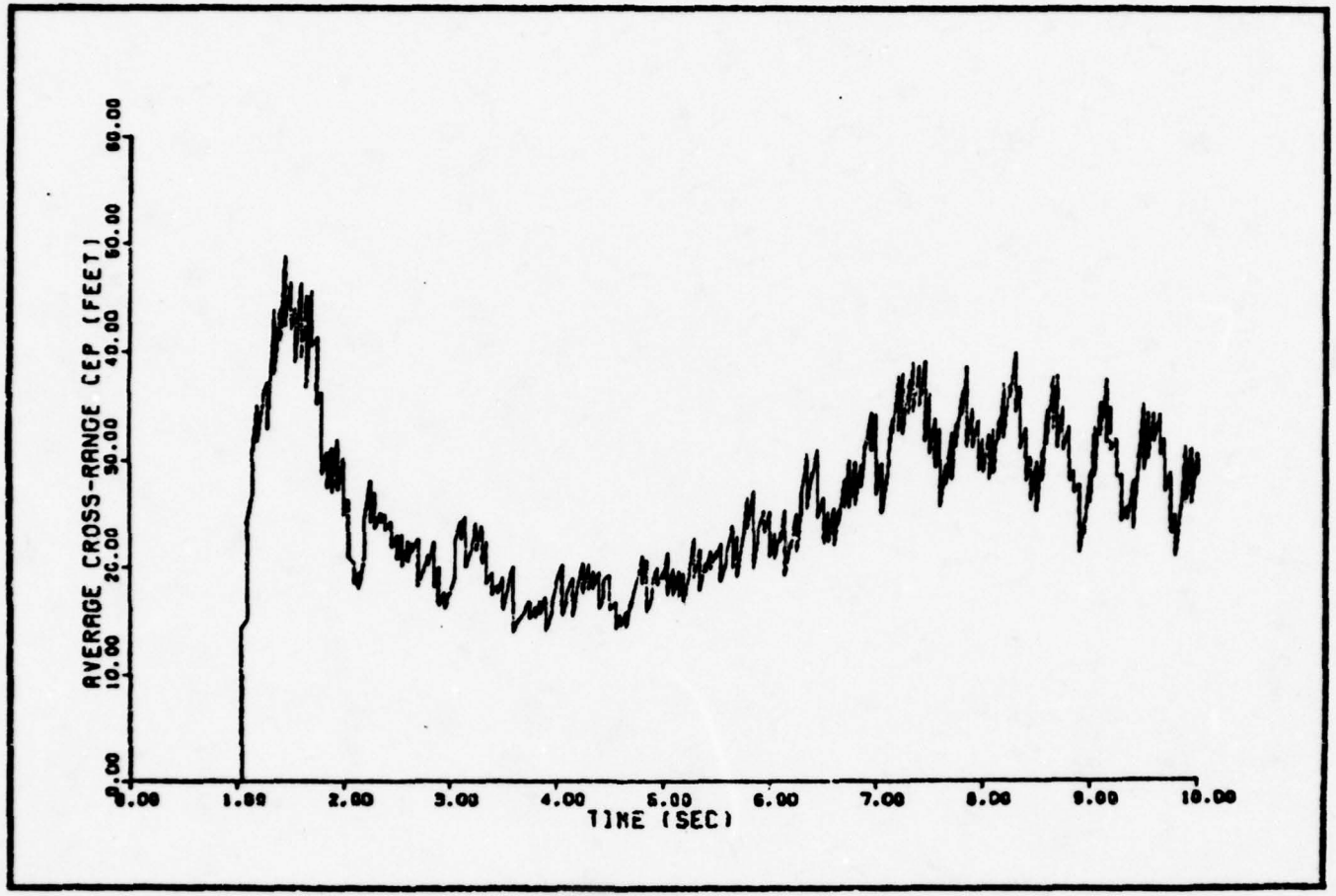


Fig. A-38. Scenario 1, Average CEP, Interactive Filter, No E-O/PR Aspect Measurements Provided

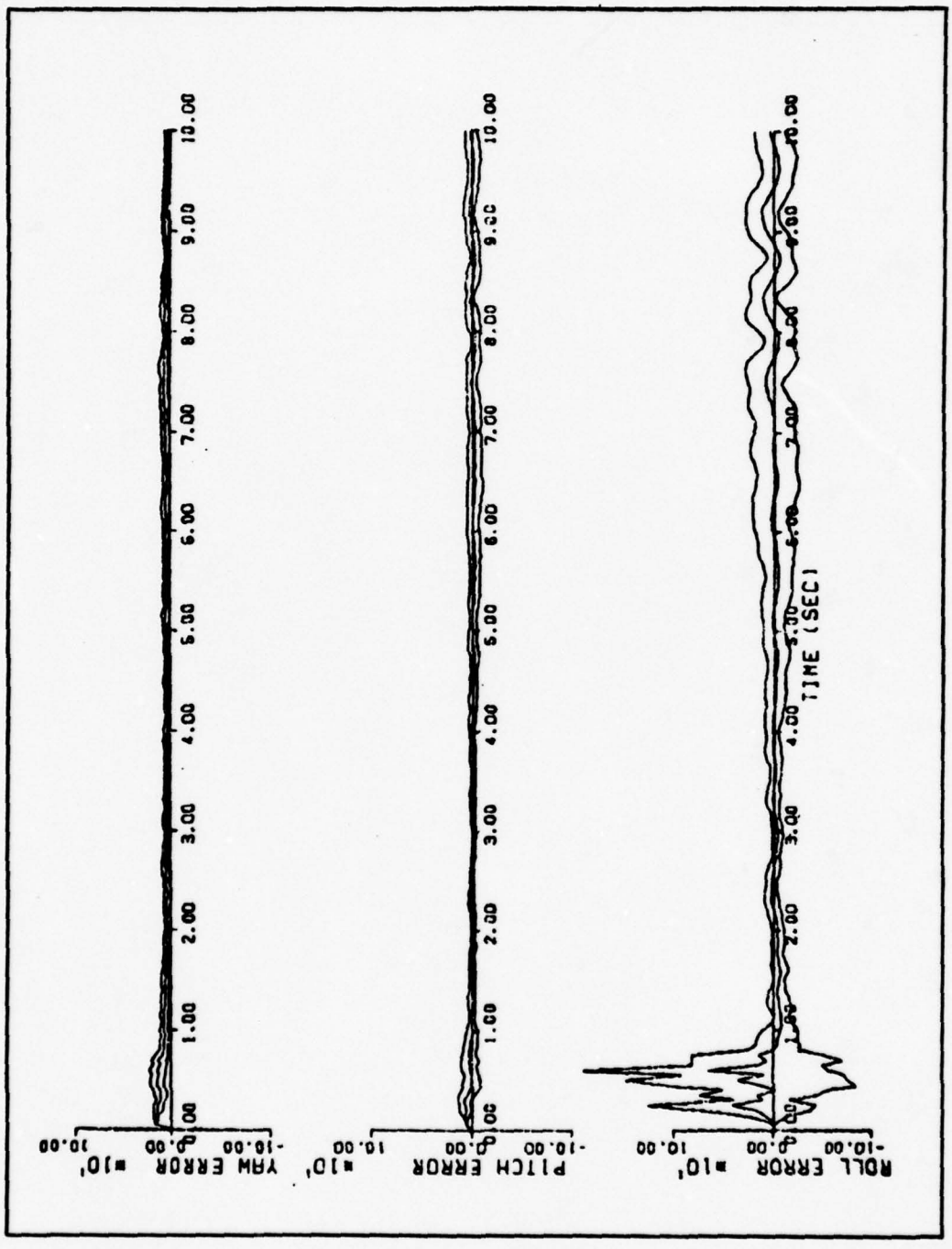


Fig. A-39. Scenario 1, Average Error in Kalman Filter Estimated Target Aspect, No E-O/PR Aspect Measurements Provided

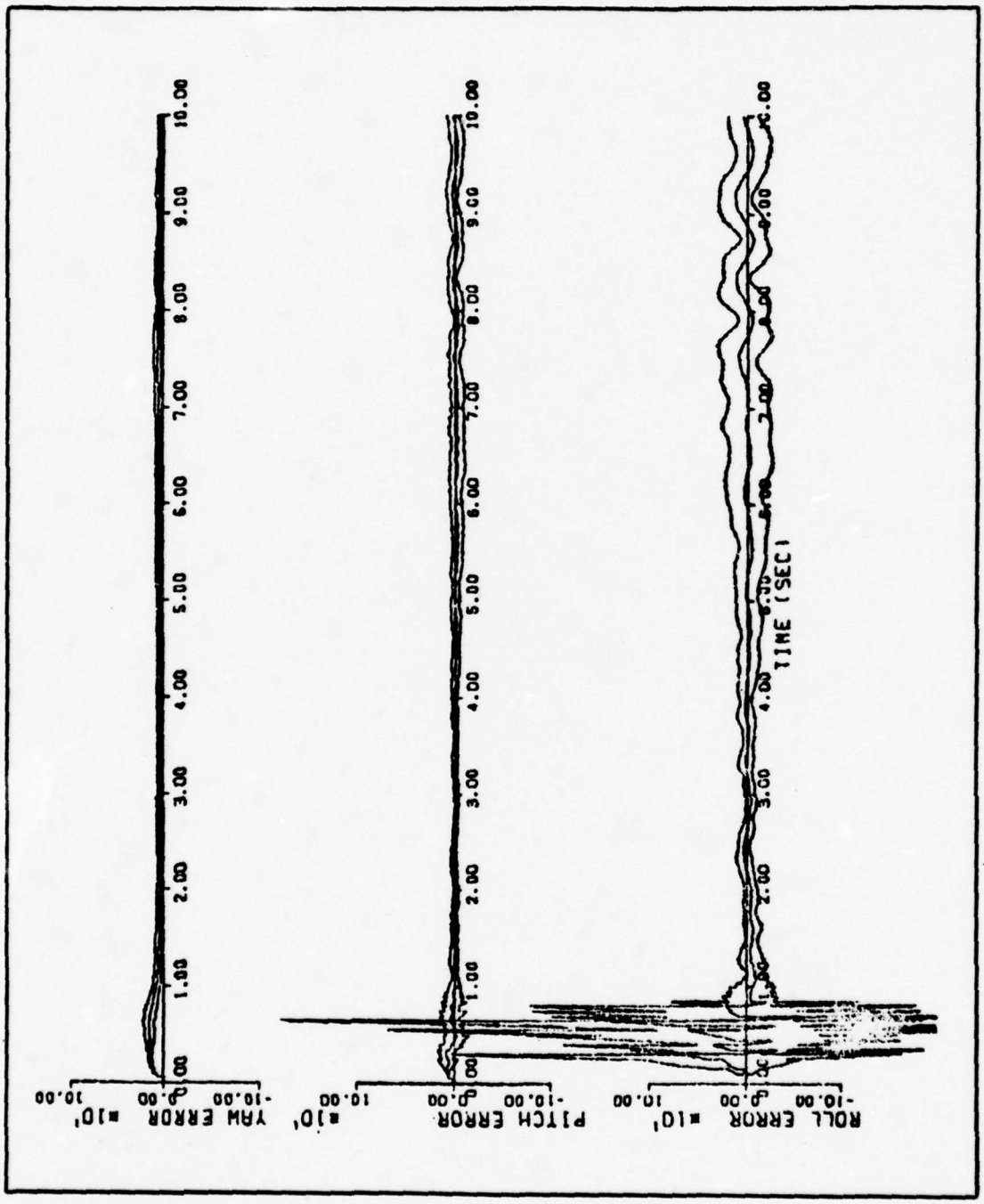


Fig. A-40. Scenario 1, Average Error in Kinematically Derived Target Aspect, No E-O/PR Aspect Measurements Provided

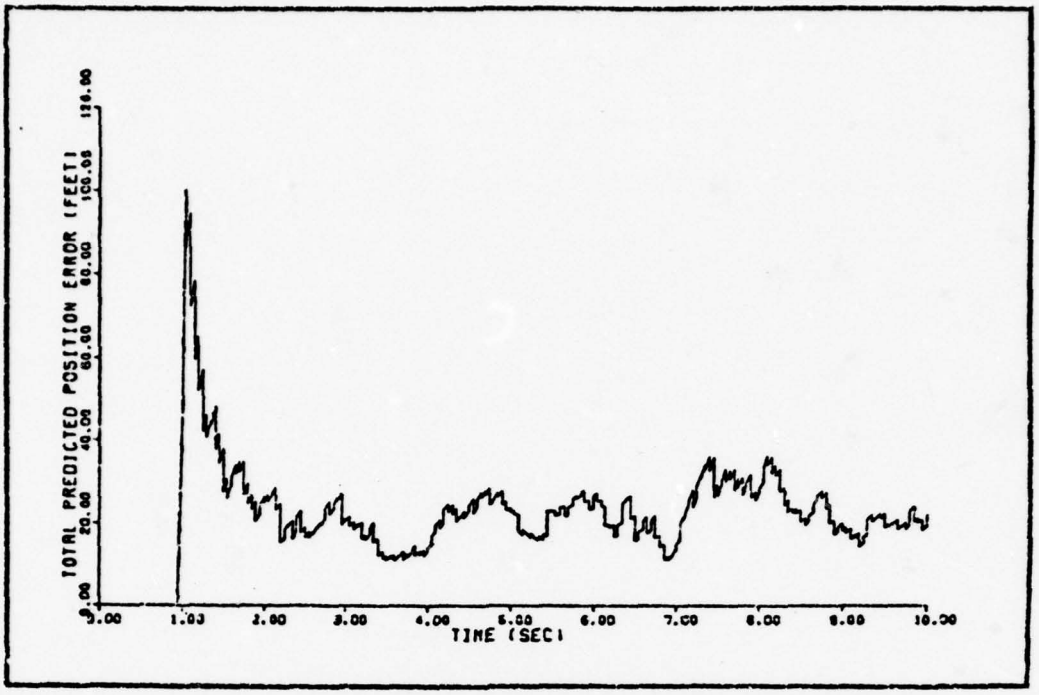


Fig. A-41. Scenario 2, Average Error in Predicted Target Position, Interactive Filter

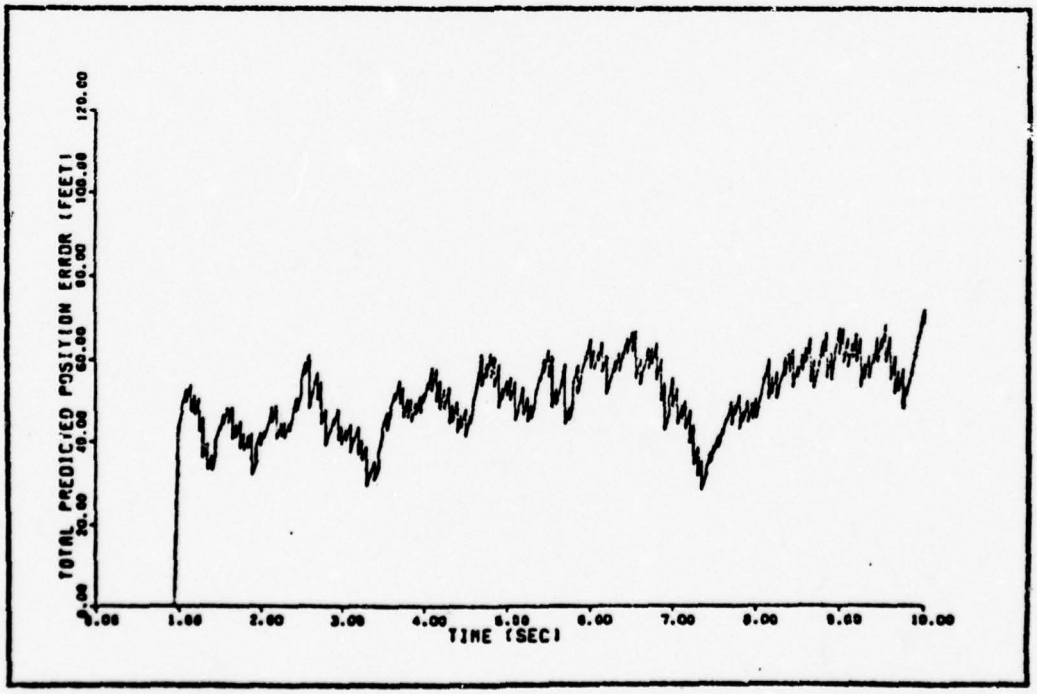


Fig. A-42. Scenario 2, Average Error in Predicted Target Position, Comparative Filter

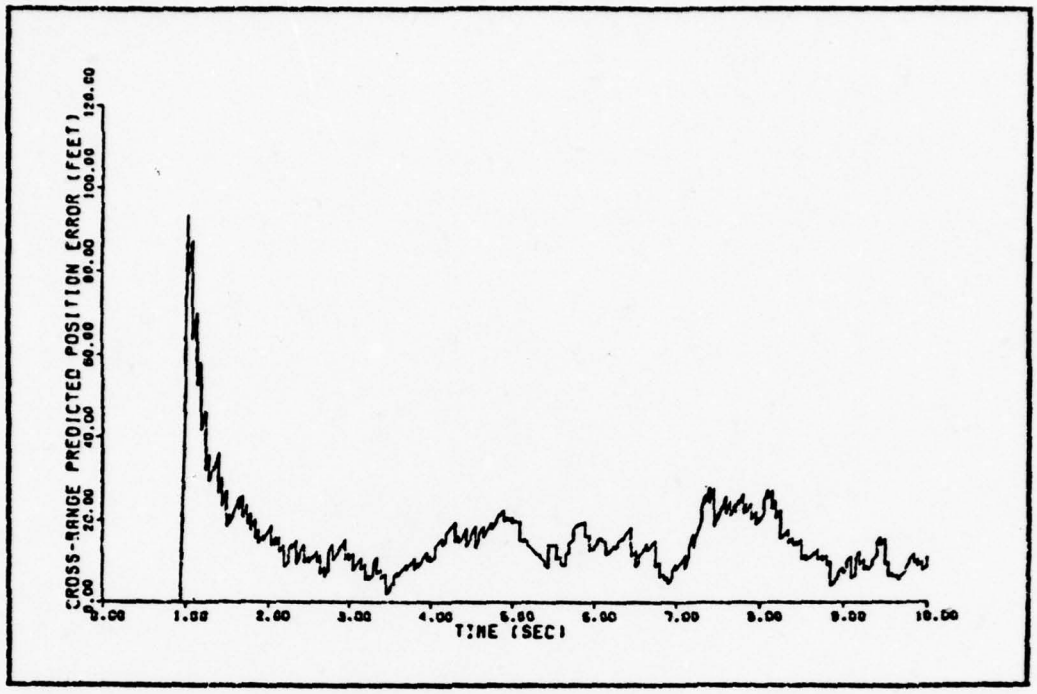


Fig. A-43. Scenario 2, Average Error in Predicted Cross-Range Target Position, Interactive Filter

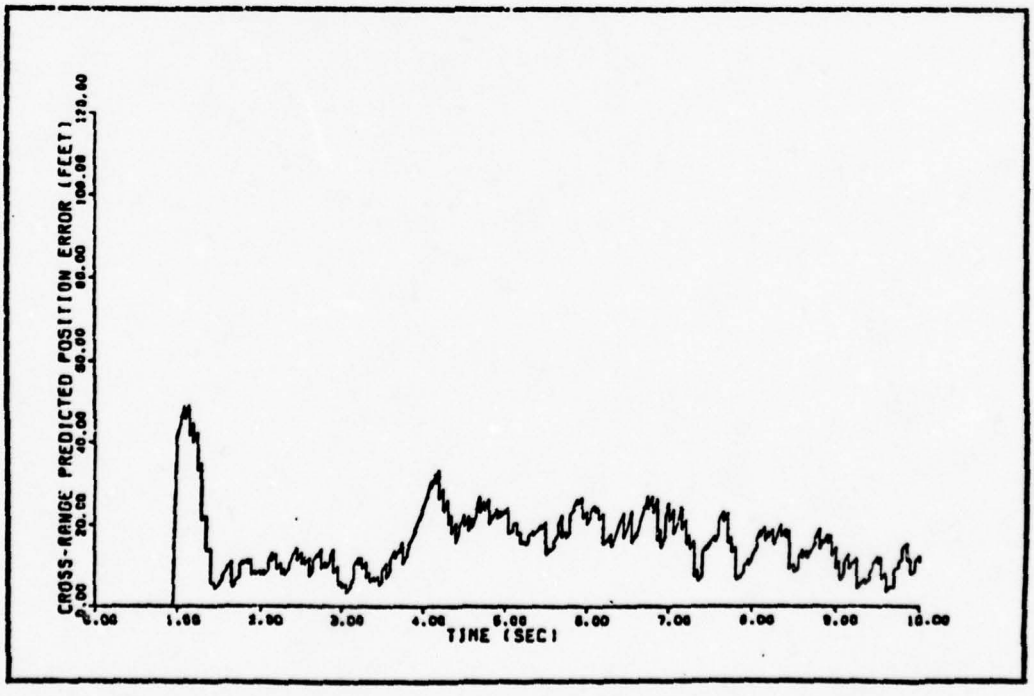


Fig. A-44. Scenario 2, Average Error in Predicted Cross-Range Target Position, Comparative Filter

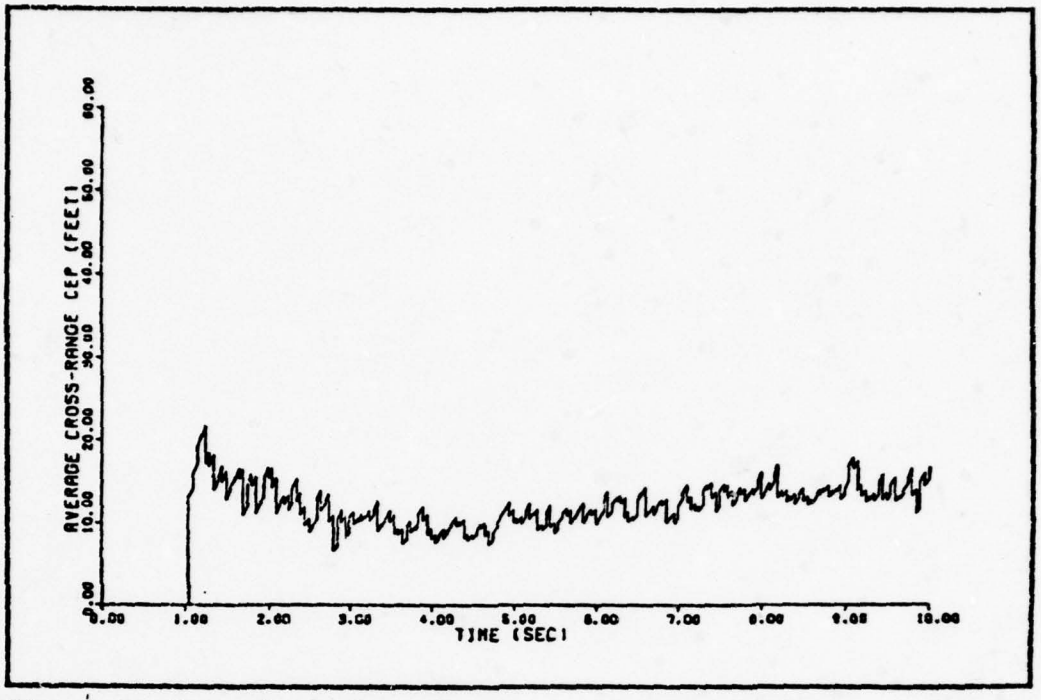


Fig. A-45. Scenario 2, Average CEP, Interactive Filter

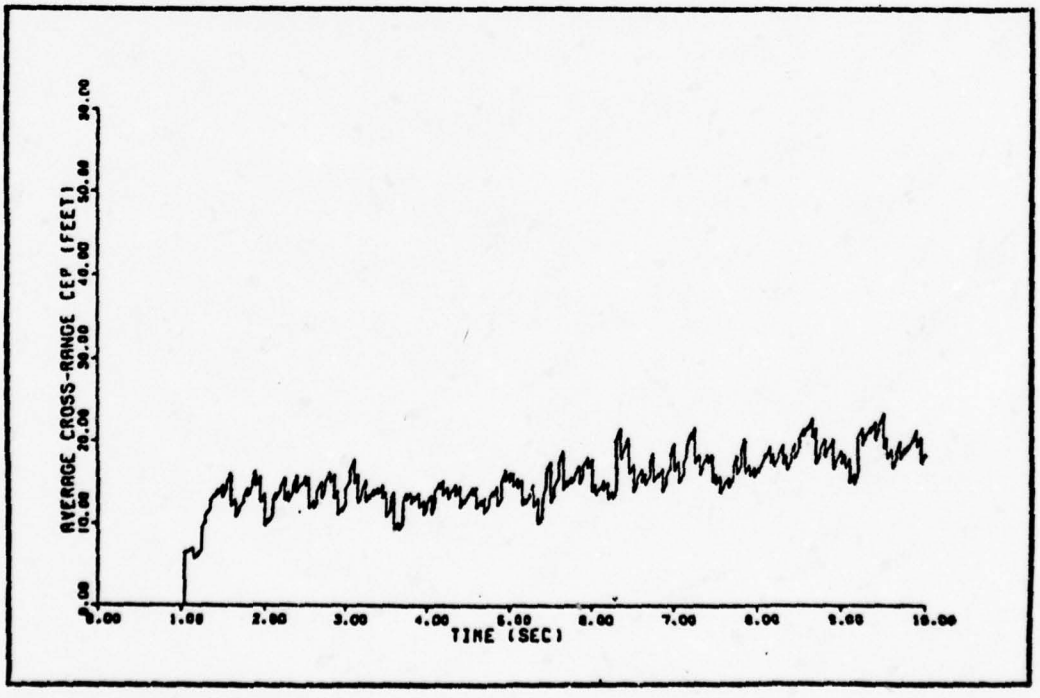


Fig. A-46. Scenario 2, Average CEP, Comparative Filter

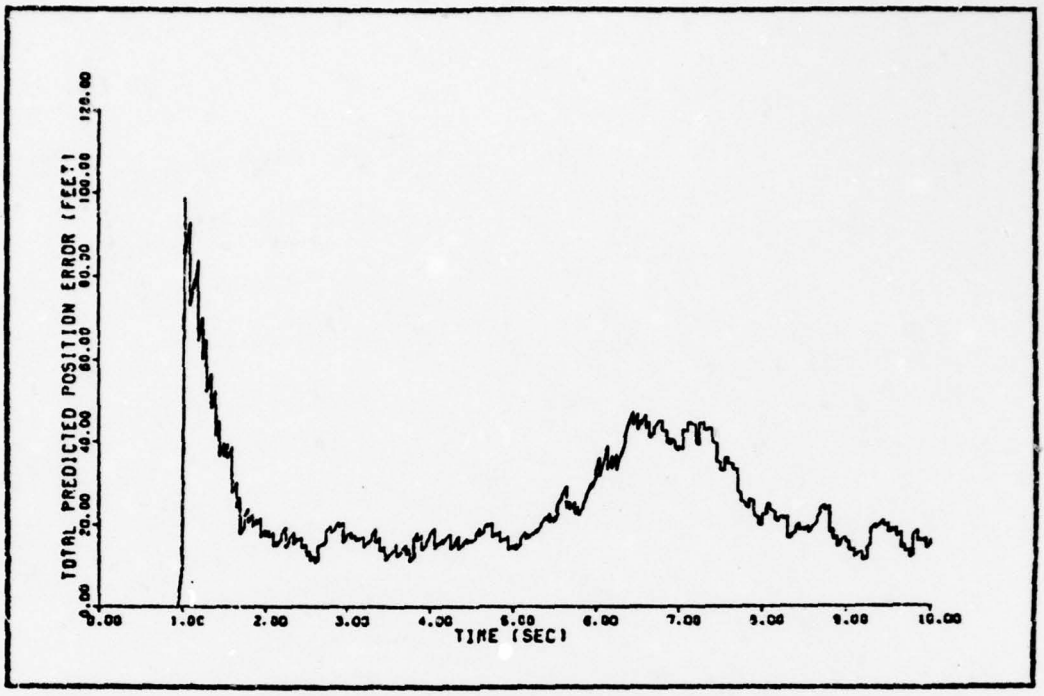


Fig. A-47. Scenario 3, Average Error in Predicted Target Position, Interactive Filter

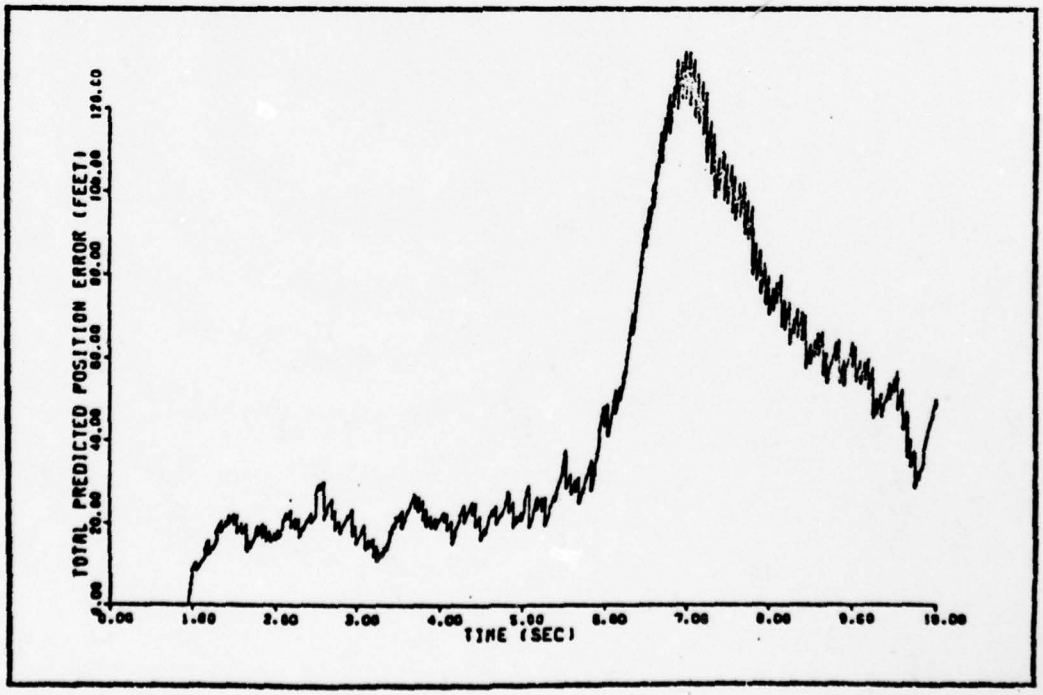


Fig. A-48. Scenario 3, Average Error in Predicted Target Position, Comparative Filter

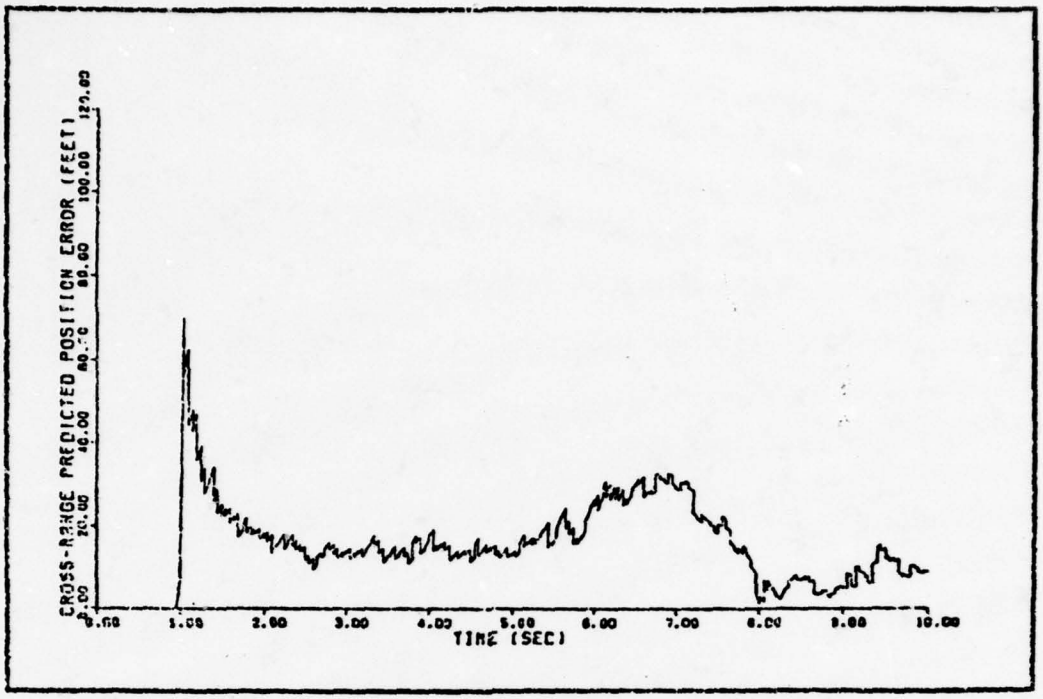


Fig. A-49. Scenario 3, Average Error in Predicted Cross-Range Target Position, Interactive Filter

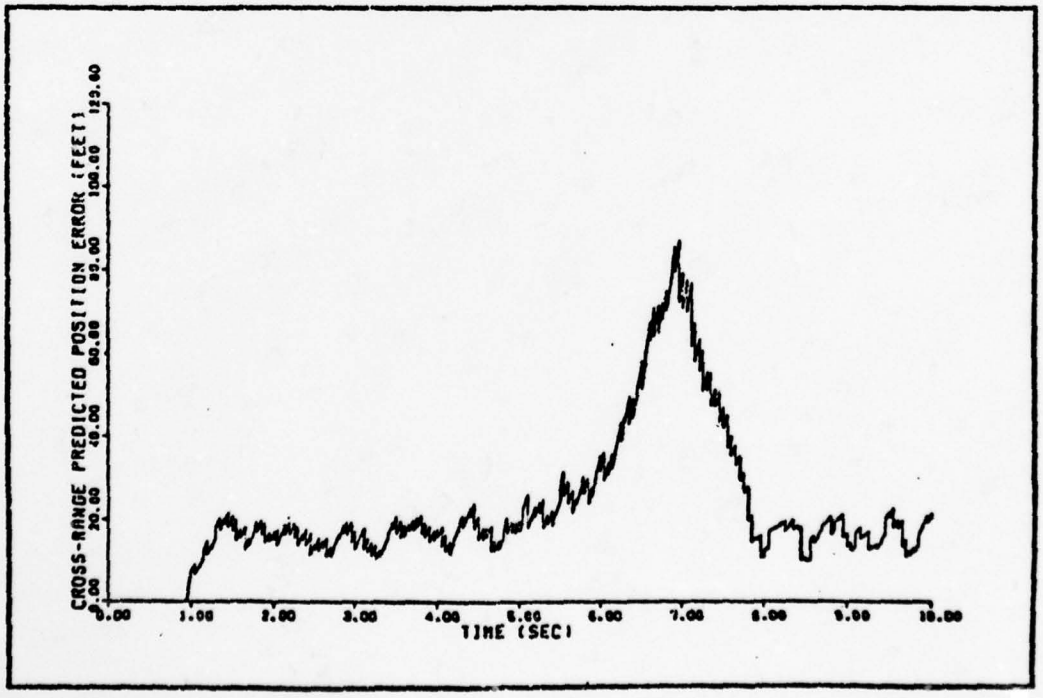


Fig. A-50. Scenario 3, Average Error in Predicted Cross-Range Target Position, Comparative Filter

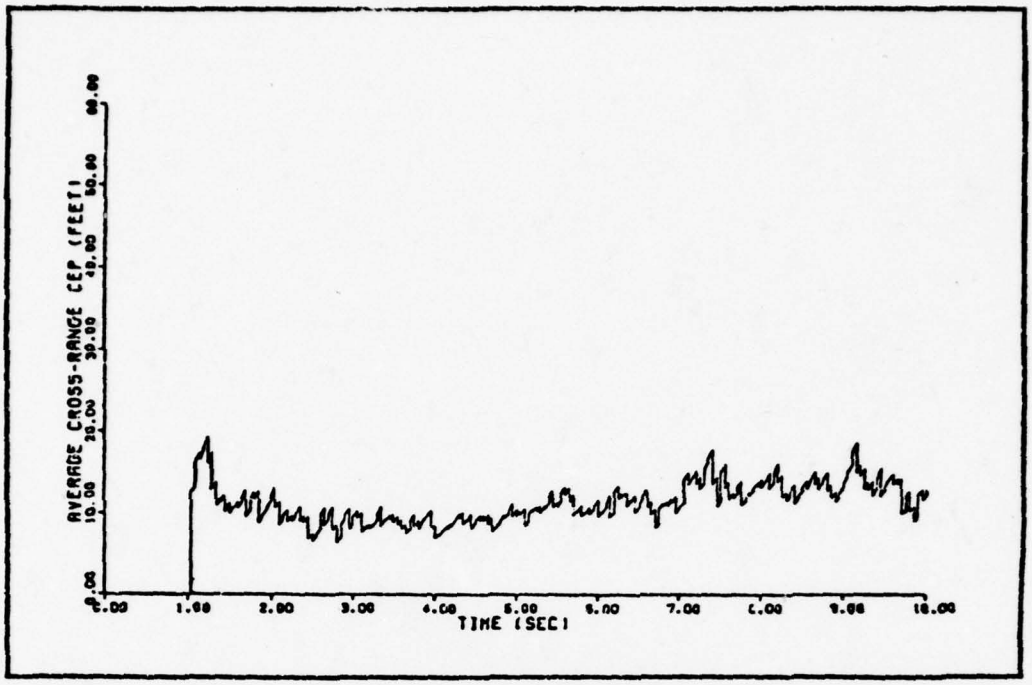


Fig. A-51. Scenario 3, Average CEP, Interactive Filter

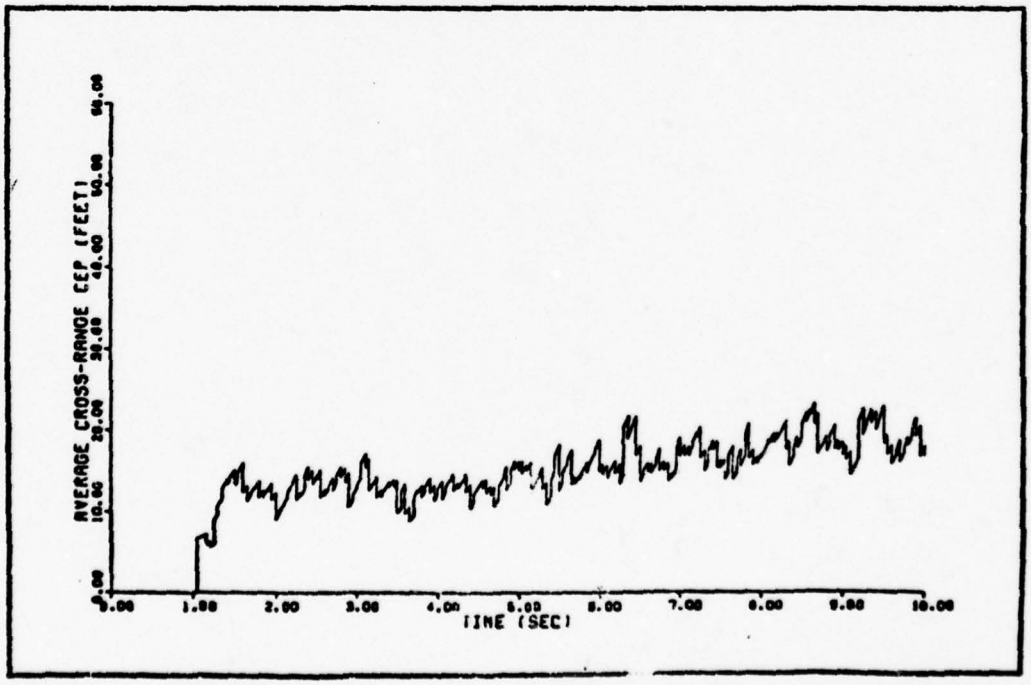


Fig. A-52. Scenario 3, Average CEP, Comparative Filter

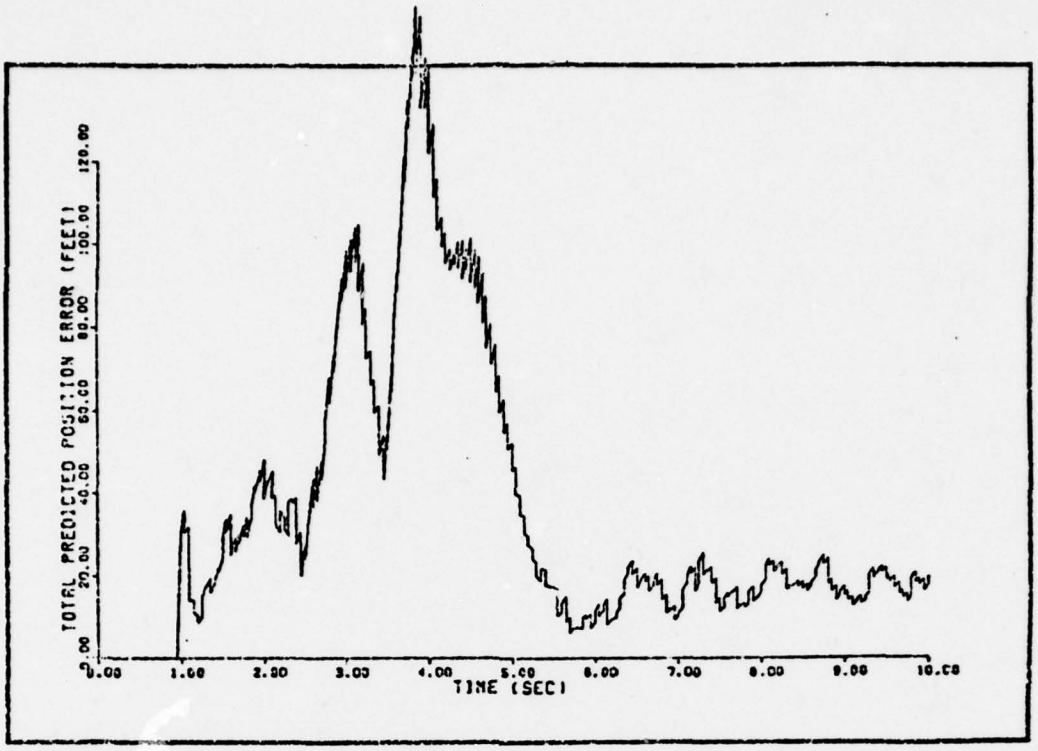


Fig. A-53. Scenario 4, Average Error in Predicted Target Position, Interactive Filter

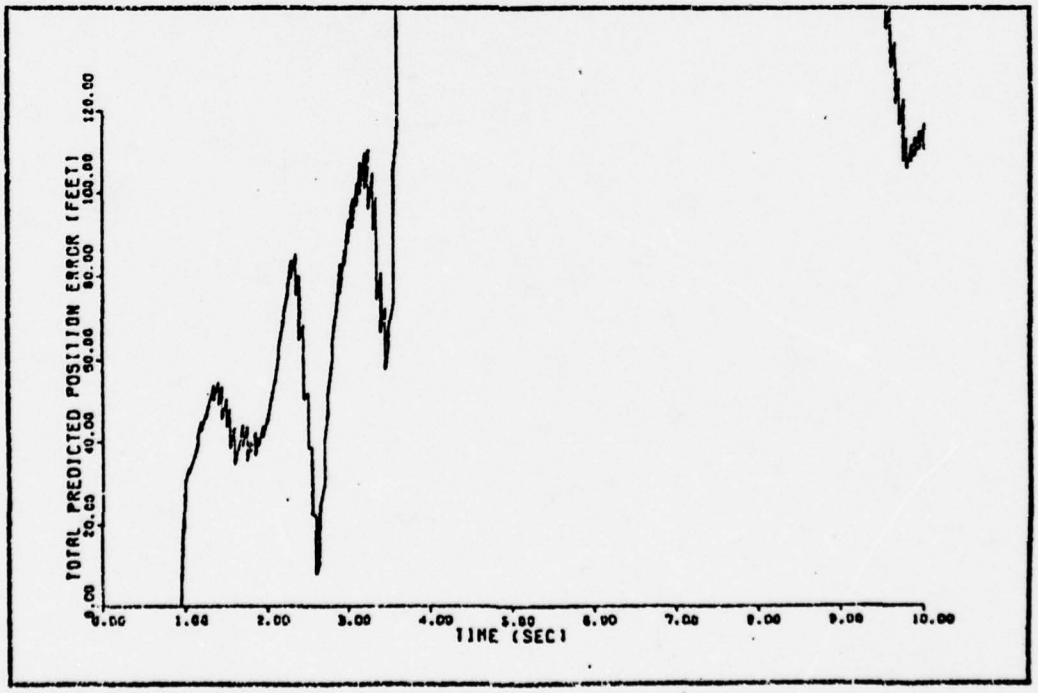


Fig. A-54. Scenario 4, Average Error in Predicted Target Position, Comparative Filter

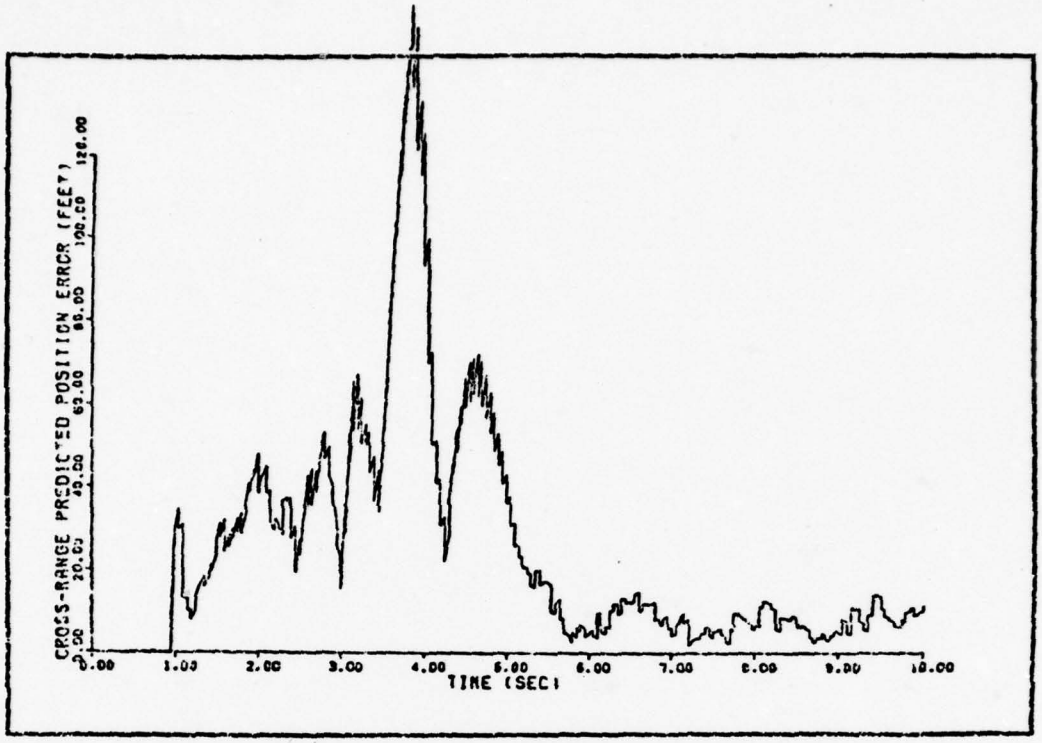


Fig. A-55. Scenario 4, Average Error in Predicted Cross-Range Target Position, Interactive Filter

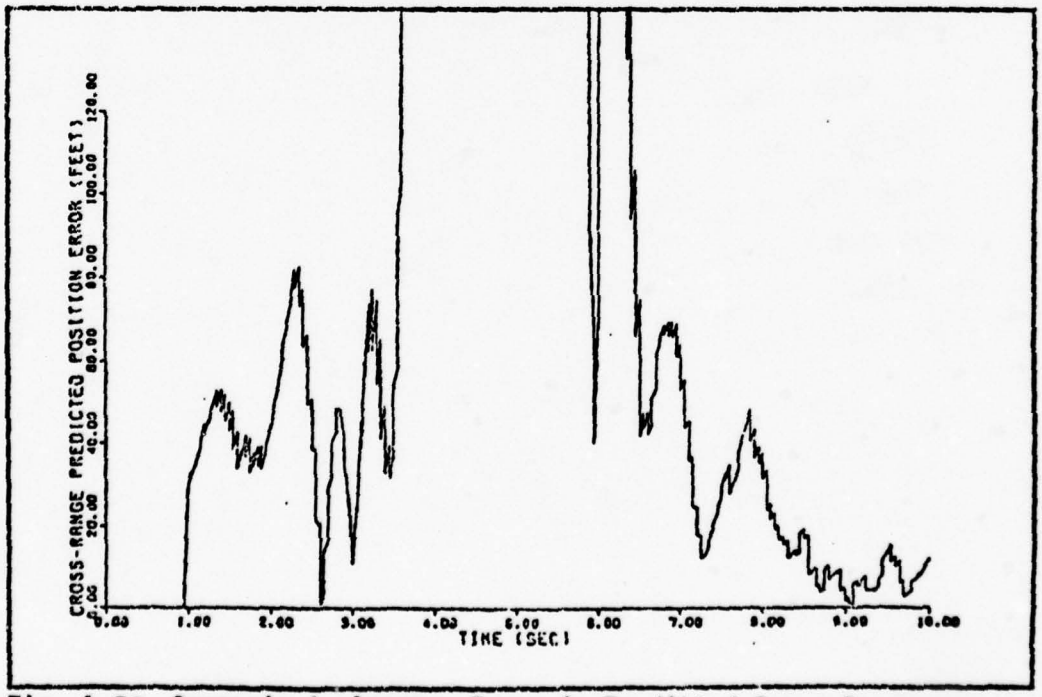


Fig. A-56. Scenario 4, Average Error in Predicted Cross-Range Target Position, Comparative Filter

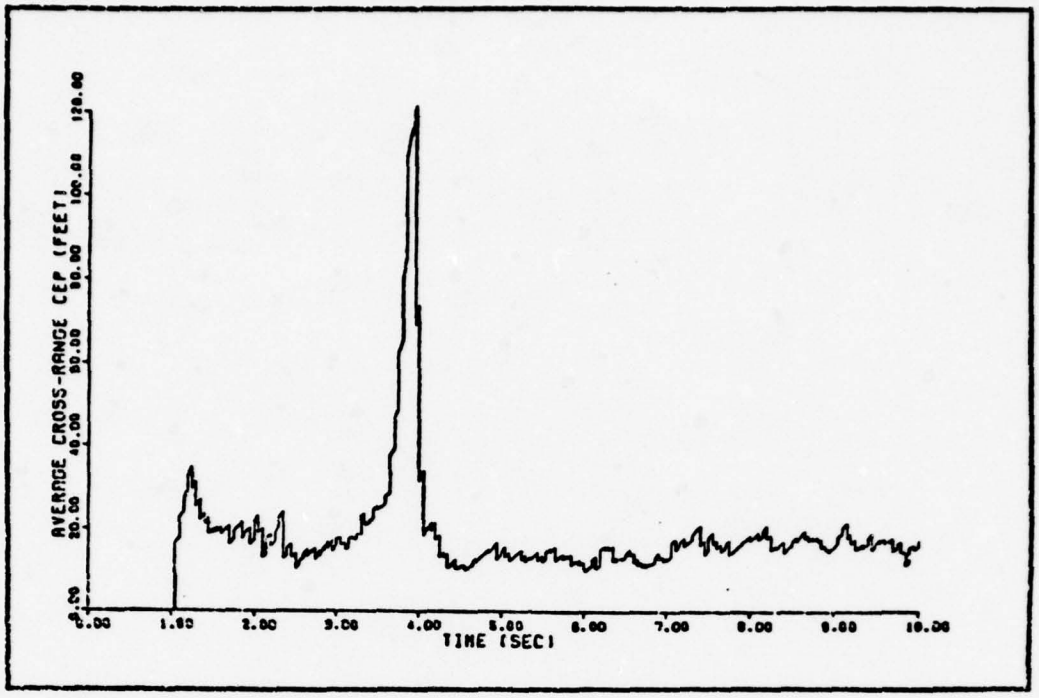


Fig. A-57. Scenario 4, Average CEP, Interactive Filter

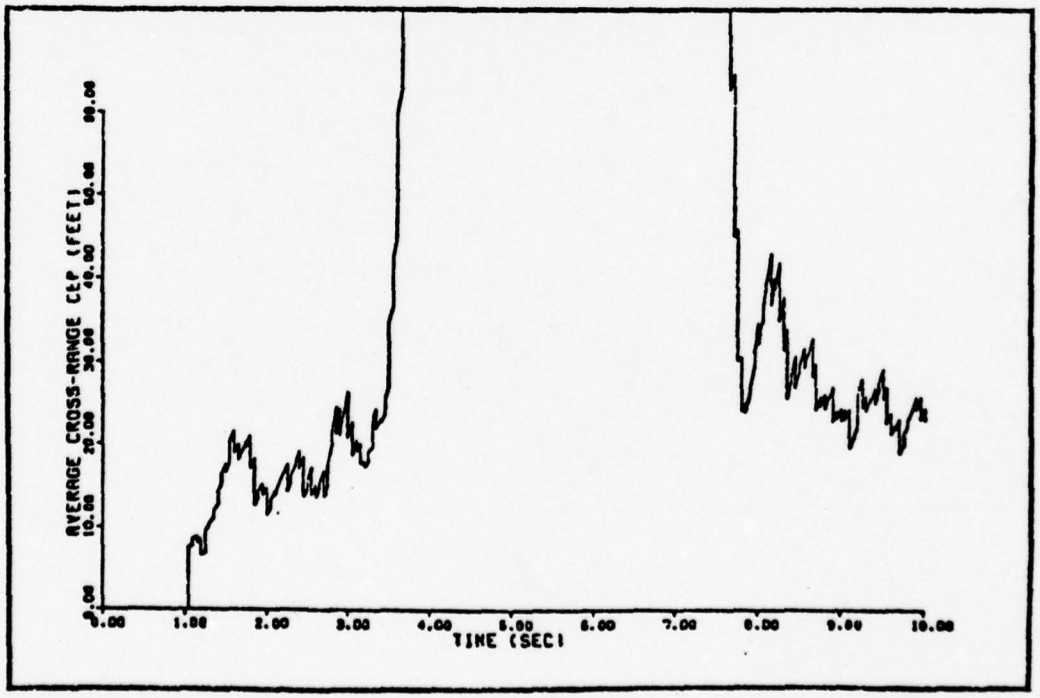


Fig. A-58. Scenario 4, Average CEP, Comparative Filter

## APPENDIX B

## Coordinate Transformations

This appendix contains details of coordinate transformations used to formulate the interactive filter:

B-1. Inertial to body (Euler angles)

B-2. Tracker base to tracker line-of-sight

B-3. Tracker line-of-sight to image plane

B-4. Image plane to target body

B-5. Tracker base to target body

### B-1. Inertial to Body (Euler Angles)

The inertial right-handed coordinate frame is oriented as:

$x^I$ - north

$y^I$ - east

$z^I$ - down

The aircraft body right-handed coordinate frame is oriented as:

$x^b$ - out nose

$y^b$ - out right wing

$z^b$ - down through aircraft underside

The following specific set of Euler angles is determined as those rotations required to re-orient the aircraft from the inertial frame orientation to the current body frame orientation. Angular rotations are made in the order yaw, pitch and roll. Zero yaw, pitch and roll correspond to the aircraft oriented toward the north, right wing toward the east and aircraft underside down.

$\psi$, yaw

Yaw is rotation about the $z^I$ axis, positive about $z^I$ in the

right-hand sense, i.e., positive clockwise looking down the $+z^I$ axis.

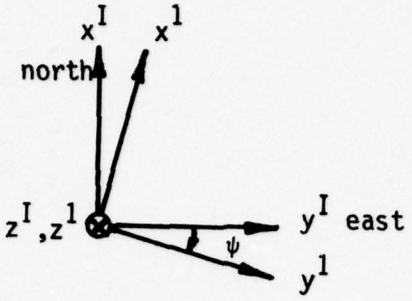


$$\begin{bmatrix} x^1 \\ y^1 \\ z^1 \end{bmatrix} = \begin{bmatrix} \cos\psi & \sin\psi & 0 \\ -\sin\psi & \cos\psi & 0 \\ 0 & 0 & 1 \end{bmatrix} \begin{bmatrix} x^I \\ y^I \\ z^I \end{bmatrix} = T_1^I \begin{bmatrix} x^I \\ y^I \\ z^I \end{bmatrix} \qquad \text{(B-1-1)}$$

where $T_1^I$ = transformation <u>from</u> frame I <u>to</u> frame 1.

<u>θ, Pitch</u>

Pitch is rotation about the newly created $y^1$ axis. Positive pitch is a clockwise (CW) rotation about the $+y^1$ axis.

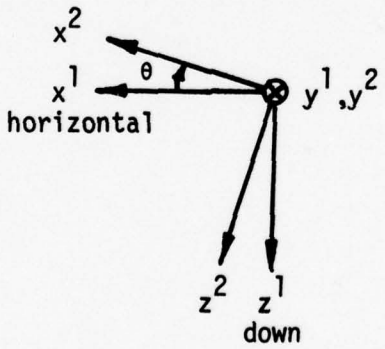


$$\begin{bmatrix} x^2 \\ y^2 \\ z^2 \end{bmatrix} = \begin{bmatrix} \cos\theta & 0 & -\sin\theta \\ 0 & 1 & 0 \\ \sin\theta & 0 & \cos\theta \end{bmatrix} \begin{bmatrix} x^1 \\ y^1 \\ z^1 \end{bmatrix} = T_2^1 \begin{bmatrix} x^1 \\ y^1 \\ z^1 \end{bmatrix} \qquad \text{(B-1-2)}$$

$\phi$, Roll

Roll is rotation about the newly created $x^2$ axis. Positive roll is a CW rotation about the $+x^2$ axis.

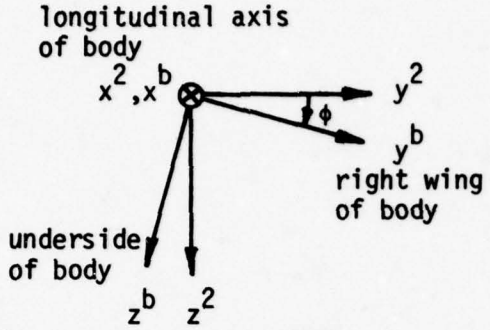


$$\begin{bmatrix} x^b \\ y^b \\ z^b \end{bmatrix} = \begin{bmatrix} 1 & 0 & 0 \\ 0 & \text{Cos}\phi & \text{Sin}\phi \\ 0 & -\text{Sin}\phi & \text{Cos}\phi \end{bmatrix} \begin{bmatrix} x^2 \\ y^2 \\ z^2 \end{bmatrix} = T_b^2 \begin{bmatrix} x^2 \\ y^2 \\ z^2 \end{bmatrix} \qquad \text{(B-1-3)}$$

Combining in the proper order, the overall transformation from inertial coordinates to body coordinates is given by:

$$\begin{bmatrix} x^b \\ y^b \\ z^b \end{bmatrix} = T_b^2 \, T_2^1 \, T_1^I \begin{bmatrix} x^I \\ y^I \\ z^I \end{bmatrix} = T_b^I \begin{bmatrix} x^I \\ y^I \\ z^I \end{bmatrix} \qquad \text{(B-1-4)}$$

where

$$T_b^I = \begin{bmatrix} C\theta C\psi & C\theta S\psi & -S\theta \\ S\phi S\theta C\psi - C\phi S\psi & S\phi S\theta S\psi + C\phi C\psi & S\phi C\theta \\ C\phi S\theta C\psi + S\phi S\psi & C\phi S\theta S\psi - S\phi C\psi & C\phi C\theta \end{bmatrix} \qquad \text{(B-1-5)}$$

and C and S denote cosine and sine respectively.

B-2. Tracker Base to Tracker Line-of-sight

The transformation between the inertially stabilized tracker base (tb) frame and the cartesian tracker line-of-sight (tl) frame is determined by the measured azimuth and elevation angles, $\eta$ and $\xi$ respectively. The two tracker frames are aligned whenever $\xi = \eta = 0$. $y^{tl}$ is always kept aligned

with the elevation pivot axis of the tracker, i.e., in the horizontal plane and perpendicular to $x^{tl}$.

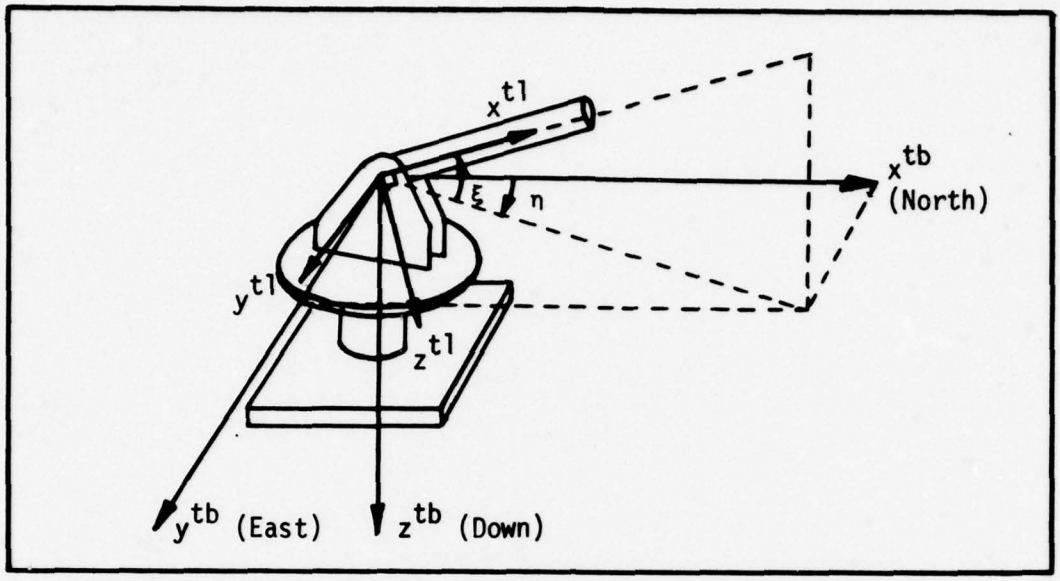


Fig. B-1. Tracker Line-of-Sight Geometry

<u>η, Azimuth</u>

Azimuth is rotation about the $z^{tb}$ axis. Positive azimuth is a CW rotation about the $+z^{tb}$ axis.

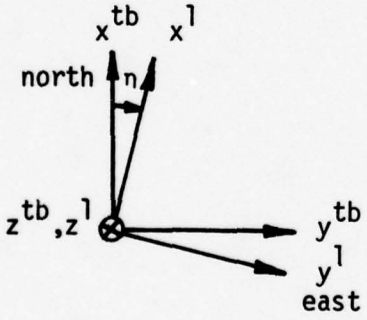


$$\begin{bmatrix} x^{l} \\ y^{l} \\ z^{l} \end{bmatrix} = \begin{bmatrix} \text{Cos}\eta & \text{Sin}\eta & 0 \\ -\text{Sin}\eta & \text{Cos}\eta & 0 \\ 0 & 0 & 1 \end{bmatrix} \begin{bmatrix} x^{tb} \\ y^{tb} \\ z^{tb} \end{bmatrix} = T_{l}^{tb} \begin{bmatrix} x^{tb} \\ y^{tb} \\ z^{tb} \end{bmatrix} \qquad \text{(B-2-1)}$$

$\xi$, Elevation

Elevation is rotation about the newly formed $y^1$ axis. Positive elevation is CW about the $+y^1$ axis.

$$\begin{bmatrix} x^{tl} \\ y^{tl} \\ z^{tl} \end{bmatrix} = \begin{bmatrix} \text{Cos}\xi & 0 & -\text{Sin}\xi \\ 0 & 1 & 0 \\ \text{Sin}\xi & 0 & \text{Cos}\xi \end{bmatrix} \begin{bmatrix} x^1 \\ y^1 \\ z^1 \end{bmatrix} = T_1^{tb} \begin{bmatrix} x^1 \\ y^1 \\ z^1 \end{bmatrix} \qquad \text{(B-2-2)}$$

The overall transformation from inertially stabilized tracker base to tracker line-of-sight is given by:

$$\begin{bmatrix} x^{tl} \\ y^{tl} \\ z^{tl} \end{bmatrix} = T_{tl}^{1} \, T_{1}^{tb} \begin{bmatrix} x^{tb} \\ y^{tb} \\ z^{tb} \end{bmatrix} = T_{tl}^{tb} \begin{bmatrix} x^{tb} \\ y^{tb} \\ z^{tb} \end{bmatrix} \qquad \text{(B-2-3)}$$

where

$$T_{tl}^{tb} = \begin{bmatrix} C\xi C\eta & C\xi S\eta & -S\xi \\ -S\eta & C\eta & 0 \\ S\xi C\eta & S\xi S\eta & C\xi \end{bmatrix} \qquad \text{(B-2-4)}$$

B-3. Tracker Line-of-sight to Image Plane

The image plane geometry is shown in Fig. B-2, where superscript i denotes image plane.

$$\begin{aligned} x^i &= y^{tl} \\ y^i &= -z^{tl} \\ z^i &= -x^{tl} \end{aligned} \qquad \text{(B-3-1)}$$

$$\begin{bmatrix} x^i \\ y^i \\ z^i \end{bmatrix} = T_i^{tl} \begin{bmatrix} x^{tl} \\ y^{tl} \\ z^{tl} \end{bmatrix} \qquad \text{(B-3-2)}$$

where

$$T_i^{tl} = \begin{bmatrix} 0 & 1 & 0 \\ 0 & 0 & -1 \\ -1 & 0 & 0 \end{bmatrix} \qquad \text{(B-3-3)}$$

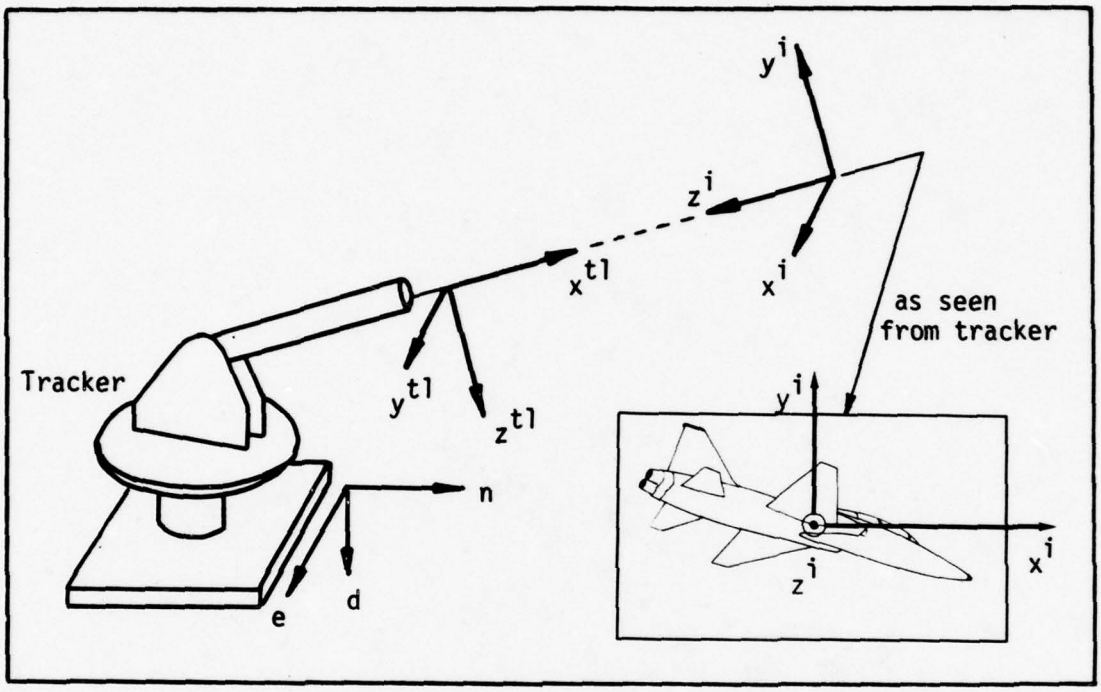


Fig. B-2. Image Plane Geometry

B-4. Image Plane to Target Body

The target imagery is provided to the pattern recognition subsystem for aspect determination. The specification of aspect will be expressed as Euler angles with respect to the image plane. The transformation between the image plane (i) and the target body (t) is the same as developed in B-1, except that the angles will be called image yaw, image pitch and image roll. Zero image yaw, image pitch and image roll will occur when the target aircraft frame is aligned with the image frame, i.e., the target nose is to the right, the right wing is up and aircraft underside is the image view. Use the same convention for positive

angular rotations and make the following definitions:

$\psi_i$, image yaw - rotation about $+z^i$

$\theta_i$, image pitch - rotation about the newly formed lateral axis, positive out right wing, using right-hand rule.

$\phi_i$, image roll - rotation about the newly formed longitudinal axis, positive out the nose.

The transformation between image plane and target body is given by:

$$\begin{bmatrix} x^t \\ y^t \\ z^t \end{bmatrix} = T_t^i \begin{bmatrix} x^i \\ y^i \\ z^i \end{bmatrix} \qquad \text{(B-4-1)}$$

where

$$T_t^i = \begin{bmatrix} C\theta_i C\psi_i & C\theta_i S\psi_i & -S\theta_i \\ S\phi_i S\theta_i C\psi_i - C\phi_i S\psi_i & S\phi_i S\theta_i S\psi_i + C\phi_i C\psi_i & S\phi_i C\theta_i \\ C\phi_i S\theta_i C\psi_i + S\phi_i S\psi_i & C\phi_i S\theta_i S\psi_i - S\phi_i C\psi_i & C\phi_i C\theta_i \end{bmatrix} \qquad \text{(B-4-2)}$$

B-5. Tracker Base to Target Body

The transformations developed in B-2, B-3 and B-4 can be combined to form the overall transformation from the inertially stabilized tracker base to the target body. Once this transformation is obtained, the inertially referenced Euler angles can be found directly by comparing the terms with those of the transformation obtained in B-1.

$$T_t^{tb} = T_t^i \, T_i^{tl} \, T_{tl}^{tb} \qquad \text{(B-5-1)}$$

where $T_{tl}^{tb}$, $T_i^{tl}$, and $T_t^i$ are developed in B-2, B-3 and B-4 respectively.

The transformation from inertial to body is available from B-1. Since the tracker base is assumed to be inertially stabilized and oriented, and the body, in this case, is the target, the transformations can be equated.

$$T_b^I = T_t^{tb} \triangleq [t_{ij}] \tag{B-5-2}$$

The Euler angles can be obtained from this matrix equation as described below. The Euler angles are restricted as follows to achieve unique angles.

$$\begin{aligned} -\pi &< \psi \leq \pi \\ -\pi/2 &< \theta \leq \pi/2 \\ -\pi &< \phi \leq \pi \end{aligned} \tag{B-5-3}$$

Pitch may be obtained by equating the 1-3 elements.

$$-\mathrm{Sin}\theta = t_{13} \tag{B-5-4}$$

$$\theta = -\arcsin t_{13} \tag{B-5-5}$$

Yaw can be found by taking the ratio of the 1-2 and 1-1 elements.

$$\frac{\mathrm{Cos}\theta\mathrm{Sin}\psi}{\mathrm{Cos}\theta\mathrm{Cos}\psi} = \frac{t_{12}}{t_{11}} \tag{B-5-6}$$

$$\psi = \arctan\left(\frac{t_{12}}{t_{11}}\right) \tag{B-5-7}$$

Finally, roll is obtained by taking the ratio of the 2-3 and 3-3 elements.

$$\frac{\mathrm{Sin}\phi\mathrm{Cos}\theta}{\mathrm{Cos}\phi\mathrm{Cos}\theta} = \frac{t_{23}}{t_{33}} \tag{B-5-8}$$

$$\phi = \arctan\left(\frac{t_{23}}{t_{33}}\right) \tag{B-5-9}$$

If the arctangent algorithm used to obtain $\psi$ and $\phi$ cannot distinguish a $(\frac{-}{+})$ ratio from a $(\frac{+}{-})$ ratio, the following scheme may instead be used to find $\psi$ and $\phi$. Since $-\pi/2<\theta\leq\pi/2$, sign (Cos$\theta$) is +. Therefore,

$$\mathrm{sign}(\mathrm{Sin}\,\psi) = \mathrm{sign}\,(t_{12}) \tag{B-5-10}$$

$$\text{sign}(\text{Cos}\ \psi) = \text{sign}\ (t_{11}) \tag{B-5-11}$$

$$\text{sign}(\text{Sin}\ \phi) = \text{sign}\ (t_{23}) \tag{B-5-12}$$

$$\text{sign}(\text{Cos}\ \phi) = \text{sign}\ (t_{33}) \tag{B-5-13}$$

Assuming sign [Sin(0.0)] and sign [Cos(0.0)] is +, the unique values of $\psi$ and $\phi$ satisfy the following table where $\delta$ is either $\psi$ or $\phi$.

Table B-I. Angles and Corresponding Trigonometric Functions

| | sign(Sin$\delta$)+ | sign(Sin$\delta$)- |
|---|---|---|
| sign(Cos$\delta$)+ | $0 \leq \delta \leq \pi/2$ | $-\pi/2 \leq \delta < 0$ |
| sign(Cos$\delta$)- | $\pi/2 < \delta \leq \pi$ | $-\pi < \delta < -\frac{\pi}{2}$ |

## APPENDIX C

## Statistical Characteristics of Modeled Normal Load Acceleration Magnitude

This appendix derives the probability density function (pdf), mean, variance, mode and autocorrelation function for the magnitude of normal load acceleration based upon the non-linear relation

$$\underline{a}_N = \alpha + \beta e^{\gamma \underline{\varepsilon}} \tag{C-1}$$

where $\alpha$, $\beta$ and $\gamma$ are target dependent pdf-shaping parameters, and $\underline{\varepsilon}$ is a zero-mean, unit-variance, Gaussian random variable. Later consideration is expanded to let $\underline{\varepsilon}$ be a first-order Gauss-Markov process. Throughout this appendix, the letter "$\underline{a}$" is used for "$\underline{a}_N$", $\gamma$ is a positive parameter, and the trivial case of $\beta=0$ is not considered. The underbar ( _ ) represents a random variable or random process.

Probability Density Function (First-order pdf)

The cumulative distribution function (CDF) for $\underline{a}$ is given by

$$P_{\underline{a}}(a) = P[\underline{a} \leq a] = P[\alpha+\beta e^{\gamma \underline{\varepsilon}} \leq a] = P[\beta e^{\gamma \underline{\varepsilon}} \leq a-\alpha] \tag{C-2}$$

$\beta>0$

$$P_{\underline{a}}(a) = P[e^{\gamma \underline{\varepsilon}} \leq \frac{a-\alpha}{\beta}] = P[\underline{\varepsilon} \leq \frac{1}{\gamma} \ln(\frac{a-\alpha}{\beta})]$$

$$= \begin{cases} \frac{1}{\sqrt{2\pi}} \int_{-\infty}^{\frac{1}{\gamma}\ln(\frac{a-\alpha}{\beta})} \exp(-\frac{\lambda^2}{2}) d\lambda, & a>\alpha \\ 0, & a \leq \alpha \end{cases} \tag{C-3}$$

Differentiating the CDF, the pdf is given by

$$p_{\underline{a}}(a) = \begin{cases} \frac{1}{\sqrt{2\pi}\,\gamma(a-\alpha)} \exp\left\{-\tfrac{1}{2}\left[\frac{1}{\gamma}\ln\left(\frac{a-\alpha}{\beta}\right)\right]^2\right\}, & a>\alpha \\ 0, & a\leq\alpha \end{cases} \tag{C-4}$$

$\underline{\beta<0}$

$$p_{\underline{a}}(a) = P\left[e^{\gamma\underline{\varepsilon}} \geq \frac{a-\alpha}{\beta}\right] = P\left[\underline{\varepsilon} \geq \frac{1}{\gamma}\ln\left(\frac{a-\alpha}{\beta}\right)\right]$$

$$= 1 - P\left[\underline{\varepsilon} \leq \frac{1}{\gamma}\ln\left(\frac{a-\alpha}{\beta}\right)\right]$$

$$= \begin{cases} 1-\int_{-\infty}^{\frac{1}{\gamma}\ln\left(\frac{a-\alpha}{\beta}\right)} \exp\left(\frac{-\lambda^2}{2}\right)d\lambda, & a<\alpha \\ 0, & \alpha\leq\alpha \end{cases} \tag{C-5}$$

Again, differentiating the CDF, the pdf is given by

$$p_{\underline{a}}(a) = \begin{cases} \frac{-1}{\sqrt{2\pi}\gamma(a-\alpha)} \exp\left\{-\tfrac{1}{2}\left[\frac{1}{\gamma}\ln\left(\frac{a-\alpha}{\beta}\right)\right]^2\right\}, & a<\alpha \\ 0, & a\geq\alpha \end{cases} \tag{C-6}$$

Combining these two cases for $\beta$, the final result follows:

$$p_{\underline{a}}(\alpha) = \begin{cases} \frac{1}{\sqrt{2\pi}\gamma\,|a-\alpha|} \exp\left\{-\tfrac{1}{2}\left[\frac{1}{\gamma}\ln\left(\frac{a-\alpha}{\beta}\right)\right]^2\right\}, & \frac{a-\alpha}{\beta}>0 \\ 0, & \frac{a-\alpha}{\beta}\leq 0 \end{cases} \tag{C-7}$$

Mean

The mean of $\underline{a} = \alpha + \beta e^{\gamma\underline{\varepsilon}}$ for the general case of $\underline{\varepsilon}$ normal with mean $m_\varepsilon$ and variance $\sigma_\varepsilon^2$, i.e., $\underline{\varepsilon} \sim N(m_\varepsilon, \sigma_\varepsilon^2)$, is given by

$$E[\underline{a}] = \alpha + \beta E[e^{\gamma\underline{\varepsilon}}] \tag{C-8}$$

Using the moment generating function

$$M_{\underline{y}}(u) = E[e^{u\underline{y}}] \tag{C-9}$$

and if $\underline{y} \sim N(\mu,\sigma^2)$, it is known that

$$M_{\underline{y}}(u) = e^{\mu u + \frac{u^2\sigma^2}{2}} \tag{C-10}$$

Thus

$$E[\underline{a}] = \alpha + \beta M_{\underline{\varepsilon}}(\gamma) = \alpha + \beta \exp(m_\varepsilon\gamma + \frac{\gamma^2\sigma_\varepsilon{}^2}{2}) \tag{C-11}$$

For the case under consideration, namely, $\underline{\varepsilon} \sim N(0, 1)$,

$$E[\underline{a}] = \alpha + \beta e^{\frac{\gamma^2}{2}} \tag{C-12}$$

Variance

The variance of $\underline{a} = \alpha + \beta e^{\gamma\underline{\varepsilon}}$ where $\underline{\varepsilon} \sim N(m_\varepsilon,\sigma_\varepsilon{}^2)$ is given by

$$\text{var}(\underline{a}) = E\{[\underline{a} - E(\underline{a})]^2\} = E(\underline{a}^2) - E^2(\underline{a}) \tag{C-13}$$

$$E(\underline{a}^2) = \alpha^2 + 2\alpha\beta E[e^{\gamma\underline{\varepsilon}}] + \beta^2 E[e^{2\gamma\underline{\varepsilon}}]$$

$$= \alpha^2 + 2\alpha\beta e^{m_\varepsilon\gamma + \frac{\sigma_\varepsilon{}^2\gamma^2}{2}} + \beta^2 e^{2m_\varepsilon\gamma + 2\sigma_\varepsilon{}^2\gamma^2} \tag{C-14}$$

From the previous section,

$$E^2(\underline{a}) = \alpha^2 + 2\alpha\beta e^{m_\varepsilon\gamma + \frac{\sigma_\varepsilon{}^2\gamma^2}{2}} + \beta^2 e^{2(m_\varepsilon\gamma + \frac{\sigma_\varepsilon{}^2\gamma^2}{2})} \tag{C-15}$$

Hence,

$$\text{var}(\underline{a}) = \beta^2(e^{2\sigma_\varepsilon{}^2\gamma^2} - e^{\sigma_\varepsilon{}^2\gamma^2})e^{2m_\varepsilon\gamma} \tag{C-16}$$

which, for $\underline{\varepsilon} \sim N(0, 1)$, becomes

$$\text{var}(\underline{a}) = \beta^2(e^{2\gamma^2} - e^{\gamma^2}) \tag{C-17}$$

Mode

The mode (or peak) value for $\underline{a}$ is found by determining the value of $\underline{a}$ at which the pdf has a zero slope. Differentiating the expression for the pdf of $\underline{a}$ and setting to zero yields the equation

$$\frac{1}{\gamma^2} \ln\left(\frac{a-\alpha}{\beta}\right) + 1 = 0 \tag{C-18}$$

The mode value for $\underline{a}$ is the solution to this equation and is given by

$$a_M = \alpha + \beta e^{-\gamma^2} \tag{C-19}$$

The peak value of the pdf is evaluated at $a_M$ and is given by

$$p_{\underline{a}}(a_M) = \frac{e^{\frac{\gamma^2}{2}}}{\sqrt{2\pi}\,\gamma|\beta|} \tag{C-20}$$

Autocorrelation Function

The autocorrelation function for the random process $\underline{a} = \alpha + \beta e^{\gamma\underline{\varepsilon}}$ depends upon the autocorrelation function for the random process $\underline{\varepsilon}$. The dynamics of $\underline{\varepsilon}$ are governed by the equation

$$\dot{\underline{\varepsilon}} = -\frac{1}{\tau_\varepsilon}\underline{\varepsilon} + \underline{W}_\varepsilon \tag{C-21}$$

where $\underline{W}_\varepsilon$ is a zero-mean, white, Gaussian noise process such that

$$E[\underline{W}_\varepsilon(t+\tau)\underline{W}_\varepsilon(t)] = q(t)\delta(\tau) \tag{C-22}$$

If $E[\underline{\varepsilon}^2(t_o)]$ is assumed known to be $\sigma^2_{\varepsilon_{t_o}}$ for some initial time $t_o$, then for some later time t,

$$\sigma^2_{\varepsilon_t} = \Phi^2(t,t_o)\sigma^2_{\varepsilon_{t_o}} + \int_{t_o}^{t} \Phi^2(t,\tau)q(\tau)d\tau \tag{C-23}$$

where

$$\Phi(t,t_o) = \Phi(t-t_o) = e^{-(t-t_o)/\tau_\varepsilon} \tag{C-24}$$

Assuming that q is not time-varying, this equation can be integrated to yield

$$\sigma^2_{\varepsilon_t} = e^{-(t-t_o)/\tau_\varepsilon}[\sigma^2_{\varepsilon_{t_o}} - \frac{q\tau_\varepsilon}{2}] + \frac{q\tau_\varepsilon}{2} \tag{C-25}$$

If $\sigma^2_{\varepsilon_{t_o}}$ is chosen to be $\frac{q\tau_\varepsilon}{2}$, then the variance of $\underline{\varepsilon}$ is not time-varying.

If, in addition, q is set to $2/\tau_\varepsilon$, $\underline{\varepsilon}(t) \sim N(0, 1)$ $\forall t$. Under these conditions, the autocorrelation of $\underline{\varepsilon}$, where $\underline{\varepsilon} \sim N(0, 1)$, becomes

$$R_\varepsilon(t_2,t_1) = E[\underline{\varepsilon}_{t_2}\underline{\varepsilon}_{t_1}] = \Phi(t_2,t_1)E[\underline{\varepsilon}^2_{t_1}] = e^{-(t_2-t_1)/\tau_\varepsilon}\,\sigma^2_{\varepsilon_{t_1}}$$

$$= e^{-(t_2-t_1)/\tau_\varepsilon} \tag{C-26}$$

Since $\sigma_{\varepsilon_t}^2$ is not time-varying under these conditions,

$$R_\varepsilon(t_2,t_1) = R_\varepsilon(t_2-t_1) = R_\varepsilon(\tau) = R_\varepsilon(-\tau) \tag{C-27}$$

where $\tau = t_2-t_1$

so $$R_\varepsilon(\tau) = e^{-|\tau|/\tau_\varepsilon} \tag{C-28}$$

Now, under the assumption that $\underline{\varepsilon} \sim N(0, 1)$, the autocorrelation for $\underline{a}$ is determined:

$$R_a(t_2,t_1) = E[\underline{a}_{t_2}\, \underline{a}_{t_1}]$$

$$= E\{[\alpha+\beta e^{\gamma \underline{\varepsilon}_{t_2}}][\alpha+\beta e^{\gamma \underline{\varepsilon}_{t_1}}]\}$$

$$= \alpha^2+2\alpha\beta e^{\gamma^2/2} + \beta^2 E[e^{\gamma(\underline{\varepsilon}_{t_2}+\underline{\varepsilon}_{t_1})}] \tag{C-29}$$

Define

$$\underline{Z}(t_2,t_1) \triangleq \underline{\varepsilon}_{t_2} + \underline{\varepsilon}_{t_1} \tag{C-30}$$

Now, $\underline{\varepsilon}_{t_2}$ and $\underline{\varepsilon}_{t_1}$ are each zero-mean, normal with unit variance.

$\underline{Z}(t_2,t_1)$ is known to be normal since $\underline{\varepsilon}_{t_2}$ and $\underline{\varepsilon}_{t_1}$ are jointly normal.

Hence, the mean and variance of $\underline{Z}(t_2,t_1)$ completely define its statistics.

$$m_Z = E[\underline{\varepsilon}_{t_2} + \underline{\varepsilon}_{t_1}] = 0 \tag{C-31}$$

$$\text{var}(\underline{Z}) = E\{[\underline{Z}(t_2,t_1) - \cancel{m_Z}^{0}]^2\}$$

$$= E[\underline{\varepsilon}_{t_2}^2 + 2\underline{\varepsilon}_{t_2}\underline{\varepsilon}_{t_1} + \underline{\varepsilon}_{t_1}^2] \qquad \text{(C-32)}$$

$$= 2(1+e^{-|\tau|/\tau_\varepsilon})$$

where $\tau = t_2 - t_1$

Note that for $t_2 = t_1$ (perfect correlation, since $\underline{\varepsilon}_{t_2}$ and $\underline{\varepsilon}_{t_1}$ are the same), $\text{var}(\underline{Z}) = 4$ since $\underline{Z} = 2\underline{\varepsilon}$. On the other hand, if $t_2 - t_1$ is very large, then $\text{var}(\underline{Z}) \approx \sigma^2_{\underline{\varepsilon}_{t_2}} + \sigma^2_{\underline{\varepsilon}_{t_1}} = 2$. This is also reasonable since little correlation exists between $\underline{\varepsilon}_{t_2}$ and $\underline{\varepsilon}_{t_1}$ for $t_2 - t_1$ large.

Since $\underline{Z}$ depends only on time difference $\tau$ and not on times $t_2$ and $t_1$, define

$$\underline{Z}(\tau) = \underline{Z}(t_2,t_1) \qquad \text{(C-33)}$$

where $\tau = t_2 - t_1$

Now,

$$E\{e^{\gamma[\underline{\varepsilon}_{t_2} + \underline{\varepsilon}_{t_1}]}\} = E[e^{\gamma\underline{Z}(\tau)}]$$

$$= e^{\gamma m_Z(\tau) + \sigma_Z^2(\tau)\gamma^2/2} \qquad \text{(C-34)}$$

$$= e^{\gamma^2(1+e^{-|\tau|/\tau_\varepsilon})}$$

Eq (C-29) now becomes

$$R_a(\tau) = \alpha^2 + 2\alpha\beta e^{\frac{\gamma^2}{2}} + \beta^2 e^{\gamma^2}(1+e^{-|\tau|/\tau_\varepsilon}) \tag{C-35}$$

noting that $R_a$ depends only on $\tau$, not on $t_2$ and $t_1$. $R_a(\tau)$ can be written in the form

$$R_a(\tau) = C_1 + C_2 \exp\left[ C_3 \exp\left(-\frac{|\tau|}{\tau_\varepsilon}\right)\right] \tag{C-36}$$

where

$$C_1 = \alpha^2 + 2\alpha\beta e^{\frac{\gamma^2}{2}} \tag{C-37}$$

$$C_2 = \beta^2 e^{\gamma^2} \tag{C-38}$$

$$C_3 = \gamma^2 \tag{C-39}$$

Note that for small values of $C_3$ (less than approximately 0.25),

$$\exp\left[C_3 \exp\left(-\frac{|\tau|}{\tau_\varepsilon}\right)\right] \approx 1 + C_3 \exp\left(-\frac{|\tau|}{\tau_\varepsilon}\right) \tag{C-40}$$

Hence, for this condition,

$$R_a(\tau) \approx C_1 + C_2(1+C_3 e^{-|\tau|/\tau_\varepsilon}) \tag{C-41}$$

$$R_a(\tau) \approx C_4 + C_5 e^{-|\tau|/\tau_\varepsilon} \tag{C-42}$$

where

$$C_4 = C_1 + C_2 = \alpha^2 + 2\alpha\beta e^{\gamma^2/2} + \beta^2 e^{\gamma^2} \tag{C-43}$$

$$C_5 = C_2 C_3 = \beta^2 \gamma^2 e^{\gamma^2} \tag{C-44}$$

The following example illustrates the similarity in the characteristics of the autocorrelation functions for normal load acceleration magnitude and the zero-mean state variable, $\underline{\varepsilon}$.

Example

$$\alpha = 8, \quad \beta = -4, \quad \gamma = 0.5$$
$$\tau_\varepsilon = 1, \quad q = 2 \tag{C-45}$$

Exact solution: (Eq C-36)

$$R_a(\tau) = -8.522 + 20.544 \exp [0.25 \exp (-|\tau|)] \tag{C-46}$$

Approximate solution: (Eq C-42)

$$R_a(\tau) \approx 12.023 + 5.136 \exp (-|\tau|) \tag{C-47}$$

These functions are plotted in Fig. C-1 along with the autocorrelation for $\underline{\varepsilon}$.

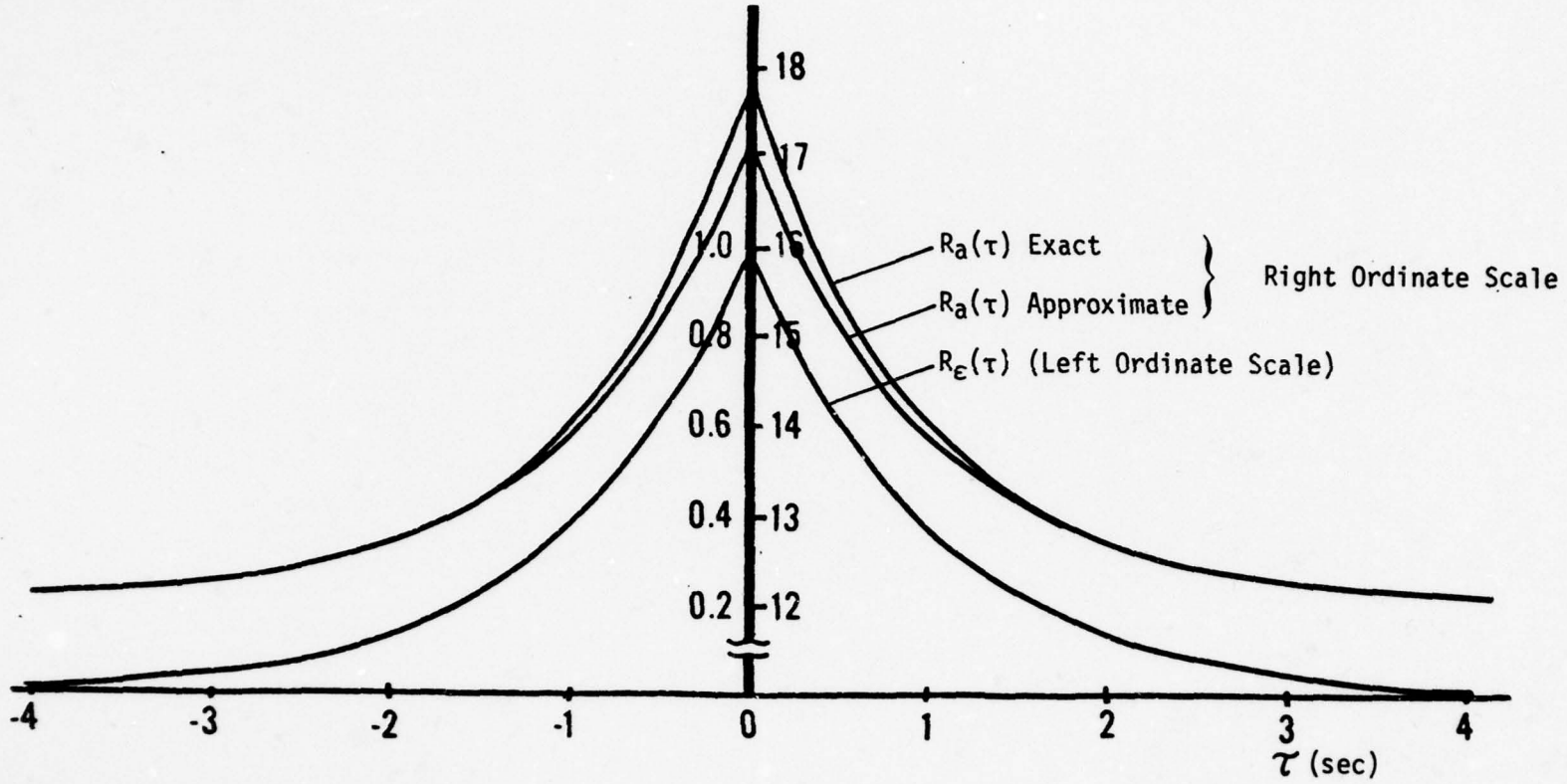


Fig. C-1. Autocorrelation Function For Normal Load Acceleration Magnitude And State Variable, $\underline{\varepsilon}$

## APPENDIX D

## Kinematically Derived Target Aspect

### Yaw and Pitch From Roll Axis Definition

This section of Appendix D determines the corresponding values of aircraft yaw and pitch assuming the roll axis is defined by the inertial velocity vector (assumes angle of attack is zero). The aircraft velocity vector in inertial coordinates is given by:

$$\bar{V}^I = \begin{bmatrix} V_x \\ V_y \\ V_z \end{bmatrix} \tag{D-1}$$

Define a unit vector in the velocity direction as:

$$\bar{1}_V = \frac{1}{V} \begin{bmatrix} V_x \\ V_y \\ V_z \end{bmatrix} \tag{D-2}$$

where

$$V = (V_x^2 + V_y^2 + V_z^2)^{\frac{1}{2}} \tag{D-3}$$

The projection into the x-y (horizontal) plane of this unit vector is simply

$$\begin{bmatrix} \frac{V_x}{V} \\ \frac{V_y}{V} \\ 0 \end{bmatrix}$$

Yaw is the angle between this projection and the x axis. Hence, by the dot product rule,

$$[1 \quad 0 \quad 0] \begin{bmatrix} \frac{V_x}{V} \\ \frac{V_y}{V} \\ 0 \end{bmatrix} = \frac{V_x}{V} = [(\frac{V_x}{V})^2 + (\frac{V_y}{V})^2]^{\frac{1}{2}} \cos \psi \tag{D-4}$$

$$\psi = \arccos\left(\frac{V_x}{[(V_x)^2 + (V_y)^2]^{\frac{1}{2}}}\right) \tag{D-5}$$

Pitch is the elevation of the total velocity vector above the x-y plane. Recalling that inertial z is down,

$$V_z = -V \sin \theta \tag{D-6}$$

$$\theta = -\arcsin (\frac{V_z}{V}) \tag{D-7}$$

Euler Angles from Target Kinematics

This section of Appendix D develops aircraft attitude from total velocity, total acceleration and the relationship between angle of attack, normal load acceleration and airspeed.

First, load acceleration is defined as acceleration minus gravity,

$$\bar{a}_L = \bar{a}_{t/I} - \bar{g} \tag{D-8}$$

where

$$\bar{a}_{t/I} = \frac{d}{dt}(\bar{V}_{t/I}) \tag{D-9}$$

and $\bar{g}$ is in the inertial z direction, with magnitude approximately 32.17 ft/sec$^2$ at sea level. Coordinated flight is assumed (no lateral component of velocity) and normal load acceleration is formed by removing from the load acceleration any component of load acceleration along the velocity vector,

$$\bar{a}_N = \bar{a}_L - \left( \frac{\bar{V}_{t/I} \cdot \bar{a}_L}{V^2_{t/I}} \right) \bar{V}_{t/I} \tag{D-10}$$

The transformation from inertial to body axes, required in order to obtain Euler angles, is given by

$$T^I_b = T^v_b \, T^I_v = T^v_b (T^v_I)^T \tag{D-11}$$

First, $T^v_I$ is obtained. Velocity is along the $x^v$ axis, normal load acceleration is along the negative $z^v$ axis and $y^v$ completes the right-hand frame. For brevity, let the components of $\bar{V}_{t/I}$ be denoted as $V_x$, $V_y$, and $V_z$.

Hence,

$$T^v_I = \begin{bmatrix} \frac{V_x}{V} & t_{12} & \frac{-a_{N_x}}{a_N} \\ \frac{V_y}{V} & t_{22} & \frac{-a_{N_y}}{a_N} \\ \frac{V_z}{V} & t_{32} & \frac{-a_{N_z}}{a_N} \end{bmatrix} \tag{D-12}$$

Since the second column of $T^v_I$ is to be perpendicular to both $\bar{V}_{t/I}$ and $\bar{a}_N$, the direction of this column vector is along the cross-product of $\bar{V}_{t/I}$ and $\bar{a}_N$. Using the skew-symmetric matrix form of the cross-product rule,

$$\begin{bmatrix} t_{12} \\ t_{22} \\ t_{32} \end{bmatrix} = - \begin{bmatrix} 0 & \frac{-V_z}{V} & \frac{V_y}{V} \\ \frac{V_z}{V} & 0 & \frac{-V_x}{V} \\ \frac{-V_y}{V} & \frac{V_x}{V} & 0 \end{bmatrix} \begin{bmatrix} \frac{-a_{N_x}}{a_N} \\ \frac{-a_{N_y}}{a_N} \\ \frac{-a_{N_z}}{a_N} \end{bmatrix} \tag{D-13}$$

$$\begin{bmatrix} t_{12} \\ t_{22} \\ t_{32} \end{bmatrix} = \frac{1}{Va_N} \begin{bmatrix} -V_z a_{N_y} + V_y a_{N_z} \\ V_z a_{N_x} - V_x a_{N_z} \\ -V_y a_{N_x} + V_x a_{N_y} \end{bmatrix} \tag{D-14}$$

The velocity frame must now be rotated through the angle of attack to form the body frame as illustrated in Figure D-1.

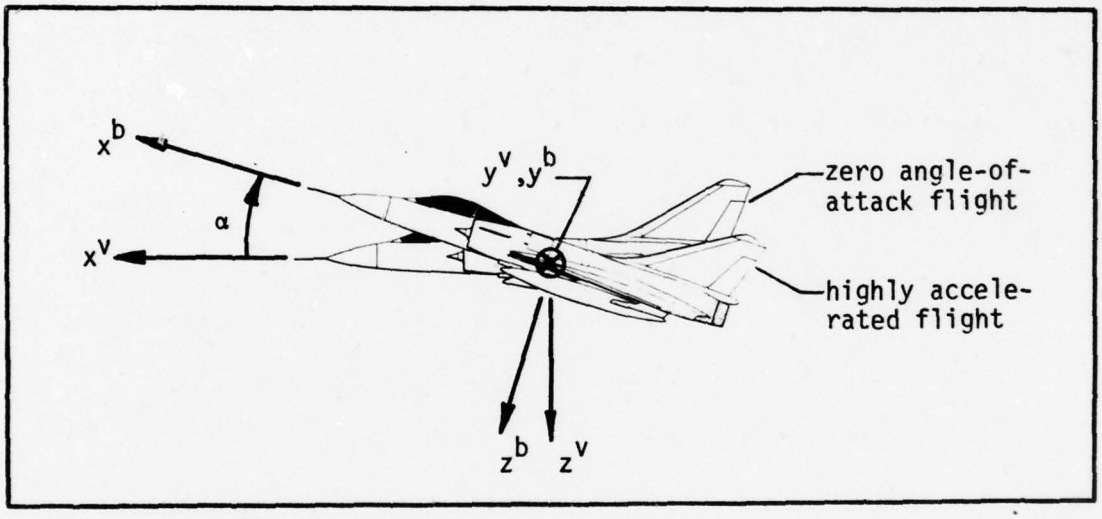


Fig. D-1. Angle-of-Attack Geometry

$$T_b^v = \begin{bmatrix} \cos\alpha & 0 & -\sin\alpha \\ 0 & 1 & 0 \\ \sin\alpha & 0 & \cos\alpha \end{bmatrix} \tag{D-15}$$

(An expression for angle of attack will be developed later in this section relating it to load factor and airspeed.) Combining the two transformations,

$$T_b^I = T_b^v \, T_v^I \tag{D-16}$$

AD-A066 195 AIR FORCE INST OF TECH WRIGHT-PATTERSON AFB OHIO SCH--ETC F/G 17/8
ESTIMATION OF AIRCRAFT TARGET MOTION USING PATTERN RECOGNITION --ETC(U)
DEC 78 J D KENDRICK

UNCLASSIFIED AFIT/DS/EE/78-6 NL

3 OF 3
AD
A066 195

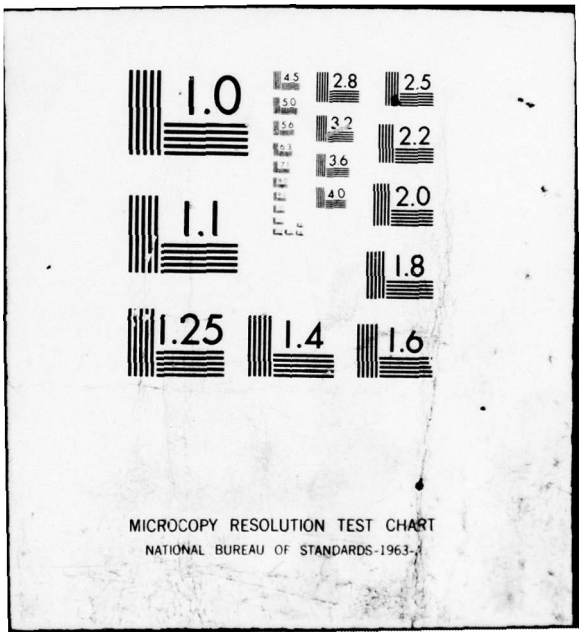
1.0
1.1
1.25
1.4
1.6
1.8
2.0
2.2
2.5
2.8
3.2
3.6
4.0
4.5
5.0
5.6
MICROCOPY RESOLUTION TEST CHART
NATIONAL BUREAU OF STANDARDS-1963-A

$$T_b^I = \begin{bmatrix} \left(\frac{V_x C\alpha}{V} + \frac{a_{N_x} S\alpha}{a_N}\right) & \left(\frac{V_y C\alpha}{V} + \frac{a_{N_y} S\alpha}{a_N}\right) & \left(\frac{V_z C\alpha}{V} + \frac{a_{N_z} S\alpha}{a_N}\right) \\ \left(\frac{V_y a_{N_z} - V_z a_{N_y}}{V a_N}\right) & \left(\frac{V_z a_{N_x} - V_x a_{N_z}}{V a_N}\right) & \left(\frac{V_x a_{N_y} - V_y a_{N_x}}{V a_N}\right) \\ \left(\frac{V_x S\alpha}{V} - \frac{a_{N_x} C\alpha}{a_N}\right) & \left(\frac{V_y S\alpha}{V} - \frac{a_{N_y} C\alpha}{a_N}\right) & \left(\frac{V_z S\alpha}{V} - \frac{a_{N_z} C\alpha}{a_N}\right) \end{bmatrix} \qquad \text{(D-17)}$$

Where C and S represent cosine and sine, respectively. From Appendix B, $T_b^I$ is known to be

$$T_b^I = \begin{bmatrix} C\theta C\psi & C\theta S\psi & -S\theta \\ S\phi S\theta C\psi - C\phi S\psi & S\phi S\theta S\psi + C\phi C\psi & S\phi C\theta \\ C\phi S\theta C\psi + S\phi S\psi & C\phi S\theta S\psi - S\phi C\psi & C\phi C\theta \end{bmatrix} \qquad \text{(D-18)}$$

Hence, solving for $\psi$, $\theta$ and $\phi$ by equating terms,

$$\psi = \arctan\left[\left(\frac{V_y C\alpha}{V} + \frac{a_{N_y} S\alpha}{a_N}\right)\Big/\left(\frac{V_x C\alpha}{V} + \frac{a_{N_x} S\alpha}{a_N}\right)\right] \qquad \text{(D-19)}$$

$$\theta = -\text{arscin}\left(\frac{V_z C\alpha}{V} + \frac{a_{N_z} S\alpha}{a_N}\right) \qquad \text{(D-20)}$$

$$\phi = \arctan\left[\left(\frac{V_x a_{N_y} - V_y a_{N_x}}{V a_N}\right)\Big/\left(\frac{V_z S\alpha}{V} - \frac{a_{N_z} C\alpha}{a_N}\right)\right] \qquad \text{(D-21)}$$

Angle of attack can be related to load factor and airspeed through the aerodynamic lift equation,

$$nW = L = \tfrac{1}{2}\rho V^2 C_L S = \tfrac{1}{2}\rho V^2 C_{L_\alpha}(\alpha - \alpha_o)S \qquad \text{(D-22)}$$

$n$ = load factor (g's)

$W$ = weight (lbs; assume sea level gravity)

$L$ = lift force (lbs = slug ft/sec$^2$)

$\rho$ = air density (slugs/ft$^3$)

$V$ = airspeed (ft/sec)

$C_L$ = coefficient of lift (dimensionless)

$C_{L_\alpha}$ = coefficient of lift for $\alpha$ (dimensionless)

$\alpha$ = angle of attack (radians)

$\alpha_o$ = angle of attack for zero lift (radians)

$S$ = effective airfoil surface area (ft$^2$)

This equation provides a good model of $\alpha$ and load factor over the full flying range of the airfoil. The coefficient $C_{L_\alpha}$ is fairly constant to within a few degrees of airfoil stall.

Solving for $\alpha - \alpha_o$,

$$\alpha - \alpha_o = K\left(\frac{n}{V^2}\right) \qquad \text{(D-23)}$$

where

$$K = \frac{2W}{\rho C_{L_\alpha} S} \qquad \text{(D-24)}$$

$\alpha_o$ is assumed zero for symmetrical airfoils such as the F-4 and is only a few degrees for other modern fighter aircraft without symmetrical airfoils.

Example.

The following example illustrates the use of this procedure to obtain target aircraft attitude from target velocity and acceleration. The data is from a typical FASTAC simulator scenario at approximately 20,000 feet altitude. The usual north-east-down inertial system is used.

Given:

$$\bar{V}_{t/I}^T = [563.95 \quad 510.25 \quad 19.58] \text{ ft/sec}, \quad V = |\bar{V}_{t/I}| = 760.77 \text{ ft/sec} \quad \text{(D-25)}$$

$$\bar{a}_{t/I}^T = [130.61 \quad -138.33 \quad 98.12] \text{ ft/sec}^2 \quad \text{(D-26)}$$

Also for comparison, the actual values of target attitude Euler angles, available from the simulator, are given as

$$\left.\begin{aligned} \psi &= 21.46^o \\ \theta &= -8.32^o \\ \phi &= -107.28^o \end{aligned}\right\} \quad \text{(D-27)}$$

Following the procedure outlined earlier,

$$\bar{a}_L^T = [130.61 \quad -138.33 \quad 65.95] \quad \text{(D-28)}$$

$$\frac{\bar{V}_{t/I} \cdot \bar{a}_L}{|\bar{V}_{t/I}|^2} = 0.00754 \quad \text{(D-29)}$$

$$\bar{a}_N = \begin{bmatrix} 130.61 \\ -138.33 \\ 65.95 \end{bmatrix} - (0.00754) \begin{bmatrix} 563.95 \\ 510.25 \\ 19.58 \end{bmatrix} = \begin{bmatrix} 126.36 \\ -142.18 \\ 65.80 \end{bmatrix} \quad \text{(D-30)}$$

$$|\bar{a}_N| = 201.28 \text{ ft/sec}^2 = 6.26 \text{ g's} \quad \text{(D-31)}$$

$$\begin{bmatrix} V_x/V \\ V_y/V \\ V_z/V \end{bmatrix} = \begin{bmatrix} 0.741 \\ 0.671 \\ 0.026 \end{bmatrix}, \quad \begin{bmatrix} a_{N_x}/a_N \\ a_{N_y}/a_N \\ a_{N_z}/a_N \end{bmatrix} = \begin{bmatrix} 0.628 \\ -0.706 \\ 0.327 \end{bmatrix} \quad \text{(D-32)}$$

Assume $\alpha_o = 0$

$$\alpha = K\left(\frac{n}{V^2}\right), \quad \text{where } n = |\bar{a}_N| = 6.26 \text{ g's} \tag{D-33}$$

A good approximation for $\rho$ for altitudes up to 35,000 feet [30 ] is

$$\rho = 0.002378\ [1 - 6.879 \times 10^{-6} h]^{4.258} \text{ slugs/ft}^3 \tag{D-34}$$

where h is in feet.

$$h = 20{,}000 \text{ feet}$$

$$\rho = (0.002378)(0.532) = 0.00127 \text{ slugs/ft}^3$$

$$C_{L_\alpha} = 3.4$$

$$S = 530 \text{ ft}^2$$

$$W = 1210 \text{ slugs} \times 32.17 \text{ ft/sec}^2 = 38{,}925.7 \text{ lbs}$$

$$K = \frac{2W}{\rho C_{L_\alpha} S} = 34{,}018 \frac{(\text{rad})(\text{ft}^2)}{\text{sec}^2}$$

$$\alpha(\text{rad}) = 34{,}018\ \left[\frac{6.26}{(760.77)^2}\right] = 0.368 \text{ rad} = 21.1^o \tag{D-35}$$

Substituting equations D-25, D-30, D-31, D-35 into equations D-19, D-20, D-21, the deduced target aircraft Euler angles are computed to be

$$\left.\begin{aligned} \psi &= \arctan\left(\frac{0.372}{0.917}\right) = 22.08^o \\ \theta &= -\arcsin\,(0.142) = -8.16^o \\ \phi &= \arctan\left(\frac{-0.945}{-0.296}\right) = -107.33^o \end{aligned}\right\} \tag{D-36}$$

Comparison of equations D-27 to equations D-36 demonstrates the feasibility of this technique for deducing approximate aircraft attitude from kinematic observations.

The methods of the two sections are compared in Table D-I for this particular example. The superiority of the second method is clearly evident.

Table D-I. Aspect Angle Determination, Example

| | True | Method Without Angle of Attack | Method Using Angle of Attack |
|---|---|---|---|
| Yaw | 21.46 | 42.14 | 22.08 |
| Pitch | -8.32 | -1.47 | -8.16 |
| Roll | -107.28 | (not computed in this method) | -107.33 |

## APPENDIX E

### Pre-Tuning and Tuned Filter Parameters

Table E-I. Kinematic Initial State Covariance, $P_o$

| Kinematic Initial State Covariance, $P_o$ | | | |
|---|---|---|---|
| Element | State | Value | Represents($1\sigma$) |
| $P_{11}$ | $p^I_{t/a_n}$ | 100 | 10 feet |
| $P_{22}$ | $p^I_{t/a_e}$ | 100 | 10 feet |
| $P_{33}$ | $p^I_{t/a_d}$ | 100 | 10 feet |
| $P_{44}$ | $V^I_{t/a_n}$ | 100 | 10 ft/sec |
| $P_{55}$ | $V^I_{t/a_e}$ | 100 | 10 ft/sec |
| $P_{66}$ | $V^I_{t/a_d}$ | 100 | 10 ft/sec |
| $P_{77}$ | $\delta a_n$ | 4096 | 2 g |
| $P_{88}$ | $\delta a_e$ | 4096 | 2 g |
| $P_{99}$ | $\delta a_d$ | 4096 | 2 g |
| $P_{10,10}$ | $\epsilon$ | 1 | 1 |

Table E-II. Kinematic Modeling Covariance, Q

| Kinematic Modeling Covariance, Q | | |
|---|---|---|
| Element | Derivative | Pre-Tuning and Tuned Value |
| $Q_{11}$ | $\dot{V}_{t/a_n}^{I}$ | 1024 |
| $Q_{22}$ | $\dot{V}_{t/a_e}^{I}$ | 1024 |
| $Q_{33}$ | $\dot{V}_{t/a_d}^{I}$ | 1024 |
| $Q_{44}$ | $\dot{\delta a}_n$ | 256 |
| $Q_{55}$ | $\dot{\delta a}_e$ | 256 |
| $Q_{66}$ | $\dot{\delta a}_d$ | 256 |
| $Q_{77}$ | $\dot{\epsilon}$ | 2 |

Table E-III. Kinematic Measurement Covariance, R

*Kinematic Measurement Covariance, R

| Element | Measurement | Value | Represents (1σ) |
|---|---|---|---|
| $R_{11}$ | Range, r | 2500 | 50 feet |
| $R_{22}$ | Azimuth, $\eta$ | .000004 | 2 milliradians(mrad) |
| $R_{33}$ | Elevation, $\xi$ | .000004 | 2 mrad |
| $R_{44}$ | Range Rate, $\dot{r}$ | 2500 | 50 ft/sec |
| $R_{55}$ | Azimuth Rate, $\dot{\eta}$ | .000016 | 4 mrad/sec |
| $R_{66}$ | Elevation Rate, $\dot{\xi}$ | .000016 | 4 mrad/sec |

* $\sigma^2$ for each measurement is the same as the corresponding element of the R matrix, i.e., no mismatching of actual noises and filter's noise model, for the baseline filter configuration.

Table E-IV. Aspect Initial State Covariance, $P_{a_o}$

| Aspect Initial State Covariance, $P_{a_o}$ | | | |
|---|---|---|---|
| Element | State | Value | Represents (1σ) |
| $P_{a_{11}}$ | $\psi$ | 16 | 4 degrees |
| $P_{a_{22}}$ | $\theta$ | 16 | 4 degrees |
| $P_{a_{33}}$ | $\phi$ | 16 | 4 degrees |
| $P_{a_{44}}$ | $\dot{\psi}$ | 100 | 10 deg/sec |
| $P_{a_{55}}$ | $\dot{\theta}$ | 100 | 10 deg/sec |
| $P_{a_{66}}$ | $\dot{\phi}$ | 100 | 10 deg/sec |

Table E-V. Aspect Modeling Covariance, $Q_a$

| Aspect Modeling Covariance, $Q_a$ | | | |
|---|---|---|---|
| Element | Derivative | Pre-Tuning Value ($deg^2/sec^3$) | Tuned Value ($deg^2/sec^3$) |
| $Q_{a_{11}}$ | $\ddot{\psi}$ | 100 | 225 |
| $Q_{a_{22}}$ | $\ddot{\theta}$ | 100 | 225 |
| $Q_{a_{33}}$ | $\ddot{\phi}$ | 100 | 225 |

Table E-VI. Aspect Measurement Covariance, $R_a$

| *Aspect Measurement Covariance, $R_a$ | | | |
|---|---|---|---|
| Element | Measurement | Pre-Tuning And Tuned Value | Represents (1σ) |
| $R_{a_{11}}$ | ψ(PR) | 25 | 5 degrees |
| $R_{a_{22}}$ | θ(PR) | 25 | 5 degrees |
| $R_{a_{33}}$ | φ(PR) | 25 | 5 degrees |
| $R_{a_{44}}$ | ψ(Kine) | 100 | 10 degrees |
| $R_{a_{55}}$ | θ(Kine) | 100 | 10 degrees |
| $R_{a_{66}}$ | φ(Kine) | 100 | 10 degrees |

* $\sigma^2$ for each actual E-O/pattern recognition measurement is set to the corresponding value of $R_a$ elements (1,1), (2,2) and (3,3). The remaining diagonal elements of $R_a$ represent an a priori estimate of uncertainty in kinematically derived target yaw, pitch and roll.

Table E-VII. Remaining Filter Parameters, Interactive Filter

| Parameter | Description | Value |
|---|---|---|
| $\alpha$ | Normal accel. parameter | 8 |
| $\beta$ | Normal accel. parameter | -4 |
| $\gamma$ | Normal accel. parameter | 0.5 |
| $\tau_n, \tau_e, \tau_d$ | Non-normal accel. time constants (north, east down directions) | 1.0 sec (Pre-Tuning) 4.0 sec (Tuned) |

Table E-VIII. Radar Initial State Covariance, $P_o$

| Radar Initial State Covariance, $P_o$ | | | |
|---|---|---|---|
| Element | State | Value | Represents (1σ) |
| $P_{11}$ | $P^{I}_{t/a_n}$ | 100 | 10 feet |
| $P_{22}$ | $P^{I}_{t/a_e}$ | 100 | 10 feet |
| $P_{33}$ | $P^{I}_{t/a_d}$ | 100 | 10 feet |
| $P_{44}$ | $V^{I}_{t/a_n}$ | 100 | 10 ft/sec |
| $P_{55}$ | $V^{I}_{t/a_e}$ | 100 | 10 ft/sec |
| $P_{66}$ | $V^{I}_{t/a_d}$ | 100 | 10 ft/sec |
| $P_{77}$ | $a^{I}_{t/a_n}$ | 4096 | 2 g |
| $P_{88}$ | $a^{I}_{t/a_e}$ | 4096 | 2 g |
| $P_{99}$ | $a^{I}_{t/a_d}$ | 4096 | 2 g |

Table E-IX. Radar Modeling Covariance, Q

| Radar Modeling Covariance, Q | | |
|---|---|---|
| Element | Derivative | Pre-Tuning and Tuned Values |
| $Q_{11}$ | $\dot{a}_{t/a_n}^{I}$ | 4096 |
| $Q_{22}$ | $\dot{a}_{t/a_e}^{I}$ | 4096 |
| $Q_{33}$ | $\dot{a}_{t/a_d}^{I}$ | 4096 |

Table E-X. Remaining Filter Parameters, Radar Filter

| Parameter | Description | Pre-Tuning Value | Tuned Value |
|---|---|---|---|
| $\tau_n$ | Relative accel. time constant (north component) | 1.0 sec | 4.0 sec |
| $\tau_e$ | Relative accel. time constant (east component) | 1.0 sec | 4.0 sec |
| $\tau_d$ | Relative accel. time constnat (down component) | 1.0 sec | 4.0 sec |

# VITA

Jerry Donald Kendrick was born on 19 August 1944 in Troy, Alabama. He graduated from high school in Vernon, Florida in 1962 and attended the University of Florida, from which he received the degrees of Bachelor of Science in Electrical Engineering with High Honors in August 1967 and Master of Electrical Engineering in August 1968. While at the University of Florida he was elected to the honorary societies of Tau Beta Pi, Eta Kappa Nu, Sigma Tau, and Phi Kappa Phi. He attended Officer Training School at Lackland AFB, Texas and received a commission in the United States Air Force in December 1968. He served as project engineer in a classified satellite system program office at the Space and Missile Systems Organization, Los Angeles, California, until entering the School of Engineering, Air Force Institute of Technology in July 1973. Upon completion of course work and PhD qualifying examinations, he joined the Air Force Avionics Laboratory, Fire Control Branch of the Reconnaissance and Weapon Delivery Division, in September 1975 to complete the degree requirements.

Permanent address: P.O. Box 214
Vernon, Florida 32462

UNCLASSIFIED

SECURITY CLASSIFICATION OF THIS PAGE (When Data Entered)

| REPORT DOCUMENTATION PAGE | | READ INSTRUCTIONS BEFORE COMPLETING FORM |
|---|---|---|
| 1. REPORT NUMBER<br>AFIT/DS/EE/78-6 | 2. GOVT ACCESSION NO. | 3. RECIPIENT'S CATALOG NUMBER |
| 4. TITLE (and Subtitle)<br>ESTIMATION OF AIRCRAFT TARGET MOTION USING PATTERN RECOGNITION ORIENTATION MEASUREMENTS | | 5. TYPE OF REPORT & PERIOD COVERED<br>PhD Dissertation<br>6. PERFORMING ORG. REPORT NUMBER |
| 7. AUTHOR(s)<br>Jerry D. Kendrick<br>Captain, USAF | | 8. CONTRACT OR GRANT NUMBER(s) |
| 9. PERFORMING ORGANIZATION NAME AND ADDRESS<br>Air Force Institute of Technology (AFIT-EN)<br>Wright-Patterson AFB, Ohio 45433 | | 10. PROGRAM ELEMENT, PROJECT, TASK AREA & WORK UNIT NUMBERS |
| 11. CONTROLLING OFFICE NAME AND ADDRESS<br>Air Force Avionics Laboratory (AFAL/RWT)<br>Wright-Patterson AFB, Ohio 45433 | | 12. REPORT DATE<br>December 1978<br>13. NUMBER OF PAGES<br>207 |
| 14. MONITORING AGENCY NAME & ADDRESS(if different from Controlling Office) | | 15. SECURITY CLASS. (of this report)<br>Unclassified<br>15a. DECLASSIFICATION/DOWNGRADING SCHEDULE |

16. DISTRIBUTION STATEMENT (of this Report)

Approved for public release; distribution unlimited

17. DISTRIBUTION STATEMENT (of the abstract entered in Block 20, if different from Report)

18. SUPPLEMENTARY NOTES

Approved for public release; IAW AFR 190-17

Joseph P. Hipps, Major, USAF
Director of Information FEB 8 1979

19. KEY WORDS (Continue on reverse side if necessary and identify by block number)

Kalman Filtering
Pattern Recognition
Maneuvering Aircraft Targets
Air-to-air Tracking
Aircraft Orientation
Acceleration Modeling

20. ABSTRACT (Continue on reverse side if necessary and identify by block number)

A new approach to estimating motion of a highly maneuvering aircraft target in an air-to-air tracking scenario is presented. An interactive filter system is developed which provides an improved estimate of target motion states by conditioning kinematic filter estimates upon target aspect angle data. Pattern recognition techniques used with an electro-optical tracker are presumed to provide this target aspect information. A target orientation filter processes the aspect angle measurements by statistically weighting measured aspect angles with the current best estimate of target kinematics. The aerodynamic lift

DD FORM 1 JAN 73 1473 EDITION OF 1 NOV 65 IS OBSOLETE

UNCLASSIFIED

SECURITY CLASSIFICATION OF THIS PAGE (When Data Entered)

equation is used to relate approximate angle of attack to target velocity and acceleration. A novel statistical model for aircraft target normal acceleration is also developed to better represent unknown target accelerations. Simulation results of realistic three-dimensional scenarios are presented to evaluate the performance of the interactive filter system. The report contains a 56-item bibliography.